Chiral active fluids

Odd viscosity, active turbulence, and directed flows of hydrodynamic microrotors

Inaugural-Dissertation
zur
Erlangung des Doktorgrades
der Mathematisch-Naturwissenschaftlichen Fakultät
der Universität zu Köln

vorgelegt von
Joscha Mecke
aus Geldern

Köln, 2022

GutachterInnen:	Dr. habil. Marisol Ripoll
	Prof. Dr. Joachim Krug
	Prof. Dr. Hartmut Löwen
Tag der mündlichen Prüfung:	25.01.2023

Contents

List of publications

Partially, results of this thesis have been prepared for publication in a peer-reviewed journal. The corresponding manuscript "Simultaneous emergence of active turbulence and odd viscosity in a colloidal chiral active system" has been prepared collaboratively by J.M., Y. Gao, C.A. Ramírez-Medina, D.G.A.L. Aarts, G. Gompper, and M. Ripoll, 28 September 2022, PREPRINT (Version 1) available at Research Square [https://doi.org/10.21203/rs.3.rs-2072915/v1], licensed under a CC BY 4.0 License (https://creativecommons.org/licenses/by/4.0/). The article is referred to as [M] in the following. According to the Doctoral Regulations of the Faculty of Mathematics and Natural Sciences of the University of Cologne of March 12, 2020, a comprehensive, in itself intelligible explanation of the significance of [M] in the context of the dissertation, as well as a clarification of which specific contributions were made by me is given here. I wrote the underlying simulation code under the supervision of M. Ripoll and G. Gompper and assistance of C.A. Ramírez-Medina, performed the simulations, analysed the numeric data and partially the experimental data, wrote the original draft collaboratively with Y. Gao and M. Ripoll, and finalised the manuscript collaboratively with Y. Gao, D.G.A.L. Aarts, G. Gompper, and M. Ripoll. The simulations in the manuscript [M] are an essential part of this thesis. The bulk behaviour emanating from pair interactions of hydrodynamically coupled colloidal rotors is discussed in [M]. The results presented in [M] are deepened in the further parts of this thesis and applied to related systems. Direct experimental evidence is only shown in the excerpts from the experiments reported in the manuscript. [M] has been submitted to a peer-review journal on 16$^{\text{th}}$ September 2022.

Chapter 1

Introduction

1.1. Soft, active, and chiral matter

The first systematic address of soft matter physics was provided by Robert Brown's observations, that pollen grains immersed in water are "very evidently in motion" [1]. The findings excited further research, where especially Einstein's calculations [2] and Perrin's experiments are noteworthy, providing explanations for the random motion of the pollen grains which finally proved the existence of atoms [3]. Today, such pollen grains are known as colloidal particles, *i.e.*, they are suspended in a fluid and of size much larger than the fluid molecules, but still small enough to be agitated by the fluid's thermal fluctuations [4]. This size range is neither atomistic, nor macroscopic and is referred to. On these length scales, thermal fluctuations play a crucial role and the relevant energy scale is $E \simeq k_{\mathrm{B}}T$. The random dynamics of colloids is known as Brownian motion, and serves as a paradigm of soft matter and biological physics. Generalisations of Brownian motion are used in order to explain polymer [5] and membrane [6] physics, processes like cell migration [7], (un-)binding and rupture of molecular bonds [8], and even finds applications in ecology, economics, or linguistics [9], just to name a few.

In biological physics, bacteria, sperm, and other organisms provide examples of living matter on the mesoscale. These systems are continually driven out of equilibrium such that the application of the concepts of equilibrium statistical mechanics, *e.g.*, Brownian motion, is not straightforwardly possible. For example, biological microswimmers like bacteria or sperm utilise rotating or beating flagella [10] in order to push the surrounding fluid into a particular direction and consequently move into the opposite direction, resulting in active dynamics as illustrated in figure 1.1a. More generally, active matter systems consist out of agents that are externally driven or are capable of converting energy into forces or torques, such that an inherent motion is induced [10,11]. Then, depending on the interactions between the active agents, different phenomena like collective dynamics or structure formation emerge. Such emergence can be found over a diverse range of length scales such as cytoskeletal dynamics in living cells [12], swarming in bacterial colonies [13], or cluster, swarm, and lane formation in self-phoretic colloids [14,15] on the mesoscopic length scale, and a related phenomenology is observed in the dynamics of flocks of birds [16], schools of fish [17], pedestrians [18], and traffic [19]. The understanding of the nonequilibrium physics of mesoscale active matter is a key challenge in order to comprehend the processes of life and ultimately to design protocols to understand and manipulate biological processes, such as cancer invasion [20–22], *in vitro* fertilisation [23], bio-film formation [24,25], or

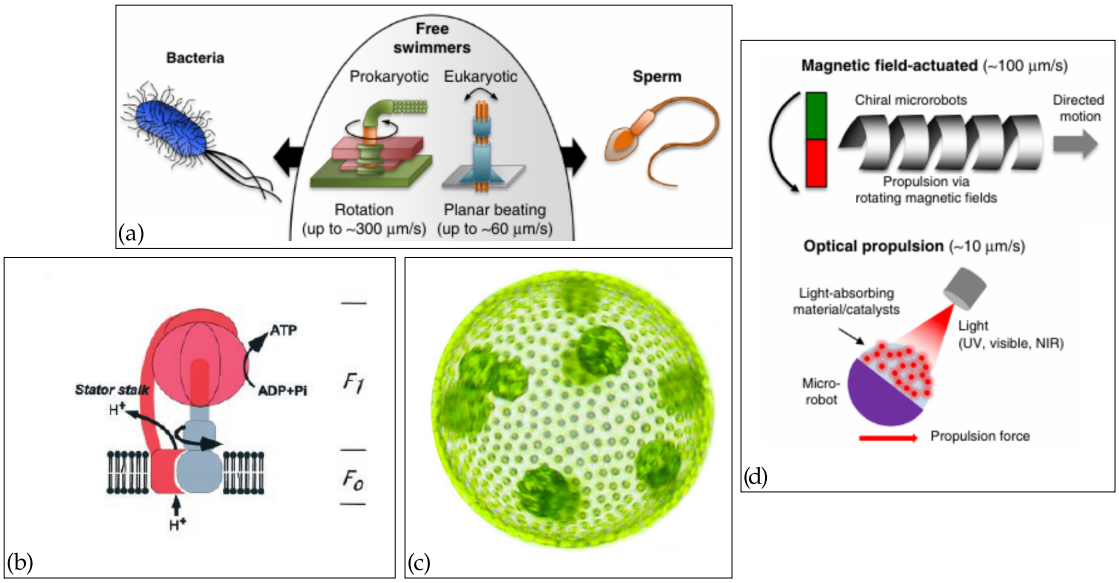

Figure 1.1: Internally active and externally actuated matter on the mesoscale. (a) Beating and rotating flagella generating propulsion. Image adapted from [20], licensed under CC BY (https://creativecommons.org/licenses/). (b) Working mechanism of the biological rotary machine ATP synthase, consisting out of the F_1 motor and the membrane embedded F_0 motor connected by a stalk in order to prevent co-rotation. The chemical potential difference for protons across the membrane is converted into chemical energy of ATP synthesis causing a rotation. The motor is reversed by the opposite chemical reaction. Image taken from [30], licensed under CC BY (http://creativecommons.org/licenses/by/4.0/). (c) A *Volvox* colony. Flagella pairs are beating on each somatic cell (small dots), leading to directed motion and rotation. Larger darker regions are germ cells forming next generations. Image taken from [31], licensed under CC BY (http://creativecommons.org/licenses/by/4.0/). (d) Two designs of artificial microswimmers. Image adapted from [20], licensed under CC BY (https://creativecommons.org/licenses/).

targetted drug delivery on the microscopic scale [26–29].

Rotations are of importance in biological systems ranging from rotating subunits to collective vortical motion [32]. Examples are rotating motor proteins in membranes [33, 34] such as ATP synthase [30] (see figure 1.1b), co-rotating bound states of *Volvox* colonies [35] (see figure 1.1c), self-organised collective vortices of circularly moving spermatozoa [36, 37], or synchronised rotating flagella of adsorbed bacteria [38, 39]. For applications such as nanomedical drug delivery, micron sized particles capable of manipulation through imposed fields provide a promising track [23, 26–29], *e.g.*, externally applied magnetic fields can be used to move chiral particles through a solvent, or Janus type colloids propel along self-generated gradients to perform self-phoresis [10, 40]. Both examples are shown in figure 1.1d, where the phoretic propulsion is represented by self-thermophoresis, *i.e.*, one hemisphere of the particle is built from a light absorbing material, such that illumination with laser light at a specific frequency leads to the formation of a temperature gradient and the corresponding thermophoretic thrust. Particles with a magnetic moment are able to co-rotate with an externally applied rotating magnetic field [41–47], granting an extension to all types of active dynamics that solely employ the translational degrees of freedom by explicitly

employing the rotational degrees of freedom [48].

However, there is a fundamental difference between the hydrodynamic flow field of externally actuated rotation, *e.g.*, by rotation of external manipulation fields, and of internally active rotation powered by local energy consumption, *e.g.*, by the rotating motion of a beating flagellum [49]. While for externally actuated particles, an infinite angular momentum reservoir, provided by the externally prescribed torque, allows for the injection of angular momentum into the fluid, the hydrodynamic flow field powered by local energy consumption conserves angular momentum together with the thus induced counter-rotation of the rotor itself. Therefore, the locally energy consuming rotating object needs a thrust centre which is located outside the centre of mass such that net rotation can be obtained and a different flow field is excited compared to actuated rotors [50]. The work presented in this thesis focuses on externally actuated particles.

A key ingredient to transform rotational into translational energy is symmetry breaking [51, 52]. Isolated rotating particles do not show any net propulsion, while rotating colloids in the vicinity of walls or further nearby rotating colloids show the emergence of directed motion and rich collective phenomena, such as states of coherent rotational motion, vortex formation, or rotating flocks [53–55]. Hydrodynamic interactions between the rotating particles are a very important ingredient for long-ranged interactions [56] on different length scales ranging from micrometers to millimetres, which typically relates to a Reynolds number, *i.e.*, the ratio of inertial to frictional forces in the solvent, ranging from orders of 10^{-7} to 10 [57, 58]. Thereby, the Reynolds number $\mathcal{R}e$ of the corresponding flow plays an important role determining whether the interaction is attractive or repulsive. While for small but finite $\mathcal{R}e \gtrsim 1$ the nonlinear inertial terms of the Navier-Stokes equation imply repulsive interactions leading to the formation of lattice-like structures, at exceedingly small $\mathcal{R}e$, neither repulsion, nor attraction, but only a collective orbital rotation transmitted via frictional forces is observed [43, 45, 46, 59].

The hydrodynamic equations of motion are built on conservation laws and symmetry considerations. As a result, similar systems follow similar equations of motion, *e.g.*, liquids and gases both can be described by the Navier-Stokes equations. However, such an approach is not only limited to *usual* fluids, but can also be applied to any continuum, or as continuum approximated material, such as divers active matter continua [60–65]. For a chiral active fluid, *i.e.*, a *fluid* consisting out of particles that inherently rotate, *e.g.*, particles with an electromagnetic dipole in an externally rotating field [41–47, 58, 66], the internal stresses imply the emergence of a transport coefficient called odd viscosity which is absent in usual fluids [67]. The effects of odd viscosity have been experimentally elusive for years [68], but quite recently, several articles revealed theoretical [67, 69–72] and experimental [41, 73–76] insight into chiral active fluids with odd viscosity and related effects like odd elasticity [77–79] or odd diffusivity [80, 81]. Although, the studies also include the effects of odd viscosity on particles swimming through chiral active baths [82, 83] and active rheology [84, 85], odd viscosity itself has only sparsely been explicitly measured. While odd stresses in chiral active fluids leading to unidirectionally driven surface waves of cohesive droplets have been reported in an experimental study [41], correlations between vorticity and density [86] due to odd stresses pointing into the direction of gradients of vorticity have only been predicted analytically [67], but neither reported experimentally, nor in particle based simulations. The experimental and computational study of chiral active fluids is thus an important contribution to the understanding of such systems which can also foster

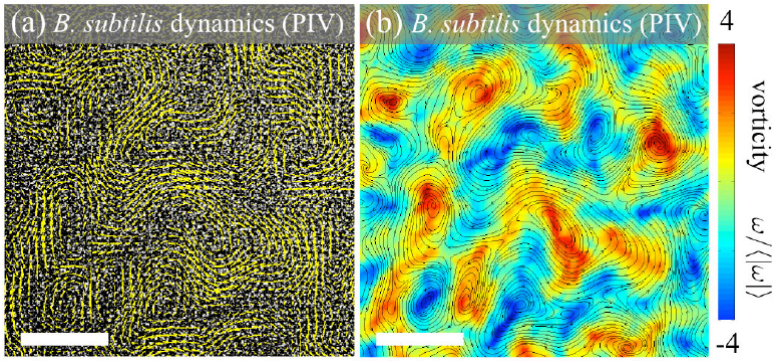

Figure 1.2: Experimental flow field (a) and streamlines with corresponding vorticity field (b) of bacterial turbulence in a dense and homogeneous suspension of *B. subtilis*, obtained from particle image velocimetry. Image taken from [87], licensed under CC BY (http://creativecommons.org/licenses/by/3.0/).

potential applications.

Another feature of hydrodynamically interacting rotors, *i.e.*, rotating colloids, is active turbulence [45, 58, 88], a term which is used for the chaotic dynamics of different types of dense active matter on the mesoscale bearing complex spatiotemporal structure, that is reminiscent of classical turbulence (see figure 1.2). To the realisations of active turbulence belong the coherent motion of swarming sperm [89], bacterial suspensions [87], or dense suspensions of filament and motor protein mixtures [63], which display chaotic flows of jets and swirls with long-ranged correlations at multiple length scales [90]. These active systems have microscopic differences in the interaction mechanics, *e.g.*, nematic or active stresses and hydrodynamics, leading to quantitative and qualitative differences between the diverse active systems [91–96]. A universal theory explaining the transport mechanisms of active turbulent systems is lacking, instead, different theoretical models and experiments show various scaling behaviours of the energy spectrum E_q [89, 90, 92, 97–100], *i.e.*, the amount of kinetic energy stored at wavenumber q, while for classical self-similar turbulence $E_q \propto q^{-5/3}$ is obtained. The relevant range of wavenumbers is for active and classical turbulence defined by the length scales at which energy is injected to the system and at which length scales it is dissipated. In the case of bacterial turbulence the dissipation length scale results from the interplay of hydrodynamics, steric alignment, inherent activity, and rotational noise [98, 101] and leads to the emergence of a dominant vortex scale. In these systems, energy is injected at the length scale l_0, *i.e.*, the size of the active units [92, 102], and dissipated at the dissipation length, typically on the order of $10l_0$. Thus an inverse energy cascade ranging over several orders of magnitude of length scales as in classical turbulence is impeded. In contrast to bacterial turbulence, the emergence of a dissipation scale is absent in the rotor fluid reported in reference [88] consisting out of a suspension of clockwise and counterclockwise rotating particles. Thus, energy is injected on the rotor scale and transported to larger scales and surprisingly even fulfils $E_q \propto q^{-5/3}$, which is reminiscent of the inverse energy cascade of 2D classical turbulence. Besides deepening the understanding of the differences and similarities between different systems exhibiting active turbulence and between active and classical turbulence, the study of mesoscale turbulence is of practical relevance to understand the processes of collective bacterial dynamics like colony or biofilm formation [24, 25]. Another important application of active turbulence in nature is

the effective transport and distribution of nutrients in cells or living fluids, or cancer invasion [102, 103]. Thus, active turbulence is a promising mechanism to effectively mix or stir and spread at low Reynolds numbers [97]. If the chaotic dynamics can be controlled, a predictive generation of mechanical work or fluxes could find diverse applications on the microscale [104].

In what follows, a rather technical introduction to the matter and its methods is presented. The closure of the introduction chapter is given by section 1.7, where the outline and a summary of this thesis is provided.

1.2. Colloid physics

1.2.1 Brownian motion

A standard way to describe the dynamics of a Brownian particle, *i.e.*, a colloid, is the Langevin equation, which balances the inertia of the particle of mass m with the forces stemming from the interactions of particle and fluid. The fluid contributions to the evolution of the position $\boldsymbol{r}$ and velocity $\boldsymbol{v}$ of the Brownian particle are a frictional force $-\zeta\boldsymbol{v}$, proportional to the friction coefficient ζ, and a random force $\boldsymbol{\xi}$ accounting for the thermal fluctuations in the fluid. Additionally, the particle may be subject to a conservative potential $\mathcal{U}$ and the corresponding force. Thus, the Langevin equation reads

$$m\dot{\boldsymbol{v}} = -\zeta\boldsymbol{v} - \boldsymbol{\nabla}\mathcal{U}(\boldsymbol{r}) + \boldsymbol{\xi}(t)\,. \tag{1.1}$$

The random force $\boldsymbol{\xi}(t)$ accounts for the perpetual thermal fluctuations of the fluid's molecules and is typically realised as a white noise, namely an isotropic, uncorrelated, Gaussian distributed random force [105] and is thus fully characterised by

$$\langle \boldsymbol{\xi}(t_1)\cdot\boldsymbol{\xi}(t_2)\rangle = 2dk_\mathrm{B}T\zeta\delta(t_1-t_2)\,, \tag{1.2a}$$
$$\langle \boldsymbol{\xi}(t)\rangle = 0\,, \tag{1.2b}$$

in a d-dimensional system at temperature T [106]. Here, $\langle\cdot\rangle$ denotes an average over several independent realisations of the noise. Equation (1.2a) links the strength of the driving fluctuations to the strength of the frictional dissipation and is known as the fluctuation-dissipation theorem.

Consider the case of a constant potential $\mathcal{U} \equiv \text{const}$. Even though, the solution for $\boldsymbol{r}$ does not show any net displacement, *i.e.*, $\langle\boldsymbol{r}\rangle = \boldsymbol{r}(t_0)$, the particle, driven by thermal fluctuations, explores space. A measure for the explored space is the mean-square displacement (MSD) $\langle\Delta r^2\rangle$, where $\Delta\boldsymbol{r} = \boldsymbol{r}(t) - \boldsymbol{r}(t_0) = \int_{t_0}^{t}\mathrm{d}t'\,\boldsymbol{v}(t')$, such that

$$\langle\Delta\boldsymbol{r}^2\rangle = 2d\frac{k_\mathrm{B}T}{\zeta}\left\{t - \frac{m}{\zeta} + \frac{m}{\zeta}e^{-\zeta t/m}\right\} \tag{1.3a}$$
$$\sim \begin{cases} 2d\frac{k_\mathrm{B}T}{\zeta}t\,, & \text{for } t \gg \frac{m}{\zeta} \\ d\frac{k_\mathrm{B}T}{\zeta}\left(\frac{t}{m/\zeta}\right)^2\,, & \text{for } t \ll \frac{m}{\zeta} \end{cases}, \tag{1.3b}$$

where $\sim$ denotes asymptotically equal in the corresponding limit. At early times, the particle moves ballistically, *i.e.*, $\langle\Delta\boldsymbol{r}^2\rangle \propto t^2$, and only when sufficient momentum has been transferred to the fluid via the frictional force, the dynamics becomes diffusive,

i.e., $\langle \Delta \boldsymbol{r}^2 \rangle \propto t$. The timescale on which the transition happens is the timescale of momentum relaxation $\tau_\mathrm{p} \equiv m/\zeta$.

If τ_p is sufficiently small, then the particle momentum is essentially immediately relaxed, such that the inertia of the particle can be effectively neglected in order to obtain a simpler description which is valid on slower time scales [107]. The full solution of equation (1.1) including the inertia term reads

$$\dot{\boldsymbol{r}}(t) = \boldsymbol{v}(t)\,, \tag{1.4a}$$

$$\boldsymbol{v}(t) = \boldsymbol{v}(t_0) e^{(t_0-t)/\tau_\mathrm{p}} + \frac{1}{m}\int_{t_0}^{t} \mathrm{d}t'\, e^{(t'-t)/\tau_\mathrm{p}} \left\{ -\boldsymbol{\nabla} \mathcal{U}(\boldsymbol{r}) + \boldsymbol{\xi}(t') \right\} \tag{1.4b}$$

If now a standard harmonic potential of stiffness k, *i.e.*, $\mathcal{U}(\boldsymbol{r}) = kr^2/2$, and an initial condition laying infinitely in the past ($t_0 \to -\infty$) is assumed, then upon insertion of equation (1.4b) into equation (1.4a), the obtained equation can be written as the generalised Langevin equation [106]

$$\dot{\boldsymbol{r}}(t) = -\int_{-\infty}^{t} \mathrm{d}t'\, r(t') K(t'-t) + \boldsymbol{\Xi}(t)\,, \tag{1.5}$$

with the useful definitions of the coloured noise $\boldsymbol{\Xi}(t)$ and the memory kernel $K(t)$

$$\boldsymbol{\Xi}(t) \equiv \frac{1}{m}\int_{-\infty}^{t} \mathrm{d}t'\, e^{(t'-t)/\tau_\mathrm{p}} \boldsymbol{\xi}(t')\,, \tag{1.6a}$$

$$K(s) \equiv \frac{k}{m} e^{-|s|/\tau_\mathrm{p}}\,, \tag{1.6b}$$

$$\langle \boldsymbol{\Xi}(t) \rangle = 0\,, \tag{1.6c}$$

$$\langle \boldsymbol{\Xi}(t_1) \cdot \boldsymbol{\Xi}(t_2) \rangle = \langle \boldsymbol{r}^2 \rangle\, K(t_1 - t_2)\,, \tag{1.6d}$$

where the equipartition theorem and the relationship between potential stiffness k and particle mass m for a harmonic potential $\omega^2 = k/m$ have been used, but no approximation is included. The variable $\boldsymbol{v}$ has been integrated out from the equation of motion (1.1), and the result is an equation for the position only. However, the result is no longer Markovian, *i.e.*, the dynamics at time t is no longer independent of configurations at time $t' < t$, but explicitly depends on previous realisations of the system through the memory kernel $K(t)$. This is a general consequence when integrating out *irrelevant* degrees of freedom [106]. Equation (1.6d) is a non-Markovian form of the fluctuation-dissipation-theorem. Such a generalised Langevin formalism is used typically to describe anomalous diffusion, *i.e.*, $\langle \Delta r^2 \rangle \propto t^\alpha$ with $\alpha \neq 1$ for $t \gg m/\zeta$, in complex systems like particles coupled to a polymer [108, 109] or intracellular transport [110], just to name a few.

However, in the current example if $\tau_\mathrm{p} \to 0$, a Markovian description is recovered, since then $K(s)$ may be approximated by a delta impulse of the same area [106]

$$K(s) \underset{\tau_\mathrm{p}\to 0}{\approx} 2\frac{k}{\zeta}\delta(s)$$

and the so-called overdamped equation of motion then reads

$$\zeta \dot{\boldsymbol{r}}(t) = -k\boldsymbol{r}(t) + \boldsymbol{\xi}(t)\,. \tag{1.7}$$

If the harmonic potential is removed, the mean-square displacement of equation (1.7) leads to the correct long time limit of equation (1.3a)

$$\langle \Delta \boldsymbol{r}^2 \rangle = 2d\frac{k_\mathrm{B}T}{\zeta} t\,. \tag{1.8}$$

Thus, the reasonable amount of microscopic details that should be contained in a theoretical description of statistical mechanics strongly depends on the relevant timescales of the process under consideration. Typically, the aim is to include as few microscopic details as possible to still capture the relevant physics.

The fluctuating dynamics of a Brownian particle can be alternatively described using the Fokker-Planck equation [111] which describes the evolution of the probability density $\mathcal{P}(\boldsymbol{r}, \dot{\boldsymbol{r}}, t)$ in phase space. In the case of overdamped dynamics, the corresponding equation is known as the Smoluchowski equation and describes the evolution in time and space only. It takes the following form in one dimension

$$\partial_t \mathcal{P}(x,t) = \left\{-\partial_x A + D\partial_x^2\right\} \mathcal{P}(x,t)\,. \tag{1.9}$$

Here, D is known as the diffusion constant and the term containing A is known as the drift term. If $A = 0$, then equation (1.9) is known as the diffusion equation. The connection between the Smoluchowski equation and the overdamped Langevin equation can be drawn using the Liouville equation [107]. Equation (1.9) is equivalent to

$$\dot{x} = \frac{1}{\zeta} A + \sqrt{D}\xi(t)\,, \tag{1.10a}$$

$$\langle \xi(t) \rangle = 0\,, \tag{1.10b}$$

$$\langle \xi(t_1)\xi(t_2) \rangle = \delta(t_1 - t_2)\,. \tag{1.10c}$$

The solution $\mathcal{P}$ of equation (1.9) with $A = 0$ describes the time evolution of the probability density, *i.e.*, it describes how the particle explores space according to equation (1.8). For $A = 0$ and initial condition $\mathcal{P}(x, t = 0) = \delta(x)$, it is

$$\mathcal{P}(x,t) = \frac{1}{\sqrt{4\pi D t}} e^{-\frac{x^2}{4Dt}}\,, \tag{1.11}$$

implying $\langle x^2 \rangle = 2Dt$, in accordance with equation (1.8). Furthermore, this establishes the Stokes-Einstein relation [106] that links the diffusion coefficient to the strength of thermal fluctuations $k_\mathrm{B}T$ and the friction experienced by the particle ζ

$$D = \frac{k_\mathrm{B}T}{\zeta}\,. \tag{1.12}$$

Note, that separate degrees of freedom are in general subject to separate fluctuating dynamics. Rotational Brownian motion describes the time evolution of the rotational degrees of freedom of colloidal particles. Assuming a rotational friction coefficient ζ^Ω, and a fluctuating torque $\boldsymbol{\xi}(t)^\Omega$, the overdamped equation for the rotational dynamics is [4]

$$\zeta^\Omega \boldsymbol{\Omega} = \boldsymbol{\xi}^\Omega(t)\,, \tag{1.13a}$$

$$\left\langle \boldsymbol{\xi}^\Omega(t) \right\rangle = 0\,, \tag{1.13b}$$

$$\left\langle \boldsymbol{\xi}^\Omega(t_1) \cdot \boldsymbol{\xi}^\Omega(t_2) \right\rangle = 2dk_\mathrm{B}T\zeta^\Omega \delta(t_1 - t_2)\,. \tag{1.13c}$$

The relaxation of the unit vector $\hat{e}$ indicating the orientation of the colloid follows an exponential decay [4, 106]

$$\langle \hat{e}(t) \cdot \hat{e}(0) \rangle = e^{-t/\tau_\mathrm{r}} \tag{1.14}$$

of lifetime τ_r, the timescale of rotational diffusion.

1.2.2 Active Brownian particles

The results of Brownian motion lose applicability when the system under investigation is driven out of equilibrium, because then the results of equilibrium statistical mechanics, like the fluctuation-dissipation or the equipartition theorem cease validity. Although, extensions of Brownian motion to out-of-equilibrium conditions are possible [9, 112, 113], different nonequilibrium situations will lead to a broad spectrum of interesting new effects. In that sense, the physics of a colloid in a nonequilibrium temperature profile will be different from that of a colloid that is additionally to the thermal agitation also subject to an inherent active driving. The most prominent example for an actively translating colloid is the model of active Brownian particles. Energy is locally converted into translational motion and the system is driven far from equilibrium.

An active Brownian particle is assumed to be subject to fluctuating overdamped dynamics according to equation (1.10a) with a drift term that propels the particle with a constant speed v_0 into the direction of the particle orientation $\hat{e}(t)$ [114], *i.e.*,

$$\dot{\boldsymbol{r}}(t) = v_0 \hat{e}(t) + \frac{1}{\zeta}\boldsymbol{\xi}(t)\,, \tag{1.15}$$

with the correlation and mean of the random force given by equations (1.2). The direction $\hat{e}(t)$ itself is subject to rotational Brownian motion according to equations (1.13). Using the Levi-Civita symbol

$$\varepsilon_{\alpha\beta\gamma} \equiv \begin{cases} 1 & \text{, if } \alpha = x, \beta = y, \gamma = z, \text{ and cyclic permutations} \\ -1 & \text{, for anticyclic permutations} \\ 0 & \text{, if } \alpha = \beta, \text{ or } \alpha = \gamma, \text{ or } \beta = \gamma \end{cases}, \tag{1.16}$$

with implied summation over repeated Greek indices denoting the configurational dimensions, *i.e.*, $a_\alpha b_\alpha \equiv \sum_\alpha a_\alpha b_\alpha$, equation (1.13a) can be rewritten to show explicitly the evolution of $\hat{e}(t)$

$$\partial_t e_\alpha = \frac{1}{\zeta^\Omega}\varepsilon_{\alpha\beta\gamma}\xi^\Omega_\beta e_\gamma\,. \tag{1.17}$$

Investigating the contributions in equations (1.15) and (1.17) individually, it is clear that the particle will be subject to normal diffusive dynamics according to equation (1.8) and will show a ballistic transport along the direction $\hat{e}$ until the direction itself has diffused out, *i.e.*, roughly until τ_r. A measure for the ratio of diffusion to persistent translation for an active Brownian particle of diameter σ is the Péclet number $\mathcal{P}e$. For the current case, there are two possible definitions of $\mathcal{P}e$, where the propulsion in one case is compared to translational diffusion and in the other case to rotational diffusion [114]

$$\mathcal{P}e_\mathrm{rot} \equiv \frac{v_0/\sigma}{1/\tau_\mathrm{r}}\,,$$
$$\mathcal{P}e_\mathrm{trans} \equiv \frac{v_0\sigma}{D}\,.$$

Both give a measure of how much the active Brownian particle has travelled actively before reorientation, or translational diffusion on the particle scale. Thus the larger the Péclet numbers, the more important is the role played by the active propulsion in comparison to the respective diffusive process.

The mean-square displacement for an active Brownian particle can be explicitly calculated from equations (1.15) and (1.14) yielding

$$\left\langle \Delta r^2(t) \right\rangle = 2dDt + 2v_0^2\tau_\mathrm{r}^2 \left\{ \frac{t}{\tau_\mathrm{r}} + e^{-t/\tau_\mathrm{r}} - 1 \right\} . \tag{1.18}$$

Taking three different limits highlights the different contributions to the dynamics.

$$\left\langle \Delta r^2(t) \right\rangle \sim \begin{cases} 2dDt\,, & \text{for } t \to 0 \\ v_0^2 t^2\,, & \text{for } 0 \ll t \ll \tau_\mathrm{r} \\ 2(dD + v_0^2\tau_\mathrm{r})t\,, & \text{for } \tau_\mathrm{r} \ll t \end{cases} . \tag{1.19}$$

This clearly shows the influence of the diffusive noise term in equation (1.15) in the limit of $t \to 0$. On intermediate timescales, the particle moves ballistically as a consequence of the propulsion, and after rotational diffusion has reoriented the direction of propulsion, the particle again moves diffusively, but with a modified diffusion coefficient enhanced by activity.

If in equation (1.15) additionally the inertia of the active particle is considered, then the dynamics is ballistic on short timescales similar to equation (1.3a) [115]. On timescales longer than the inertial ballistic relaxation, the dynamics are equivalent to the overdamped active Brownian particle model.

Experimentally, active Brownian particles can be realised, *e.g.*, by using Janus spheres, that have different chemical, or physical properties on each hemisphere that then generate a net thrust into the direction of one of the hemispheres. For example, one side of the colloid could be coated with a material catalysing a chemical reaction, or absorbing laser light inducing a gradient of products of a chemical reaction, or light a self-diffusiophoresis, or self-thermophoresis leading to propulsion of the colloid [10,40].

1.3. HYDRODYNAMICS

Self-propelling agents in solution must fulfil momentum conservation and thus when they move forward, an equal amount of fluid has to be moved in the opposite direction. It is thus of importance how the fluid behaves when actively moving into a particular direction, expecially in the case where more than one active agent in solution is considered. In this case, also interactions between the agents mediated by the fluid will arise and taking the solvent only via a friction and random force similar to equation (1.15) into account, may lead to incorrect results. In order to understand the influences of the dynamics of the solvent on the motion of the suspended colloidal particles, first the dynamics of the solvent itself has to be understood. In the following section, the equations of motion for a general fluid are derived and consequences and subtleties for the dynamics on the microscale are pointed out.

1.3.1 Equations of motion

In fluid mechanics, the state of a moving fluid is completely determined if the flow field $\boldsymbol{u}(\boldsymbol{r})$, pressure field $p(\boldsymbol{r})$ and density field $\rho(\boldsymbol{r})$ are given [116]. The equations of motion are then built on phenomenological investigations of conservation laws and symmetries on length scales much longer than the size of the constituents of the fluid, *e.g.*, the fluid molecules.

The conservation of matter results in the continuity equation. The mass of fluid in a certain volume V is $\int_V \mathrm{d}\boldsymbol{r}\,\rho$. Now, if the fluid is in motion, the mass of fluid flowing out through the surface ∂V around the volume in unit time is [116] by use of the divergence theorem

$$\oint_{\partial V} \mathrm{d}\boldsymbol{n}\cdot(\rho\boldsymbol{u}) = \int_V \mathrm{d}\boldsymbol{r}\,\boldsymbol{\nabla}\cdot(\rho\boldsymbol{u})\,.$$

However, the out-flowing fluid mass has to be equal to the change in mass in this volume, *i.e.*, $-\partial_t \int_V \mathrm{d}\boldsymbol{r}\,\rho$. Equating the two integrals and taking into account that the equation has to hold irrespective of the volume V leads to the conclusion that the integrands have to vanish

$$\partial_t\rho + \boldsymbol{\nabla}\cdot(\rho\boldsymbol{u}) = 0\,, \tag{1.20}$$

which is the equation of continuity.

Conservation of momentum leads to the momentum flux equation [116]. A change in the α-component of momentum in volume V is

$$\partial_t \int_V \mathrm{d}\boldsymbol{r}\,\rho u_\alpha\,,$$

whereas the momentum flowing out of volume V through its surface ∂V in terms of the momentum flux density tensor $\Pi_{\alpha\beta}$ is

$$-\oint_{\partial V} \mathrm{d}n_\beta \Pi_{\alpha\beta}\,.$$

On similar lines as above, the resulting equation for the momentum flux reads

$$\partial_t(\rho u_\alpha) = -\partial_\beta \Pi_{\alpha\beta}\,. \tag{1.21}$$

Contributions to $\Pi_{\alpha\beta}$ are reversible momentum transport due to the movement of the particles, the pressure acting on the fluid, and the internal friction leading to irreversible spreading of the momentum [116]

$$\Pi_{\alpha\beta} = \rho u_\alpha u_\beta + p\delta_{\alpha\beta} - \eta\left(\partial_\beta u_\alpha + \partial_\alpha u_\beta - \frac{2}{3}\delta_{\alpha\beta}\partial_\gamma u_\gamma\right) + \tilde{\eta}\delta_{\alpha\beta}\partial_\gamma u_\gamma \tag{1.22a}$$

$$\equiv \rho u_\alpha u_\beta - \sigma_{\alpha\beta}\,, \tag{1.22b}$$

where η and $\tilde{\eta}$ are called the coefficients of viscosity, *i.e.*, the shear and bulk viscosity, respectively. For convenience, equation (1.22b) defines the stress tensor $\sigma_{\alpha\beta}$, such that $\Pi_{\alpha\beta}$ consists of reversible momentum transport contributions and stresses in the fluid.

The most general equation of motion is now obtained by plugging equation (1.22b) into equation (1.21), yielding the Navier-Stokes equations [116]

$$\rho\left\{\partial_t u_\alpha + u_\beta\partial_\beta u_\alpha\right\} = -\partial_\alpha p + \eta\partial_\beta\partial_\beta u_\alpha + \left(\tilde{\eta} + \frac{1}{3}\right)\partial_\alpha\partial_\beta u_\beta\,. \tag{1.23}$$

The left hand side is known as a material derivative

$$\mathrm{D}_t u_\alpha \equiv \partial_t u_\alpha + u_\beta\partial_\beta u_\alpha\,, \tag{1.24}$$

which denotes the acceleration of a given fluid volume element as it moves in space, and not the acceleration at a fixed point in space. However, equation (1.23) has 5

unknowns, namely u_α, ρ and p and thus needs to be closed by supplying the continuity equation for ρ and another equation for the pressure $p(\rho)$ [116]. Together with boundary and initial conditions, the developed formalism can predict the fluid dynamics according to the model. However, this is in general very cumbersome, due to the mathematical difficulty of solving equation (1.23). Thus, one seeks for reasonable simplifications, allowing for a more systematic analysis.

Assuming the fluid to be incompressible leads to [116]

$$\partial_\alpha u_\alpha = 0\,, \tag{1.25}$$

which can be assumed for flows that are much slower than the speed of sound $u \ll c$, *i.e.*, the speed at which density inhomogeneities travel through the fluid. This assumption cancels one dependency such that the Navier-Stokes equation and the incompressibility condition equation (1.25) fully describe the fluid. In order to enforce incompressibility, the role of the pressure is redefined as an Lagrangian multiplier to equation (1.23). Note, that the last term in equation (1.23) vanishes when the fluid is incompressible, leading to the incompressible Navier-Stokes equation

$$\partial_t u_\alpha + u_\beta \partial_\beta u_\alpha = -\frac{1}{\rho}\partial_\alpha p + \frac{\eta}{\rho}\partial_\beta \partial_\beta u_\alpha\,. \tag{1.26}$$

However, this equation is still non-linear and only solvable for special cases.

1.3.2 Low Reynolds number

For further simplifications of the Navier-Stokes equations, more knowledge about the system under consideration is necessary. Given sufficient information, contributions to the flow according to equation (1.26) may be ruled out, because they are suppressed by other terms. In order to get a deeper understanding of the Navier-Stokes equations, a dimensionless form is introduced. There, lengths, velocities and times are rescaled using characteristic length L, speed v and corresponding time units L/v of the system under consideration. Consequently, the rescaling reads $\tilde{x} \equiv x/L$, $\tilde{\boldsymbol{u}} \equiv \boldsymbol{u}/v$, and $\tilde{t} \equiv t/(L/v)$. Thus, multiplying equation (1.26) by L/v^2, defining $\tilde{p} \equiv Lp/(\rho v^2)$ as a dimensionless Lagrangian multiplier, and defining the kinematic viscosity $\nu \equiv \eta/\rho$, one arrives at

$$\partial_t u_\alpha + u_\beta \partial_\beta u_\alpha = -\partial_\alpha p + \mathcal{R}e^{-1}\partial_\beta \partial_\beta u_\alpha\,, \tag{1.27}$$

where the tilde has been dropped for convenience and the Reynolds number has been defined as

$$\mathcal{R}e \equiv \frac{Lv}{\nu}\,. \tag{1.28}$$

The Reynolds number depends on the typical speed and length scale of the flow under consideration, and can be interpreted as the ratio of inertial to viscous forces in the fluid [116]. Example values for $\mathcal{R}e$ taken from the Purcell's seminal talk [117] are $\mathcal{R}e \approx 10^4$ for a swimming human, $\mathcal{R}e \approx 10^2$ for a small fish, and $\mathcal{R}e \approx 10^{-4}$ for micron sized objects. This means that inertial terms in equation (1.26) for the situation of a swimming human are significant, whereas neglecting the same terms in the case of the flow around a micron sized sphere, results in a useful approximation.

Consider stationary flows in which $\partial_t \boldsymbol{u} = 0$. For small $\mathcal{R}e$, the term $\mathcal{R}e^{-1}\partial_\beta \partial_\beta u_\alpha$ becomes much more important than the term $\partial_\beta u_\beta u_\alpha$, and ultimately for $\mathcal{R}e \to 0$ it can

be safely neglected. The dimensionless pressure p still acts as an Lagrangian multiplier ensuring incompressibility, *i.e.*, equation (1.25). Thus, the following linear equations of motion, the so-called Stokes equations, are obtained

$$\eta \partial_\beta \partial_\beta u_\alpha = \partial_\alpha p \,, \tag{1.29a}$$

$$\partial_\alpha u_\alpha = 0 \,, \tag{1.29b}$$

describing the fluid dynamics at low $\mathcal{R}e$, together with appropriate boundary conditions.

Equation (1.29) can now be used in order to calculate the hydrodynamic drag force on a colloid moving in a solvent, *e.g.*, to calculate ζ from equation (1.1). For a spherical colloid of radius R moving constantly at the small velocity v through a solvent of viscosity η with no-slip boundary on the colloid surface, we obtain for the drag force [116]

$$F_{\text{drag}} = 6\pi\eta R v \,, \tag{1.30}$$

and thus conclude $\zeta = 6\pi\eta R$.

In situations, where the $\mathcal{R}e$ is not-so-low, the inertial contributions to the Navier-Stokes equation may not be negligible throughout the whole fluid domain and thus, neglecting the inertial terms can lead to inaccuracies in the description of the Stokes equation. For the case of a sphere moving at speed v through a viscous fluid, the inertia term in equation (1.27) is not negligible at distances where $r \ll \nu/v$ is not fulfilled [116]. However, since there the velocity of the fluid is approximately equal to v, as seen from the co-moving frame, the inertia term can be reintroduced in the following way

$$v_\beta \partial_\beta u_\alpha = -\partial_\alpha p + \eta \partial_\beta \partial_\beta u_\alpha \,, \tag{1.31}$$

and thus keeping the equation linear in $\boldsymbol{u}$. Equation (1.31) defines the Oseen equation. The resulting drag force $F = 6\pi\eta R v(1 + 3/8 \cdot \mathcal{R}e)$ now involves the next term of the expansion of the drag in powers of $\mathcal{R}e$ [116]. Also the flow created in the fluid differs from that obtained from the Stokes equation, but the difference vanishes for $\mathcal{R}e \to 0$ [118]. The difference in Stokes' and Oseen's solutions does not undermine the applicability of Stokes flow, but brings to mind that the Stokes equation is an approximation that is only exact in the limit of $\mathcal{R}e \to 0$. In this sense, the Oseen equation is a better approximation than the Stokes equation and becomes important only sufficiently far from the sphere, or for sufficiently large $\mathcal{R}e$.

If we consider the flow past an infinitely long cylinder with radius R moving slowly perpendicular to the axis of symmetry, equations (1.29) have no solution that fulfills the boundary conditions at the surface of the cylinder and at infinity simultaneously [116]. Thus, for the problem of the moving cylinder, which is equivalent to that of a moving circle in a two-dimensional fluid because of the translational symmetry along the axis of symmetry, the Oseen equation is essential for finding consistent solutions [116]. The resulting drag per unit length is [119]

$$F_{\text{drag}} = \frac{4\pi\eta v}{\frac{1}{2} - \gamma_{\text{Euler}} - \ln\frac{\mathcal{R}e}{4}} \,, \tag{1.32}$$

where $\gamma_{\text{Euler}} \equiv 0.577...$ is Euler's constant [116]. The reason for the failure of the Stokes equation is the negligence of the inertia terms in equation (1.26), which in the

2D geometry become comparable to the viscous forces ($\nu\partial_\beta\partial_\beta u_\alpha$ in equation (1.26)) when r/R is of order $\mathcal{R}e^{-1}$ (for $\partial_t u_\alpha$ in equation (1.26)), or when $C\,r/R\cdot\ln r/R$ is of order $\mathcal{R}e^{-1}$ (for $u_\beta\partial_\beta u_\alpha$ in equation (1.26)) [120]. The full flow field of the moving cylinder can be obtained by matching the solution to the Stokes equation for the flow at small distances from the cylinder with the solution to the Oseen equation for the far-field [120].

Note, that in a two-dimensional geometry, the incompressibility condition reads

$$\partial_\alpha u_\alpha = \partial_x u_x + \partial_y u_y = 0\,,$$

and thus the velocities can be defined in terms of the stream function $\psi(\boldsymbol{r})$

$$u_x = \partial_y\psi\,, \tag{1.33a}$$
$$u_y = -\partial_x\psi\,, \tag{1.33b}$$

such that incompressibility is automatically fulfilled by the symmetry of the second derivatives [116]. Note, that equations (1.33) can be expressed in the more compact form $u_\alpha = \varepsilon_{\alpha\beta}\partial_\beta\psi$. The differential equation that governs the stream function is obtained after insertion of the velocity in terms of the stream function into Stokes equation (1.29a), yielding

$$\partial_\alpha\partial_\alpha\partial_\beta\partial_\beta\psi = 0\,, \tag{1.34}$$

which still needs to be supplemented by appropriate boundary conditions.

1.3.3 Hydrodynamic interactions

If a collection of objects in solution is considered, it is of interest to describe how the flow field induced by the movement of one of the objects influences the dynamics of the other objects. The hydrodynamic force on a unit area surface with surface normal $\boldsymbol{n}$ pointing into the surface is given by the stress experienced at the interface $f_\alpha = -\sigma_{\alpha\beta}n_\beta$ [116], where the velocity of the fluid at the surface equals the velocity of the surface itself, thus defining a no-slip boundary condition. The hydrodynamic force on an immersed body of volume V and surface ∂V moving at the velocity $\boldsymbol{v}(t)$ is thus determined by

$$F_\alpha = -\oint_{\partial V}\mathrm{d}n_\beta\sigma_{\alpha\beta}\,, \tag{1.35a}$$
$$\boldsymbol{u}(\boldsymbol{r})\Big|_{\boldsymbol{r}\in\partial V} = \boldsymbol{v}(t)\,. \tag{1.35b}$$

Together with equations (1.29), this gives the full low-$\mathcal{R}e$ behaviour. However, solving the equations is only possible for special cases of high symmetry and can become arbitrarily complicated as the boundary conditions become more sophisticated.

A generally more applicable way to consider hydrodynamic interactions is by assuming the fluid to be disturbed by point forces. Considering an external force applied to the fluid and introducing it to the right hand side of the Stokes equation (1.29a) as $-f_\alpha$ results in

$$-\partial_\alpha p + \eta\partial_\beta\partial_\beta u_\alpha = -f_\alpha\,. \tag{1.36}$$

In reciprocal space the velocity is defined as the Fourier (back-)transform

$$\hat{u}_{\boldsymbol{q}}^{\alpha} \equiv \int \mathrm{d}\boldsymbol{r}\, u_{\alpha}(\boldsymbol{r}) e^{-iq_{\beta}r_{\beta}}\,, \tag{1.37a}$$

$$u_{\alpha}(\boldsymbol{r}) \equiv \frac{1}{(2\pi)^{d}} \int \mathrm{d}\boldsymbol{q}\, \hat{u}_{\boldsymbol{q}}^{\alpha} e^{iq_{\beta}r_{\beta}}\,. \tag{1.37b}$$

Equation (1.36) in reciprocal, or Fourier space thus reads

$$-\eta q^{2}\hat{u}_{\boldsymbol{q}}^{\alpha} + iq_{\alpha}\hat{p}_{\boldsymbol{q}} = -\hat{f}_{\boldsymbol{q}}^{\alpha}\,. \tag{1.38}$$

To obtain a closed equation for the velocity alone, we take the divergence (multiply by $-iq_{\alpha}$ in reciprocal space) of equation (1.38) and solve for the pressure, giving $\hat{p}_{\boldsymbol{q}} = iq_{\alpha}\hat{f}_{\boldsymbol{q}}^{\alpha}/q^{2}$. Note that incompressibility in reciprocal space is expressed as $q_{\alpha}u_{\boldsymbol{q}}^{\alpha} = 0$. The closed equation for the velocity is then

$$-\eta q^{2}\hat{u}_{\boldsymbol{q}}^{\alpha} - q_{\alpha}\frac{q_{\beta}\hat{f}_{\boldsymbol{q}}^{\beta}}{q^{2}} = -\hat{f}_{\boldsymbol{q}}^{\alpha}\,, \tag{1.39}$$

and is readily solved

$$\hat{u}_{\boldsymbol{q}}^{\alpha} = \frac{1}{\eta q^{2}}\left\{\delta_{\alpha\beta} - \frac{q_{\alpha}q_{\beta}}{q^{2}}\right\}\hat{f}_{\boldsymbol{q}}^{\beta} \tag{1.40a}$$

$$\equiv \hat{H}_{\boldsymbol{q}}^{\alpha\beta}\hat{f}_{\boldsymbol{q}}^{\beta}\,, \tag{1.40b}$$

thus defining the Oseen mobility tensor $\hat{H}_{\boldsymbol{q}}^{\alpha\beta}$ in reciprocal space. Transforming back to real space gives [5]

$$H_{\alpha\beta}(\boldsymbol{r}) = \frac{1}{8\pi\eta r}\left\{\delta_{\alpha\beta} + \frac{r_{\alpha}r_{\beta}}{r^{2}}\right\}\,, \tag{1.41}$$

which is the solution for a unit delta force acting at the origin. It is thus no surprise that we obtain from equations (1.40b) via the convolution theorem

$$u_{\alpha}(\boldsymbol{r}) = \int \mathrm{d}\boldsymbol{r}'\, H_{\alpha\beta}(\boldsymbol{r}-\boldsymbol{r}')f_{\beta}(\boldsymbol{r}')\,, \tag{1.42}$$

since the Oseen mobility tensor, equation (1.41) is the Green's function of the Stokes equation. Thus, equation (1.42) gives the velocity field created by an arbitrary force field $f_{\alpha}(\boldsymbol{r})$.

Note, that the flow created by a point force is decaying roughly as r^{-1}. This very slow decay shows the importance of hydrodynamic interactions in hydrodynamically interacting many-body systems. In two dimensions, the slow decay of the hydrodynamic interactions is even *worse*, because there is one dimension less for the flow to escape into. A consequence is, that flow due to a moving body in 2D in infinite and resting fluid satisfying the Stokes equation is undefined, because the flow cannot fulfil the condition that the flow has to vanish at infinity while the force exerted on the body is nonzero [121], as has already been shown for the moving cylinder. The solution for the Oseen tensor in 2D given in reference [122] is

$$H_{\alpha\beta}(\boldsymbol{r}) = \frac{1}{4\pi\eta}\left\{-\delta_{\alpha\beta}\ln r + \frac{r_{\alpha}r_{\beta}}{r^{2}}\right\}\,. \tag{1.43}$$

Thus, the flow induced because of a point force $f_\alpha(\boldsymbol{r}) = f^0_\alpha \delta(r_\alpha - r^0_\alpha)$ obtained by inserting equation (1.43) into equation (1.42) diverges at infinity. The origin of the divergence, as has already been discussed in section 1.3.2, is the negligence of inertia terms in the Stokes equation and can be handled by matching solutions of the Stokes and Oseen equations [121]. Although inertia terms also play a role in the far field of a 3D point force, a divergence as in 2D is prevented because of the decay of the 3D flow field [121].

1.4. Classical turbulence

In order to understand the phenomenology of active turbulence, a brief summary of classical turbulence at high $\mathcal{R}e$, where inertia plays a key role, is given here. However, inertial effects do not play a crucial role for active turbulence [98], because on small length scales, where $\mathcal{R}e \ll 1$ and thus viscous dominate over inertial forces. Nevertheless, active turbulent systems show spatiotemporal structure reminiscent of classical turbulence.

In contrast to the creeping flow equations (1.29) at low $\mathcal{R}e$, we have completely different and non-linear flow dynamics at high $\mathcal{R}e$. The fluid velocity typically varies irregular in time and space, in which case one may speak of fully developed turbulence. However, the irregular dynamics still exhibits a particular order that may be regarded as the linear combination of *turbulent eddies* of different sizes λ, where the order of magnitude of the velocity in this eddy is v_λ. A complete quantitative theory of turbulence is still lacking, however, some important results are well-known [116, 123].

While the high $\mathcal{R}e$ allows for dissipationless dynamics over a wide range of eddy sizes λ, on sufficiently small length scales the Reynolds number of associated eddies will be small [116]. Since the Reynolds number is the ratio of inertial to viscous forces, it is thus concluded that the turbulent dynamics dissipates energy only on the smallest length scale λ_0, whereas larger eddies are effectively dissipationless. Energy is passed from large to small eddies, *i.e.*, from small to large wavenumbers $q_\lambda = 1/\lambda$, where the energy is eventually turned into heat on the smallest of scales λ_0 [124]. This energy transfer is called an energy cascade. If the system is assumed to be in a stationary state, a constant energy influx at large length scales has to be guaranteed [116].

Let ϵ be the energy dissipation per unit time and unit fluid mass in units of length^2/time^3 and the energy per unit mass in a small range of wavenumbers $\mathrm{d}q$ in units of length^2/time^2 be $E_q \mathrm{d}q$, where E_q is the energy spectrum in reciprocal space. Following self-similarity arguments, the energy spectrum in reciprocal space in units length^3/time^2 as a scale-invariant, *i.e.*, self-similar, combination of ϵ and q is then [116]

$$E_q \propto \epsilon^{2/3} q^{-5/3} . \tag{1.44}$$

It should be noted, however, that there is a fundamental difference between two- and three-dimensional turbulence arising from the symmetries of the geometries. From equation (1.26) and the definition of the energy $E = \frac{1}{2}\langle u^2 \rangle$, it follows that the rate of energy dissipation can be expressed as the product of viscosity and enstrophy $Z = \langle \omega^2 \rangle / 2$ [125], *i.e.*,

$$\dot{E} = -2\nu Z . \tag{1.45}$$

Taking the curl of equation (1.26) yields the following equation for the vorticity $\boldsymbol{\omega}$ in two or three dimensions

$$\partial_t \omega_\alpha + u_\beta \partial_\beta \omega_\alpha = \omega_\beta \partial_\beta u_\alpha + \nu \partial_\beta \partial_\beta \omega_\alpha . \tag{1.46}$$

In 2D, ω_α always points into the third dimension, *i.e.*, out of the 2D plane, and therefore the term $\omega_\beta \partial_\beta u_\alpha$ is only non-zero in three dimensions, where it is associated with vortex stretching [125]. In the relevant limit for turbulent flows, *i.e.*, $\mathcal{R}e \to \infty$, the term proportional to viscosity can be neglected. Thus, for 2D turbulent flows, equation (1.46) reduces to $\partial_t \omega_\alpha + u_\beta \partial_\beta \omega_\alpha = 0$, meaning that vorticity is conserved along the streamlines. On the other hand, in 3D turbulence, vorticity is not conserved and can be stretched out into the third dimension [126]. In this phenomenon called vortex stretching, a vortex line becomes narrower and longer resulting in a local vorticity increase while the the strength of the vortex stays constant. Thus, in three dimensions, for $\nu \to 0$, there is still finite energy dissipation independent of the viscosity, because vortex stretching, $Z \to \infty$ compensates the decrease of viscosity [127], implying a direct inertial cascade of energy from large to small scales according to equation (1.44). Here, the term inertial indicates that the energy transport is independent of the value of viscosity until the dissipation range is reached. On the other hand, in 2D, Z is constant and $\nu \to 0$ implies no energy dissipation according to equation (1.45). As a result, energy is not turned into heat on the small scales, but is transported from the energy injection scale to larger scales, giving rise to the so-called inverse inertial cascade. This transport in principle continues until the largest possible eddies fill the whole system. But in reality, there is no realisation of a true two-dimensional system giving rise to a frictional cutoff taking energy out of the system at large scales and thus allowing for a steady state. A prominent example for 2D turbulence is the fluid dynamics in a thin film, similar to a soap bubble, where the friction of the fluid with the surrounding air acts as a frictional cutoff. However, the dimensional arguments leading to equation (1.44) hold for both, direct and inverse energy cascades for $d \geq 2$ [128], leading to the Kolmogorovian spectrum $\propto q^{-5/3}$ in the relevant inertial regime distant from the cutoff.

The energy spectrum E_q is defined via the kinetic energy in the system E

$$E = \int_0^\infty \mathrm{d}q \, E_q \,, \tag{1.47}$$

which can be rewritten in an alternative way using the Wiener-Khinchin theorem to express the correlation function $\langle \boldsymbol{u}(0) \cdot \boldsymbol{u}(\boldsymbol{r}) \rangle \Big|_{\boldsymbol{r}=0}$ in terms of the power spectral density $\langle \hat{\boldsymbol{u}} \cdot \hat{\boldsymbol{u}}^* \rangle_{\boldsymbol{q}}$. Assuming isotropy and performing the Fourier back-transform in polar coordinates yields

$$\langle u^2 \rangle = \frac{1}{2\pi} \int_0^\infty \mathrm{d}q \, q \, \langle \hat{\boldsymbol{u}} \cdot \hat{\boldsymbol{u}}^* \rangle_{\boldsymbol{q}} \,. \tag{1.48}$$

Again, $\hat{\boldsymbol{u}}_{\boldsymbol{q}}$ is the Fourier transform according to equation (1.37a). Thus, the energy spectrum is

$$E_q = \frac{q}{4\pi} \langle \hat{\boldsymbol{u}} \cdot \hat{\boldsymbol{u}}^* \rangle_{\boldsymbol{q}} \,. \tag{1.49}$$

A discretised version, where the polar integration becomes a summation over annular shells (2D), can be stated as

$$E_q = \frac{1}{8\pi \Delta q} \sum_{q-\Delta q < k < q+\Delta q} \langle \hat{\boldsymbol{u}} \cdot \hat{\boldsymbol{u}}^* \rangle_k \,. \tag{1.50}$$

1.5. CHIRAL ACTIVE FLUIDS

A fluid consisting out of inherently rotating particles bears additional transport coefficients due to the internal stresses implied by the inherent rotation. Here, the focus is on the following two additional contributions to the stress tensor. Subsequently, hydrodynamic equations of motion for the dynamics of chiral active fluids are obtained. On the one hand, the frictional stress between the rotating particles leads to a coupling of the inherent rotation and the translation of the fluid particles. This means, that the inherent rotation is coupled to a collective rotation, as if two non-fixed gears of the same orientation of rotation touch each other [67, 129]. The resulting stress will be proportional to the rotational viscosity η_R and can be written as

$$\sigma^{\text{rot}}_{\alpha\beta} = \varepsilon_{\alpha\beta}\eta_R \left(2\widetilde{\Omega} - \omega\right) , \tag{1.51}$$

where $\widetilde{\Omega}(\boldsymbol{r}) = \langle \sum_i \delta(\boldsymbol{r} - \boldsymbol{r}_i)\Omega_i \rangle$ is the density of intrinsic rotation for the elementary particles at positions $\boldsymbol{r}_i$ rotating at angular velocity Ω_i, ω is the vorticity field of the flow, which can be interpreted as twice the local circulation, and $\varepsilon_{\alpha\beta} \equiv \varepsilon_{\alpha\beta z}$. Thus, if the local angular velocity density equals the local circulation of the fluid particles, $\sigma^{\text{rot}}_{\alpha\beta}$ vanishes. The rotational stress tries to synchronise the intrinsic with the local fluid rotation, by coupling $\widetilde{\Omega}$ to ω and thus to v_α.

The second contribution to the stress tensor as a consequence of the intrinsic rotation is the odd stress proportional to so-called odd viscosity η^{odd} [67]

$$\sigma^{\text{odd}}_{\alpha\beta} = \eta^{\text{odd}} \left(\partial_\alpha \varepsilon_{\beta\gamma} v_\gamma + \varepsilon_{\alpha\gamma}\partial_\gamma v_\beta\right) . \tag{1.52}$$

This stress is odd under time-reversal symmetry, is not associated with dissipation [68] and can thus be derived from a Hamiltonian formalism for ideal fluids [67]. The term *viscosity* might thus be misleading because it is not associated with dissipation, but if $\sigma^{\text{rot}}_{\alpha\beta}$ and $\sigma^{\text{odd}}_{\alpha\beta}$ are used to obtain the generalised incompressible Navier-Stokes equations, *i.e.*,

$$\rho\left(\partial_t v_\alpha + v_\beta\partial_\beta v_\alpha\right) = -\partial_\alpha p + \eta\partial_\beta\partial_\beta v_\alpha + \eta_R\varepsilon_{\alpha\beta}\partial_\beta\left(2\widetilde{\Omega} - \omega\right) + \varepsilon_{\alpha\gamma}\eta^{\text{odd}}\partial_\beta\partial_\beta v_\gamma , \tag{1.53}$$

then it is apparent that the contributions stemming from σ^{odd} act similar as the dissipative viscosity η, yet orthogonal to the direction of flow. The directions of the resulting forces are illustrated in the shear flow in figure 1.3b. At $t = 0$, two infinitely extended parallel no-slip boundaries confining a chiral active fluid start to translate into opposite directions. Dissipative stresses, as a result of ordinary viscosity η, act parallel to the direction of shear (red), while stresses resulting from odd viscosity act perpendicular to the direction of shear. Qualitatively, the flow and the resulting force density is shown in figure 1.3c, showing the presence of forces only in regions of non-vanishing Laplacian. For $t \to \infty$ the shear flow leads to a linear velocity profile, such that the forces acting on the fluid resulting from odd stresses then vanish. In equation (1.53) a constant parameter η^{odd} is assumed, which is not necessarily the case. Instead, the odd viscosity transport coefficient is proportional to the local intrinsic angular momentum density [67] and thus $\eta^{\text{odd}} \propto \widetilde{\Omega}$. The angular momentum density field itself follows an own evolution equation balancing input torque, frictional dissipation and advection of angular momentum [41]. The evolution of $\widetilde{\Omega}$ is then coupled to equation (1.53) via the rotational stress equation (1.51). However, for a homogeneous system and a constant energy input, $\widetilde{\Omega} \equiv$ const. and thus $\eta^{\text{odd}} \equiv$ const. can be regarded for simplicity.

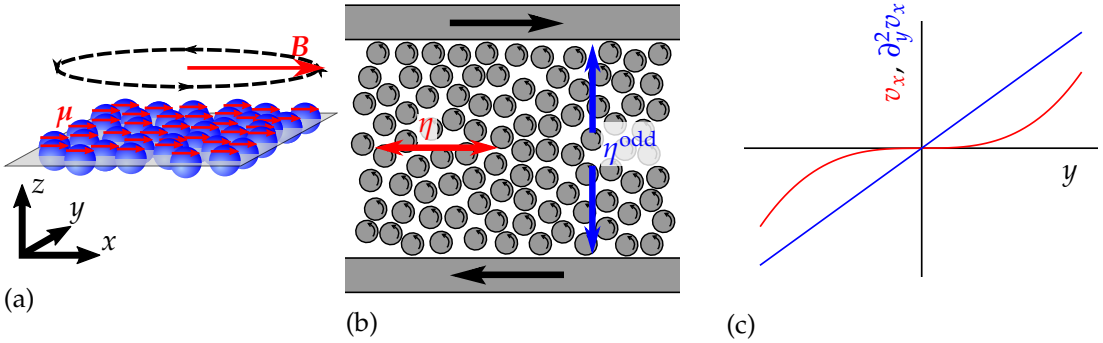

(a) (b) (c)

Figure 1.3: Stresses in chiral active fluids. (a) Schematic representation of a possible realisation for a two-dimensional chiral active fluid of spherical magnetic particles each carrying the magnetic moment $\boldsymbol{\mu}$ synchronously spinning with an externally applied magnetic field $\boldsymbol{B}$. The dynamics of the rotors are constrained to two dimensions in the x-y-plane. (b) Sketch of the stress forces resulting from odd viscosity in shear flow. (c) The corresponding fluid velocity profile and forces due to odd viscosity according to equation (1.54) at $0 < t < \infty$.

Note, that for an incompressible chiral active fluid, the contribution to the fluid flow resulting from the odd viscosity can be rewritten as [67]

$$\varepsilon_{\alpha\gamma}\eta^{\mathrm{odd}}\partial_\beta\partial_\beta v_\gamma = \eta^{\mathrm{odd}}\partial_\alpha\omega\,. \tag{1.54}$$

Thus, this contribution can be regarded as an additional pressure resulting in forces pointing into the direction of the gradient of vorticity, and thus implies correlations between vorticity and density for weakly compressible fluids, which has, to the best of my knowledge, neither been experimentally, nor numerically observed until now.

1.6. Numerical simulation

Within the framework of statistical mechanics, and thus soft matter physics, exactly solvable non-trivial problems, like the ideal gas, are rare [130, 131]. Computer simulations allow for essentially exact solutions for systems which elseways would only be solvable approximately, if at all. Computer simulations thus play an important role in modern physics as a link between theoretical and experimental studies. On the one hand, computer simulations can be used as a test of theories, but on the other hand, they can also be used for the interpretation of experimental results.

Coupled colloidal degrees of freedom, *e.g.*, the monomers in a polymer, can be integrated by solving the coupled Langevin equations [132]. However, this is only appropriate when the hydrodynamic interactions between the coupled degrees of freedom are not of primary interest or can be neglected. When hydrodynamics cannot be neglected or are crucial to the physics, a more sophisticated simulation that also regards the solvent degrees of freedom has to be employed.

A standard way to simulate a physical system with a computer, is to incorporate the underlying microscopic degrees of freedom and then extract the macroscopic details that are of interest [130]. For example, considering a colloidal particle in solution, simulating the equations of motion of the solvent particles, *i.e.*, Hamiltonian dynamics, leads to correct results for the colloidal particle. Such methods are known as molecular dynamics simulation techniques. These methods, however, can become

arbitrarily complicated when applied to complex systems evolving on macroscopic space and time scales [133]. As a result, the method develops a large compute intensity, because a large number of microscopic degrees of freedom have to be followed for long times. On the other hand, coarse-grained or mesoscopic simulations techniques capture the essential properties of the microscopic degrees of freedom in a computationally efficient way [131]. One mesoscopic simulation technique is multiparticle collision dynamics (MPC), which is used in the scope of this thesis and is introduced in the remainder of this section.

1.6.1 Multiparticle collision dynamics

The basic idea of multiparticle collision dynamics is to describe the dynamics of explicit solvent particles in continuous phase space but at discrete points in time in terms of alternating streaming and collision steps [131, 133, 134]. The point-like fluid particles undergo coarse-grained interactions during the collision protocol allowing for a straightforward implementations of parallel computing. The simulation code developed in the scope of this thesis operates on GPUs and is highly parallelised, allowing for an efficient simulation of a large amount of fluid particles. The streaming and collision protocols are defined in such a way, that the hydrodynamic conservation laws of mass, linear momentum and energy are fulfilled, and thus are equivalent to solve the Navier-Stokes equations.

Consider a multiparticle collision dynamics solvent consisting of homogeneously distributed point particles of equal mass m at positions $\boldsymbol{r}_i$ with velocities $\boldsymbol{v}_i$ in accordance with the Maxwell-Boltzmann distribution. During the streaming step, the point-like fluid particles are ballistically transported into the direction that the velocity points into for the duration of the time h. The streaming scheme is illustrated in figure 1.4a. Note, that the point-like particles cannot collide and thus the protocol can be stated as

$$\boldsymbol{r}_i(t+h) = \boldsymbol{r}_i(t) + \boldsymbol{v}_i(t)h\,. \tag{1.55}$$

After the streaming process, when the particles take their new positions, a coarse-grained collision takes place. To this end, the particles are sorted into square collision boxes or cells of length a, such that the particles with indices $i \in \zeta$ belong to the given collision cell ζ, with $\sum_{i\in\zeta} = N_\zeta$. Then, the relative velocities of each particle with respect to the centre of mass velocity of the collision cell $\boldsymbol{v}_\zeta(t) = \frac{1}{N_\zeta}\sum_{i\in\zeta}\boldsymbol{v}_i(t)$ are rotated by an angle α around an axis that is chosen randomly for each cell[1] and collision step individually

$$\boldsymbol{v}_i(t+h) = \boldsymbol{v}_\zeta(t) + \mathcal{R}(\alpha)\cdot\big(\boldsymbol{v}_i(t) - \boldsymbol{v}_\zeta(t)\big) \tag{1.56}$$

where $\mathcal{R}(\alpha)$ denotes the rotation matrix around the random axis. Typically, α is a fixed system parameter [131]. The procedure is illustrated in figure 1.4b.

The streaming and collision routines define the core of the multiparticle collision dynamics solvent. That the routines fulfil the hydrodynamic conservation laws is shown in the following. The conservation of mass is trivial—the mass of the solvent is conserved locally and globally, *i.e.*, no fluid particles are taken out or introduced to the

[1] In two-dimensional multiparticle collision dynamics solvents, the rotation axis is chosen randomly from the two possible directions, *i.e.*, either pointing in the positive or negative z-direction for a solvent confined to the x-y-plane.

system during collision and streaming. Also, the conservation of linear momentum during streaming is trivial, since the velocities of the fluid particles are not altered and only the positions are updated. The conservation of linear momentum upon collision, *i.e.*, $\boldsymbol{v}_\zeta(t) = \boldsymbol{v}_\zeta(t+h)$ can be shown for each collision cell ζ

$$\begin{aligned} N_\zeta \boldsymbol{v}_\zeta(t+h) &= \sum_{i\in\zeta} \boldsymbol{v}_i(t+h) \\ &= \sum_{i\in\zeta} \big(\boldsymbol{v}_\zeta(t) + \mathcal{R}(\alpha)\cdot\big(\boldsymbol{v}_i(t) - \boldsymbol{v}_\zeta(t)\big)\big) \\ &= N_\zeta \boldsymbol{v}_\zeta(t)\,, \end{aligned}$$

showing that linear momentum is conserved locally, and thus also globally. For the conservation of energy, note that the magnitude of an arbitrary vector $\boldsymbol{u}$ after rotation through rotation matrix $\mathcal{R}(\alpha)$ is conserved, *i.e.*, $|\boldsymbol{u}| = |\mathcal{R}(\alpha)\cdot\boldsymbol{u}|$. Then,

$$\begin{aligned} \sum_{i\in\zeta} \boldsymbol{v}_i^2(t+h) &= \sum_{i\in\zeta} \Big\{ \boldsymbol{v}_\zeta^2(t) + \big\{\mathcal{R}(\alpha)\cdot\big(\boldsymbol{v}_i(t) - \boldsymbol{v}_\zeta(t)\big)\big\}^2 \\ &\qquad + 2\boldsymbol{v}_\zeta(t)\cdot\big\{\mathcal{R}(\alpha)\cdot\big(\boldsymbol{v}_i(t) - \boldsymbol{v}_\zeta(t)\big)\big\}\Big\} \\ &= \sum_{i\in\zeta} \Big\{ \boldsymbol{v}_\zeta^2(t) + \boldsymbol{v}_i^2(t) + \boldsymbol{v}_\zeta^2(t) - 2\boldsymbol{v}_i(t)\cdot\boldsymbol{v}_\zeta(t)\Big\} \\ &= \sum_{i\in\zeta} \boldsymbol{v}_i^2(t)\,, \end{aligned}$$

showing that the energy is exactly conserved in each collision cell, and consequently also the total energy of the simulated fluid is conserved. This simulation scheme is thus prescribing dynamics in the microcanonical ensemble.

If the step size in the streaming step is much smaller than the length a of the collision cells, the same fluid particles will repeatedly collide with each other, before leaving the respective collision cell [135]. Consequently, the corresponding particles will be correlated for several time steps. If now a homogeneous flow is imposed, then the correlations will adjust to the flow leading to a lack of Galilean invariance as the fluid's transport processes now depend on the direction of the imposed flow [131]. Thus, in order to restore Galilean invariance, the collision cell grid is shifted in each dimension by a random distance drawn from the interval $[0, a]$ before each collision. Accordingly, the particles are regularly sorted into cells with new neighbours such that the particles' velocities decorrelate faster. Additionally, the moving collision grid also enhances the momentum transport, since the collisional contribution of the momentum transport is no longer restricted to the interior of a fixed collision cell.

1.6.2 Angular momentum conservation

As has been pointed out by Pooley and Yeomans [136], the viscous stress tensor is not symmetric for the MPC fluid, which appears to be unphysical behaviour in order to describe a simple fluid [137]. This effect can be illustrated considering a simple fluid subject to a solid-body-like rotation. Here, the appearance of the antisymmetric contributions in the viscous stress tensor leads to unphysical non-zero viscous dissipation [131]. The effect is for most applications negligible and physically correct flow behaviour is obtained. However, when torques are acting on surfaces, the antisymmetric contributions lead to unphysical torques acting in the fluid [138]. The antisymmetric

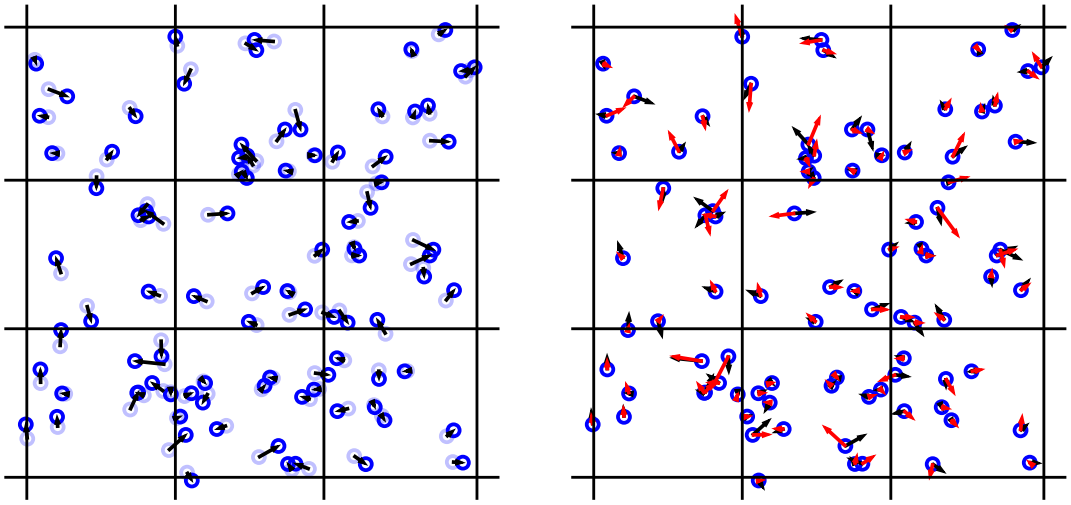

(a) (b)

Figure 1.4: Illustration of the streaming (a) and collision protocols (b) of MPC. In the streaming step, the particle positions $\boldsymbol{r}_i(t)$ (light blue) are transported ballistically to the new positions $\boldsymbol{r}_i(t+h)$ (dark blue). In the collision step, the particle velocities $\boldsymbol{v}_i(t)$ (black) are updated such that the new velocities $\boldsymbol{v}_i(t+h)$ (red) are composed of the centre of mass velocity of the respective collision cell, plus a rotation of the relative velocity of each particle with respect to the centre of mass velocity.

contribution of the viscous stress tensor can be traced back to the lack of systematic angular momentum conservation in the collision scheme [131]. But the protocol in equation (1.56) can be modified in order to fulfil angular momentum conservation for the cost of increased computational effort.

The change of angular momentum $\Delta\boldsymbol{L} = \boldsymbol{L}(t+h) - \boldsymbol{L}(t)$ of the fluid particles in cell ζ with respect to the centre of mass $\boldsymbol{r}_\zeta = \frac{1}{N_\zeta}\sum_{i\in\zeta}\boldsymbol{r}_i$ upon collision prescribed by the protocol in equation (1.56) can be expressed as

$$\begin{aligned}\boldsymbol{L}(t+h) - \boldsymbol{L}(t) &= \sum_{i\in\zeta}\left(\boldsymbol{r}_i - \boldsymbol{r}_\zeta\right)\times\left(\boldsymbol{v}_i(t+h) - \boldsymbol{v}_i(t)\right)\\ &= \sum_{i\in\zeta}\left(\boldsymbol{r}_i - \boldsymbol{r}_\zeta\right)\times\left\{\left[\boldsymbol{v}_\zeta(t) - \boldsymbol{v}_i(t)\right] + \mathcal{R}(\alpha)\cdot\left[\boldsymbol{v}_i(t) - \boldsymbol{v}_\zeta(t)\right]\right\}. \end{aligned} \tag{1.57}$$

Thus, in order for the collision scheme to fulfil angular momentum conservation, the velocities of the fluid particles $\boldsymbol{v}_i(t+h)$ at positions $\boldsymbol{r}_i$ with a momentum of inertia

$$I_\zeta^{(\alpha\beta)} = \sum_{i\in\zeta}\left\{\left(\boldsymbol{r}_i - \boldsymbol{r}_\zeta\right)^2\delta^{(\alpha\beta)} - \left(r_i^{(\alpha)} - r_\zeta^{(\alpha)}\right)\left(r_i^{(\beta)} - r_\zeta^{(\beta)}\right)\right\} \tag{1.58}$$

have to be corrected by the additive term $-\left(\boldsymbol{I}_\zeta^{-1}\cdot\Delta\boldsymbol{L}\right)\times\left(\boldsymbol{r}_i - \boldsymbol{r}_\zeta\right)$. The angular momentum conserving collision protocol can thus be written as [139]

$$\begin{aligned}\boldsymbol{v}_i(t+h) =& \boldsymbol{v}_\zeta(t) + \mathcal{R}(\alpha)\cdot\left(\boldsymbol{v}_i(t) - \boldsymbol{v}_\zeta(t)\right)\\ &+\left\{\boldsymbol{I}_\zeta^{-1}\cdot\sum_{j\in\zeta}\left(\boldsymbol{r}_j - \boldsymbol{r}_\zeta\right)\times\left\{\left[\boldsymbol{v}_j(t) - \boldsymbol{v}_\zeta(t)\right] + \mathcal{R}(\alpha)\cdot\left[\boldsymbol{v}_j(t) - \boldsymbol{v}_\zeta(t)\right]\right\}\right\}\\ &\times\left(\boldsymbol{r}_i - \boldsymbol{r}_\zeta\right). \end{aligned} \tag{1.59}$$

However, this collision protocol does not necessarily conserve energy. Thus, in order to simulate an angular momentum conserving fluid on an equal energy shell in the microcanonical ensemble, the velocity update in equation (1.59) has to be combined with a deterministic velocity rescaling scheme, guaranteeing that kinetic energy is conserved in each cell exactly [139].

Compared to the collision protocol in equation (1.56), an angular momentum conserving collision protocol is approximately by a factor of 2 computationally more expensive [131]. Therefore, the implementation of an angular momentum conserving collision scheme is only recommended if the antisymmetric contributions to the stress tensor give rise to non-negligible unphysical behaviour.

1.6.3 Cell level thermostat

Sometimes, it is more appropriate to simulate a fluid in the canonical instead of the microcanonical ensemble. That is, the system is coupled to a heat bath, thus, not the energy but the temperature is constant. In computer simulations, this can be achieved by exchanging momentum between the simulation particles and virtual heat bath particles with velocities drawn from a Maxwell-Boltzmann distribution [130]. This is especially important when the system is subject to a constant energy input, *e.g.*, an external field or shear, where a control mechanism has to be implemented in order to keep the temperature constant [140]

For the multiparticle collision dynamics method, a convenient scheme to ensure a constant temperature is a cell level rescaling of the relative velocities according to the distribution of kinetic energy in a cell. The herein reported method has been proposed in reference [140]. When the system is subject to an external energy source, only the relative velocities follow the Maxwell-Boltzmann distribution. The corresponding kinetic energy

$$E_{\text{kin}} = \frac{1}{2}\sum_{i\in\zeta}(\boldsymbol{v}_i - \boldsymbol{v}_\zeta)^2$$

is distributed according to [140]

$$\mathcal{P}(E_{\text{kin}}) = \frac{1}{E_{\text{kin}}\Gamma(f/2)}\left(\frac{E_{\text{kin}}}{k_{\text{B}}T}\right)^{f/2}\exp\left[-\frac{E_{\text{kin}}}{k_{\text{B}}T}\right], \tag{1.60}$$

where f is the degrees of freedom, *i.e.*, $f = d(N_\zeta - 1)$ for the relative velocities, and $\Gamma(x)$ is the usual gamma function. The velocities $\boldsymbol{v}_i$ of the fluid particles can then be thermalised on the cell level, by rescaling the velocity difference $\Delta\boldsymbol{v}_i \equiv \boldsymbol{v}_i - \boldsymbol{v}_\zeta$ according to

$$\Delta\boldsymbol{v}_i' = \sqrt{\frac{2\tilde{E}_{\text{kin}}}{\sum_{i\in\zeta}\Delta\boldsymbol{v}_i}}\,\Delta\boldsymbol{v}_i\,, \tag{1.61}$$

where $\tilde{E}_{\text{kin}}$ is drawn from the distribution in equation (1.60). This rescaling scheme should be applied to all collision cells after each collision.

Coupling the simulation dynamics to a thermostat is typically necessary for simulations of active matter systems, since energy is constantly injected into the system leading to the production of head. In systems, where heat is produced non-homogeneously, *e.g.*, because of an inhomogeneous distribution of energy injection,

controlling the temperature locally, *i.e.*, on the cell level, is especially advantageous compared to global rescaling schemes, in order to simulate the dynamics in the canonical ensemble. When simulating active matter in angular momentum conserving variants of MPC, the application of the rescaling scheme from reference [139] to conserve energy in each collision cell after the application of equation (1.59) is not necessary. Instead, the violation of energy conservation in equation (1.59) [141] and of the active energy injection is counteracted by the application of the cell-level thermostat introduced here.

1.6.4 Walls and solute particles

For the sake of practical applications, it is typically necessary to couple the solvent dynamics to immersed walls or solute particles, in order to include or exclude the fluid in or from a domain, respectively, and thus introduce boundaries to the fluid flow. Common boundary conditions include slip or no-slip boundary conditions. The latter is motivated by the continuity across the boundary of the component of the velocity tangential to the boundary [120]. The velocity of the fluid equals the velocity of the boundary, as has also been used in equation (1.35b). In terms of multi-particle collision dynamics, this boundary condition can be implemented in different ways [131, 142, 143], in order to obtain the position $\boldsymbol{r}''$ and velocity $\boldsymbol{v}'$ of the fluid particles after the interaction with the boundary. A common way is to stream the fluid particles freely, as described by equation (1.55), yielding the positions $\boldsymbol{r}_i(t+h)$. However, if the particles have penetrated no-slip boundaries during that process, the following bounce-back protocol is applied [130, 131, 142]. First, the fluid particles are moved back along their ballistic trajectory onto the interface, *i.e.*, onto the position where a physical collision between fluid particle and wall would have taken place, yielding the intermediate position $\boldsymbol{r}_i'(t+h) = \boldsymbol{r}_i(t+h) - \Delta\boldsymbol{r}_i$, where $\Delta\boldsymbol{r}_i = \boldsymbol{v}_i\tau_{\text{pen}}$ with penetration time $\tau_{\text{pen}} = d_{\text{pen}}/v_i$ and penetration depth d_{pen}, as illustrated in figure 1.5a. Note, that the intermediate position might also be described as $\boldsymbol{r}_i'(t+h) = \boldsymbol{r}_i(t+h-\tau_{\text{pen}})$. Then, the velocities are inverted, *i.e.*, $\boldsymbol{v}_i' = -\boldsymbol{v}_i$ and the particles are again ballistically transported to the final positions

$$\begin{aligned}\boldsymbol{r}''(t+h) &= \boldsymbol{r}_i'(t+h) + \boldsymbol{v}_i'\tau_{\text{pen}} \\ &= \boldsymbol{r}_i(t+h-\tau_{\text{pen}}) - \boldsymbol{v}_i\tau_{\text{pen}}\,.\end{aligned}$$

If the wall is subject to positional updates itself, *e.g.*, to model an immersed colloid with no-slip boundary at position $\boldsymbol{R}$ with velocity $\boldsymbol{V}$ and angular velocity $\boldsymbol{\Omega}$, the post-bounce velocity $\boldsymbol{v}_i'$ is slightly altered, in order to account for momentum exchange between fluid and colloid [51, 141, 144]

$$\begin{aligned}\boldsymbol{v}_i' =& \boldsymbol{v}_i - \frac{1}{m}\Delta\boldsymbol{P}_i \\ =& \boldsymbol{v}_i - 2\left\{\boldsymbol{v}_i - \boldsymbol{V} - \boldsymbol{\Omega}\times\left(\boldsymbol{r}_i' - \boldsymbol{R}\right)\right\}\,.\end{aligned} \tag{1.62}$$

The linear and angular momentum that is transferred to the colloid is then the sum of all single particle changes $\Delta\boldsymbol{P}_i$ and $\Delta\boldsymbol{L}_i = (\boldsymbol{r}_i' - \boldsymbol{R})\times\Delta\boldsymbol{P}_i$

$$\Delta\boldsymbol{P} = \sum_i \Delta\boldsymbol{P}_i\,, \tag{1.63a}$$

$$\Delta\boldsymbol{L} = \sum_i \Delta\boldsymbol{L}_i\,. \tag{1.63b}$$

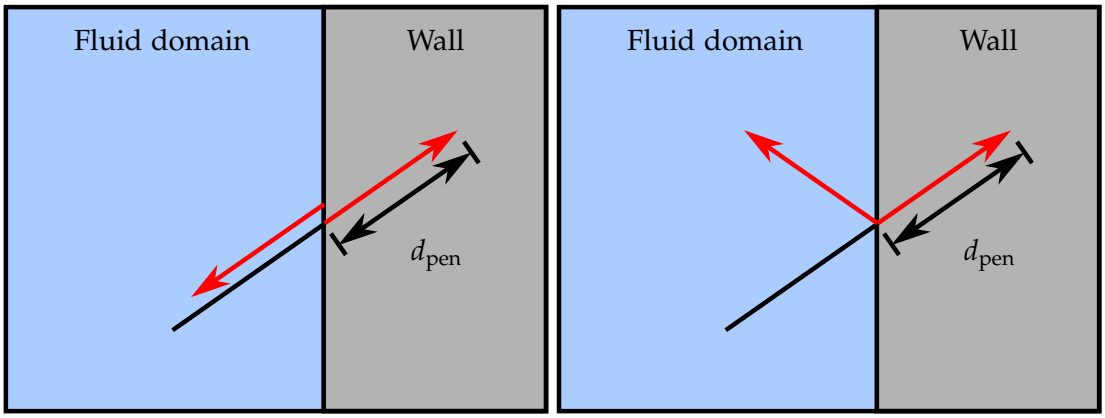

Figure 1.5: Illustration of the no-slip (a) and slip (b) boundary conditions.

Nevertheless, it is important to check whether the position $\boldsymbol{r}_i''$ after scattering the fluid particle and a boundary is laying in yet another boundary, especially in the case of a suspension of colloids. These may be subject to an unphysical, depletion-like attraction because of not properly resolving the repeated momentum transport between the colloids within one streaming step.

In the case of only partially filled collision boxes, or if the edges of the boundary and a collision box do not coincide, the bounce-back rule is not sufficient to guarantee a no-slip boundary condition [142]. In this case, the bounce-back rule has to be supplemented with the following modification of the MPC-collision [142, 144]. The collision cells, that are only partially filled with fluid particles because of the intersection with a no-slip boundary, are randomly filled with virtual, or "ghost" particles at $\boldsymbol{r}_i^{\text{vir}}$ in the inner region of the wall or colloid that overlaps with a collision cell. The velocities of these virtual particles are drawn from a Maxwell-Boltzmann distribution centred at the velocity $\langle \boldsymbol{v}_i^{\text{vir}} \rangle = \boldsymbol{V} + \boldsymbol{\Omega} \times (\boldsymbol{r}_i^{\text{vir}} - \boldsymbol{R})$, where $\boldsymbol{R}$, $\boldsymbol{V}$ and $\boldsymbol{\Omega}$ are again centre of mass, velocity and angular velocity of the no-slip boundary. The virtual particles then exchange linear and angular momentum with the fluid particles in the MPC collision protocol, but are of no further importance for the dynamics. Additionally, in the case of momentum transfer between fluid and boundary, as, *e.g.*, in the case of an immersed colloid, the linear and angular momentum transfer from the fluid to the virtual particles upon collision is transferred to the colloid momentum $\boldsymbol{P}$ and angular momentum $\boldsymbol{L}$, such that the sums in equation (1.63) go over fluid and virtual particles.

Fluid flows subject to no-slip boundary conditions on fixed walls, where $\boldsymbol{V} = 0$ and $\boldsymbol{\Omega} = 0$, are thus fully described. However, if the boundary itself is subject to positional updates as, *e.g.*, in the case of the immersed colloid with no-slip boundary, also the colloidal degrees of freedom, $\boldsymbol{R}$, $\boldsymbol{V}$, and $\boldsymbol{\Omega}$, have to be updated. Additionally, the colloids may interact pairwise. A straight-forward and well established method for doing so is the velocity-Verlet algorithm [145], which is numerically stable and exactly reversible in time, *i.e.*, it conserves energy [130]. The simulation of pairwise interacting particles according to the velocity-Verlet algorithm is typically referred to as molecular dynamics.

Theoretically, any arbitrary boundary condition could be employed in order to solve the Navier-Stokes equations. Another frequently used boundary condition complementing the no-slip condition is the slip, or free-boundary condition [120]. It is

motivated not by the continuity of velocity across the boundary, but by the continuity of stresses (*e.g.*, fluid stresses and surface tension) across the boundary. Numerically, it is accomplishes in multiparticle collision dynamics as follows. The scheme is very similar to the one given by the no-slip condition, explained above. However, the new velocity after the physical collision v' is different. The velocity component normal to the boundary is reflected, but the velocity component parallel to the boundary remains unchanged. In case of a slip boundary, no virtual particles are needed.

It should be noted, however, that also different protocols to couple the fluid dynamics to immersed objects, *e.g.*, colloids, are possible. The simplest way is to model immersed colloids, or the monomers of a polymer by point particles that take part in the MPC collision protocol as if it would be a heavy fluid particle [146]. The internal degrees of freedom of the solute particles, *i.e.*, colloid-colloid, or monomer-monomer interactions, still have to be considered separately, *e.g.*, by employing molecular dynamics [133]. A more detailed approach would be to model the solvent-solute and solute-solute interactions according to a full molecular dynamics scheme [14]. However, the different coupling methods, *i.e.*, treating the solute as an impenetrable boundary, heavy fluid particle, or coupling via molecular dynamics, all have advantages and disadvantages, and may be superior or inferior compared to other methods, depending on the application. In particular, explicit solvent-solute pair-interactions are necessary for thermophoretic effects, whereas the flow induced by a rotating colloid cannot be studied if the colloid is modelled as a point particle.

1.6.5 Transport coefficients and simulating low-$\mathcal{R}e$ hydrodynamics

The multiparticle collision dynamics algorithm can be employed for solving the Navier-Stokes equations, that can range from high-$\mathcal{R}e$ dynamics described by the Euler equation, to low-$\mathcal{R}e$ dynamics described by the Stokes equation [134]. In biological and soft matter systems, the fluid dynamics are typically fully captured by the latter limit. Thus, the system parameters, *i.e.*, the collision time h, the rotation angle α, the linear dimension of collision cells a, the density of MPC particles ρ, and the thermal energy $k_\mathrm{B}T$, have to be tuned accordingly [133].

In a MPC fluid, there are different transport mechanisms. The viscous spreading of momentum is controlled by the viscosity η, which exhibits contributions stemming from the streaming (η_kin) and the collision (η_col) steps. Both contributions can be calculated explicitly by considering the momentum flux due to streaming and collision crossing a unit plane in unit time, as is described in reference [139]. The authors therein obtain for the viscosity of an angular momentum conserving MPC fluid under the assumption of molecular chaos in d dimensions

$$\eta = \eta_\mathrm{kin} + \eta_\mathrm{col}\,, \tag{1.64a}$$

$$\eta_\mathrm{kin} = \frac{\rho k_\mathrm{B} T h}{a^d}\left\{\frac{1}{c_\mathrm{m}} - \frac{1}{2}\right\}, \tag{1.64b}$$

$$\begin{aligned} c_\mathrm{m} = {} & (1-\cos 2\alpha)\left\{1 - e^{-\rho}\left(1+\rho\right)\right\} \\ & + \left\{2\left(1-\cos\alpha\right) - \frac{(1-\cos 2\alpha)\,(3d+2)}{2}\right\}\frac{1 - e^{-\rho}\left(1+\rho+\rho^2/2\right)}{2\rho}\,, \end{aligned} \tag{1.64c}$$

$$\eta_\mathrm{col} = \frac{1-\cos\alpha}{12 d a^{d-2} h}\left\{\rho - \frac{7}{5} + e^{-\rho}\left(\frac{7}{5} + \frac{2\rho}{5} - \frac{3\rho^2}{10}\right)\right\}. \tag{1.64d}$$

Thus,

$$\eta \sim \begin{cases} \rho\,, & \rho \to \infty \\ h\,, & h \to \infty\,, \\ h^{-1}\,, & h \to 0 \end{cases} \tag{1.65}$$

where $\sim$ means asymptotically equal up to constants in the respective limit.

Mass transport is accounted for by the self-diffusion coefficient. For an angular momentum conserving MPC fluid, the authors of reference [139] arrive at the following self-diffusion constant under the assumption of molecular chaos

$$D = k_\mathrm{B}Th\left(\frac{1}{s_\mathrm{m}} - \frac{1}{2}\right)\,, \tag{1.66a}$$

$$s_\mathrm{m} = \frac{2}{d}\left(1-\cos\alpha\right)\left\{1 - \frac{d+1}{2\rho} + \frac{e^{-\rho}}{2}\left(\frac{(d-3)\rho}{2} + d - 1 + \frac{d+1}{\rho}\right)\right\} \tag{1.66b}$$

In liquids, the viscous transport dominates over the diffusive mass transport. A convenient measure to estimate the relative importance of these transport mechanisms is the Schmidt number. It is the ratio of the kinematic viscosity $\nu = \eta/\rho$, *i.e.*, momentum diffusivity due to the concept of viscous momentum spreading, to the self-diffusion coefficient D

$$\mathcal{S}c \equiv \frac{\nu}{D}\,. \tag{1.67}$$

In gases, the Schmidt number is on the order of unity, showing that diffusive mass transport is roughly as important as viscous transport, whereas in dense fluids or liquids, $\mathcal{S}c$ is (much) larger than unity, showing that the viscous transport and interparticle collisions become more important [131, 143].

The MPC fluid bears an ideal gas equation of state and is therefore highly compressible, with a low speed of sound c [131]. Thus, the interplay of MPC system parameters and solute particle parameters are not arbitrarily combinable. For the simulation of active matter systems not only the dimensionless quantities $\mathcal{S}c$, $\mathcal{P}e$ and $\mathcal{R}e$ are of importance, but also the Mach number, *i.e.*, the ratio of the fluid flow to the speed of sound

$$\mathcal{M}a \equiv \frac{u}{c}\,. \tag{1.68}$$

In order to avoid strong density inhomogeneities [147] resulting from compressibility, $\mathcal{M}a$ should be sufficiently small [131]. As a result, density inhomogeneities, caused by directed motion at speed u, are neutralised faster than created, consequently, the fluid can be regarded as effectively incompressible. On the other hand, this implies limitations on the maximum applicable speed of directed motion, as compared to the *fixed* speed of sound [148, 149]

$$c = \sqrt{\frac{5}{3}\frac{k_\mathrm{B}T}{m}}\,. \tag{1.69}$$

Concluding, the MPC system parameters have to be adjusted to the additional parameters, such that the method correctly describes the Navier-Stokes equation in the respective limit.

1.7. ABSTRACT OF THIS THESIS

While the number of publications on rotating active matter has rapidly increased in recent years, studies on purely hydrodynamically interacting rotors on the microscale are still rare, especially from the perspective of particle based hydrodynamic simulations. The work presented here targets to fill this gap. By means of high-performance computer simulations, performed in a highly parallelised fashion on graphics processing units, the dynamics of ensembles of up to 70,000 rotating colloids immersed in an explicit mesoscopic solvent consisting out of up to 30 million fluid particles, are investigated. Some of the results presented in this thesis have been worked out in collaboration with experimentalists, such that the theoretical considerations developed in this thesis are supported by experiments, and *vice versa*. The studied system, modelled in order to resemble the essential physics of the experimentally realisable system, consists out of rotating magnetic colloidal particles, *i.e.*, (micro-)rotors, rotating in sync to an externally applied magnetic field, where the rotors solely interact via hydrodynamic and steric interactions. Overall, the agreement between simulations and experiments is very good, proving that hydrodynamic interactions play a key role in this and related systems.

While already an isolated rotating colloid is driven out of equilibrium, only collections of two or more rotors have experimentally shown to be able to convert the rotational energy input into translational dynamics in an orbital rotating fashion. The rotating colloids inject circular flows into the fluid, such that detailed balance is broken, and it is not *a priori* known whether equilibrium properties of colloids can be extended to isolated rotating colloids. A joint theoretical and experimental analysis of isolated, pairs, and small groups of hydrodynamically interacting rotors is given in chapter 2. While the translational dynamics of isolated rotors effectively resemble the dynamics of non-rotating colloids, the orbital rotation of pairs of rotors can be described with leading order hydrodynamics and a two-dimensional analogy of Faxén's law is derived.

In chapter 3, a homogeneously distributed ensemble of rotors (bulk) as a realisation of a chiral active fluid is studied and it is explicitly shown computationally and experimentally that it carries odd viscosity. The mutual orbital translation of rotors and an increase of the effective solvent viscosity with rotor density lead to a non-monotonous behaviour of the average translational velocity. Meanwhile, the rotor suspension bears a finite osmotic compressibility resulting from the long-ranged nature of hydrodynamic interactions such that rotational and odd stresses are transmitted through the solvent also at small and intermediate rotor densities. Consequently, density inhomogeneities predicted for chiral active fluids with odd viscosity [67] can be found and allow for an explicit measurement of odd viscosity in simulations and experiments. At intermediate densities, the collective dynamics shows the emergence of multi-scale vortices and chaotic motion which is identified as active turbulence with a self-similar power-law decay in the energy spectrum, showing that the injected energy on the rotor scale is transported to larger scales, similar to the inverse energy cascade of classical two-dimensional turbulence. While either odd viscosity or active turbulence have been reported in chiral active matter previously, the system studied here shows that the emergence of both simultaneously is possible resulting from the osmotic compressibility and hydrodynamic mediation of odd and active stresses. The collective dynamics of colloids rotating out of phase, *i.e.*, where a constant torque instead of a constant angular velocity is applied, is shown to be qualitatively very similar. However, at smaller

densities, local density inhomogeneities imply position dependent angular velocities of the rotors resulting from inter-rotor friction.

While the friction of a quasi-2D layer of active colloids with the substrate is often not easily modifiable in experiments, the incorporation of substrate friction into the simulation models typically implies a considerable increase in computational effort. In chapter 4, a very efficient way of incorporating the friction with a substrate into a two-dimensional multiparticle collision dynamics solvent is introduced, allowing for an explicit investigation of the influences of substrate on active dynamics. For the rotor fluid, it is explicitly shown that the influence of the substrate friction results in a cutoff of the hydrodynamic interaction length, such that the maximum size of the formed vortices is controlled by the substrate friction, also resulting in a cutoff in the energy spectrum, because energy is taken out of the system at the respective length. These findings are in agreement with the experiments.

Since active particles in confinement are known to organise in states of collective dynamics [10, 41, 51, 103, 150–153], ensembles of rotationally actuated colloids are studied in circular confinement and in the presence of periodic obstacle lattices in chapters 5 and 6, respectively. The results show that the chaotic active turbulent transport of rotors in suspension can be enhanced and guided resulting from edge flows generated at the boundaries, as has recently been reported for a related chiral active system [150]. The consequent collective rotor dynamics can be regarded as a superposition of active turbulent and imposed flows, leading to on average stationary flows. In contrast to the bulk dynamics, the imposed flows inject additional energy into the system on the long length scales, and the same scaling behaviour of the energy spectrum as in bulk is only obtained if the energy injection scales, due to the mutual generation of rotor translational dynamics throughout the system and the edge flows, are well separated. The combination of edge flow and entropic layering at the boundaries leads to oscillating hydrodynamic stresses and consequently to an oscillating vorticity profile. In the presence of odd viscosity, this consequently leads to non-trivial steady-state density modulations at the boundary, resulting from a balance of osmotic pressure and odd stresses.

Relevant for the efficient dispersion and mixing of inert particles on the mesoscale by means of active turbulent mixing powered by rotors, a study of the dynamics of a binary mixture consisting out of rotors and passive particles is presented in chapter 7. Because the rotors are not self-propelled, but the translational dynamics is induced by the surrounding rotors, the passive particles, which do not inject further energy into the system, are transported according to the same mechanism as the rotors. The collective dynamics thus resembles the pure rotor bulk dynamics at the respective density of only rotors. However, since no odd stresses act between the passive particles, only mutual rotor interactions lead to odd stresses leading to the accumulation of rotors in the regions of positive vorticity. This density increase is associated with a pressure increase, which balances the odd stresses acting on the rotors. However, the passive particles are only subject to the accumulation induced pressure increase such that these particles are transported into the areas of low rotor concentration, *i.e.*, the regions of negative vorticity. Under conditions of sustained vortex flow, this results in segregation of both particle types.

Since local symmetry breaking can convert injected rotational into translational energy, microswimmers can be constructed out of rotor materials when a suitable breaking of symmetry is kept in the vicinity of a rotor. One hypothetical realisation, *i.e.*, a coupled rotor pair consisting out of two rotors of opposite angular velocity and

of fixed distance, termed a birotor, are studied in chapter 8. The birotor pumps the fluid into one direction and consequently translates into the opposite direction, and creates a flow field reminiscent of a source doublet, or sliplet flow field. Fixed in space the birotor might be an interesting realisation of a microfluidic pump [42]. The translational dynamics of a birotor can be mapped onto the active Brownian particle model for single swimmers. However, due to the hydrodynamic interactions among the rotors, the birotor ensemble dynamics do not show the emergence of stable motility induced clustering. The reason for this is the flow created by birotor in small aggregates which effectively pushes further arriving birotors away from small aggregates, which eventually are all dispersed by thermal fluctuations.

Chapter 2

Diluted rotating microparticles—hydrodynamic coupling

The results of this chapter partially have been prepared in manuscript [M]. Quotes from [M] are denoted as "..." [M]. Symbols, references, and citations are modified in order to fit to the remaining parts of this thesis.

An isolated rotor in solution is a system driven out of equilibrium, such that the concepts of equilibrium statistical mechanics do not apply. The inherent rotation of the colloid is injected into the fluid such that detailed balance is broken in the hydrodynamic degrees of freedom. By means of multiparticle collision dynamics simulations and in comparison to experiments [M], a study of the nonequilibrium dynamics of single rotors and small groups of rotors is presented in this chapter. Although hydrodynamic modes generated by the colloid dynamics are known to act back on the colloid [112, 154, 155], in the limit of $\mathcal{R}e \to 0$, the translational dynamics of isolated rotor may be mapped onto its equilibrium counterpart. However, when two rotors approach each other, they mutually exert hydrodynamic forces which lead to an orbital translation around the centre of mass. The frequency of the orbital dynamics can be accurately described within a leading order hydrodynamic approach with a two-dimensional analogy of Faxén's law. The results are in agreement with experiments from [M], proving that hydrodynamic interactions play the key role for the dynamics observed in the experiments. In a group of rotors, the hydrodynamic interactions lead to the formation of a rotating vortex.

2.1. Experimental setup and simulation design

"The rotors are silica rod-like colloids with a magnetic tip at one end, with the direction of the magnetic moment perpendicular to the rod axis (see appendix B). The sedimented rotors follow an externally applied magnetic field almost instantaneously, and in a particular frequency range, they precess perpendicular to the container basis, resulting in an ensemble of synchronously rotating cylinders with parallel symmetry axes." [M]

"The magnetic field is generated by two pairs of orthogonally placed Helmholtz coils hosted on a home-built microscope stage, figure 2.1b. Under a slowly rotating magnetic field ($B = 150$ Gauss), the rod lays flat on the substrate due to gravity, with

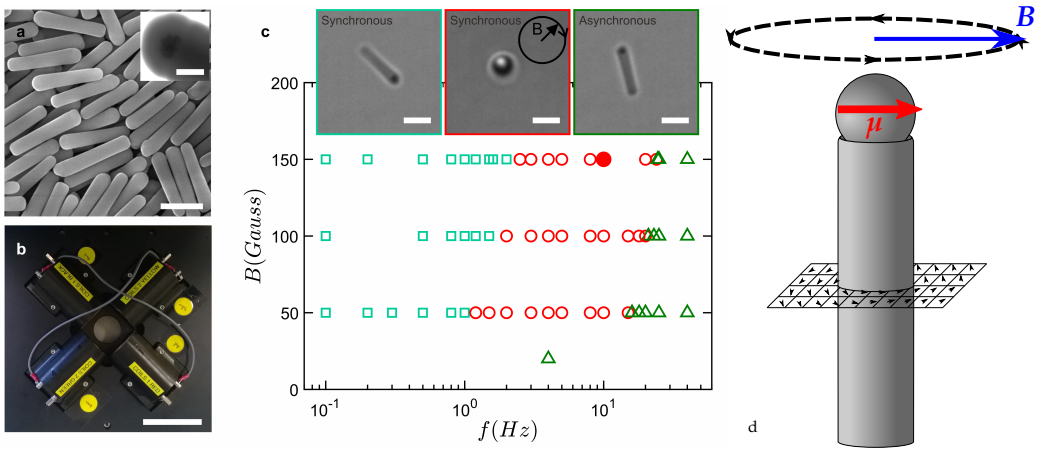

Figure 2.1: "Experimental system and dynamics of single rotors. (a) An SEM image of ferromagnetic Janus rods; the inset is a transmission electron microscopy image of the magnetic head of a rod. (b) Experimental setup with two-pairs of orthogonally placed Helmholtz coils for generating a rotating magnetic field. (c) State diagram of a single rod under a rotating magnetic field as a function of the frequency and the field strength. Insets show images of rods corresponding to the three dynamic states observed, horizontal rod rotating synchronously (light green squares), standing rod rotating synchronously (red circles), and horizontal rod rotating asynchronously (dark green triangles) with applied dynamic magnetic field. Most of experiments in the later work are conducted at a dynamic magnetic field of $10Hz$ and 150Gauss (red bullet). Scalebars are 2μm in (a), (c), 10 cm in (b), and 200 nm in the inset of (a)." [M] (d) Illustration of a rotor and co-rotating fluid. Images a, b, and c taken from [M].

long axis aligned perpendicular to the applied field, figure 2.1c. As a rotating magnetic field is applied between a certain range of frequency, typically $2-20$Hz, the rod stands up against gravity and rotates synchronously with the applied field, figure 2.1c, which we therefore term a rotor. In this study, we primarily focus on a rotating frequency of 10 Hz." [M]

"In parallel, we conduct large-scale simulations with a model of discs rotating at a fixed angular velocity Ω, immersed in an explicit hydrodynamic solvent, and interacting with other discs by steric interactions [51, 52, 134]. This assumes that the relevant interactions between the rotating rods take place only perpendicularly to their cylinder axes." [M] By employing a two-dimensional solvent, the finite length of the rotor and thus the hydrodynamic influences emanating from the rotors lower and upper ends are neglected. Instead, the same fluid flow along an infinitely long rotor is assumed, which is equivalent to regarding only one 2D layer of fluid, similar to the sketch in figure 2.1d. The simulation scheme for the fluid is in detail described in appendix A.

"The comparison between experiments and simulations is done via dimensionless quantities. Although single rotors cannot be considered as self-propelled particles, the magnetic activation can be quantified with the velocity at the colloid surface such that we consider the system Péclet number as $\mathcal{P}e = \Omega(\sigma/2)^2/D$ and the Reynolds number $\mathcal{R}e = \Omega\sigma^2/(2\nu)$ with σ the particle diameter, D the colloid diffusion coefficient, and ν the fluid kinematic viscosity. With specified default values, in experiments we are working with $\mathcal{R}e \approx 10^{-5}$ and $\mathcal{P}e \simeq 38$, for which the rod-head diameter has been considered. Meanwhile in simulations, $\mathcal{R}e \simeq 0.09$ and $\mathcal{P}e \simeq 20$, respectively. Clearly,

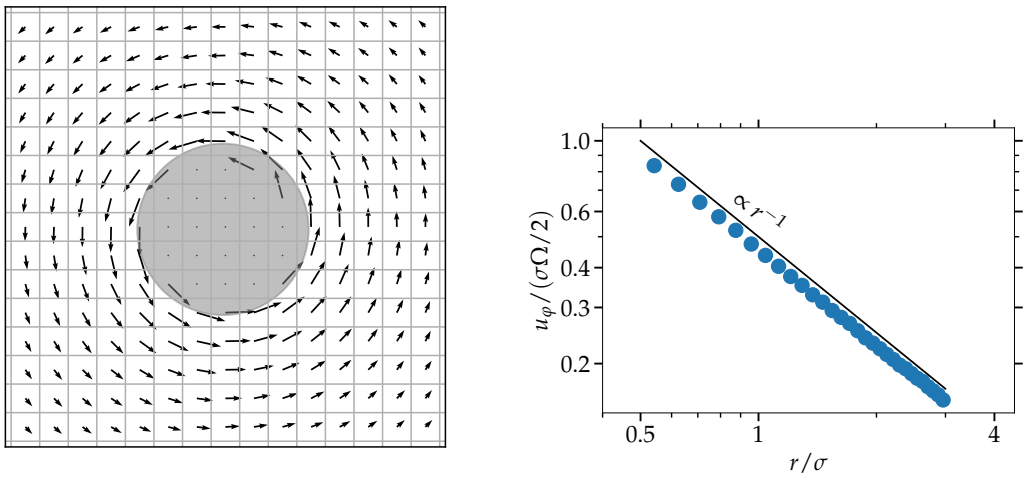

(a) (b)

Figure 2.2: Flow induced by a single rotating particle in two dimensions. (a) Azimuthal flow velocity, the black line is equation (2.1). On the surface of the colloid, a finite slip occurs implying an effective angular velocity of $\Omega_{\text{eff}} = 0.91\Omega$. (b) Two-dimensional flow field generated by a rotating disc.

the input parameters do not perfectly match, but these dimensionless numbers ensure that both simulations and experiments, are performed in the regime of low Reynolds and large Péclet numbers, where the same physical behaviour is to be expected." [M]

2.2. ISOLATED ROTATING COLLOIDS IN SOLUTION

In a two-dimensional system, a colloid of diameter σ rotating at constant angular velocity Ω in solution induces a purely azimuthal flow field in the co-moving frame

$$u_\varphi(r) = \frac{\sigma^2\Omega}{4}\frac{1}{r}, \tag{2.1}$$

where a no-slip boundary on the colloid surface is assumed. The flow field obtained from simulations is presented in figure 2.2a which shows to be in very nice agreement with the flow in equation (2.1) as can be seen from figure 2.2b.

According to equation (1.1) the equations of motion of a colloid in solution are local in time. However, a colloid moving in solution has to push the fluid volume elements ahead in order to move, such that this is in general not the case. As a consequence of the continuity of the flow, the induced fluid flow will act back onto the colloid [154] (confer figure 2.3), leading to a memory effect, *i.e.*, the influence of the fluid on the dynamics of the colloid is no longer local in time. The colloid excites hydrodynamic modes in the fluid, that in return act back onto the dynamics of the colloid (back-flow) at a later point in time, and equation (1.7) ($\mathcal{U} \equiv$ const.) then takes the non-Markovian form

$$\int_{-\infty}^{t} \mathrm{d}t' \dot{\boldsymbol{r}}(t') K(t-t') = \boldsymbol{\xi}(t)\,, \tag{2.2a}$$

$$\left\langle \boldsymbol{\xi}(t) \cdot \boldsymbol{\xi}(t') \right\rangle = 2k_{\mathrm{B}}TK(t-t')\,. \tag{2.2b}$$

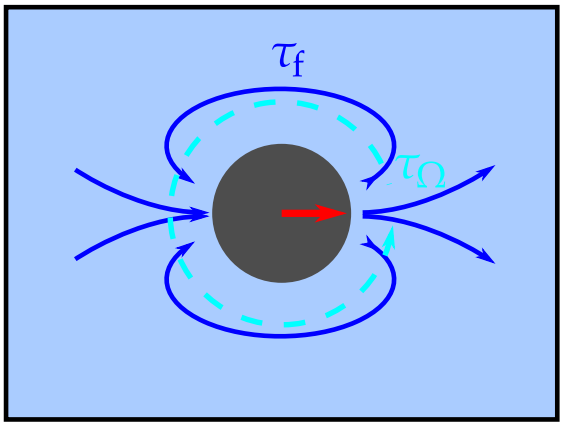

Figure 2.3: Illustration of the hydrodynamic back-flow. The colloid moves into the direction of the red arrow and as a result pushes the fluid volume ahead (blue). Consequently, the induced flow is acting back on the colloid. The relevant timescale for the back-flow is τ_f. If the colloid is rotating, an additional rotatory flow is created (cyan), with a relevant timescale of τ_Ω.

The friction kernel $K(t)$ denotes how the fluid influences the dynamics of the colloid at time t because of the colloid's dynamics at times $t' < t$. Experimental evidence for this phenomenon can be found in reference [154], where the authors measure long-range correlation as a consequence of the hydrodynamic memory $K(t)$.

In order to consider the hydrodynamic self-interactions in a solvent fulfilling equation (2.1) without solving the Stokes equation to obtain $K(t)$ for the rotating colloid explicitly, the consequences of the rotational flow on the translational degrees of freedom of the colloid can be estimated as follows. The Reynolds number $\mathcal{R}e$ of the rotating colloid is

$$\mathcal{R}e = \frac{\sigma^2\Omega}{2\nu}\,, \tag{2.3}$$

where the kinematic viscosity ν, σ and Ω are chosen such that $\mathcal{R}e \ll 1$. Furthermore, due to the linearity of the Stokes equation it is assumed that the flow field of a moving, rotating colloid can be regarded as the combination of equation (2.1) and the Stokes solution for a non-rotating colloid moving through a fluid [116]. Momentum transport as a result of the rotation of the colloid on a distance comparable to the size of the colloid takes place on a timescale $\tau_\Omega = \frac{1}{\Omega}$. In contrast, the timescale for vorticity diffusion on distances σ, *i.e.*, the viscous momentum back-flow, is $\tau_f = \frac{\sigma^2}{\nu}$. The influences of the colloid's rotation on the viscous momentum back-flow can be neglected if

$$\tau_f \ll \tau_\Omega\,, \tag{2.4}$$

because then the rotational momentum transport is much slower compared to the back-flow and the colloid can be regarded as essentially non-rotating on timescales $t \simeq \tau_f$. Note, that equation (2.4) can be cast into the following form, $\sigma^2\Omega/\nu \ll 1$, which is equivalent to $\mathcal{R}e \ll 1$. Thus, if the Stokes equation applies, *i.e.*, $\mathcal{R}e \ll 1$, then the hydrodynamic back-flow due to the rotational dynamics of a rotor can be neglected, and the equation of motion for a rotating colloid is essentially the same as for a non-rotating colloid in an infinite fluid domain. Therefore, the translational dynamics of isolated rotors and equilibrium colloids in solution at low $\mathcal{R}e$ can be regarded as essentially equivalent.

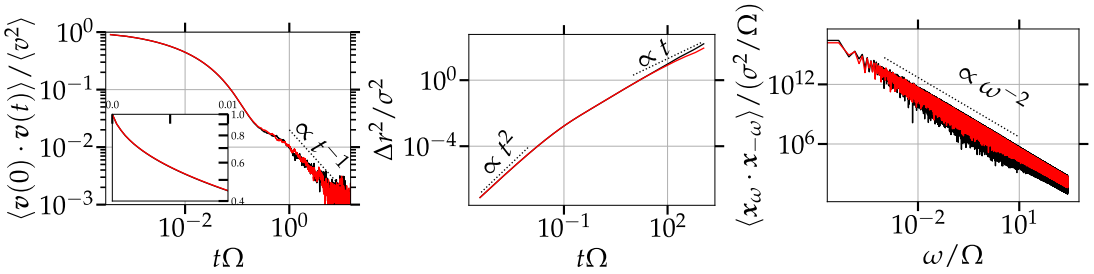

(a) (b) (c)

Figure 2.4: Dynamical quantities of a rotor rotating at constant angular velocity Ω (red) in comparison to a passive colloid (black). For convenience, frequency and time scales of both data sets are normalised using the angular velocity of the actively rotating colloid. Here, $\tau_f\Omega \approx 0.2$. (a) Velocity correlation function. The inset shows the short time evolution of $\langle v(0)\cdot v(t)\rangle$ on a linear-logarithmic scale. (b) Mean-square displacement. (c) Positional power spectral density.

The equivalence of the translational dynamics of a rotating and non-rotating colloid at low $\mathcal{R}e$, can be shown by the following computer simulations. The results of two independent sets of simulations of isolated colloids are shown in figure 2.4. On the one hand, simulations of a two-dimensional colloid rotating at fixed angular velocity Ω were performed, whereas in the other set of simulations, the angular velocity of the colloid is not restricted and the colloid freely exchanges angular momentum with the fluid. Both simulations show qualitatively and quantitatively the same results.

Figure 2.4a shows the velocity correlation functions $\langle v(t)\cdot v(0)\rangle$ of a colloid in equilibrium and a rotating one in two dimensions, which are in perfect agreement. At short times, the velocity correlation functions are not exponentially decaying, but carry an additional non-trivial dependency, as can be observed in the inset of figure 2.4a. The same behaviour was found in reference [156], where also a colloid in a multiparticle collision dynamics solvent was studied, such that it is concluded that, hydrodynamics even dominate on very short timescales in a MPC solvent. On long timescales, the velocity correlation functions develop a long time tail, because of the vortex flow on timescales τ_f [157,158] sketched in figure 2.3. A mode-mode coupling theory for transport phenomena predicts a long time tail of $\langle v(t)\cdot v(0)\rangle \propto t^{-d/2}$, in $d \geq 2$ dimensions [159], in agreement with molecular dynamics simulations [157]. This long time tail is also shown in figure 2.4a, and is in agreement with both simulation results, up to noise in the data.

Note, however, that in a two-dimensional system, the decay $\langle v(t)\cdot v(0)\rangle \propto t^{-1}$ must be incorrect. This is because of plugging the velocity correlation function in the Green-Kubo relation to define the diffusion coefficient [160]

$$D = \frac{1}{d}\int_0^\infty \mathrm{d}t\ \langle v(t)\cdot v(0)\rangle \tag{2.5}$$

yields a divergence for $d = 2$, since the integral $\int_0^\infty \mathrm{d}t\, t^{-1}$ is divergent. This issue can be taken care of within a self-consistent mode coupling approach, leading to a marginally faster decay of $\langle v(t)\cdot v(0)\rangle \propto \left(t\sqrt{\ln t}\right)^{-1}$ and the introduction of a time-dependent diffusion coefficient $D(t)$ [158]. However, the main interest of the present work is not to determine the very exponent for the long time tails of two-dimensional hydrodynamic theories, which goes outside the scope of this thesis. Here, it is shown

that the rotating and the equilibrium 2D-colloid show the same behaviour in the hydrodynamic regime.

The mean-square displacements are shown in figure 2.4b, and both show the expected asymptotic behaviour of a Brownian particle given by equations (1.3b). Similar to the velocity-autocorrelation, the mean-square displacements do not show strong inertia effects at short times, *i.e.*, a fully developed ballistic regime where $\langle \Delta \boldsymbol{r}^2 \rangle \propto t^2$ is not obtained, but the dependency might be extrapolated from the data. In order to obtain the short time inertial behaviour of the colloid for at least one decade, the integration time of the simulation would have to be significantly lowered such that a higher time resolution is achieved. This, however, is not beneficial, since the main focus of this work is on the hydrodynamic behaviour, on timescales much larger than the momentum relaxation time. At late times, $\langle \Delta \boldsymbol{r}^2 \rangle$ attains a diffusive regime, as is indicated by the $\langle \Delta \boldsymbol{r}^2 \rangle \propto t$ behaviour[1], as is also expected from the experimental mean-square displacement in section 2.1. Up to a mismatch at late times the two simulation data sets (active, passive) lie on top of each other, providing and extrapolated diffusion coefficient of $D = 3.73 \times 10^{-4} \sigma^2 / (a\sqrt{m/(k_\mathrm{B}T)})$. The mismatch is expected to originate from insufficient statistics, and thus to vanish if more data is considered. However, it becomes increasingly difficult to obtain reliable time-correlations of points that are far apart on the time-line. In the experiments, consider "the translational motion of a single rotor or a dilute suspension of rotors when they are far apart by measuring the mean squared displacements (MSD, $\langle r^2 \rangle$), which grows linearly with time" [M] in accordance with the simulations. The experimentally measured diffusion coefficient is $D = 0.171 \pm 0.001 \mu\mathrm{m}^2/\mathrm{s}$.

In Fourier space, equation (1.1) (with $\mathcal{U} \equiv$ const. and $d = 2$) reads

$$-m\omega^2 \hat{\boldsymbol{x}}_\omega = i\zeta\omega \hat{\boldsymbol{x}}_\omega + \hat{\boldsymbol{\xi}}_\omega \,, \tag{2.6a}$$

$$\left\langle \hat{\boldsymbol{\xi}}_{\omega_1} \cdot \hat{\boldsymbol{\xi}}_{\omega_2} \right\rangle = 4k_\mathrm{B}T\zeta\delta(\omega_1 + \omega_2) \,. \tag{2.6b}$$

Consequently, the positional power spectral density can be written as

$$\langle \hat{\boldsymbol{x}}_\omega \cdot \hat{\boldsymbol{x}}_{-\omega} \rangle = \frac{4\zeta k_\mathrm{B}T}{m^2 \left(\omega^4 + \frac{\zeta^2}{m^2}\omega^2 \right)} \,. \tag{2.7}$$

Thus, at frequencies $\omega \gg \zeta/m$ where inertia dominates, the power spectral density is following a power-law, $\langle \hat{\boldsymbol{x}}_\omega \cdot \hat{\boldsymbol{x}}_{-\omega} \rangle \propto \omega^{-4}$, whereas at low frequencies, $\omega \ll \zeta/m$, the corresponding power-law is $\langle \hat{\boldsymbol{x}}_\omega \cdot \hat{\boldsymbol{x}}_{-\omega} \rangle \propto \omega^{-2}$. In the overdamped case, where $\zeta/m \to \infty$, the power spectral density is $\langle \hat{\boldsymbol{x}}_\omega \cdot \hat{\boldsymbol{x}}_{-\omega} \rangle \propto \omega^{-2}$ $\forall \omega > 0$. The simulation results for the power spectral density for a rotating and equilibrium colloid are shown in figure 2.4c. Again, up to numerical instability, the results coincide. Similar to the velocity correlation function, inertia effects do not show to play a role in the power spectral density at high frequencies such that the overdamped limit, *i.e.*, $\langle \hat{\boldsymbol{x}}_\omega \cdot \hat{\boldsymbol{x}}_{-\omega} \rangle \propto \omega^{-2}$, is fulfilled at any ω.

The identity of the simulation results of the rotating and equilibrium rotor in solution show that in the limit of $\tau_\mathrm{f} \ll \tau_\Omega$ the rotating fluid flow around an isolated rotor does not affect the back-flow dynamics of the colloid. The translational degrees of freedom of isolated rotors can thus be regarded as only weakly perturbed from equilibrium, and standard equilibrium principles like the diffusion or the friction coefficient still apply. The translational dynamics of isolated rotors suspended to

[1] The self-consistent mode coupling approach suggests a slight variation in the mean-square displacement $\langle \Delta \boldsymbol{r}^2 \rangle \propto \sqrt{\ln t}\, t$, with a time-dependent diffusion coefficient [158].

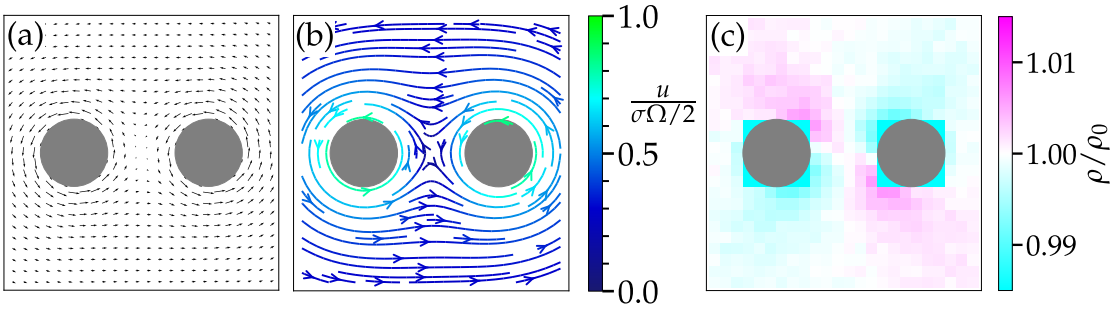

Figure 2.5: Flow field (a), streamlines (b), and density field (c) created by a rotor pair.

an infinitely extended solvent may thus be regarded to perform standard Brownian motion.

2.3. TWO-ROTOR HYDRODYNAMIC INTERACTIONS

A single rotor in solution induces the flow given in equation (2.1), but does not show any significant difference from an equilibrium colloid in the translational dynamics. However, the symmetry of an isolated rotor is broken if another rotor is in the vicinity of the first rotor. The induced flow fields of both rotors interact and the flow is no longer rotationally symmetric around the rotors, such that there are preferred directions the rotors move into. Because of the linearity of the Stokes equation, a linear combination of individual solutions also serves as a solution. Though, note, that the boundary conditions are in general not linear, rendering many body problems nonlinear. But sufficiently far away from the rotors surfaces, a linear combination of the individually induced flow fields can be regarded as a good approximation to the flow field excited by both rotors [161]. The study of rotor pair interactions therefore serves as a basis to understand rotor ensemble dynamics.

2.3.1 Flow fields

A starting point for the study of hydrodynamically interacting rotor pairs is the investigation of the mutually induced flow field. To this end, simulations of a rotor pair of fixed positions are performed, where the velocity of the fluid in the (non-grid-shifted) collision cells is averaged. The result is shown in figure 2.5a and figure 2.5b, which show the vector field of the fluid flow $\boldsymbol{u}(\boldsymbol{r})$ and the corresponding streamlines, respectively.

Resulting from the symmetry of the system, the flow has a stagnation point in the middle between the rotors. The fluid flow is decaying with distance from the pair, as can be seen by the length of the vectors in figure 2.5a, or by the colour code in figure 2.5b. Additionally, the fluid flow has a rotational symmetry upon rotations about an angle of π about the middle between the rotors. Figure 2.5c shows the density inhomogeneities in the multiparticle collision dynamics fluid because of the finite compressibility of the fluid. For the chosen system parameters, the density inhomogeneities are of the order of 1% and the resulting pressure gradient thus may be neglected [147].

A quantitative analysis of the fluid flow is provided by figure 2.6. The blue line in figure 2.6a shows the horizontal flow component u_x on the vertical line going through the middle of the left rotor in figure 2.5a, whereas the blue line in figure 2.6b shows

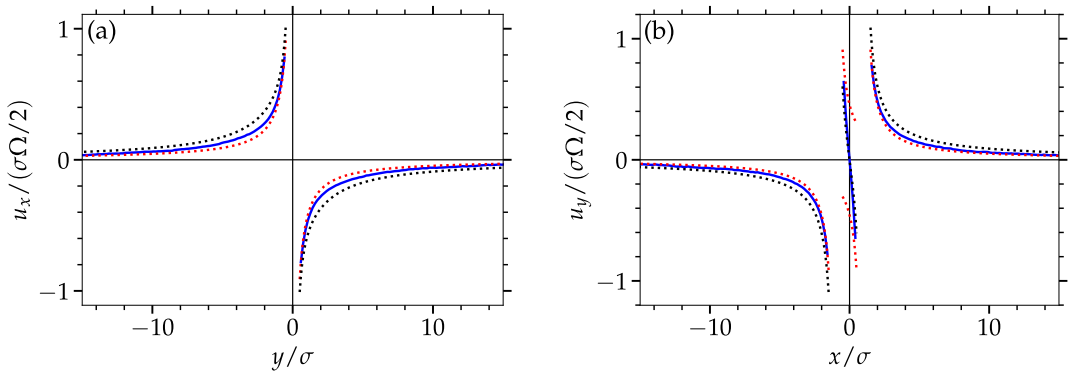

Figure 2.6: Flow perpendicular to the vertical (a) and horizontal (b) lines through the centres of the colloids as shown in figure 2.5. The solid blue lines depict the measured flow, the red dashed lines represent the flow field of the closest rotor if it was isolated in an infinite fluid, and the dashed black line is the sum of the isolated flow fields of the two rotors. Both, the blue and red data is corrected for the finite slip measured in figure 2.2b.

the vertical flow component u_y on the horizontal line going through both colloid centres. For reference, the red dotted lines represent the theoretical fluid flow from equation (2.1) of the nearest rotor, where the flow induced by the second rotor is neglected, and the black dotted lines are the respective components of the superposition of the flow of two isolated rotors

$$\boldsymbol{u}_\Sigma(\boldsymbol{r}) = u_\varphi(|\boldsymbol{r}_1 - \boldsymbol{r}|)\hat{e}_\varphi^{(1)}(\boldsymbol{r}) + u_\varphi(|\boldsymbol{r}_2 - \boldsymbol{r}|)\hat{e}_\varphi^{(2)}(\boldsymbol{r})\,,$$

where $\boldsymbol{r}_i$, $i = 1,2$ are the rotors positions, and $\hat{e}_\varphi^{(i)}(\boldsymbol{r})$ is the vector at position $\boldsymbol{r}$ pointing into the azimuthal direction with respect to a polar coordinate system located at position $\boldsymbol{r}_i$. Along both directions, *i.e.*, figure 2.6a and b, the measured fluid flow happens to agree better to the red reference line, than the black linear combination. The primary reason for this is that the latter does not regard the individual boundary conditions. The presence of another rotor does not alter the boundary conditions on the rotors' surfaces, *i.e.*, $\boldsymbol{u}(\boldsymbol{r})\big|_{\boldsymbol{r}\in\partial V_i} = \sigma\Omega/2 \cdot \hat{e}_\varphi^{(i)}(\boldsymbol{r})$ for $i = 1,2$. Thus at short distances, the individual solutions, which fulfil the boundary conditions, will always perform better than the superposition approximation. With increasing distances from the colloids, the measured flow decays slower than the individual solution and approaches the linear combination of the individual solutions, because far away from the surfaces the boundary conditions play a negligible role. However, between the rotors the situation is opposite, *i.e.*, the measured flow is in better agreement with the linear combination, even though the respective fluid volume elements are close to the surfaces. Nonetheless, the simultaneous fulfilment of the boundary conditions at $x = \pm 0.5\sigma$ enforces the fluid to be at rest at $x = 0$, which is also fulfilled by the linear combination, in contrast to the individual solutions. Thus, the better agreement of the measured flow to the sum of the individual flow fields in the vicinity of the rotors, *i.e.*, the boundaries, is a result of the continuity of the linear combination and not a result of the quality of the approximation. It can thus be concluded, that the sum of individual flow fields can be regarded as a good approximation for the induced flow field of interacting rotors, as long as the flow is not evaluated in the direct vicinity of the colloids, *i.e.*, the

boundaries.

2.3.2 Hydrodynamic forces

Revisiting equations (1.35) and equation (1.22b), the hydrodynamic forces acting on the rotors can be calculated by the knowledge of the flow field $\boldsymbol{u}(\boldsymbol{r})$ shown in figure 2.5a and b. For an analytical solution, the Stokes equation fulfilling the boundary conditions on the rotors' surfaces has to be solved. Although it is not possible to obtain a solution for the Stokes equation that fulfils the boundary conditions on the rotors' surfaces and is resting at infinity [162], similar to the case of a moving disc in a two-dimensional fluid, mentioned in section 1.3.2, the particular case here allows for matching an inner Stokes solution to an outer solution of the steady Navier-Stokes equations [163, 164]. This outer solution is the flow caused by a line (point in 2D) vortex, which in contrast to the two discs can be solved exactly. The motivation for matching the inner Stokes flow to the line vortex Navier-Stokes flow is that infinitely far away from the discs, the flow induced by the two rotating discs should not vary drastically from that of a single rotating disc [163]. A detailed calculation for the solution of the stream function for the rotor pair can be found in reference [163], where the equations are solved in terms of bipolar coordinates, considering the problem's symmetry. Bipolar coordinates are related to Cartesian coordinates (x, y) by

$$x = \frac{d \sinh \xi}{\cosh \xi - \cos \eta}\,, \tag{2.8a}$$

$$y = \frac{d \sin \eta}{\cosh \xi - \cos \eta}\,, \tag{2.8b}$$

with $-\pi \leq \eta < \pi$, $-\alpha < \xi < \alpha$ and $d > 0$. The resulting hydrodynamic forces can be decomposed in two contributions. On the one hand, $F_\perp$ acts in the direction perpendicular to the line connecting the rotors' centres, whereas $F_\parallel$ acts parallel to the centres' line into the direction of repelling rotors. The forces are point-symmetric with respect to the centre of symmetry, *i.e.*, the point between the rotors. Figure 2.7 illustrates the directions of the forces and an intiutition of bipolar coordinates. To the current level of approximation the hydrodynamic forces are [164]

$$F_\parallel = 0\,, \tag{2.9a}$$

$$F_\perp = \frac{4\pi\eta\sigma\Omega d}{\sinh 2\alpha + 2\alpha} \left\{ \frac{\sinh 2\alpha}{2\sinh^2 \alpha} - \frac{2\alpha \sinh^2 \alpha}{S(\alpha)\,[\sinh 2\alpha + 2\alpha]} \right\}\,, \tag{2.9b}$$

with

$$S(\alpha) = \frac{\alpha \sinh^2 \alpha \tanh \alpha}{\sinh \alpha \cosh \alpha + \alpha} + \frac{1}{2} - 4 \sum_{n=2}^{\infty} \frac{n^2 \sinh^2 \alpha + n \sinh \alpha \cosh \alpha + e^{-n\alpha} \sinh n\alpha}{n(n^2-1)(\sinh 2n\alpha + n \sinh 2\alpha)}\,.$$

Here, d and α are expressed in terms of bipolar coordinates and can be written using the rotor diameter and centre-to-centre distance r according to

$$\sinh \alpha = \frac{d}{\sigma/2}\,,$$

$$\cosh \alpha = \frac{r}{\sigma}\,.$$

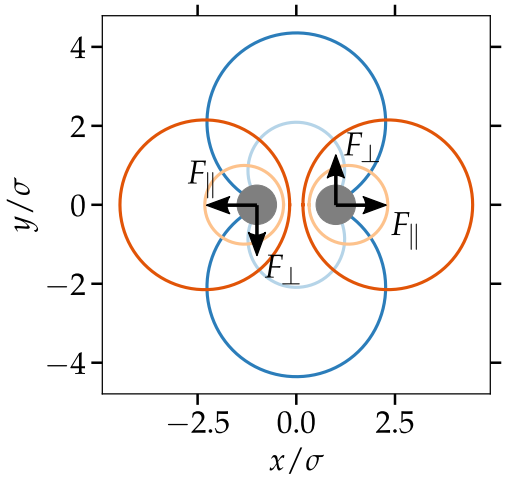

Figure 2.7: Sketch of the hydrodynamic forces and bipolar coordinates. The grey circles illustrate the rotors. The lines in orange and blue gradients depict the bipolar coordinates of fixed ξ and η, respectively.

Interestingly, the above calculation at vanishing $\mathcal{R}e$ predicts no hydrodynamic forces in the parallel direction. In contrast, at small, but finite $\mathcal{R}e$, *i.e.*, on the order of one, rotors are known to mutually exert repulsive forces onto each other as a consequence of the Magnus force [43–46], *i.e.*, a pressure imbalance resulting from the nonlinear terms in the Navier-Stokes equation. However, if inertia effects do not contribute, *i.e.*, $\mathcal{R}e = 0$, the repulsion is negligible and the rotors should neither repel, nor attract [44, 59], as is predicted by equation (2.9a). In order to predict the parallel force in the limit of $\mathcal{R}e \to 0$ more accurately, a higher order approximation is needed, which also involves non-linear terms and thus becomes very involved [164].

The hydrodynamic forces acting on the rotors as a result of the average flow field can be straight-forwardly calculated using multiparticle collision dynamics simulations. To this end, the momentum exchange between the fluid and the rotors is calculated per unit time and averaged. In order to only count contributions as a result of the average flow field $\boldsymbol{u}(\boldsymbol{r})$, the positions of the rotors are fixed for the whole simulation. In this way, attractive contributions to $F_\parallel$ because of the hydrodynamic back-flow of moving colloids [59] are excluded. Figure 2.8 shows the simulation results in comparison to the analytical prediction from equations (2.9). The simulation results for the perpendicular force $F_\perp$ are in very good agreement with the analytical prediction. The force decreases with increasing inter-rotor distance r and only becomes comparable to the strength of thermal fluctuations $k_\mathrm{B}T/\sigma$ for $r \approx 10\sigma$. However, the numerical results are systematically weaker than the prediction. This mismatch can be explained with the finite slip at the rotors' surfaces, which in turn reduces the hydrodynamic forces. The red line in figure 2.8a takes the finite slip obtained from the measurement in figure 2.2b into account, such that the simulation results and equation (2.9b) are almost in perfect agreement. Nevertheless, the finite slip at the surfaces of the rotors is very small and it might be neglected in further analyses.

In contrast to the analytical prediction for the parallel force $F_\parallel$, a non-zero attraction between the rotors can be measured in the simulations. The attractive force becomes stronger as the rotors approach each other, but is only observable for $r < 2\sigma$ and is

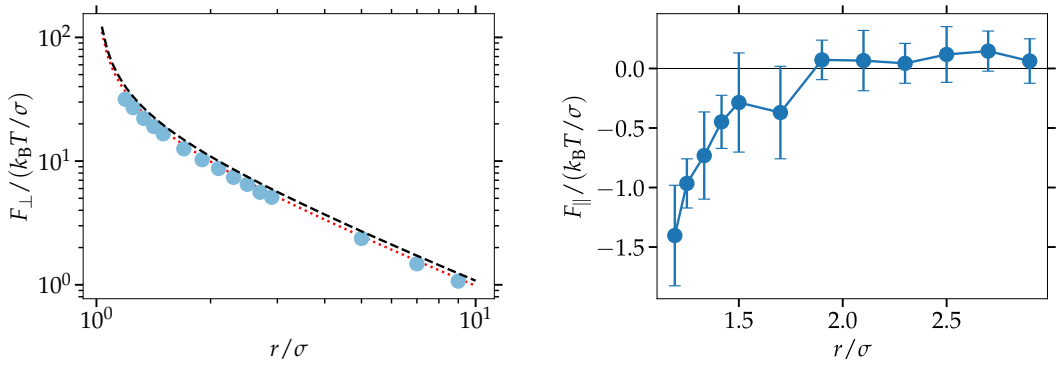

(a) (b)

Figure 2.8: Mutual hydrodynamic forces of the rotor pair in units of the typical strength of thermal fluctuations experienced by the rotors k_BT/σ. (a) Perpendicular $F_\perp$ and (b) parallel force $F_\parallel$. Symbols denote simulation results and lines correspond to the analytical prediction in equations (2.9). In figure 2.8a, the black line is the prediction using input parameters, whereas the red line takes the finite slip into account. The forces are calculated for a unit time of $t\Omega/(2\pi) \approx 3$ and averaged over 1000 measurements. For $F_\perp$, the errors are smaller then the symbol size. The forces are calculated in a system with periodic boundary conditions of size $L = 33\sigma$ (for inter-rotor distances $r < 3\sigma$) and $L = 100\sigma$ ($r > 3\sigma$).

on the order of the strength of thermal fluctuations. However, the attractive force between the rotors in figure 2.8b does not necessarily prove an attraction between rotors at small $\mathcal{R}e$, complementing the first order approximation in equation (2.9a) from reference [164]. The fixed colloids are constantly pumping the compressible multiparticle collision dynamics solvent, which potentially leads to small density inhomogeneities and thus to small pressure differences. The fluid particles oppose the pumping by diffusion [147]. The pumping number $\mathcal{P}u$ is defined as the ratio of the time for diffusion on distances of the rotor size and the time scale for active transport along the rotor surface, *i.e.*, $\mathcal{P}u \equiv \sigma^2\Omega/(4D_f)$. Thus, if $\mathcal{P}u \gg 1$, strong density inhomogeneities can arise as a consequence of constant pumping. The weak density inhomogeneities observable in figure 2.5, where $\mathcal{P}u = 13$, are therefore result of the pumping. For the standard parameters employed, with $\mathcal{P}u = 13$, the incompressibility of the simulation fluid only leads to a weak attraction on short distances that can easily be overcome by thermal fluctuations. The perpendicular force still is in very nice agreement with the analytical prediction, also for short inter-rotor distances and the density inhomogeneities are on the order of 1%. We thus conclude that for this standard parameters, the compressibility artefacts can be neglected. A more detailed investigation of this artefact is given in appendix C.

"Provided the use of magnetic colloids, we experimentally quantify pair interactions parallel to the line of centres by estimating the effective pair potential as a function of radial distance [165], $U(r) = -k_BT \log g(r)$." [M] However, moving colloids give rise to additional hydrodynamic back-flow interactions [59]. "Results are shown in figure 2.9 for a dilute suspension of rotors for three values of the magnetic rotating frequency. At the lower frequency, the rotors only display repulsive interactions, while for increasing frequencies, a weak short-range attraction on the order of $0.2k_BT$

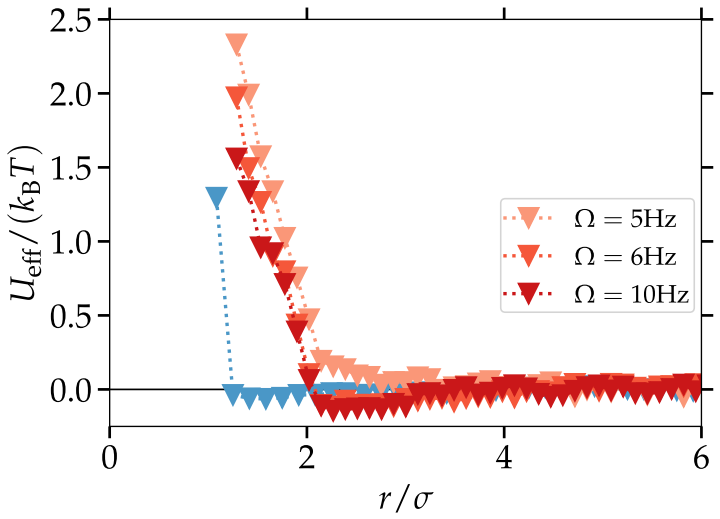

Figure 2.9: "Effective pair potential. Estimated from the radial distribution function as $U(r) = -k_{\mathrm{B}}T \log g(r)$ at density $\phi = 0.007$ for simulations (in blue) and $\phi = 0.0002$ for experiments (in red) at three input spin frequency values, showing the absence of significant dipolar magnetic interactions." [M] Image taken from [M].

emerges. For reference, one simulation data set is also displayed showing the same qualitative behaviour. This proves that dipolar magnetic interactions between rotors are negligible in experiments, since they should be noticeable and decrease in intensity with frequency." [M]

As a consequence of the hydrodynamic forces, the rotors perform a meta-stable orbital rotation about the centre of mass, *i.e.*, the particles will be separated by thermal fluctuations and the angular velocity of the orbital rotation will decrease with increasing inter-rotor distance.

2.3.3 Leading order hydrodynamics

If a pair of rotors is freely moving, the hydrodynamic forces in equations (2.9) imply a metastable orbital rotation around the centre of mass. Figure 2.10 shows simulation and experimental trajectories of a rotor pair that show the expected behaviour, *i.e.*, at short inter-particle distances r the pair performs a fast orbital rotation that becomes slower with increasing r. For a sufficient spacing between the rotors, we might assume the two induced flow fields, equation (2.1), to add up. Thus, the rotors are each influenced by the flow field created by the opposite rotor. For the hydrodynamic interactions of an immersed colloid in a prescribed velocity field, Faxén's law provides an approximation to calculate the velocity of the colloid in the prescribed flow [4]. Here, the two-dimensional analogy of Faxén's law is derived. The idea of Faxén's law is to use the Green's function approach given in equation (1.42), where the point forces are acting on the surfaces of the (2D) colloid [4]. Additionally, the prescribed flow $\boldsymbol{U}$ dictated by the other rotor is added, such that the flow is obtained as

$$u_\alpha(\boldsymbol{r}) = U_\alpha(\boldsymbol{r}) + \oint_{\partial V} \mathrm{d}S\, H_{\alpha\beta}(\boldsymbol{r} - \boldsymbol{r}') \cdot f_\beta(\boldsymbol{r}')\,.$$

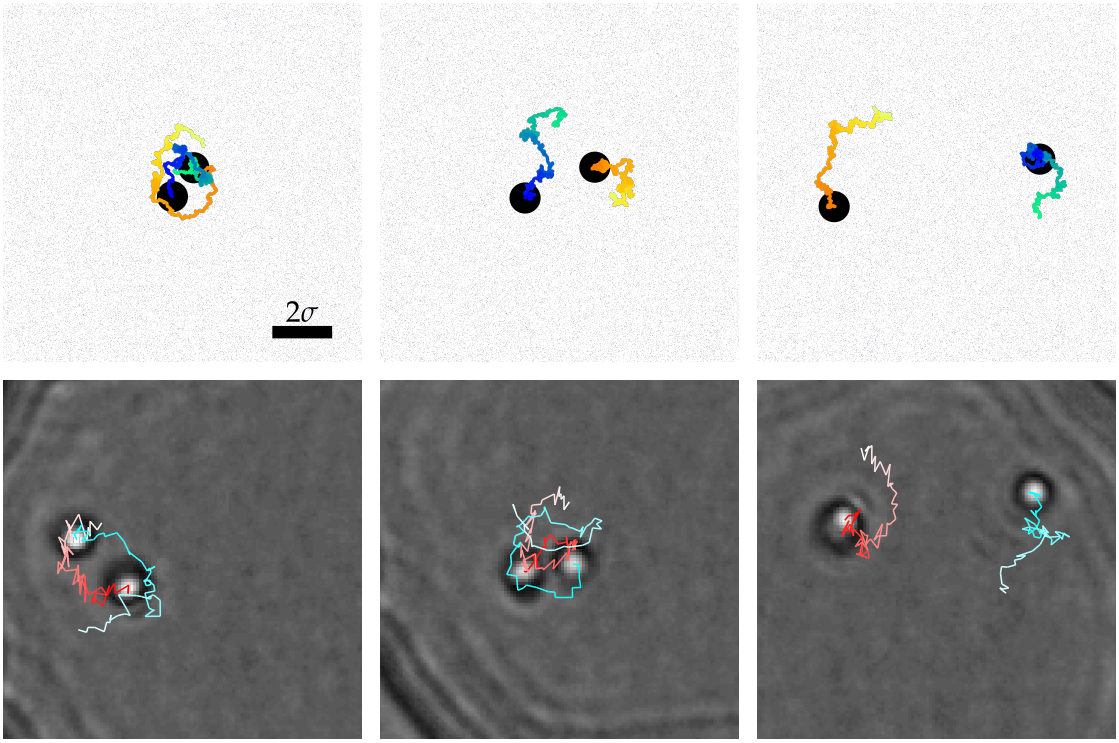

Figure 2.10: Trajectories of hydrodynamically interacting rotors. First row simulation results. The black circles represent the rotors, whereas the small blue points depict the point-like fluid particles. Second row experiment results. The trajectories of the rotors (scale of blues and oranges) are coded such that the lighter coloured segments represent times more distant in the past. During the duration of both trajectories, the rotors perform $t\Omega/(2\pi) \approx 5$ circulations.

Here, ∂V is the surface of the colloid, and $\boldsymbol{f}$ is the force per unit area exerted by surface elements on the fluid. On the surface of the colloid, *i.e.*, $\boldsymbol{r} \in \partial V$, a no-slip boundary condition implies

$$v_\alpha + \Omega\varepsilon_{\beta\alpha}(r_\beta - r_\beta^{(0)}) = U_\alpha(\boldsymbol{r}) + \oint_{\partial V} \mathrm{d}S\, H_{\alpha\beta}(\boldsymbol{r}-\boldsymbol{r}')\cdot f_\beta(\boldsymbol{r}')\,, \tag{2.10}$$

where $\boldsymbol{v}$, Ω, and $\boldsymbol{r}^{(0)}$ are the colloid's velocity, angular velocity, and centre of mass-position, respectively. If equation (2.10) is integrated over ∂V, the angular velocity part on the left hand side vanishes, when a circular colloid of radius R and surface $S = \pi\sigma$ is assumed. The result is thus

$$v_\alpha = \frac{1}{\pi\sigma}\oint_{\partial V} \mathrm{d}S\, U_\alpha(\boldsymbol{r}) + \frac{1}{\pi\sigma}\oint_{\partial V}\mathrm{d}S' \oint_{\partial V} \mathrm{d}S\, H_{\alpha\beta}(\boldsymbol{r}-\boldsymbol{r}')\cdot f_\beta(\boldsymbol{r}')\,. \tag{2.11}$$

The second term on the right hand side of equation (2.11) is the opposing velocity due to the hydrodynamic flow created when the colloid is subject to an external force [4]. Here, this term is neglected and only the flow due to the second rotor is regarded. The first term on the right hand side can be simplified by approximating $\boldsymbol{U}(\boldsymbol{r})$ as its Taylor series at the centre of the colloid, up to second order. However, as a consequence of the circular symmetry of the colloid only even terms contribute to the integral over the surface ∂V [4]. Hence, the integral on the right hand side of equation (2.11) can be

approximated as

$$\oint_{\partial V} \mathrm{d}S\, U_\alpha(\boldsymbol{r}) \approx \oint_{\partial V} \mathrm{d}S \left\{ U_\alpha\left(\boldsymbol{r}^{(0)}\right) + \frac{1}{2}\partial_\lambda \partial_\mu U_\alpha\left(\boldsymbol{r}^{(0)}\right)(r_\lambda - r_\lambda^{(0)})(r_\mu - r_\mu^{(0)}) \right\} . \quad (2.12)$$

The integral over the first summand simply gives the size of ∂V, *i.e.*, $\oint_{\partial V} \mathrm{d}S = \pi\sigma$. For the second integral, the origin is shifted to $\boldsymbol{r}^{(0)}$, where the surface of the colloid is then expressed by $\partial V'$. The integral is then performed over tensor elements $r_\lambda r_\mu$, which can be expressed in terms of polar coordinates. The integral over the surface of the circular colloid over the off-diagonal elements of $r_\lambda r_\mu$ vanish, *i.e.*, $\int_0^{2\pi} \mathrm{d}\varphi \cos\varphi \sin\varphi = 0$. The diagonal elements are $r_1 r_1 = \cos^2\varphi$ and $r_2 r_2 = \sin^2\varphi$, thus giving

$$\frac{1}{\pi\sigma} \oint_{\partial V} \mathrm{d}S'\, r_\lambda r_\mu = \frac{\sigma^2}{8}\delta_{\lambda\mu} . \quad (2.13)$$

Without external force, Faxén's law in two dimensions consequently yields

$$v_\alpha = U_\alpha\left(\boldsymbol{r}^{(0)}\right) + \frac{\sigma^2}{16}\partial_\beta\partial_\beta U_\alpha(\boldsymbol{r}_0) . \quad (2.14)$$

In the picture of the two rotors, the prescribed flow $\boldsymbol{U}$ that influences the rotor at $\boldsymbol{r}^{(0)}$ is induced by the other rotor (confer equation (2.1)) and can be expressed as

$$U_\alpha(r_\beta) = \frac{\sigma^2\Omega}{4}\varepsilon_{\beta\alpha}\frac{r_\beta}{r^2} , \quad (2.15)$$

for $\boldsymbol{r} \notin V$. The Laplacian of this flow, however, vanishes

$$\partial_\beta\partial_\beta U_\alpha = 0 , \quad (2.16)$$

such that the correction to zeroth order in equation (2.14) does not contribute, as is also the case for the flow created by a rotating sphere in 3D [50]. Consequently, the rotors are advected by the flow of the opposite rotor and are on average transported along the streamlines. For the magnitude of the orbital linear and angular velocities of two rotors separated by a distance r, v_φ and Ω_{pair}, respectively, this yield

$$v_\varphi = \frac{\sigma^2\Omega}{4}\frac{1}{r} , \quad (2.17a)$$

$$\Omega_{\mathrm{pair}} = \frac{\sigma^2\Omega}{2}\frac{1}{r^2} . \quad (2.17b)$$

Figure 2.11a shows the measured angular velocity of the orbital dynamics Ω_{pair}. The simulations are in excellent agreement to equations (2.17). "The experimental values are in qualitative agreement with these results, although systematically lower by approximately a factor two. The sedimented magnetic rods in experiments rotate in a container of height much larger than the rod length, such that the induced flow partially escapes into the upper fluid layers above the rods. Furthermore, the friction between the solvent and the substrate implies a no-slip boundary condition between fluid and substrate which diminishes the effective flow experienced by nearby rotors. Both effects are more pronounced at larger inter-particle distances. The overall agreement between experiments and simulations, however, is very good, especially at short distances, where pair interactions are substantially stronger than the thermal noise." [M] Therefore, the hydrodynamic orbital dynamics can be successfully described with leading order hydrodynamic interactions.

The radial dynamics, *i.e.*, the relative distance between the rotors is not covered by the leading order description above. Starting from equations (2.9a) and (2.17), the only contribution to the radial dynamics is thermal noise. Thus, the relative distance can be regarded as being subject to a random process and its value increases with time. The relative distance grows diffusively, assuming that the rotors are initially close to each other ($r \to \sigma$). The process may be approximated by the drift-free diffusion equation with solution (1.11). The relative distance r is then a measure for the spreading of the diffusion. As a consequence, when averaging over independent realisations of the dynamics $r(t)$, it will follow

$$\langle r \rangle \propto \sqrt{t}\,. \tag{2.18}$$

However, there are subtle differences between the free one-dimensional diffusion and the relative distance between the rotors. On the one hand, the weak hydrodynamic attraction in the simulations (confer figure 2.8b) breaks the scale invariance in r, as the attraction is predominantly important at short inter-rotor distances and becomes irrelevant at large distances. On the other hand, the rotors will feel a hydrodynamic coupling because of the mutual influences of the back-flow, that is only present when the rotors are allowed to move through and thus displace the solvent [59]. The behaviour can be explained similar to a moving colloid that induces a flow field which drags nearby colloids. As a consequence of this hydrodynamic interactions, at small distances, $r(t)$ only grows very slowly since the rotors tend to follow each other, until thermal fluctuations increase the distance between the rotors sufficiently, such that the hydrodynamic attraction is negligible. That is, the diffusive behaviour in equation (2.18) is only valid for sufficiently large distances between the particles. The results shown in figure 2.11b are in very nice agreement with the above consideration. For distances $r \gtrsim 3\sigma$ the scaling approximately follows the diffusive behaviour in equation (2.18). On the other hand, the hydrodynamic attraction becomes relevant for $r < 3\sigma$. Comparison to figure 2.8b shows that the hydrodynamic attraction caused by a moving rotor is stronger than the weak attraction as a consequence of the finite compressibility of the fluid.

2.4. ISOLATED ROTOR GROUPS

2.4.1 Vortex formation

It is only of numerical challenge to calculate the velocities of the rotors for a fixed geometry according to equation (2.17a). But since the thermal fluctuations will constantly change the geometry of a given assembly of rotors, this task is rather cumbersome. In order to predict the dynamics of the N rotor assembly shown in figure 2.12 according to equation (2.17a), all the distances and relative angles of the connecting lines have to be known. On a coarse-grained level, however, we may approximate the density of the circular assembly as constant and accordingly also the angular velocity density, implying a linear dependence of the azimuthal velocity component, such that the assembly is considered to rotate in a solid body fashion. As the rotors diffusively spread, the size of the assembly will increase. In order to estimate the size, the time dependent radius of gyration

$$R_\mathrm{g}(t) \equiv \sqrt{\frac{1}{N}\sum_i^N \left(\boldsymbol{r}_i(t) - \boldsymbol{r}_\mathrm{cm}(t)\right)^2} \tag{2.19}$$

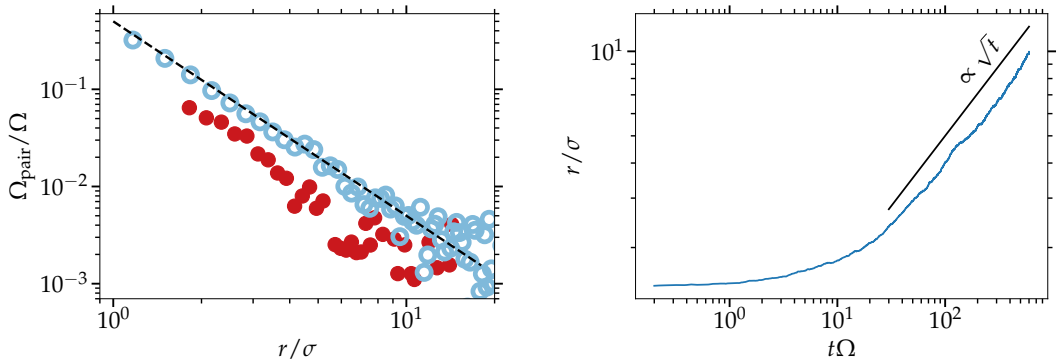

(a) (b)

Figure 2.11: Angular and radial dynamics of the hydrodynamically coupled rotor-pair. (a) "Co-rotation angular velocity Ω_{pair} as a function of the separation of the two rotors: red, experimental results; blue, simulations. Dashed line is the theoretical prediction $\Omega_{\mathrm{pair}}/\Omega = \sigma^2/(2r^2)$." [M] Image taken from [M]. (b) Evolution of the inter-rotor distance r. The black line shows the scaling of the prediction according to diffusive behaviour of r, equation (2.18). The data was obtained by performing 240 independent simulations of initially equally spaced rotors ($r(t=0) = 1.33\sigma$).

serves as a measure to estimate the spreading of the rotors around the centre of mass position $\boldsymbol{r}_{\mathrm{cm}}$.

The rotational dynamics of the assembly is initiated by a driving torque M_{d} which is opposed by a frictious torque M_{f} leading to a constant angular velocity, for a given configuration size R_{g}. The driving torque is generated by the outermost layers of the assembly, that are propelled along the azimuthal direction. Torques acting on the outer layers viscously translate into the middle of the assembly. Here, the viscosity of a colloidal suspension at packing fraction ϕ in two dimensions has to be taken into account $\eta(\phi) = \eta_0(1-\phi/\phi_{\mathrm{cp}})^{-2\phi_{\mathrm{cp}}}$, where η_0 is the viscosity of the solvent and ϕ_{cp} is the packing fraction at close packing [166–168]. Since the magnitude of the torque cam be expressed as force times radius and the force is proportional to the line density of rotors in the outermost layer,

$$M_{\mathrm{d}} \propto 2\pi\sqrt{n}R_{\mathrm{g}}^2\,,$$

with n being the number density in the assembly, *i.e.*,

$$n(r) \equiv \frac{N}{\pi R_{\mathrm{g}}^2}\theta(R_{\mathrm{g}}-r)\,, \tag{2.20}$$

where θ is the Heaviside step function. If the constant density rotor assembly is regarded as a rotating disc experiencing a frictional torque in an infinite fluid that is resting at infinity, then

$$M_{\mathrm{f}} \propto 4\pi\eta\hat{\Omega}R_{\mathrm{g}}^2\,,$$

where η is the viscosity of the fluid and $\hat{\Omega}$ is the constant angular velocity of the assembly. Balancing the torques thus yields

$$\hat{\Omega} \propto \frac{\sqrt{n}}{2\eta}\,.$$

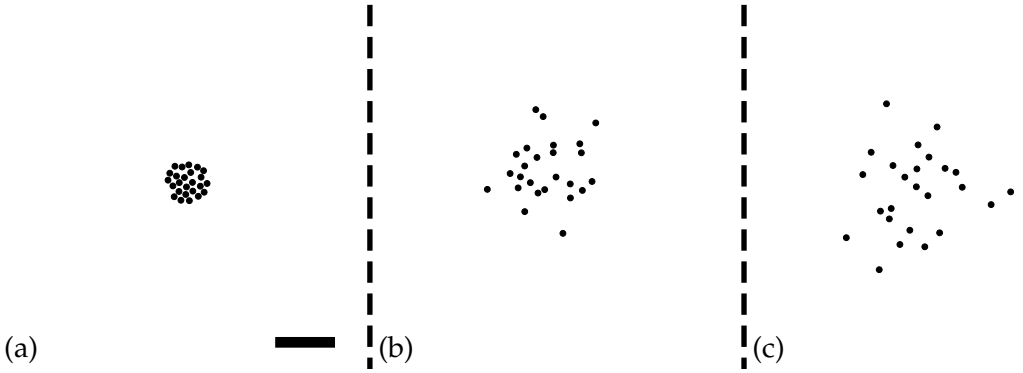

Figure 2.12: Simulation of a circular assembly. (a) Geometry of the initialisation ($t = 0$). The scale bar is 10σ. (b) and (c) display configurations at $t\Omega/(2\pi) = 118$ and $t\Omega/(2\pi) = 236$, respectively.

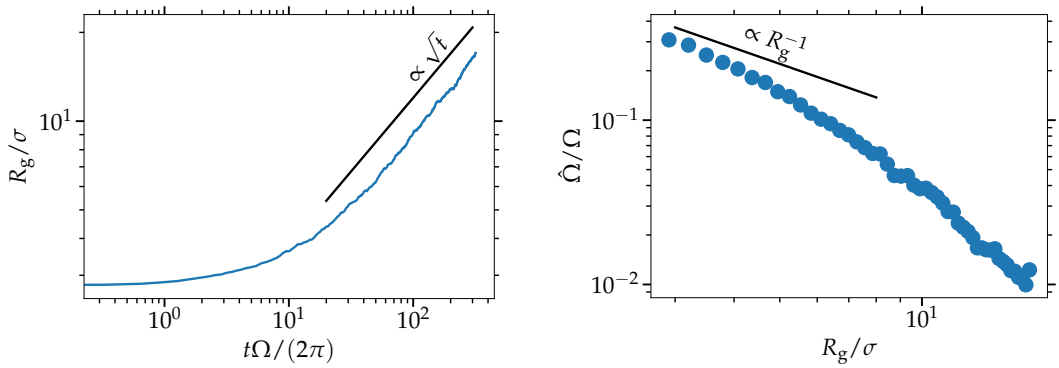

(a) (b)

Figure 2.13: Characterisation of the dynamics of a hydrodynamically coupled group of rotors. (a) Evolution of the radius of gyration R_g. (b) Average angular velocity. The data was obtained by simulating 25 rotors initially randomly distributed in a circular domain of radius $R_{ini} = 4\sigma$ in a circular simulation contained of size $R_o = 50\sigma$ with a no-slip boundary condition on the container wall. The results were obtained by averaging over 8 independent simulations.

This relation bears a dependency on the size of the assembly R_g. Inserting the R_g-dependent density from equation (2.20) leads to

$$\hat{\Omega} \propto R_g^{-1}\,. \tag{2.21}$$

The diffusive spreading of the arrangement is qualitatively related to the evolution of the relative distance of two rotors. Thus, the density is not constant, but evolves to a Gaussian distribution that is spreading in time as $\sqrt{t}$ and thus

$$R_g \propto \sqrt{t}\,. \tag{2.22}$$

Similar to the discussion of figure 2.11b, again mutual hydrodynamic interactions in the radial direction are present at short inter-particle distances, such that the actual power-law is only developed at later times, as can be seen in figure 2.13a. Figure 2.13b shows the dependency of the angular velocity $\hat{\Omega}$ on the size of the assembly R_g, where

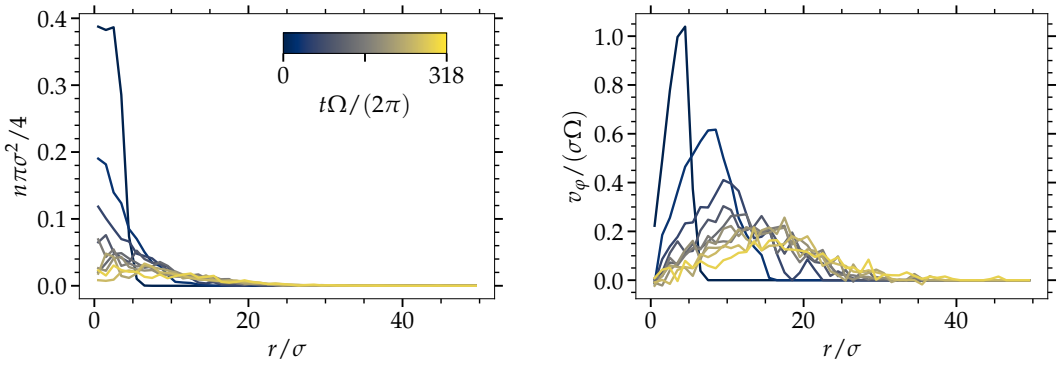

(a) (b)

Figure 2.14: Time evolution of the radial density and the associated deviations from a linear velocity profile. (a) Radial rotor number density. (b) Azimuthal velocity $v_\varphi = r\hat{\Omega}$. The time evolution is indicated by the colour scale in the inset of figure 2.14a and the associated colours of the lines. The underlying data is the same as in figure 2.13. Each colour represents an average over a time of duration $t\Omega/(2\pi) \approx 3$.

the angular velocity is obtained in terms of the rotors positions $\boldsymbol{r}_i$ and velocities $\boldsymbol{v}_i$ by averaging over all rotors, *i.e.*,

$$\hat{\Omega} = \frac{1}{N}\sum_i^N \frac{1}{(\boldsymbol{r}_i - \boldsymbol{r}_{\mathrm{cm}})^2}\varepsilon_{\alpha\beta}\left(r_i^{(\alpha)} - r_{\mathrm{cm}}^{(\alpha)}\right)v_i^{(\beta)}\,. \tag{2.23}$$

The time evolution of the size of the arrangement is following the above presented reasoning, similar to the time evolution of the relative distance of a rotor pair. However, the dependency of $\hat{\Omega}$ on R_g only approaches equation (2.21) for small R_g and $\hat{\Omega}$ decays faster with increasing R_g. Figure 2.14a shows the time evolution of the radially varying number density in the assembly. The rotor density can only be regarded as constant at very early times and then quickly relaxes from the uniform initial condition to a Gaussian distribution $n \propto e^{-a\,r^2/R_\mathrm{g}^2}$, with a scaling factor a, as expected for the diffusive process. As a consequence, also the angular velocity density follows a Gaussian distribution, such that the azimuthal component of the corresponding velocity only follows a linear relationship for $r \to 0$, where $e^{-r^2} \approx 1$, as can be seen in figure 2.14b. Thus, for fixed n and $R_\mathrm{g} \to R_\mathrm{g}^\mathrm{min}$, where $R_\mathrm{g}^\mathrm{min}$ is the minimal dimension of the assembly approaching close-packing, the scaling of the angular velocity approaches equation (2.21), because in this limit $n \approx$ const.

2.5. Summary

Colloidal microrods with an adhered magnetic moment perpendicular to the rod axis have shown to orient in a rotating magnetic field. In the non-equilibrium state of vertical orientation the rotating rods are termed rotor. While single, isolated rotors do not show translational dynamics qualitatively different from Brownian particles at equilibrium, a co-rotating flow is induced in the surrounding solvent. Consequently, if two suspended rotors approach, the mutually induced hydrodynamic flows generate to a net hydrodynamic force leading to a metastable orbital rotation around the centre of

mass. According to a generalisation of Faxén's law to two dimensions, the angular velocity of the orbital rotation decays with inter-rotor distance as r^{-2}, in agreement with simulations and experiments, showing that the hydrodynamic interactions among rotors can be described successfully with two-dimensional hydrodynamics. The relative distance between the rotors is subject to diffusive spreading. When more than two rotors are involved in the dynamics, making predictions from the superposition of hydrodynamic flows becomes very cumbersome. However, a continuum approach yields qualitative insight and when the rotor density is approximately constant also agrees quantitatively. For a group of densely packed rotors, the mutual hydrodynamic interactions lead to the formation of a collective vortex rotation, where the density of the group is expanding diffusively.

Chapter 3

Microrotor bulk dynamics: Odd viscosity and active turbulence

The results of this chapter partially have been prepared in manuscript [M]. Quotes from [M] are denoted as "..." [M]. Symbols, references, and citations are modified in order to fit to the remaining parts of this thesis.

The two-dimensional bulk dynamics of microrotor suspensions shows the emergence of net translational actuation, correlations between vorticity and density due to odd viscosity, and active turbulence. The mutually induced orbital rotation in a rotor ensemble leads to a chain of translational actuation, which is non-monotonous in the rotor density. Increasing density on the one hand leads to an increase in mutual actuation, but on the other hand also increases the effective solvent viscosity, which in turn reduces the translational actuation, leading to a non-monotonous behaviour of the actuated velocity with rotor density. Experiments and simulations reveal the emergence of multi-scale vortices, in which the rotors are dragged into the centres of circulation of the same angular direction as the rotor's angular velocity, allowing for an explicit measurement of odd viscosity. A power-law decay in the energy spectrum shows the presence of active turbulence with self-similarity in the multi-scale vortex formation without the emergence of a dominant vortex scale. In the experiments, however, the friction between the solvent and the substrate implies the introduction of an energy dissipation scale which thus limits the extent of the power-law and initiates the occurrence of a dominant vortex scale. By the development of an efficient way to incorporate the effect of substrate into the numerical model, this behaviour is explicitly shown. Furthermore, a study of non-synchronous rotors, by keeping the applied torque instead of the input angular velocity constant, reveals no qualitative differences compared to the rotor ensemble rotating in sync.

3.1. Converting rotation into propulsion

Symmetry breaking is a necessary ingredient in order to convert the intrinsic rotation into actuated propulsion [51, 52]. As has been shown in chapter 2, in the case of a rotor pair, the presence of the first rotor renders the flow field around the other rotor asymmetric (and *vice versa*) leading to non-vanishing contributions to the stress exerted on the rotors surfaces and consequently to an orbital rotation. For an isolated group of rotors, the breaking of translational symmetry implies the generation of the application of a torque on the outermost rotor layer and consequently the rotation of

the assembly as a whole. However, in an infinitely extended ensemble of rotors, there is, on average, no breaking of translational symmetry expected, *i.e.*, the rotor density is on average constant throughout the whole domain. Thus, the hydrodynamic forces $F_\perp$ between the rotors on average cancel in a pairwise fashion. Nevertheless, local in time and space, thermal noise leads to the emergence of density inhomogeneities, such that the mutual hydrodynamic interactions yield a net force implying non-equilibrium actuated dynamics. "The fluid in contact with the colloids surface co-rotates with it, generating long-range interactions between rotors, which induce the rotors' propulsion. This leads to similar ensemble dynamics and rich cooperative effects, such as dynamic vortex formation and mesoscale turbulence, all of which is a function of the packing fraction." [M]

"The motion of more than two interacting rotors is now investigated as a function of the packing fraction ϕ. Rotor configurations and typical trajectories are shown in Figs. 3.1a-c for experiments and in figures 3.1d-f for simulation results. In simulations, trajectories are easy to track and all are marked in grey, while experimentally, due to the limited frame rate of the image acquisition, full trajectories of all particles cannot be automatically tracked, such that typically 15-30 rotors are tracked, with a few representative ones shown in figures 3.1a-c.

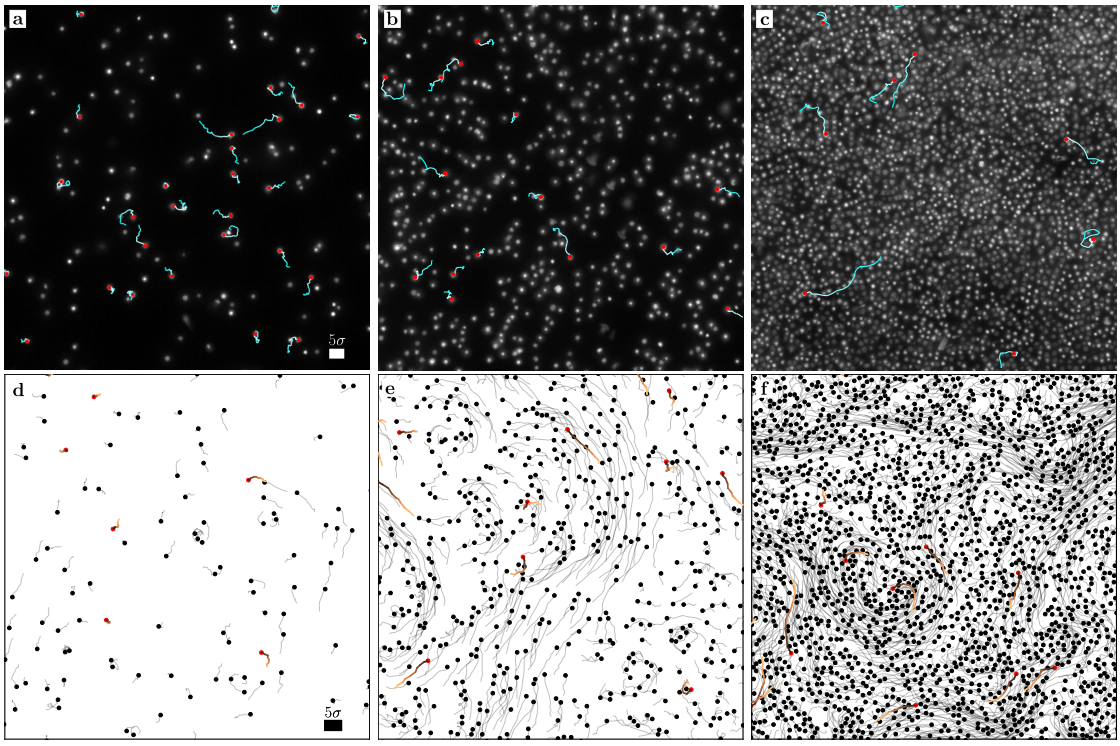

Figure 3.1: "Collective dynamics of hydrodynamically interacting rotors. (a) - (c) Fluorescent optical images of rotors at $\phi = 0.008, 0.031$, and 0.144 with an overlay of a few typical trajectories. Here, only a quarter of the full probe chamber is shown. (d) - (f) Simulated rotors configurations at $\phi = 0.007, 0.04$, and 0.14 with all trajectories in grey and few highlighted ones for comparison with experimental images. Trajectories are all drawn for a time $\Omega t = 6$. Only a part of the full simulation domain is shown." [M] Image taken from [M].

At low ϕ, rotors are far from each other, displaying merely Brownian motion, as can be seen in figures 3.1a and d. At medium densities, rotors are more likely to in-

teract in pairs, triplets, or larger ensembles, and the trajectories become ballistic and curved, reminiscent of active Brownian particles (figures 3.1b and e). Two neighbouring colloids rotate around each other in the same angular direction as the intrinsic rotation. When additional rotors get in their proximity, they get incorporated into the same motion nucleating a rotating group, or *vortex*. These vortices grow in size until they start to interact with neighbouring vortices. The ensemble exhibits therefore a rich vortex dynamics where the rotating groups coalesce or break up dynamically, and individual rotors vividly interchange between different rotating groups. Although all colloids are spinning in sync with the external magnetic field, the resulting vortices rotate at different speeds, and they can eventually rotate in opposite direction when they need to adjust to the boundary conditions imposed by neighbouring vortices. The curvature of the trajectories shown in figures 3.1b and e depend on the configuration of nearby rotors, *i.e.*, on the size of the rotating group the respective rotor belongs to. Small groups lead to strongly curved trajectories, whereas larger groups lead to almost straight trajectories. Curiously, a few experimental and simulated trajectories show a looping behaviour, resulting from the change of orbiting motion of one rotor from one to a different partner, triplet, or small group. For larger densities, the phenomenology is basically the same, but trajectories are on average longer and some of them might even exhibit segments bending into different directions, which occurs when rotors change from one vortex to another. Figures 3.1c and f show the system at highest experimental trackable $\phi(= 0.14)$, and figures 3.2a - c, correspond to full simulation domains where the ensemble dynamics of multi-scale vortex formation is more obvious.

Each individual rotor is propelled through the system with an instantaneous linear and rotational velocity, which depends on the local rotor configuration. On average the motion can be mapped to that of active Brownian particles, and the averaged mean squared displacement (MSD) shows the three expected regimes: purely thermal diffusion at very short times, actuated at intermediate times, and enhanced diffusion at long times. The rotational diffusion is related here to the change of direction of the motion instead of to the change of to orientation of the rotor axis. Experimental and simulation results are shown in figure 3.3a for several available packing fractions. The measured MSD for each fixed ϕ are then fitted to that of an active Brownian particle [40] which provides well-defined values for the actuated velocity v_a and the rotational time τ_r both in experiments and in simulations, as summarized in figures 3.3b and c. At low ϕ, the rotors barely interact with others, and in the limit of $\phi \to 0$, there is no propulsion on average. In fact, at very low densities, the experimental MSD barely shows active behaviour, rendering a reasonable fit impossible. This is remarkably different to ordinary active Brownian particles, which at low ϕ exhibit an active gas phase [169] due to their inherent propulsion. With increasing density, the interactions between rotors become more frequent such that the active velocity first grows with ϕ. Upon further increase of the rotor density, the motion is increasingly restricted by steric interactions, and the effective fluid viscosity experienced by the rotors also grows, which eventually completely impedes their motion. These trends qualitatively explain the maximum of v_a at intermediate values of ϕ seen in figure 3.3b for both simulations and experiments. In order to provide a quantitative estimate of this dependence [170], we assume first that the thrust velocity $v_\perp$ of a rotor is simply due to pair interactions $v_\perp \simeq \pi\Omega_{pair}\bar{r}$, as shown in Fig. 2.11a, and secondly, that the average distance between the rotors is that of a homogeneous system $\bar{r} \simeq (\sigma/2)\sqrt{\pi/\phi}$, such that $v_\perp \simeq (\pi\sigma\Omega)\sqrt{\phi/\pi}$. Simultaneously, the rotors dissipate momentum via mutual interactions and rotor density

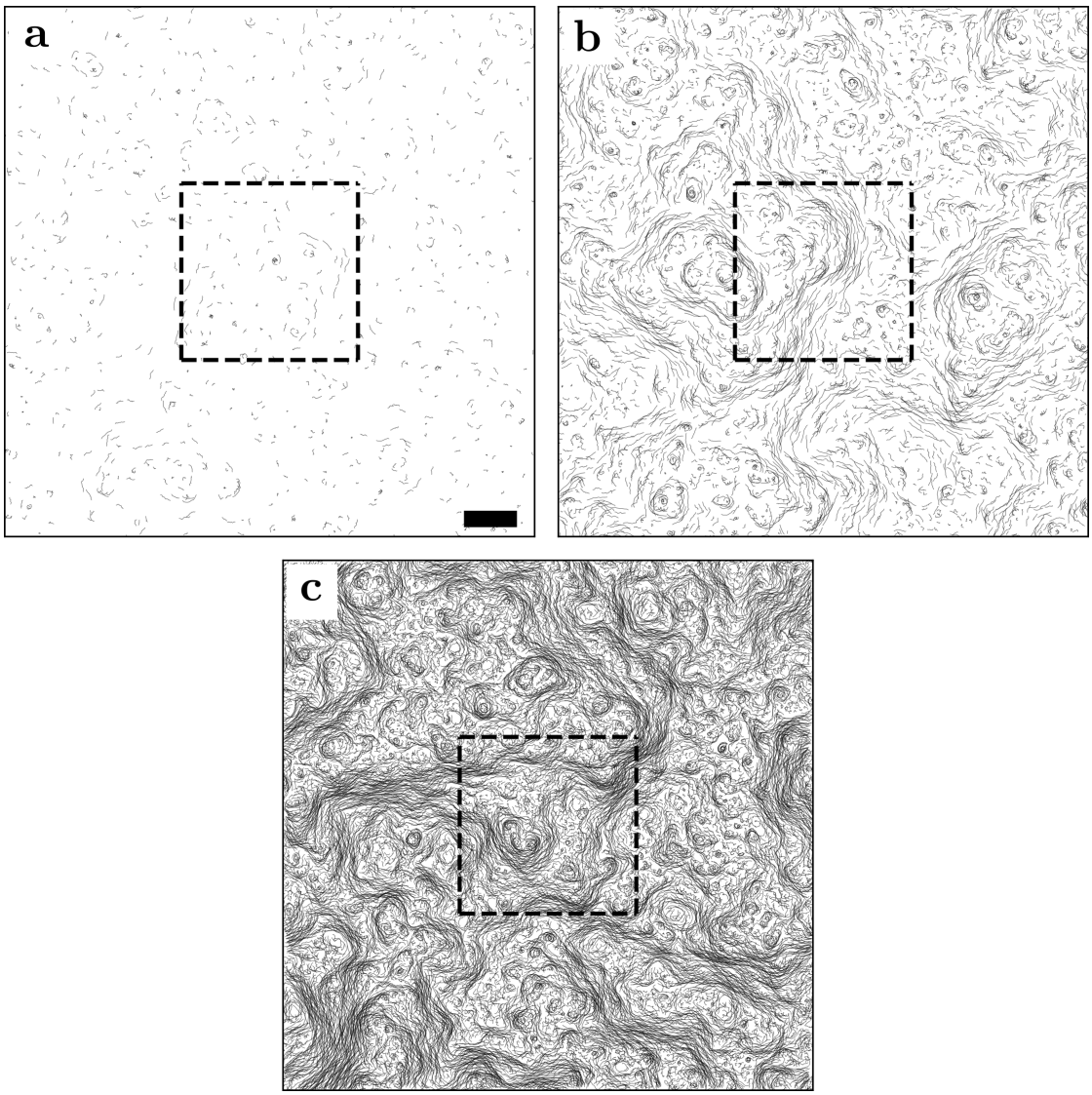

Figure 3.2: "Full simulation domains with trajectories, showing the formation of multi-scale vortices. Dashed inset frames indicate the domains in figure 3.1d - f." [M] Image taken from [M].

increases the effective fluid viscosity experienced by the rotors [166] which results in a decrease of the velocity at high density, as expected also for active Brownian particles [171]. The increase in viscosity for a 2D system of passive colloidal particles in linear order [168] is $\eta(\phi)/\eta_0 = 1 + 2\phi$, although in order to account for the abrupt increase when approaching the close packing density ϕ_{cp}, it is more appropriate to consider the phenomenological equation $\eta(\phi)/\eta_0 \simeq (1 - \phi/\phi_{cp})^{-2\phi_{cp}}$ [167]. The drag force considered for the thrust velocity $F_\perp \propto \eta_0 v_\perp$ can then be considered to balance with the drag of the effective velocity in a dense system $F_a \propto \eta(\phi) v_a$ which provides a full estimate of the effective active velocity $v_a \simeq \eta_0/\eta(\phi)\, v_\perp$ in the full density range, as shown in figure 3.3b. This estimate agrees qualitatively very well with the simulation results, and perhaps somewhat surprisingly even quantitatively with the experimental measurements.

The measured τ_r obtained from the MSD in figure 3.3a and shown in figure 3.3c

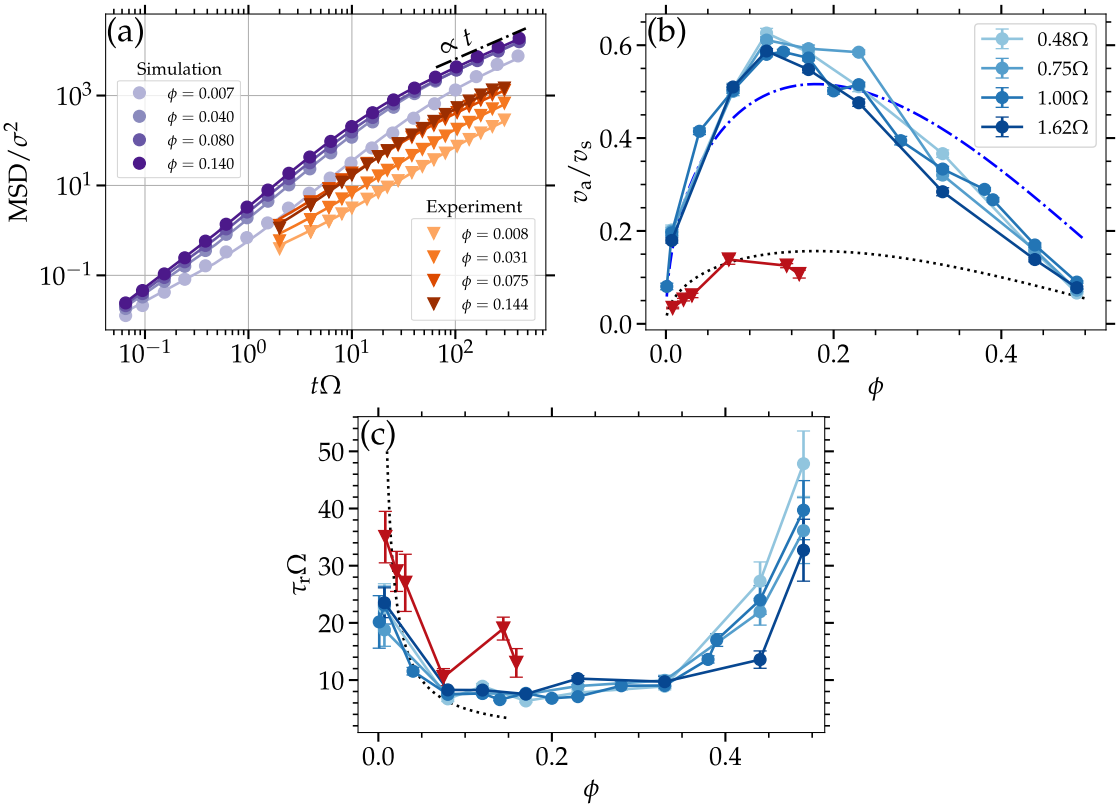

Figure 3.3: "(a) Mean-square displacements for experiments (orange triangles) and simulations (purple bullets) at different packing fractions in a square simulation box of length $L = 100\sigma$ with periodic boundary conditions. The lines correspond to respective least square fits to the active Brownian particle mean-square displacement. (b) and (c) normalised active velocity v_a, and rotational diffusion time τ_r corresponding to the fits in (a). Dotted (black) lines correspond to the analytical prediction $v_a \simeq \pi\Omega\sigma(1-\phi/\phi_{cp})^{2\phi_{cp}}\sqrt{\phi/\pi}$; dash-dotted line take into account an additional multiplicative fit factor of 3.3." [M] Image taken from [M].

corresponds to a rotational diffusion time only in the dilute limit. At larger densities, this time is related with rotational diffusion but also with an intrinsic rotation or change of direction, due the orbital motion in the vortices. To estimate τ_r, we consider the average time a rotor orbits another rotor before moving into a different orbit. In the regime of small densities, this time decreases with density; at intermediate densities, the presence of vortices of multiple sizes leads on average to τ_r remaining constant, while for very high densities, where the rotors are basically not moving, τ_r rapidly increases. In the limit of small densities, the time can then be approximated as $\tau_r \simeq \bar{r}/v_\perp \simeq 1/(2\Omega\phi)$. This estimate works for both experiments and simulations, even at medium densities, as shown in figure 3.3c." [M]

3.2. ODD VISCOSITY IN ROTOR MATERIALS

"With the ensemble configurations in figure 3.2 and the related velocity fields, the corresponding coarse-grained vorticity $\omega = \partial_x v_y - \partial_y v_x$ and local density ϕ_{loc} fields can be computed, as shown in figure 3.4. Areas with positive vorticity correspond to underlying vortices rotating in the same direction as the imposed magnetic field, areas

with negative vorticity appear for vortices rotating in the opposite direction, which essentially fill the space in between the positive vorticity areas. Although qualitatively similar, the vorticity field measured in experiments is weaker than in simulations, due to the friction with the substrate.

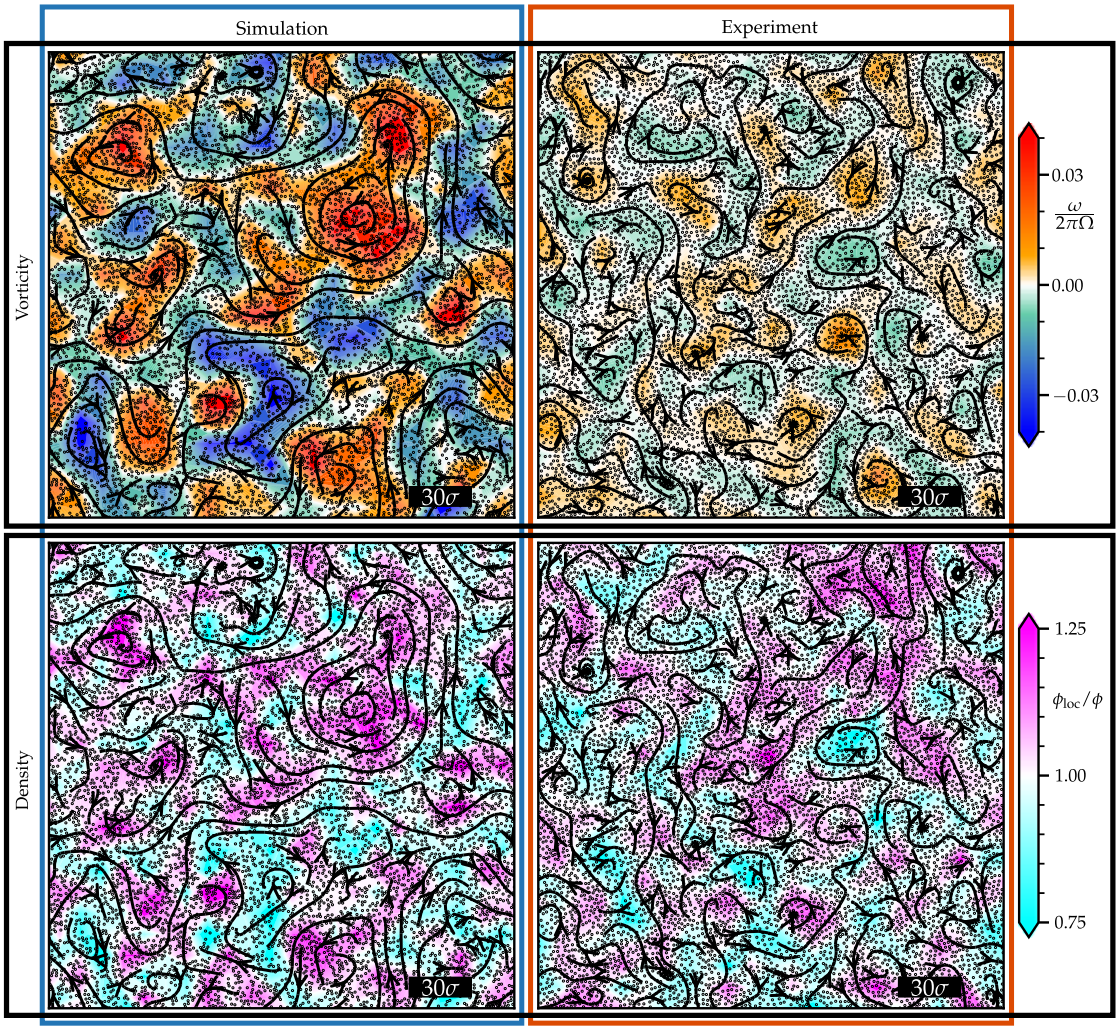

Figure 3.4: "Vorticity and density fields. Coarse-grained vorticity and local packing fraction fields of the rotor dynamics on a 2D square grid of binning length $l_0 = 10\sigma$ for simulation and experiment. In each column, the same system configuration has been used to generate the respective fields. Superimposed streamlines and rotor positions are displayed. The packing fraction used in experiments, simulations is $\phi = 0.144$, $\phi = 0.14$, respectively. The simulations have been performed in a square simulation box of length $L = 300\sigma$ with periodic boundaries." [M] Image taken from [M]. Calculation of coarse-graining values explained in appendix E.

The corresponding density fields in figure 3.4 also show clear inhomogeneities. Positive vorticity areas tend to be more populated than negative vorticity areas, both for experiments and simulations. This accumulation indicates the presence of a radial pressure on the rotating vortex originating from a non-vanishing *odd viscosity* [67, 68]. As a first quantification of this effect, the probability density distribution is calculated separately for areas of positive and negative vorticity, displaying that both distributions are clearly displaced relative to each other, as shown in figure 3.5a. For positive

vorticity, the maximum of the distribution occurs for densities larger than the average density, and conversely for negative vorticity. This means that areas with $\omega > 0$ tend to attract particles, and that they are depleted from $\omega < 0$ areas. The separation of the maximum of the distribution for a given density is larger for the lower average density in the investigated cases, which also show a broader distribution, and the trend can be clearly seen both in experiments and simulations.

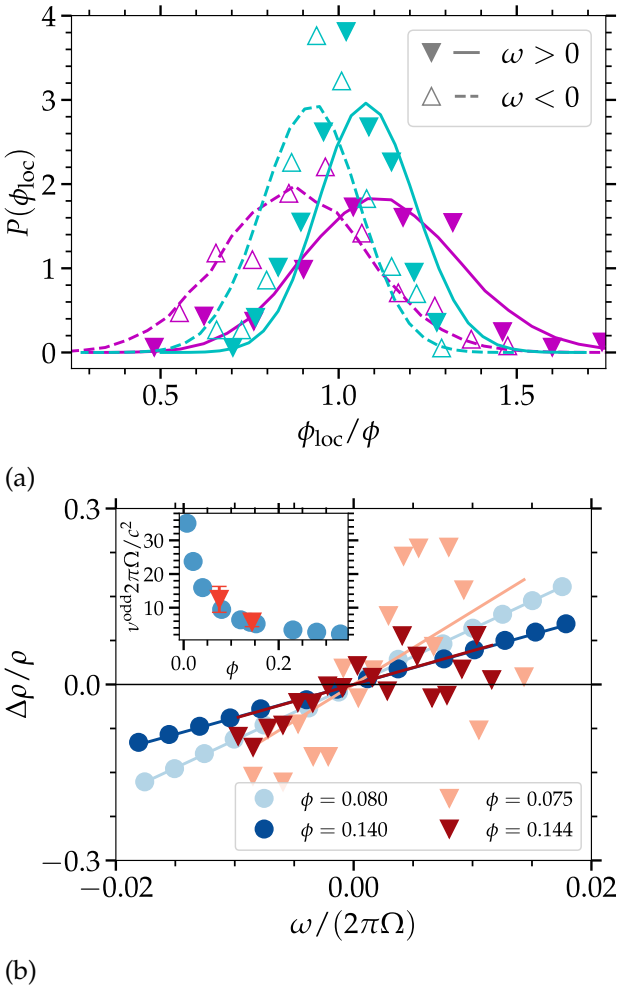

Figure 3.5: "Vorticity-density correlations. (a) Normalised probability distribution of the local packing fraction ϕ_{loc} of the areas with positive vorticity (solid lines and solid symbols) and negative vorticity (dashed lines and open symbols). Lines correspond to simulation results and symbols to experimental ones. Results for lower volume fraction are shown in magenta (experiments $\phi = 0.075$ and simulations $\phi = 0.08$). Higher volume fraction results are shown in cyan (experiments $\phi = 0.144$ and simulations $\phi = 0.14$). (b) Normalized variation of the local rotor mass density ρ as a function of the local vorticity ω. The lines indicate least-squares fits according to equation (3.6) with which ν^{odd} can be determined. The inset shows the estimates for the normalized odd viscosity as a function of the density for experiments (red symbols) and simulations (blue symbols)." [M]

In order to provide a quantitative characterisation of the odd viscosity, at a coarse-grained level, the rotors can be described using the continuum theory for chiral active fluids." [M] "The Stokes equation of a chiral active fluid describes the time evolution of

the flow velocity $\boldsymbol{v}$, in terms of its density ρ, pressure p, kinematic viscosity ν, vorticity $\omega = \varepsilon_{\alpha\beta}\partial_\alpha v_\beta$ [...], and importantly also by the odd kinematic viscosity ν^{odd}, which is proportional to the field of intrinsic rotation $\widetilde{\Omega} = \Omega\langle\sum_i \delta(\boldsymbol{r} - \boldsymbol{r}_i)\rangle$, as [67,68]

$$\rho\partial_t v_\alpha = -\partial_\alpha\left(p - \rho\nu^{\text{odd}}\omega\right) + \rho\nu\partial_\beta\partial_\beta v_\alpha\,, \tag{3.1}$$

Taking the curl of Eq. (3.1) leads to the vorticity diffusion equation

$$\partial_t\omega = \nu\partial_\beta\partial_\beta\omega\,. \tag{3.2}$$

which can be solved with Fourier transform methods. The initial condition of a line or punctual vortex $\omega(\boldsymbol{r}, t = 0) = \Lambda\delta(\boldsymbol{r})$ which later diffuses due to viscosity can be considered, in order to account for the internal vortex dynamics of the system together with equation (3.2). The solution is then,

$$\omega(\boldsymbol{r}, t) = \frac{\Lambda}{4\pi\nu t}e^{-\frac{r^2}{4\nu t}}\,. \tag{3.3}$$

Integrating this expression results in an expression for the velocity profile in polar coordinates when incompressibility is ensured, $\partial_\alpha v_\alpha = 0$, leading to

$$v_\varphi(r, t) = \frac{\Lambda}{2\pi r}\left(1 - e^{-\frac{r^2}{4\nu t}}\right) \tag{3.4}$$

and $u_r = 0$. These expressions of the flow field together with equation (3.1) yields to the following relation in the radial direction

$$0 = \partial_r\left(p - \rho\nu^{\text{odd}}\omega\right)\,, \tag{3.5}$$

and thus $p - p_0 = \rho\nu^{\text{odd}}\omega$, with $p_0 \equiv p(r \to \infty)$. This means, that the pressure compensates the antisymmetric stress stemming from odd viscosity in order to satisfy incompressibility. If small changes in density due to finite compressibility are now considered [116], and assuming $\Delta p = c^2\Delta\rho$ with $\Delta p = p - p_0$ and $\Delta\rho = \rho - \rho_0$, we obtain [...]" [M]

$$\frac{\Delta\rho}{\rho} = \nu^{\text{odd}}\frac{\omega}{c^2}\,. \tag{3.6}$$

"This expression is also valid when the vorticity ω is locally varying, such that $\Delta\rho = \rho(\boldsymbol{r}) - \langle\rho(\boldsymbol{r})\rangle$ is the local density change with respect to the average density in the system, with c the speed of sound, and ν^{odd} the kinematic odd-viscosity, *i.e.*, the momentum diffusivity due to the presence of the odd stresses. Therefore, a circular flow of vorticity $\omega > 0$ is experiencing stress forces pointing to the centre of circulation, leading to rotor accumulation in the centre of the circular flow [67]. Similarly, a circular flow $\omega < 0$ leads to rotor depletion in the centre of circulation. The advantage of equation (3.6) is that it can be directly employed to quantify the system's odd viscosity. From data such as in figure 3.4, a histogram relating local vorticities and local densities can be evaluated, both in experiment and in simulation. The results presented in figure 3.5b show a linear dependence between local density changes and vorticity in the simulations as well as in the experiments. Fitting the lines in figure 3.5b with equation (3.6) allows then the accurate quantification of ν^{odd} at different densities in the system, with resulting values shown in the inset of figure 3.5b. Interestingly, the

experimentally measured odd viscosity is in reasonable agreement with the numerical results, which reflects that in both systems the two dimensional hydrodynamic rotation is responsible for the propagation of the stresses. In the investigated density range, ν^{odd} decreases with density, due to the decrease of the compressibility of the system with increasing density. This decrease of ν^{odd} can also be observed in the larger separation of the maxima for lower densities in figure 3.5a. To the best of our knowledge, the odd viscosity was only quantified before in few very different systems, such as the so-called edge-pumping effect [41] in experiments, via the power spectra of the surface waves, measuring deformation of a flexible boundary, or as for a system of granular rotors, in simulations, measuring the normal stresses [74]." [M]

3.3. DYNAMICS REMINISCENT OF ACTIVE TURBULENCE

"The colloid trajectories in figures 3.2a-c and the vorticity-density fields in figure 3.4 show the simultaneous presence of eddies of different sizes, which is clearly reminiscent of turbulence [116]. To provide a quantification of the turbulent dynamics, we investigate the rotor velocity field $\boldsymbol{v}(\boldsymbol{r})$ and its corresponding energy spectra E_q as a function of the wave vector q, defined in equation (1.50), see figure 3.6.

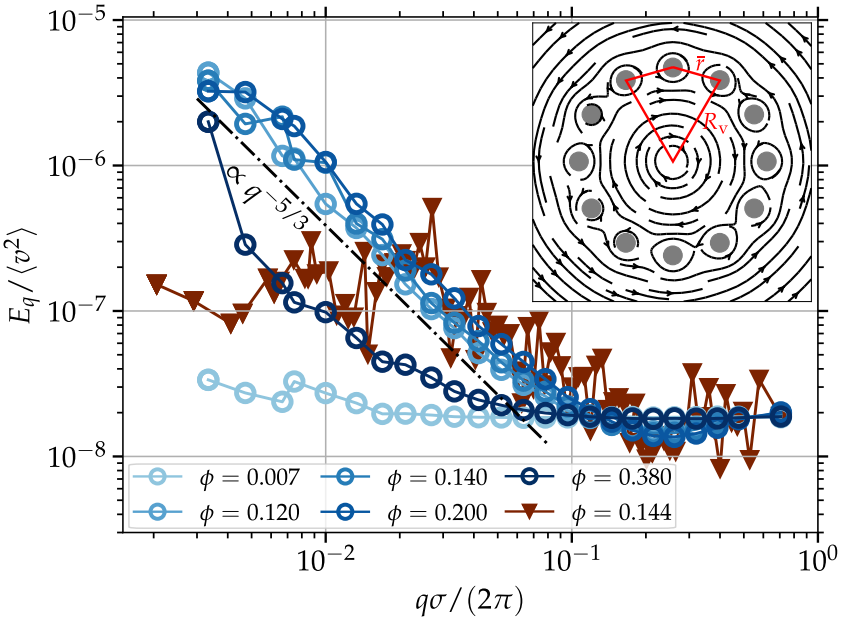

Figure 3.6: "Energy spectra of the colloid dynamics. Energy spectra obtained from the power-spectral-density of the rotor dynamics as in equation (1.48) divided by the mean-square velocity. Blue circles depict simulation data whereas red triangles denote experimental data. The experimental data is multiplied by a constant factor to match the high-q simulation values. The minimum and maximum wave numbers are $q_{\text{min}}\sigma/(2\pi) = 3 \times 10^{-3}$ and $q_{\text{max}}\sigma/(2\pi) = 7 \times 10^{-1}$. Inset: Averaged flow field in a simplified vortex, rotors arranged in a circle of radius R_v, with a fixed separation $\bar{r}$ between nearest neighbours." [M] Image taken from [M].

Energy is injected in the system on the rotor size scale which determines a limiting maximum wave vector $q_{\text{max}} \simeq 2\pi/\sigma$. Since the colloids only propel when nearby rotors break local symmetry, energy propagates because of the hydrodynamic forces, and is then transported to larger scales following self-similar dynamics along an inverse

energy cascade. On the other hand, the vortex size has a maximum limit given by the system size, such that the minimum possible wave vector is $q_{\min} \simeq 2\pi/(L/2)$. In the limit $\phi \to 0$, the amount of cooperative motion is almost negligible and the colloids move like passive Brownian particles, such that the energy spectrum in figure 3.6 is almost white, *i.e.*, it practically does not display any dependence with the wave vector q. For intermediate ϕ, vortices of all sizes are taking part in the dynamics. The energy spectrum then follows a power-law decay $q^{-5/3}$. Approaching $q_{\max}$, the energy distribution deviates from the power-law and approaches a constant, which is related to the particle size. Simulations show the presence of very big vortices in figure 3.4, and the power law decay in figure 3.5 is valid almost up to $q_{\min}$. Experiments in figure 3.4 show that the maximum size of vortices is clearly smaller than the system size, and the power law decay is valid in a smaller range, namely until $q_1\sigma/(2\pi) \gtrsim 0.02$. This is due to the dissipation of energy through the substrate friction, which truncates the energy cascade. This is similar to 2D classical turbulence where the inverse cascade is truncated at $l_{\gamma_{\text{subs}}} \simeq \rho v_0(\phi)/\gamma_{\text{subs}}$, with a linear substrate friction density γ_{subs} [125]. From the value q_1, the maximum experimental vortex size can be estimated to be 50σ, which is consistent with the vortices in figure 3.5, and implies $\gamma_{\text{subs}} = 7.63\,\text{kg}\,\text{m}^{-2}\,\text{s}^{-1}$. Finally, at very high densities, steric interactions suppress rotor motion, and the free formation of vortices, such that it becomes increasingly difficult to measure the energy spectra. In contrast to bacterial turbulence, there is no dominant vortex scale that is introduced by the interplay of hydrodynamics, alignment interactions, activity, and rotational noise [92, 101].

To get a more intuitive insight on the self-similar behaviour of the system, we consider a simplified picture of a vortex formed by a few rotors with fixed positions in a circle of radius R_v, as shown in the inset of figure 3.6. If we approximate the drag on each rotor induced by the flow of its neighbours, the only a contribution remaining is, due to symmetry, tangential to the circular trajectory. This is the reason for the emergence of the circular arrangements, independent on their size, which are then perturbed by the presence of collisions, compressibility effects, and thermal fluctuations." [M]

3.4. Influence of the synchronicity—non-synchronous rotors

Considering that all of the rotors rotate in sync is a characteristic valid in the case where the magnetic moment of the rotors follow the externally applied field instantaneously. This means that whenever the magnetic moment of the particles and the externally applied homogeneous magnetic field starts to be minimally misaligned, an infinitely large torque is applied in order to compensate the misalignment resulting in an angular velocity which is immediately following the frequency of the applied field. In that way, the compensating torque immediately overcomes the rotational friction which opposes rotations and thus the alignment correction. On the other hand, the rotational friction increases with rotor density resulting from the increasing mutually exerted shear and the assumption of synchronous rotation ultimately breaks down when the rotors touch and block each other. In the experimental results presented in this chapter, the assumption of synchronous rotation breaks down at high packing fractions, such that the colloids are rotating out of phase of the rotating magnetic field.

In such dense systems, or in other chiral active systems where the rotation of the colloids has a different origin [55, 172], a more appropriate assumption would be

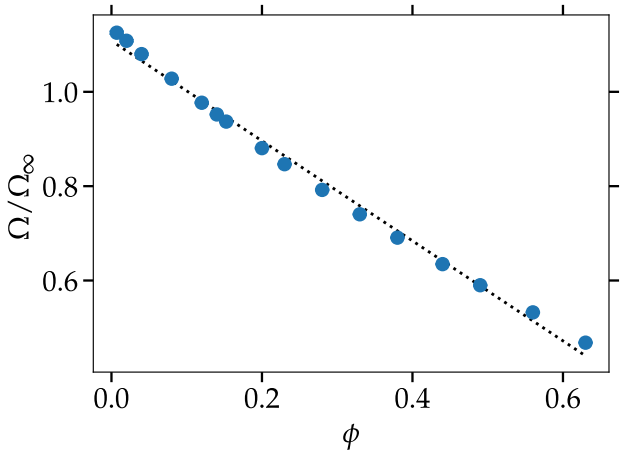

Figure 3.7: Average angular velocity of the rotors versus the rotor density ϕ. Each rotor is subject to a constant torque of $M = 25k_BT$. The dotted line is a fit according to $\Omega = \Omega_0 - \hat{\Omega}\phi$ yielding $\Omega_0/\Omega_\infty = 1.11$ and $\hat{\Omega}/\Omega_\infty = 1.06$. The simulations have been performed in a simulation domain of size $L = 300\sigma$ with periodic boundary conditions.

that the driving torque instead of the angular velocity is constant. Then, resulting from viscous dissipation and fluctuations, the angular velocity will fluctuate around an average value, but inhomogeneities in the angular velocities among the rotors are allowed. Assuming an isolated rotor of radius R in a fluid of viscosity η, the average angular velocity in radians per time unit that establishes after applying a torque M in an unconfined domain is

$$\Omega_\infty = \frac{M}{4\pi\eta R^2}\,. \tag{3.7}$$

However, this relation is only valid if the rotor is infinitely far from further influences on the fluid such as boundaries representing a wall or another rotor. In general, the presence of no-slip boundaries or further rotors will increase the frictional drag resulting from flow continuity, *e.g.*, the flow induced by an isolated rotor decays to zero for $r \to \infty$, while a resting no-slip boundary enforces a much faster decay as can be seen in figure 4.2. Thus, the frequency will be diminished by resting no-slip boundaries. However, the rotor's angular velocity might also be increased with respect to Ω_∞, *e.g.*, in the case of a boundary which is co-rotating such that the frictional drag on the rotor is reduced. Accordingly, in a rotor suspension the average angular velocity depends on density. Figure 3.7 shows the average angular velocity Ω in a rotor suspension measured in simulations, revealing that Ω decreases monotonically with rotor density ϕ by reason of the viscous friction between the rotors which increases as the rotors approach. Thus, the decrease of the average distance between rotors with increasing density leads to an on average smaller angular velocity. The dependence of Ω on ϕ can be approximated as a linear decrease

$$\Omega(\phi) = \Omega_0 - \hat{\Omega}\phi\,, \tag{3.8}$$

as is shown by a fit to the data. Here, $\hat{\Omega}$ is the decrease rate of angular velocity with rotor density and Ω_0 is the limit $\Omega(\phi \to 0)$. Interestingly, this limit is not approaching Ω_∞. Which is probably due to the following two counteracting effects. On the one

hand, also in the simulations performed at the lowest density ($\phi = 0.007$, same density as in figure 3.1d), the rotors cannot be regarded as isolated due to the long-ranged hydrodynamic interactions according to equation (2.1). On the other hand, loosely organised rotating groups reduce the frictional drag on rotors in the centre of rotation, such that on average higher angular velocities than Ω_∞ are reached. The same effect can of course also occur at higher densities, but there is impeded by the increase in mutual friction with increasing density, such that $\Omega(\phi) > \Omega_\infty$ only occurs at low rotor densities, *i.e.*, in systems where large density inhomogeneities, and thus isolated groups, can occur due to thermal fluctuations.

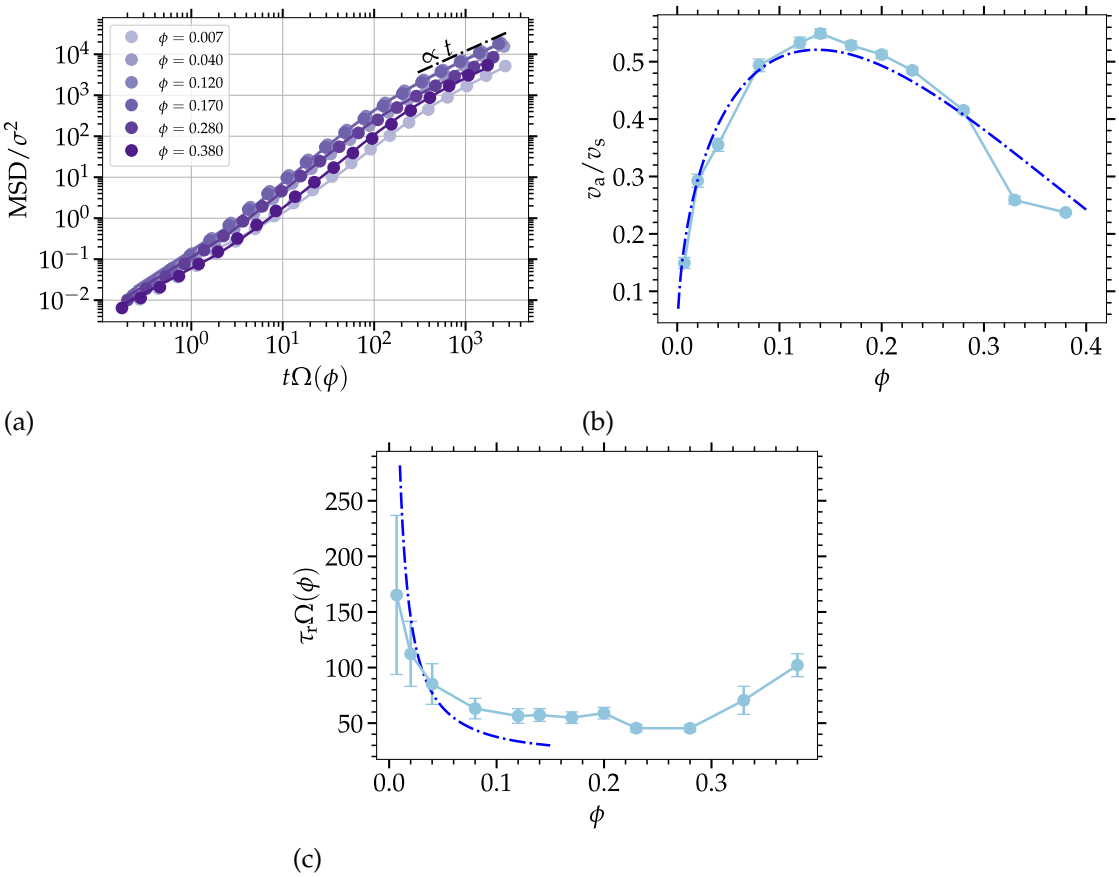

Figure 3.8: Actuated dynamics of rotors subject to a constant torque $M = 25k_BT$ in a simulation domain of size $L = 100\sigma$ with periodic boundary conditions. (a) Mean-square displacements obtained from simulations (symbols). The dash-dotted line shows diffusive behaviour. The solid lines are least-square fits according to equation (1.18). The diffusion coefficient D of colloids in a 2D suspension taken from reference [173] and measured diffusion coefficient for an isolated rotor from section 2.2. (b) and (c) show fit parameters for τ_r and v_a. Here, $v_a = \sigma\Omega(\phi)/2$. The dash-dotted lines correspond to the estimates from section 3.1 with $\Omega = \Omega(\phi)$.

The collective dynamics of rotors subject to constant torque are qualitatively similar to the collective dynamics of rotors with constant angular velocity. The colloids drag the adjacent fluid and thus actuate the neighbouring rotors leading to multi-vortex formation. Figure 3.8 shows the actuated dynamics extracted from the mean-square displacements assuming an active Brownian particle scheme for the actuated motion. Both, the mean-square displacements in figure 3.8a and the parameters v_a in

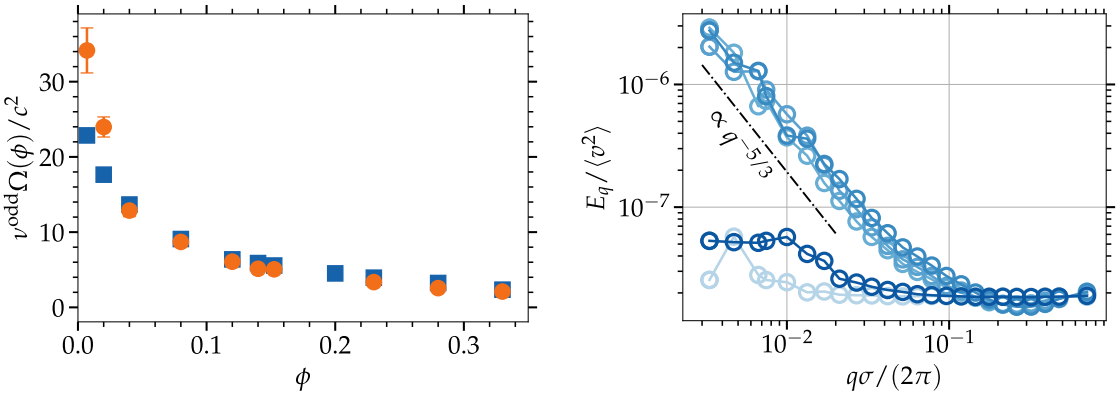

(a) (b)

Figure 3.9: Kinematic odd viscosity and energy spectrum for a system of non-synchronous rotors. (a) ν^{odd} of a rotor system subject to constant torque $M = 25k_{\mathrm{B}}T$ normalised with the measured average angular velocity $\Omega(\phi)$ (blue squares) and for reference data from figure 3.5b for a system at constant angular velocity (orange bullets) versus density. (b) Energy spectrum of the system subject to constant torque $M = 25k_{\mathrm{B}}T$ at densities $\phi = 0.007, 0.12, 0.14, 0.20, 0.38$, where darker colour corresponds to higher density.

figure 3.8b and τ_{r} in figure 3.8c show the same qualitative behaviour as for the rotors with fixed angular velocity, explained in section 3.1. A difference, however, is the density dependent normalisation $\Omega(\phi)$ according to equation (3.8), which is necessary in order to compare the ensembles at different densities, which evolve on different timescales due to the density dependence of the angular velocity $\Omega(\phi)$.

The formation of vortices in a chiral active fluid bearing odd viscosity will lead to density accumulation, depletion in the centre positively, negatively rotating vortices, respectively. Figure 3.9a shows the measured ν^{odd} versus density in comparison to a system of constant angular velocity. Especially at high densities, figure 3.9a barely shows a difference between the measurements, *i.e.*, if a constant angular velocity according to equation (3.8) is chosen, ν^{odd} of the system of constant torque can be regarded as that of a constant angular velocity system. However, at low densities the two ν^{odd} values significantly vary, which is a consequence of the density inhomogeneities in the dilute limit, where small isolated rotor groups and even single isolated rotors may occur. These density inhomogeneities are only due to the low density and the random contribution of the rotors' dynamics and are not associated to come from odd stresses or due to the non-synchronous behaviour. While regions of locally higher density ϕ', *i.e.*, low intermediate densities in terms of the density range, compared to the overall average system density ϕ give rise to smaller local values of $\Omega(\phi')$, it is also these regions that dominantly contribute to the density inhomogeneities resulting from ν^{odd}, since isolated rotors do neither show rotor accumulation nor depletion. This means that the first squares at low density in figure 3.9a show ν^{odd} of an effective system at $\phi' > \phi$, leading to a smaller odd viscosity. This effect does not play a role at higher densities, because large density inhomogeneities are impeded there.

The mesoscale turbulent trajectories of a rotor ensemble at constant external torque cannot be phenomenologically distinguished from those of an ensemble at constant angular velocity. This means that at intermediate densities in both cases multi-scale vortices over the whole system form and the dynamics are self-similar as can be seen

from the energy spectrum in figure 3.9b. Furthermore, the same behaviour is observed at low and high densities, *i.e.*, the self-similarity is destroyed at high densities by steric interactions which prevent the formation of vortices an all scales simultaneously, while at low densities the amount of cooperative motion is smaller than the individual random walk, leading to a Brownian, *i.e.*, white spectrum.

3.5. Summary

"We have shown that rotating micrometer-sized particles are an interesting model system of chiral active matter, where the emergence of turbulence and odd viscosity can be simultaneously observed, as demonstrated here in experiments and simulations. While different types of rotating colloids are known to convert rotational into translational energy in symmetry-breaking situations, such as in the presence of confinement [41, 52], investigations of this effect in bulk were fragmentary, and the precise measurement of odd viscosity effects in low-Reynolds-number soft-matter systems was elusive until now [45, 58, 170, 174]. Simulations and experiments are to a large degree in agreement, showing very similar behavior and dependence on system variables. Individual rotors behave similarly as active Brownian particles with their propulsion and rotational diffusion dependent on the configuration of neighbouring rotors. Translational velocity and rotational charateristic time can be measured and satisfactorily compared with an analytical prediction, for all the range of available concentrations. We furthermore present an effective method that allows the quantitative measurement of the bulk odd viscosity, shown here for experiments and simulations, and of use for a wide range of systems, such as roller liquids [54, 174], chiral granular gases [175], or colloidal Janus asymmetric rotors [176, 177].

Active turbulence in rotor materials is due to long-ranged hydrodynamic interactions and not due to the inherent particle properties: it can therefore be regarded as a new subclass of active turbulence in which the existence of a dominant vortex scale between lower and upper cutoff is lacking, a key feature of bacterial turbulence [92]. The appearance of both odd viscosity and active turbulence has its origin in the mechanism that converts rotational into translational energy. We expect these two concepts to be useful for various related hydrodynamic rotor systems of biological relevance, such as rotating membrane macromolecules, algae, or sperm, and also for the design of microrobots, and microrobots assemblies [26, 33, 35, 36]." [M]

Since a perfect synchronous rotation is sometimes not feasible experimentally, asynchronous rotor ensembles have been studied in terms of an applied constant torque. The numerical study presented here does not show significant differences between rotor systems at constant angular velocity or constant applied torque. However, since mutual rotor interactions increase frictional coupling among the rotors, the effective average angular velocity in a system with constant applied torque decreases with increasing rotor density, such that the time scales for these systems explicitly depend on ϕ. A non-trivial consequence of the constant torque rotor system is that in systems capable of strong density inhomogeneities, *i.e.*, dilute suspensions, vortex formation and corresponding density accumulation takes place in the on average higher populated regions of the dilute suspension where the average angular velocity is lower due to the mutual frictional drag. Accordingly, in these situations, the measured odd viscosity is lower than for a constant angular velocity rotor suspension with rotation frequency at the average angular velocity of the constant torque system.

Chapter 4

Introduction of a dominant vortex scale by substrate friction

The negligence of the substrate friction in the theoretical modelling of the rotor fluid is a simplification that can either be appropriate or not depending on the strength of the coupling of the rotor dynamics to the substrate [41]. The influence of the friction acts like an infinite momentum reservoir with zero mean momentum, that accordingly partially absorbs the net solvent momentum as the result of collisions of fluid volume elements with interface volume elements. Such interfaces can be air or a solid wall at a solvent-air or solvent-substrate interface, respectively. It is standard to assume a constant rate of momentum absorption at the interface proportional to the velocity of the fluid volume element [67, 125, 151], similar to the dissipation of momentum of a Brownian particle into the fluid. Thus, in order to take a substrate friction in the theoretical model into account, a linear friction term $-\gamma u_\alpha$ with substrate friction coefficient γ is introduced to the hydrodynamic equations of motion. The Stokes equation (1.29a) thus takes the form of a Brinkman equation, which is known for low-$\mathcal{R}e$ flow in porous media [178]

$$\frac{1}{\rho}\partial_\alpha p = \nu\partial_\beta\partial_\beta u_\alpha - \gamma u_\alpha \,. \tag{4.1}$$

In order to simulate flows described by equation (4.1), the momentum exchange with the substrate has to be incorporated. A possible solution for a quasi two-dimensional flow would be to introduce a third dimension in the z direction to the fluid and simulate the flow in a thin fluid layer coupled to walls from above and below at $z = 0$ and $z = h$, where at least one of the walls acts on the fluid as a no-slip boundary. For the sake of simulating flows close to 2D hydrodynamics, the height of the fluid layer has to be much smaller than the extend L of the simulation domain in the x and y directions, *i.e.*, $L \gg h$. A similar realisation has been implemented in the study of reference [141], where the authors study the cooperative swimming of squirmers in a narrow slit. This realisation, however, is accompanied with an increase of computational effort as a result of the increased size of the simulation domain and thus the raise of fluid particles. But the influence of the substrate friction does not alter the mechanism of the mutual hydrodynamic actuation, such that in general no qualitatively new physics is expected.

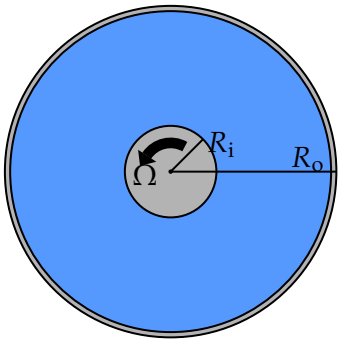

Figure 4.1: Circular couette flow. The fluid is restricted to the blue area, *i.e.*, $R_i < r < R_o$.

4.1. Efficient momentum dissipation by virtue of virtual particles

In a model that also takes the substrate friction into account developed in this thesis, the momentum exchange between solvent particles and substrate is simulated efficiently by the introduction of virtual, or ghost particles that are randomly scattered over the simulation domain before each collision step. The velocities of these particles are randomly drawn from a Maxwell-Boltzmann distribution thermalised at the average temperature and they only take part in the sorting and collision routines. In that way, momentum can be transferred from the fluid to the substrate, *i.e.*, the ghost particles, with only minor adjustments in the simulation code and with marginally increased computational effort. The average density of the ghost particles ρ_{subs} has then to be adjusted such that the desired strength of coupling between fluid and substrate is modelled.

In order to test the efficient model of 2D flows with substrate friction, the dynamics described by equation (4.1) in circular couette flow is considered. The fluid is restricted to the area enclosed by two concentric circles with radii $R_i < R_o$, where the inner circle is rotating at angular frequency Ω and the outer cylinder is fixed at $\Omega = 0$ with no-slip boundary conditions on both surfaces. The setup is schematically shown in figure 4.1. Taking only stationary solutions into account and employing the setup's rotational symmetry, the pressure p and flow u_α can only be a function of the distance from the centre and the velocity can only point into the azimuthal direction. In polar coordinates, this implies $p = p(r)$ and $\boldsymbol{u} = u_\varphi(r)\hat{e}_\varphi$, and equation (4.1) is

$$0 = \partial_r^2 u_\varphi + \frac{1}{r}\partial_r u_\varphi - \frac{1}{r^2}u_\varphi - \frac{\gamma}{\nu}u_\varphi \,. \tag{4.2}$$

Defining the length scale $\lambda \equiv \sqrt{\nu/\gamma}$ and substituting $\tilde{r} \equiv ir/\lambda$, where i is the imaginary unit, transforms the equation to

$$0 = \tilde{r}^2\partial_{\tilde{r}}^2 u_\varphi + \tilde{r}\partial_{\tilde{r}} u_\varphi + (\tilde{r}^2 - 1)u_\varphi \,. \tag{4.3}$$

This is the Bessel equation which is fulfilled by the Bessel functions of the first and second kind, *i.e.*, $J_1(\tilde{r})$ and $Y_1(\tilde{r})$, respectively [179]. Thus, the general solution is $u_\varphi(\tilde{r}) = aJ_1(\tilde{r}) + bY_2(\tilde{r})$, with integration constants a and b which have to be fixed by use of the boundary conditions. Substituting back thus yields the solution of equation (4.2) as

$$u_\varphi(r) = aJ_1(-ir/\lambda) + bY_2(-ir/\lambda) \,. \tag{4.4}$$

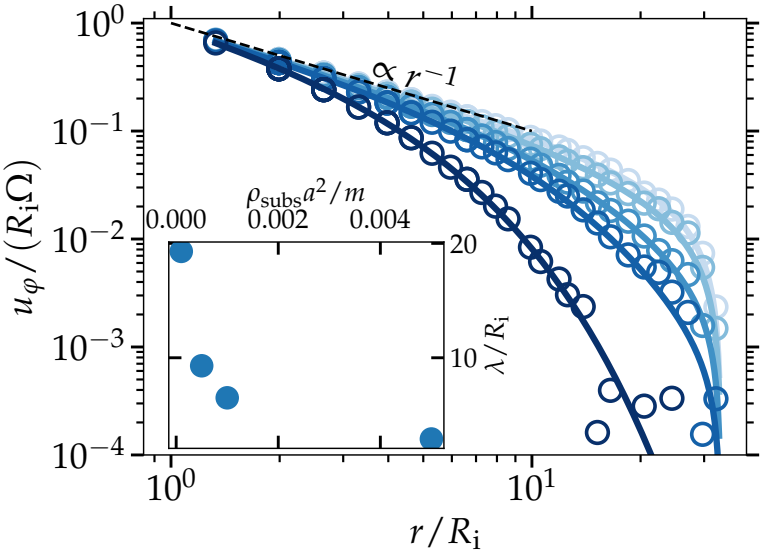

Figure 4.2: Circular Couette flow under the influence of substrate friction. The inner cylinder of radius R_i is rotating at frequency Ω, whereas the outer cylinder is fixed. Fluid is coupled to both cylinders via no-slip boundary conditions. Symbols show measured fluid velocity, darker colours denote increasing substrate friction ($\rho_{subs}a^2/m = 0$, 10^{-4}, 5×10^{-4}, 10^{-3}, 5×10^{-3}). Lines correspond to least square fits of the data to equation (4.6), yielding substrate friction coefficients $\gamma\Omega = 1.0\times10^{-3}$, 1.0, 2.1, 3.1, 6.9. Corresponding length scale λ/R_i shown in the inset. Due to the finite slip at the colloids surface, Ω is treated as a fit parameter yielding consistent results of $\Omega_{eff} = 0.91\Omega$, in accordance with the measurement in figure 2.2. Dashed black line corresponds to flow field of a rotating cylinder in an unconfined fluid, *i.e.*, $u_\varphi \propto r^{-1}$.

Employing the boundary conditions

$$u_\varphi(R_1) = R_1\Omega\,, \tag{4.5a}$$
$$u_\varphi(R_2) = 0\,, \tag{4.5b}$$

provides the flow field

$$u_\varphi(r) = \frac{R_1\Omega\left\{J_1(-iR_2/\lambda)Y_1(-ir/\lambda) - Y_1(-iR_2/\lambda)J_1(-ir/\lambda)\right\}}{J_1(-iR_2/\lambda)Y_1(-iR_1/\lambda) - Y_1(-iR_2/\lambda)J_1(-iR_1/\lambda)}\,. \tag{4.6}$$

Figure 4.2 shows the stationary flow obtained in the setup in figure 4.1. The simulation results are in excellent agreement with the theory, showing that the influence of the substrate can be accurately simulated by the use of ghost particles. The flow is induced at $r = R_i$ such that the no-slip boundary condition implies a solvent velocity of $u_\varphi(r = R_i) = R_i\Omega$ for all values of the substrate friction. With increasing distance $r > R_i$, the friction results in an exponential decay of the flow velocity on the length scale λ, which is particularly pronounced for high values of the average density of ghost particles ρ_{subs}. For $\rho_{subs} \to 0$, $\lambda \to \infty$ and the flow profile attains the result of the Stokes equation without substrate friction

$$u_\varphi(r) = -\frac{\Omega R_i^2}{R_o^2 - R_i^2}r + \frac{\Omega R_i^2 R_o^2}{R_o^2 - R_i^2}\frac{1}{r}\,, \tag{4.7}$$

which follows $u_\varphi \propto r^{-1}$ at short distances $r \gtrsim R_\mathrm{i}$. As dictated by the no-slip boundary at the outer circle, $u_\varphi(r \to R_\mathrm{o}) \to 0$. The inset shows the normalised friction length scale λ, showing a rapid decrease for increasing densities of ghost particles. For $\rho_\mathrm{subs} \to 0$ the substrate friction parameters γ and λ tend to zero, infinity, respectively.

Remarkably, only a very small number of ghost particles is necessary in order to simulate the influence of a frictious substrate, since the effect is already very pronounced for $\rho_\mathrm{subs} a^2/m = 5 \times 10^{-3}$. This means, that the ghost particles already have a large impact on the flow when fluid to ghost particle density ratio is $\rho_\mathrm{subs}/\rho = 5 \times 10^{-4}$, such that the major computational effort is still resulting from the simulation of the fluid particles.

4.2. Influence of the substrate friction on the vortex size

Simulating a rotor fluid under the influence of the substrate friction is now achieved by suspending the rotors into the fluid with substrate friction. Thereby, the rotor degrees of freedom are not subject to an additional friction which is a reasonable assumption for the studied experimental system, since the rotating rods are dragged by the generated flows and not directly in touch with the surface of the substrate. However, the mutual flows experienced by the individual rotors will still be subject to the exponential decay. Figure 4.3 shows the isotropic velocity correlation function $\langle \boldsymbol{v}(r) \cdot \boldsymbol{v}(0) \rangle = \langle \boldsymbol{v}(\boldsymbol{r}) \cdot \boldsymbol{v}(0) \rangle_{r=|\boldsymbol{r}|}$ in a rotor suspension at different values of λ and without friction ($\rho_\mathrm{subs} = 0$ and $\lambda \to \infty$) for reference in periodic simulation domains of varying size. The efficient calculation using the Wiener-Khnichin theorem explained in appendix D is employed here. The first value of the velocity correlation function, *i.e.*, $\langle \boldsymbol{v}(0) \cdot \boldsymbol{v}(0) \rangle = \langle v^2 \rangle$, is not displayed here, because the self-correlations are much stronger than the long ranged correlations as a result of the strong thermal fluctuations. The velocity correlation attains a maximum at $r \approx \sigma$ as a result of rotors collectively travelling into the same direction in a larger vortex. With increasing r, the correlation decays, turns negative, and attains a minimum at the dominant vortex size [180] r_d, since negative correlations indicate rotors going on average into opposite directions[1].

Figure 4.3a reveals two influences of the substrate friction. First, with decreasing λ/σ the strength of the average inter rotor correlation is decreased and second that the decay of the correlation is much faster at higher friction. In the case of no substrate friction ($\lambda/\sigma = \infty$) the minimum of the velocity correlation is reached only at $L/2$, *i.e.*, at half of the periodic simulation domain, such that the dominant vortex is ranging over the whole system. On the other hand, for finite λ the minimum of the velocity correlation is located closer to $r = 0$, *i.e.*, the decay is faster, and after the minimum $\langle \boldsymbol{v}(r) \cdot \boldsymbol{v}(0) \rangle$ attains zero. Thus, with increasing friction, the dominant size of the vortices decreases. While without substrate friction the maximum vortex size is, as a result of continuity and the periodic boundary conditions, dictated by the system size L, as is shown explicitly in figure 4.3b for different L, for sufficiently small values of λ the decay of the velocity correlation is governed by the momentum dissipation into

[1] Note, that in principle also different definitions for r_d are possible, *e.g.*, the position r where $\langle \boldsymbol{v}(\boldsymbol{r}) \cdot \boldsymbol{v}(0) \rangle$ turns zero, *i.e.*, where the velocities are on average perpendicular, see reference [87]. However, the two listed definitions give the same order of magnitude—in a perfectly circular vortex, the position at the minimum gives the diameter of the circular motion, whereas the first zero of the velocity correlation gives $\sqrt{2}/2$ of its diameter.

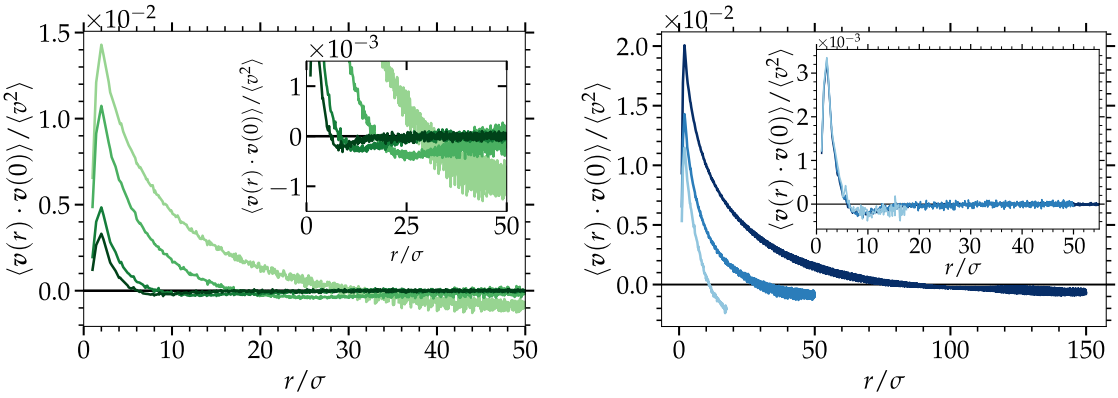

(a) (b)

Figure 4.3: Characterisation of the influence of the substrate friction on the velocity correlation function. (a) Velocity correlation functions for $\lambda/\sigma = \infty, ..., 6.5$, for $L = 100\sigma$. Darker lines correspond to smaller λ. Inset: Zoomed in version of same data. (b) Velocity correlation function at $\lambda/\sigma = \infty$ for varying $L = 300\sigma$, 100σ, 35σ. Inset: Velocity correlation function at $\lambda/\sigma = 6.5$ for same values of L.

the substrate and thus the decay of $\langle \boldsymbol{v}(r) \cdot \boldsymbol{v}(0) \rangle$ is independent of the system size. Quantitatively, this is shown in the inset of figure 4.3b, where the decay of the velocity correlation for varying L but with equal λ is identical. Note, that the respective friction scale $\lambda/\sigma = 6.5$ roughly corresponds to the dominant vortex size r_d here.

Figure 4.4a shows the corresponding energy spectra of the rotor ensemble in a simulation domain of size $L = 300\sigma$ with periodic boundary conditions at the different values for the substrate friction. For $\lambda = \infty$, *i.e.*, no substrate friction, the ensemble exhibits the self-similar behaviour with a $q^{-5/3}$ power-law, even on the smallest q scales, hence validating that the largest vortex ranges over the whole system and furthermore that self-similar vortices are populating all scales on which $E_q \propto q^{-5/3}$ holds. For finite values of λ, the power-law behaviour is clearly disrupted. While for large q, the E_q data agree qualitatively for different values of λ, following the data into the direction of small q shows that the energy spectra of systems with larger λ agree to the substrate friction less system longer than the systems with smaller λ. However, for all of the investigated values of the substrate friction, the friction with the substrate introduces a cutoff that limits the extend of the self-similarity in the way that larger vortices cannot be formed. The emergence of a cutoff acting as a maximum vortex scale with the introduction of substrate friction can qualitatively be observed in the vorticity and density plots shown in figure 4.5. There, it is clearly shown that with decreasing λ the size of the largest vortices in the system decreases, and therewith also the size of the density inhomogeneity domains resulting from odd viscosity.

The energy spectra of rotor ensembles without substrate friction in systems of different sizes L (figure 4.4b) clearly show, that irrespective of L the collective dynamics evolves a power-law in E_q that is only limited by the system size. This once more emphasises the nature of the self-similar dynamics of the rotor ensemble without substrate friction with an energy spectrum $E_q \propto q^{-5/3}$. Figure 4.4c shows the energy spectra E_q of the collective rotor dynamics for a fixed value of the friction scale λ in three differently sized systems. Analogous to the data in figure 4.3c, the structure of E_q coincides irrespective of the system size L, since the cutoff due to the substrate friction becomes dominant. The energy spectrum attains a maximum indicating the

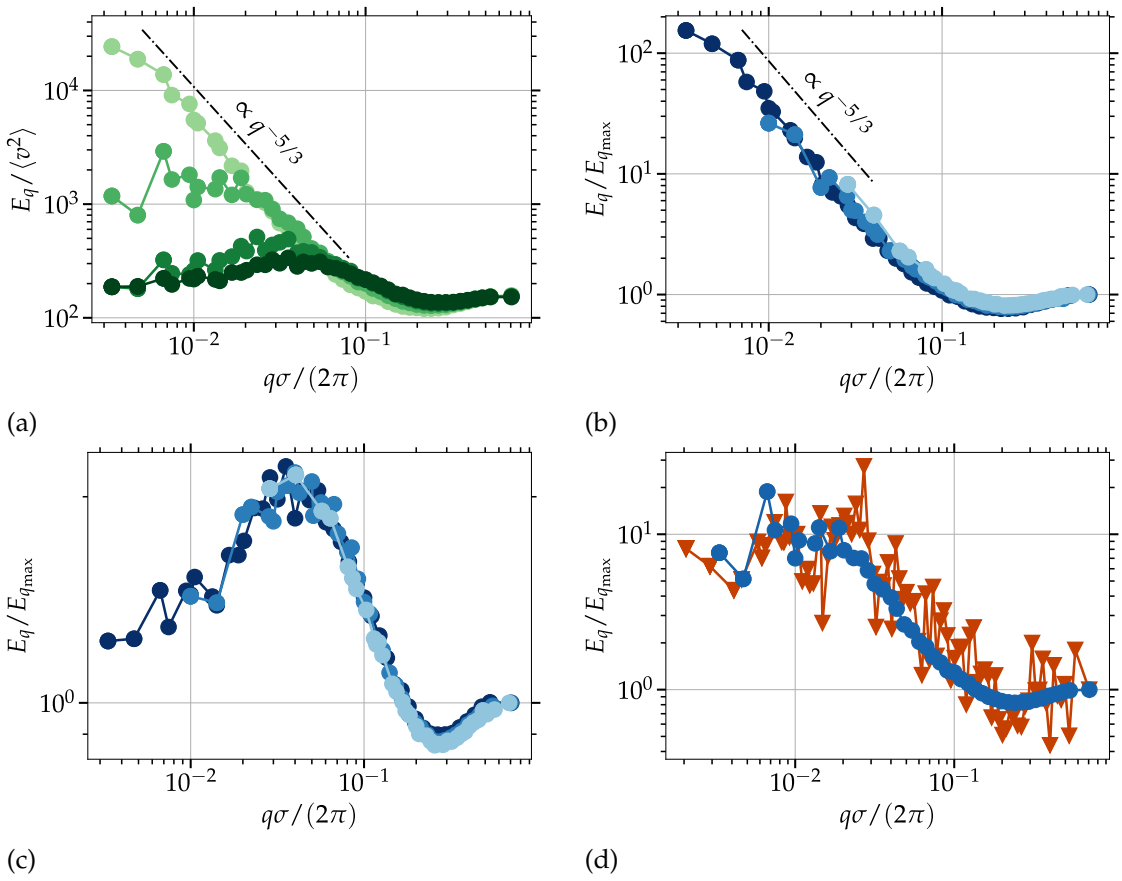

Figure 4.4: Characterisation of the influence of the substrate friction on the energy spectra. (a) Energy spectra for $\lambda/\sigma = \infty, ..., 6.5$, for $L = 100\sigma$. Darker lines correspond to small λ. (b) Energy spectra at $\lambda = \infty$ for varying L. (c) Energy spectra at $\lambda/\sigma = 6.5$ for varying L. (d) Energy spectra of experiments (orange) and simulations. Experimental data taken from [M] and simulation data obtained in a system of size $L = 300\sigma$ and $\rho_{\text{subs}}a^2/m = 5 \times 10^{-5}$.

existence of a frictional cutoff at characteristic dissipation scale $l_\gamma = 2\pi/q_\gamma$ [125]. The maximum is developed at $q\sigma/(2\pi) \approx 4 \times 10^{-2}$, while the inverse friction length is $q_\lambda\sigma/(2\pi) = \sigma/\lambda \approx 10^{-1}$, which is only off by roughly a factor of 2, showing the close relation between the two scales. Following E_q from the maximum to smaller q scales leads to a decay of E_q, since energy is taken out at the dissipation scale such that it is barely transported from the energy injection scale to the longest length scales $L/2 \simeq 2\pi/q_{\text{min}}$. The value $\rho_{\text{subs}}a^2/m = 5 \times 10^{-5}$ matches the value necessary to reproduce the effective substrate friction observed in experiments by the simulation, as can be seen from figure 4.4d.

4.3. Substrate friction reduces the rotors' actuated dynamics

Since the formation of vortices prescribes vortical trajectories for the rotors, the time evolution of the dynamics is affected by the size of the vortices and thus by the strength of the friction between fluid and substrate. Regarding the rotors' dynamics as those

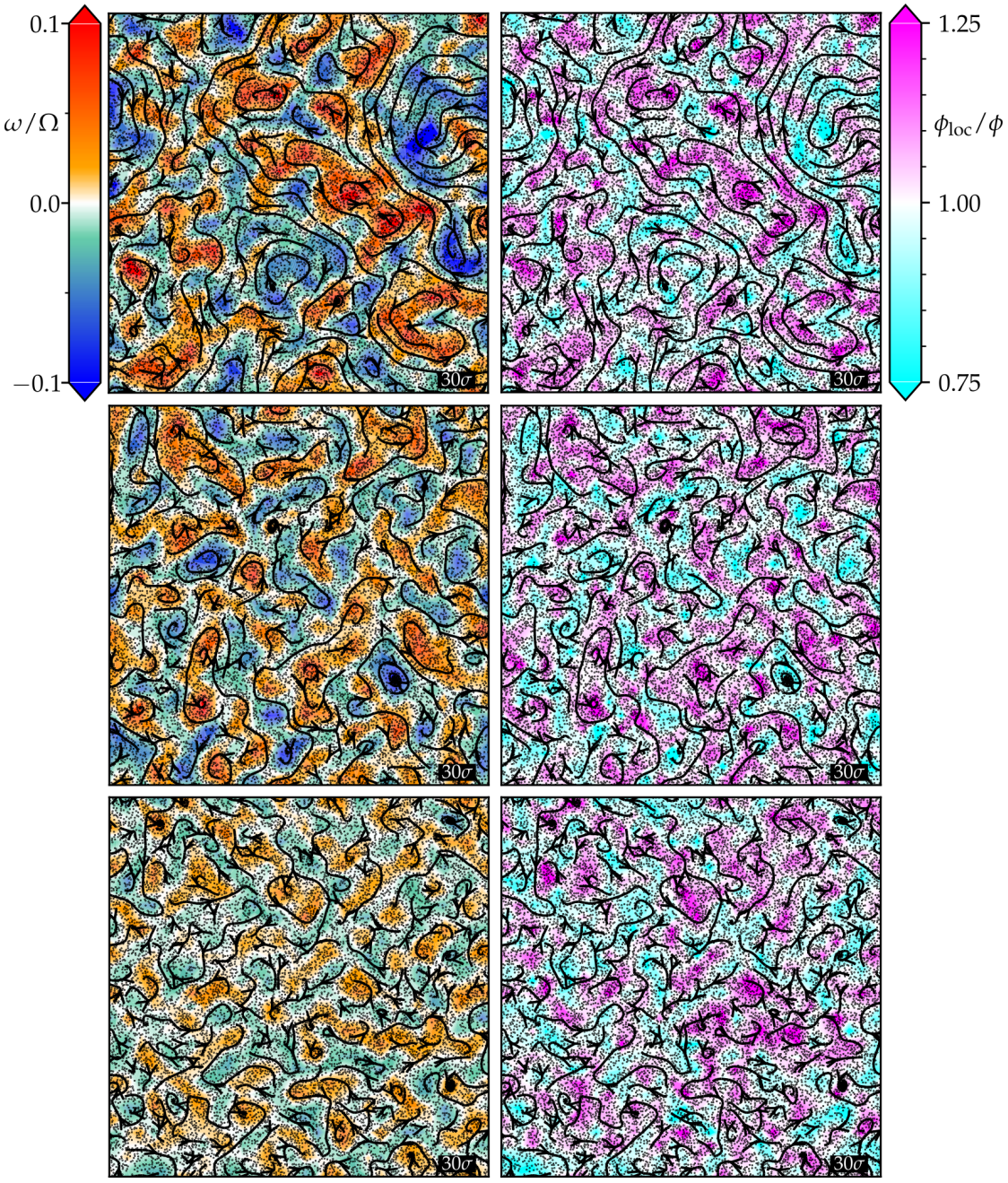

Figure 4.5: Vorticity and density fields under the influence of substrate friction with superimposed streamlines. First row corresponds to $\rho_{\mathrm{subs}}a^2/m = 0$, $(\lambda/\sigma = \infty)$, second row to $\rho_{\mathrm{subs}}a^2/m = 5 \times 10^{-5}$, and last row to $\rho_{\mathrm{subs}}a^2/m = 5 \times 10^{-4}$, $(\lambda/\sigma = 9.3)$. Left, right columns show vorticity, density fields, respectively. The simulations have been performed in a square simulation box of length $L = 300\sigma$ with periodic boundary conditions. All rows are normalised in the same way corresponding to the respective colourbars in the first row.

of active Brownian particles as in chapter 3, he rotors' dynamics become diffusive on timescales $t \gg \tau_{\mathrm{r}}$, where the directed advection of the rotors in the largest vortex ceases, *i.e.*, after the rotors have on average exited the largest vortex. This timescale decreases as the vortices' size decreases. Figure 4.6a shows the time-normalised mean-

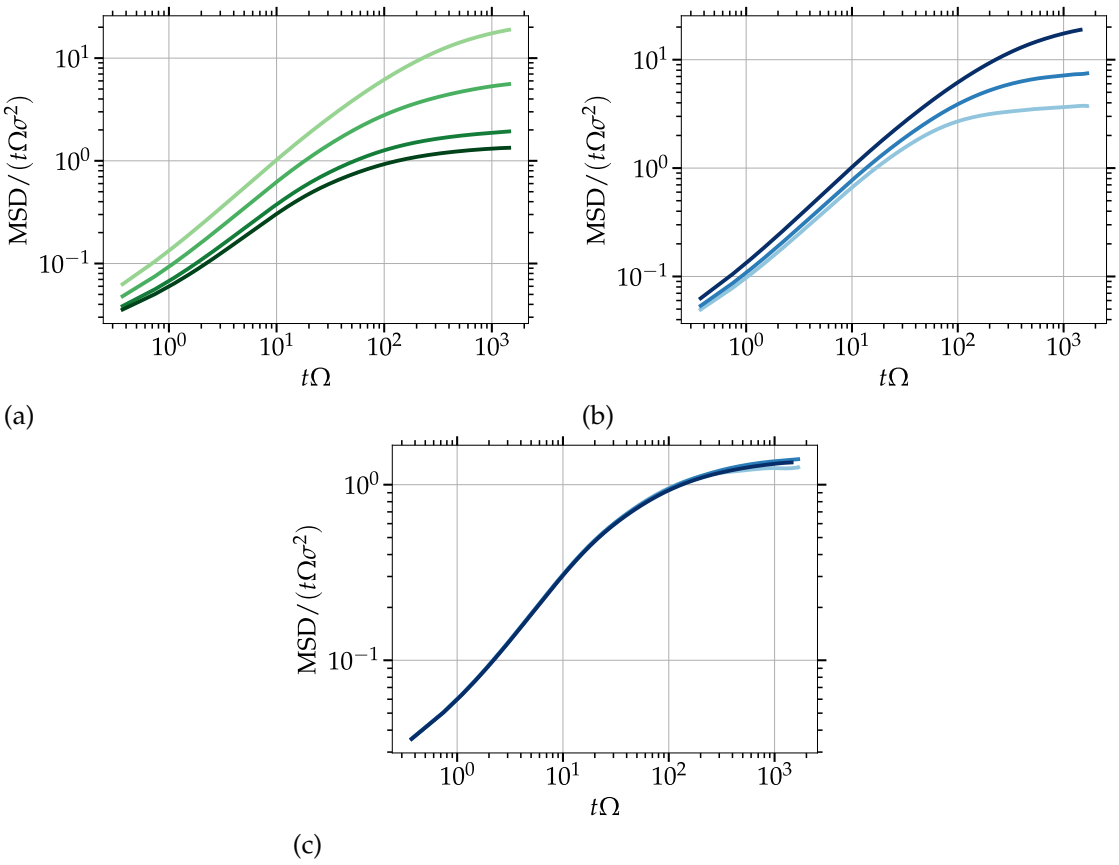

Figure 4.6: Characterisation of the influence of the substrate friction on the mean-square displacement. (a) Time-normalised mean-square displacements for $\lambda = \infty, ..., 6.5$, for $L = 100\sigma$. Darker lines correspond to higher ρ_{subs}. (b) Time-normalised MSD at $\lambda = \infty$ for varying L. (c) Time-normalised MSD at $\lambda/\sigma = 6.5$ for varying L.

square displacement $\left\langle (r(t) - r(0))^2 \right\rangle / t$ of the rotors in a system of size $L = 300\sigma$ for the different values of the friction scale λ. For smaller values of λ, the dynamics become earlier diffusive, *i.e.*, the corresponding timescale of rotational diffusion of the velocity direction τ_r decreases. Note, that the time-normalised mean-square displacement is constant for diffusive dynamics. Additionally, the actuated velocity v_a of the rotors decreases as λ decreases, analogous to the decrease in the velocity correlation function in figure 4.3a. As a consequence, the mean-square displacements for the different values of the substrate friction already considerably varies after $t\Omega \simeq 1$. As a result of the largest possible vortex in a system without substrate friction, *i.e.*, $\lambda = \infty$, the mean-square displacement will differ for different sizes of the systems L, as is shown in figure 4.6b. On the other hand, for finite λ, the maximum vortex size is not dictated by the system size L but by the amount of momentum dissipation into the substrate, then consequently also the mean-square displacement does not depend on L and is quantitatively unaffected upon changing the system size, for the whole trajectory. This is shown in figure 4.6c, where the time-normalised mean-square displacement for fixed λ and varying L is shown, displaying conformity of the mean-square displacements up to noise in the data at late times.

4.4. Summary

The influence of substrate friction on the hydrodynamically interacting rotor ensembles and the mutually induced collective dynamics has been addressed systematically. An efficient way of incorporating the influences of a frictious substrate to two-dimensional flows is proposed in this chapter, which consists of virtual multiparticle collision dynamics particles with velocities randomly drawn from a zero-mean Maxwell-Boltzmann distribution that take part in the MPC collision protocol and thus absorb momentum of the fluid. The momentum dissipation into the substrate effectively mimics the influences of a third dimension into quasi-two-dimensional setups and thus removes difficulties of very slow decay in 2D hydrodynamics. For weak coupling of the fluid to the substrate, it can thus be regarded as a natural alternative of enforcing the outer boundary condition of a resting fluid at infinity. The friction with the substrate introduces a length scale λ which for the rotor dynamics acts like a cutoff to the multi-vortex formation, *i.e.*, it prevents the formation of the biggest of vortices, similar to 2D classical turbulence [125]. This cutoff is not present in a true two-dimensional hydrodynamic system. The Stokes equation is then turned into a Brinkman equation, known from low-$\mathcal{R}e$ flow in porous media [178]. The smaller and weaker vortices in a rotor ensemble with finite substrate friction diminish the mutual actuation of the rotors. To define the dependency of the actuated velocity of the rotors on the friction scale λ is an interesting task for the future which can be used in order to match the density of the virtual substrate particles in the simulation to an explicit experimental setup. However, the very mechanism of propagation of active stresses via the solvent is qualitatively equivalent in systems with and without substrate friction, such that an explicit incorporation of the frictious substrate is only necessary for quantitatively matching model and experiments, or explicitly investigating the influences of the friction.

Chapter 5

Microrotors in circular confinement: Global rotation, layering enhanced by odd viscosity, and active turbulence

Breaking of symmetry in rotor materials renders a local net flux generation possible [51, 52, 181]. For a circular container, translational symmetry is broken in all directions, but a rotational symmetry is retained, leading to net rotational dynamics [41, 47, 151, 182] capable of robust cargo transport along the wall [75]. Here, it is shown that in a circularly confined chiral active fluid an edge flux is generated at the boundary. Entropic layering of rotors at the confining walls leads to oscillating rotational stresses [151] which also imply an oscillating vorticity profile. In the compressible microrotor fluid, vorticity gradients yield a stationary modulation of the density profile at the boundary leading to enhanced layering. In the absence of a frictious substrate, the edge flux viscously propagates into the interior of the container and thus establishes a linear velocity profile, similar to circular couette flow as described with the Stokes equation. But the linear profile is only fulfilled on average and individual rotor trajectories are still predominantly governed by the mutual translational actuation giving rise the active turbulence, where energy is injected on the rotor scale and along the boundary, *i.e.*, on long scales. The energy spectrum of the turbulent dynamics still shows power-law behaviour, but the scaling exponent only attains the exponent observed in bulk when the two energy injection scales are well separated.

5.1. Solid body-like rotation caused by edge flow

In this chapter, a study of the dynamics of hydrodynamically interacting rotor ensembles in circular confinement is presented. The fluid sticks at the confining boundary, *i.e.*, there is a no-slip boundary condition between wall and solvent, whereas the rotors interact via a short-ranged repulsive interaction with the walls, such that at least one collision cell is in between the wall and the rotors in order to guarantee proper hydrodynamic coupling. Accordingly, the rotors are viscously coupled to the walls via the solvent.

If the intrinsic rotation of an ensemble of rotors confined in a circular arrangement is turned on at $t = 0$, the fluid in the vicinity of the rotors starts to be dragged at

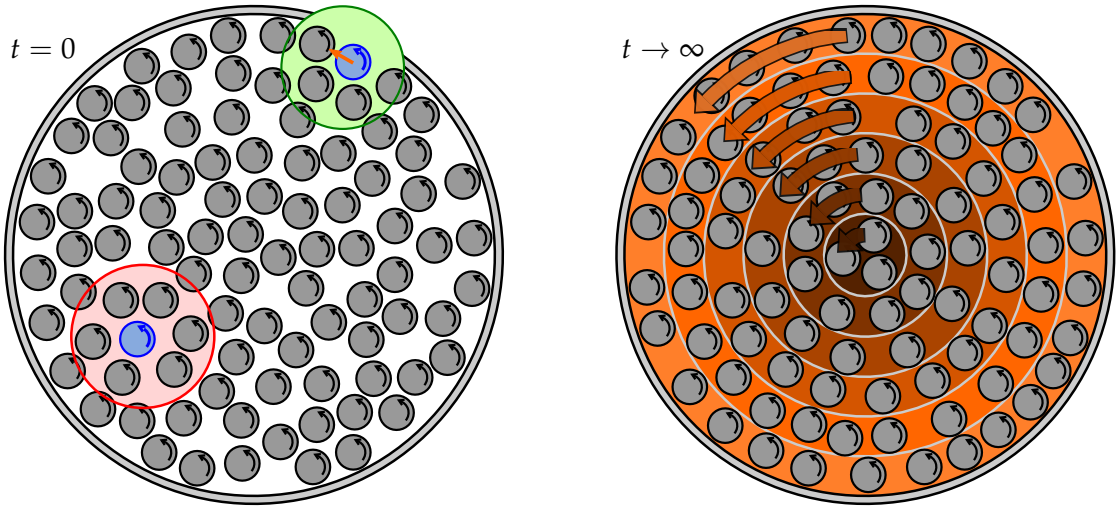

(a) (b)

Figure 5.1: Sketch of rotors in circular confinement. (a) Local symmetries leading to the formation of a boundary flow within the red and green circles. (b) For the sake of demonstrating the viscous propagation of momentum into the centre, explicit distinct layers are highlighted by the use of arrows and different colours. The momentum created by the boundary flow is passed from layer to layer until the centre is reached. Here, the image of this concept is exaggerated and the rotors will in general not display strong layering.

the colloids surface. If approximately evenly spaced rotors with relative distance $\bar{r}$ are assumed, the mutual hydrodynamic interactions become relevant after a time $\tau_f(\bar{r}) = \bar{r}^2/\nu$, *i.e.*, the time scale for viscous momentum transport between the rotors. Here, ν is the kinematic viscosity of the solvent. For the common system parameters (see appendix A) and assuming a high density such that $\bar{r} \approx \sigma$, $\tau_f(\bar{r})\Omega/(2\pi) \approx 6 \times 10^{-3}$, *i.e.*, the rotors experience the mutually generated flow before 1% of the first circulation of the intrinsic rotation. For times $t \gg \tau_f(\bar{r})$, a pair interaction as described in section 2.3 can be assumed. Consequently, many-body interactions similar to the bulk dynamics, *e.g.*, multi-vortex formation and chaotic individual trajectories are expected. However, the dynamics will bear a signature of the very precise symmetry introduced by the confining geometry. Consider the setup sketched in figure 5.1a after turning on the intrinsic rotation at times $t \gtrsim \tau_f(\bar{r})$. The pair interactions acting on the highlighted (blue) rotor in the red area stemming from the other rotors in that area will on average cancel each other, such that the blue rotor is on average not subject to any net motion. On the other hand, as a result of the steric repulsion between boundary and rotors, the highlighted rotor in the green area is subject to asymmetric pair interactions leading to a net propulsion along the wall into the direction opposite to the direction expected for a rolling motion. The rotational symmetry of the confinement, *i.e.*, the same mechanism applies to any position near the boundary, thus implies the formation of an edge flow.

As a result of the viscous propagation of shear stresses in the rotor suspension with effective kinematic suspension viscosity $\nu(\phi)$ [166–168], the edge flow leads to a flow profile which is on average and in a stationary state free from viscous stresses. The suspension viscosity implies a time scale $\tau_f(r) = r^2/\nu(\phi)$ for viscous momentum spreading over distances r. The outer suspension layers, where the edge flow

is initiated, exert viscous stresses on the neighbouring inner layers which in turn propagate the stresses into the next layers until a solid body-like rotation with a linear flow profile is established, as shown in figure 5.1b. The steady state flow $\boldsymbol{v}(\boldsymbol{r}) = v_r(r,\varphi)\hat{e}_r + v_\varphi(r,\varphi)\hat{e}_\varphi$ thus obeys $v_\varphi \propto r$ and $v_r = 0$. However, the linear profile here is only fulfilled on average, *i.e.*, the rotors in suspension are still subject to mutual actuation and thermal motion and the relative distances between the rotors are not fixed. The initiation of the edge flow and the propagation of the viscous stresses is quantitatively shown in figure 5.2a, where the flow profile is shown at different points in time after turning on the intrinsic rotation. At early times, a net flux is only generated at the boundary, whereas the flow in the interior of the confinement on average vanishes. At late times, a linear profile is established starting at zero in the middle of the circle and reaching a maximum at the boundary. The transportation of viscous signals from the boundary to the middle of the container through the rotor suspension is relatively fast, *i.e.*, $\tau_\mathrm{f}(R_\mathrm{o})\Omega/(2\pi) \approx 1.2$, such that a linear profile is already established after ≈ 5 intrinsic rotations as can be seen in figure 5.2a. Figure 5.2c shows the quantitative time evolution of the profile at different radii. At the boundary, the flow is initiated almost immediately, whereas in the inner region the flow is only launched after the viscous signal has propagated into the middle. From the blue data in figure 5.2c this takes $t\Omega/(2\pi) \approx 1$, in accordance with $\tau_\mathrm{f}(R_\mathrm{o})$.

A quantitative prediction for the steady state profile $v_\varphi(r)$ can be derive using the theory of chiral active fluids. The general incompressible equation of motion is equation (1.53), which can be simplified by dropping the time derivatives and assuming constant density, angular velocity density $\widetilde{\Omega} = n\Omega$ and thus also constant odd viscosity, yielding

$$0 = -\partial_\alpha p^\mathrm{eff} + \eta\partial_\beta\partial_\beta v_\alpha + \eta_\mathrm{R}\varepsilon_{\alpha\beta}\partial_\beta(2\widetilde{\Omega} - \omega)\,, \tag{5.1}$$

where the odd viscosity has been absorbed into the effective pressure $p^\mathrm{eff} \equiv p - \eta^\mathrm{odd}\omega$. As a consequence of the rotational symmetry, steady state solutions can only entail azimuthal contributions, such that the investigation of the azimuthal component of equation (5.1), *i.e.*,

$$0 = \eta\left(\frac{1}{r}\partial_r\left(r\partial_r v_\varphi\right) - \frac{v_\varphi}{r^2}\right) + \eta_\mathrm{R}\varepsilon_{\varphi r}\partial_r\left(2\widetilde{\Omega} - \frac{1}{r}\partial_r\left(rv_\varphi\right)\right)\,, \tag{5.2}$$

suffices for finding a solution of $v_\varphi(r)$. Thus, for rotational symmetry and constant (angular velocity) density, the odd viscosity has no impact on the steady state velocity profile. Simplifying equation (5.2) yields

$$0 = (\eta + \eta_\mathrm{R})\left\{\partial_r^2 v_\varphi + \frac{1}{r}\partial_r v_\varphi - \frac{v_\varphi}{r^2}\right\}\,, \tag{5.3}$$

which is the equation for the flow of a passive fluid between two cylinders [116] in a fluid with modified effective viscosity $\eta + \eta_\mathrm{R}$. However, the viscosity has no impact on the steady state flow field. Solutions are of the form $v_\varphi(r) = ar + b/r$ with coefficients a and b determined by the boundary conditions. As a result of the symmetry, the flow has to vanish in the middle $v_\varphi(0) = 0$, implying $b = 0$. However, the boundary condition at the container wall is not trivial to define, since the fluid is subject to a no-slip boundary condition at the wall, but the individual rotors are subject to a slip boundary condition. In order to proceed analytically, a slip condition is assumed, *i.e.*,

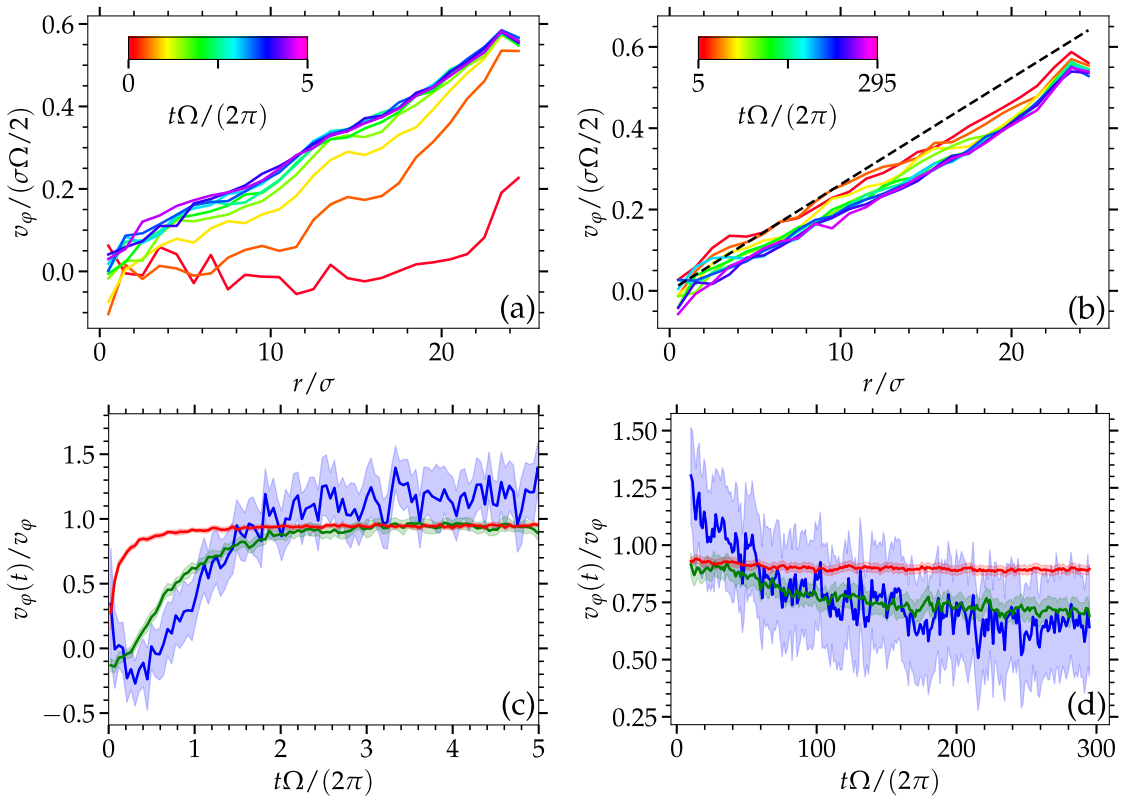

Figure 5.2: Evolution of azimuthal flow in a circular container of radius $R_o = 25\sigma$ at density $\phi = 0.37$ averaged over 120 independent simulations in annular bins of width σ. (a) and (b) azimuthal velocity $v_\varphi(r)$ as a function of time (colour code) and radius. Dashed line corresponds to equation (5.5). (c) and (d) time evolution of the azimuthal velocity at fixed radii, red, green, and blue lines correspond to $v_\varphi(23.5\sigma)$, $v_\varphi(12.5\sigma)$, and $v_\varphi(4.5\sigma)$. (c) shows the short time, whereas (d) the long time evolution. Data points correspond to time averages over 80 (c) or 2000 (d) consecutive time values corresponding to time intervals of length $\Delta T\Omega/(2\pi) \approx 0.05$, $\Delta T\Omega/(2\pi) \approx 1.18$, for (c) and (d), respectively. Points in (a) and (b) are all time averaged over intervals of length $\Delta T\Omega/(2\pi) \approx 0.06$. The light coloured enclosure in (c) and (d) shows the standard deviation. Lines in (c) and (d) are normalised by predictions according to equation (5.5).

the stress between rotor fluid and wall vanishes

$$0 = \sigma_{\varphi r}\Big|_{r=R_o} \tag{5.4a}$$

$$= \eta\left\{\partial_r v_\varphi - \frac{v_\varphi}{r}\right\}_{r=R_o} + \eta_R\left\{\frac{v_\varphi}{r} + \partial_r v_\varphi - 2\widetilde{\Omega}\right\}_{r=R_o}. \tag{5.4b}$$

Plugging in the solution $v_\varphi(r) = ar$ yields $a = \widetilde{\Omega}$ and accordingly

$$v_\varphi(r) = \widetilde{\Omega} r \tag{5.5a}$$

$$= n\Omega r\,. \tag{5.5b}$$

Thus, the intrinsic rotation drives the solid body-like rotation. The behaviour $v_\varphi(r \to \infty) \to \infty$ creates infinite shear stress at the fluid container wall interface and is an artefact of assuming a perfect slip boundary condition at R_o. The finite friction between the rotors and the container thus limits the rotor velocity at the outer boundary

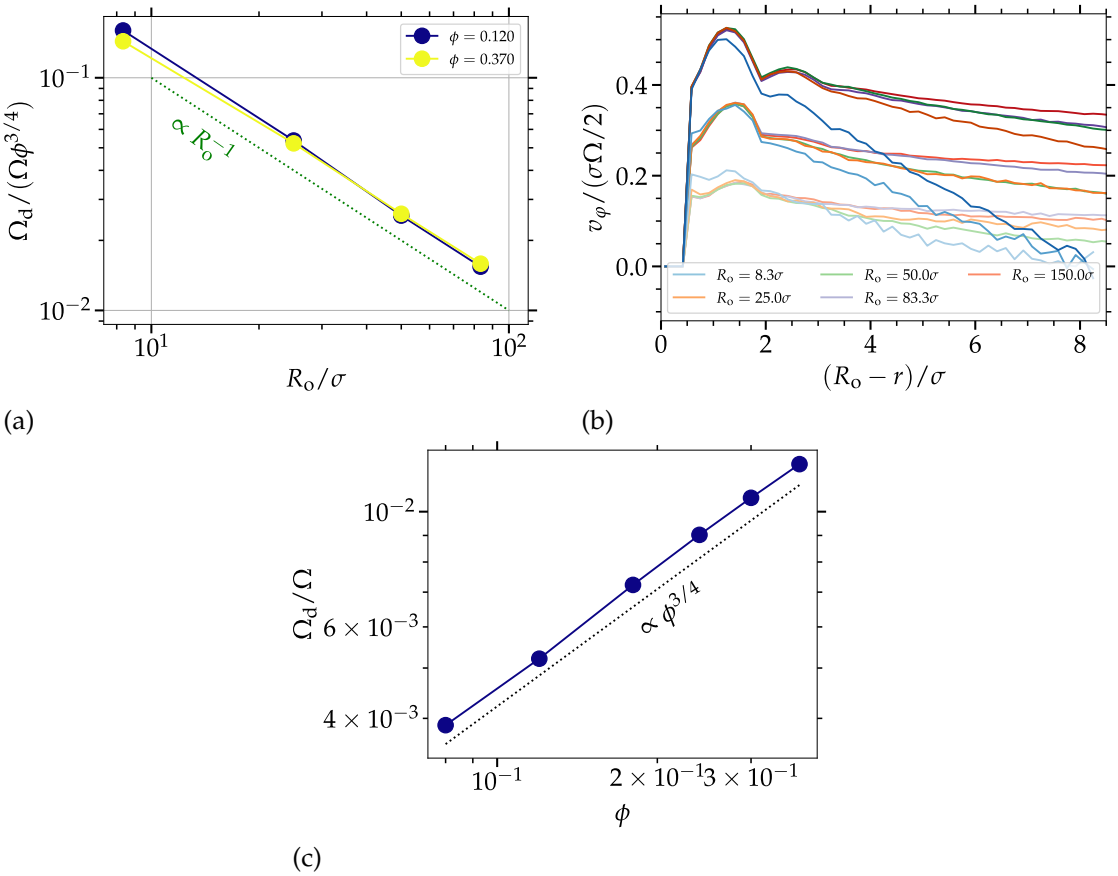

Figure 5.3: Normalised angular and azimuthal velocity Ω_d and v_φ as a consequence of the edge flow, (a) Ω_d as a function of confinement radius. (b) v_φ as a function of distance from the boundary for varying R_o and densities $\phi = 0.08, 0.18, 0.30$ (ϕ increases with colour darkness). (c) Ω_d as a function of density ϕ. In (a) a data collapse is achieved by normalising the angular velocities additionally with $\phi^{3/4}$, which is also the scaling shown in (c).

for $R_o \to \infty$. Because the flow profile due to equation (5.3) is necessarily linear in order to reduce frictional stress, $v_\varphi(r)$ is thus given by linearity and the viscous interactions between container wall and rotors at the boundary prescribing $v_\varphi(R_o)$, which can be used to find the integration constant a. Figure 5.2b shows simulation results of $v_\varphi(r)$ at different times after propagation of the boundary shear into the interior of the container, shown in figure 5.2a. At short times $t\Omega/(2\pi) \approx 5$, the simulation data is in agreement with the prediction (5.5) in the interior of the container, where the rotational stress $\sigma^{\mathrm{rot}}_{\alpha\beta}$ (equation (1.51)) drives the flow. However, as the system evolves, the flow relaxes to a constant profile for $t\Omega/(2\pi) \gtrsim 200$, as can be seen in figure 5.2d. On the one hand, the rotational stress drives the fluid in the interior, whereas the flow profile at the boundary is dictated by the hydrodynamic interaction between the rotors and the no-slip wall. Only for $t\Omega/(2\pi) \gg 5$, the influence of the finite boundary flow $v_\varphi(R_o)$ becomes dominant in the interior of the container.

Although the exact derivation of the boundary condition $v_\varphi(R_o)$ is cumbersome, its dependence on the system size R_o can be estimated accurately via the angular velocity of the solid body-like rotation. To this end, the relative motion of the rotors is neglected and the rotor distribution is approximated as a solid disc rotating at angular velocity

Ω_d. This disc is then subject to a driving and damping torque yielding a constant angular velocity. The driving torque M_d is proportional to the shearing force of the rotors in the outer layer, *i.e.*, to the number of rotors in this layer which is proportional to the size of its circumference. The torque is then obtained by multiplying with the radius where the force acts, such that

$$M_d \propto 2\pi R_o^2 . \tag{5.6}$$

For the damping torque between the *disc* and the container, assume the friction between two concentric cylinders of radii R_1 and R_2 and $|R_1 - R_2| = \Delta R$ in the limit of $\Delta R \to 0$ such that [116]

$$M_f = \frac{2\pi\eta}{\Delta R}\Omega_d R_o^3 . \tag{5.7}$$

Balancing driving and damping torques yields

$$\Omega_d \propto R_o^{-1} . \tag{5.8}$$

Figure 5.3a shows the angular velocity Ω_d obtained from simulations for different container sizes R_o, which show good qualitative agreement with the expected scaling. Note, that $\Omega_d \propto R_o$ implies an outer boundary condition independent of the container size, *i.e.*, $v_\varphi(R_o) = R_o\Omega_d$ does not depend on R_o, the curvature of the confinement, but only on the interactions among the rotors. This explicitly shows, that the edge flow is not an effect of the hydrodynamic forces experienced by single rotors at a curved wall, because this would entail a dependency on the curvature [52]. Instead, the edge flow only depends on the rotor density and thus has its origin in the inter rotor interactions. This behaviour, already entailed in figure 5.3a, is shown explicitly in figure 5.3b where the azimuthal velocity v_φ in the vicinity of the boundary is displayed at different densities for varying container radii. While the value of v_φ directly at the boundary coincides for the same ϕ and different R_o, the values with increasing distance from the boundary separate as dictated by the inner boundary condition which is realised at different positions for varying R_o. Additionally, the simulations reveal that Ω_d bears a dependency on the density $\Omega_d \propto \phi^{3/4}$, shown in figure 5.3c. The origin of the exponent is unclear and non-trivial dependencies on ϕ are expected in M_d and M_f.

5.2. Self-enhanced boundary layering due to odd viscosity

Colloidal suspensions near a boundary show an oscillatory density in the vicinity of a boundary [183, 184] resulting from entropy increase and steric repulsion. Determining the oscillatory density can be considered as a special case of finding the correlation function $g(\boldsymbol{r})$ in a binary mixture where the colloids represent one species and the boundary represents another infinitely large and diluted species [185]. Consequently, the equilibrium density distribution at the boundary can be well described in the framework of the Ornstein-Zernike equation [4] allowing for solutions if the colloids are considered as solely sterically interacting hard spheres (discs). The introduction of intrinsic rotation to the colloids in circular confinement and accordingly also the introduction of the velocity profile $v_\varphi(r)$ renders the situation much more complicated. Then, hydrodynamics transmit rotational and odd stresses, which have shown to be responsible for density inhomogeneities in chapter 3.

The radial density distribution normalised with the average density in the rotor fluid in the vicinity of the boundary is shown in figure 5.4a. Clearly, the density

distribution exhibits oscillations (*layering*) with a period of $\approx \sigma$ as is also observed in equilibrium systems [183–185]. The oscillations are more pronounced at higher density, because here steric interactions are more important. Furthermore, the layering is independent of the system size as can be inferred from figure 5.4b. Note, that the colloid-colloid and colloid-wall interaction diameters are defined via the effective hard core repulsion using the diameter $\sigma_* = 1.162\sigma$ (see appendix A.1). The oscillatory density yields oscillatory rotational stresses [151]. In figure 5.1, the outermost layer will exert rotational stresses on the neighbouring layer into the clockwise direction, whereas the inner layers exert rotational stresses into the counter-clockwise direction on the neighbouring outer layers. As shown in figure 5.5b, depending on the relative velocity and the oscillatory average number of particles in the respective layers, the collective motion oscillates and thus bears a signature of the steric layering, as has been pointed out by Liu and co-workers [151]. They studied a granular version of a rotor fluid, consisting of discs that only apply rotational stresses when in touch, similar to freely moving gears. In the gear-like system, as well as in the system studied in the scope of this thesis, the rotor density attains a constant far away from the boundary and thus the flow oscillations vanish in the interior of the container.

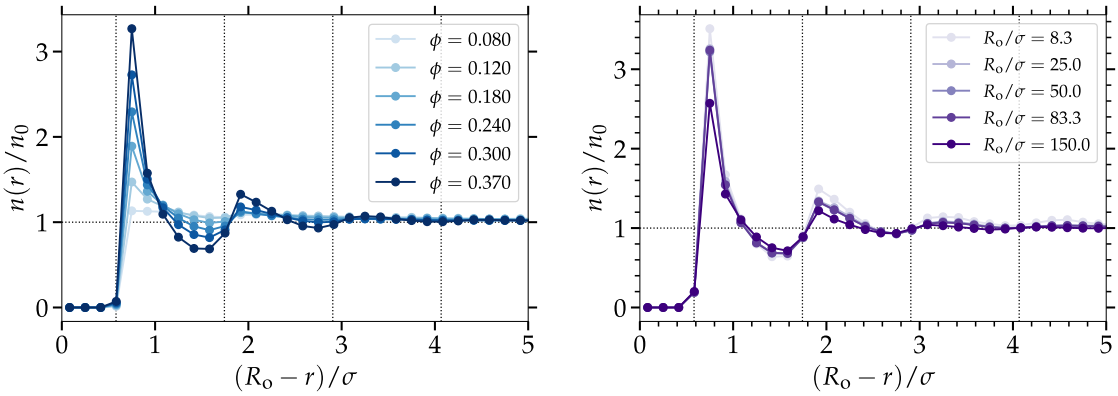

(a) (b)

Figure 5.4: Normalised radial number density in a rotor fluid. (a) Varying density in confinement of radius $R_o = 50\sigma$. (b) Varying confinement radius R_o for fixed density. The dashed vertical lines denote the effective hard core repulsion diameter between the colloid-colloid (σ_*) and colloid-wall interactions ($\sigma_*/2$).

A steady state flow profile $v_\varphi(r)$ gives rise to a vorticity profile that only depends on the radius

$$\omega(r) = \frac{\partial_r \left[r v_\varphi \right]}{r} . \tag{5.9}$$

Applying equation (5.9) to the rotors flow profiles leads to constant vorticity in the region of linear profiles, whereas in the vicinity of the outer boundary, as a consequence of the oscillating flow profile, also the vorticity oscillates. Following equation (1.54), the force density acting on the rotor fluid as a consequence of the presence of odd viscosity in the oscillating collective flux $v_\varphi(r)$ can be written as $\eta^{\text{odd}} \partial_\alpha \omega$, assuming incompressible flow and a constant angular velocity density. Therefore, the odd stresses force the rotors to the maxima of the vorticity profile—along the gradient of vorticity—implying correlations between vorticity and density changes. The density modulations $n(r)$ in a rotor fluid are thus a result of two effects. The effective pressure resulting from odd viscosity induces density changes until the resulting entropic

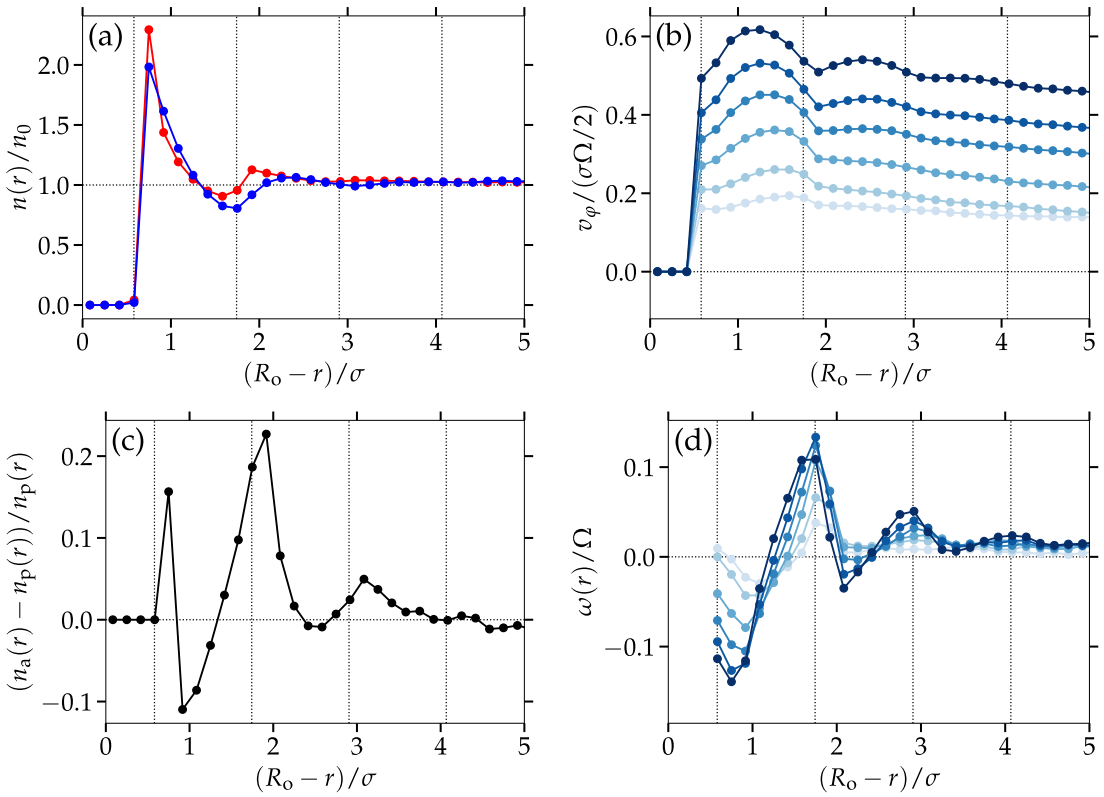

Figure 5.5: Vorticity-density correlations at the boundary. (a) Radial number density of passive colloids in solution (blue) in comparison to data from figure 5.4 (red) at the same density $\phi = 0.24$ normalised with the average value n_0. (b) Zoomed in perspective on the data in figure 5.8. (c) Changes in the $n(r)$ of the rotor fluid relative to the passive analogue. The difference at $\sigma_*/2$ is set to zero, since the density is here predominantly controlled by the strong repulsion. (d) Normalised vorticity and velocity profiles in figure 5.8b. The dashed vertical lines denote the effective hard core repulsion diameter between the colloid-colloid (σ_*) and colloid-wall interactions ($\sigma_*/2$). Colour coding in (b) and (d) same as in figure 5.4.

counterpart, *i.e.*, osmotic pressure, balances the effective pressure $p^{\text{eff}} \equiv \eta^{\text{odd}}\omega$, establishing a steady state. The finite compressibility of the rotor fluid prevents the rotors from further accumulating in the regions of maximum vorticity.

Figure 5.5 shows the correlations between local vorticity and density inhomogeneities. Figure 5.5a shows the density distributions of an active (red) hydrodynamically interacting and a passive (blue) rotor system for reference in comparison and figure 5.5c shows the local difference introduced by the chiral activity normalised by the local density in the passive system. From the direct comparison, it is noticeable that the primary density maximum at $\approx \sigma_*/2$ remains unchanged in position upon chiral activity, but is more pronounced by an increase of $\approx 15\%$. The second maximum, however, is more pronounced and also is shifted in comparison to the passive system. The same behaviour is also observed for the third peak, even though the effect becomes less striking with increasing distance from the boundary. Figure 5.5b and 5.5d show the flow v_φ in the vicinity of the boundary and the corresponding vorticity. Comparison to figure 5.5c shows a correlation between vorticity and local density changes, particularly pronounced in the region between $\sigma_*/2$ and $3\sigma_*/2$, similar to

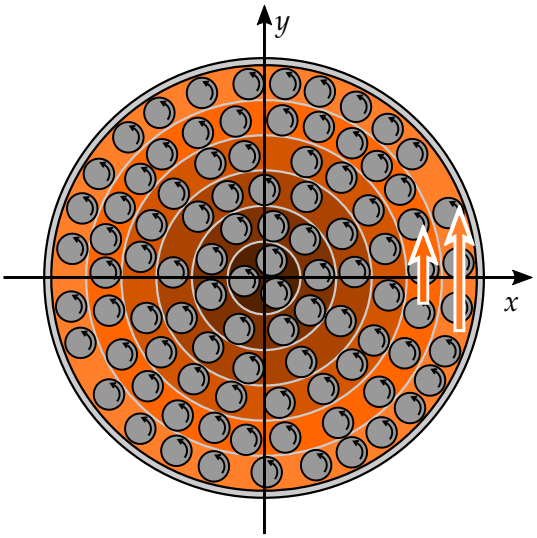

Figure 5.6: Illustration of the vanishment of the the third term on the right hand side of equation (5.10).

section 3.2. The rotors are transported along the vorticity gradients, showing that odd stresses have an impact on the structural order of chiral active fluids near boundaries.

In previous studies of chiral active matter in circular geometries [41, 74, 75, 151] the influence of vorticity on steady-state density modulations stemming from odd viscosity was not reported. In the respective systems, the radial density $n(r)$ for rotationally actuated colloids does not bear a signature of odd viscosity. In these cases, the rotor fluid is realised as a granular system such that odd stresses are only transported when the rotors are in touch [74, 75, 151]. A different system displays a high rotor fluid density as a result of cohesive magnetic dipolar interactions [41]. In both cases the small density inhomogeneities shown in figures 5.5a and 5.5c are impeded by the weak compressibility of the respective rotor fluid. However, for the system investigated in the scope of this thesis, the odd stresses are transmitted via the solvent also at small and intermediate densities, resulting in a rotor fluid simultaneously bearing odd viscosity and high compressibility, implying the realisation of density-vorticity correlations.

Note, that the introduction of the odd stresses to the dynamics of the rotor fluid solely in terms of an effective pressure p^{eff} is only possible under the assumptions of incompressible flow and constant angular velocity, *i.e.*, constant odd viscosity $\eta^{\mathrm{odd}} \propto \widetilde{\Omega}$. The entropic density modulation clearly introduces a non-constant density $n(r)$ and thus a non-constant angular velocity $\widetilde{\Omega}(r) = \Omega n(r)$. The force density resulting from odd viscosity in vector notation in a general form is

$$\begin{aligned}\boldsymbol{\nabla}\cdot\boldsymbol{\sigma}^{\mathrm{odd}} = \eta^{\mathrm{odd}}\boldsymbol{\nabla}^2\boldsymbol{v}^* + \begin{pmatrix} \omega & \boldsymbol{\nabla}\cdot\boldsymbol{v} \\ \boldsymbol{\nabla}\cdot\boldsymbol{v} & \omega \end{pmatrix}\cdot\boldsymbol{\nabla}\eta^{\mathrm{odd}} \\ + 2\begin{pmatrix} \partial_y v_x & \partial_y v_y \\ \partial_x v_x & \partial_x v_y \end{pmatrix}\cdot\boldsymbol{\nabla}\eta^{\mathrm{odd}}, \end{aligned} \tag{5.10}$$

where $v_\alpha^* = \varepsilon_{\alpha\beta}v_\beta$. The divergence $\frac{1}{r}\partial_r(rv_r) + \frac{1}{r}\partial_\varphi v_\varphi$ vanishes for the stationary flow with $v_r = 0$ and $v_\varphi(r)$. Hence, for the circularly confined rotor fluid the first term on the right hand side of equation (5.10) can be rewritten[1] as $\eta^{\mathrm{odd}}\boldsymbol{\nabla}\omega$, which is identical

[1] Note, that $\partial_x v_x + \partial_y v_y = 0$ implies $\partial_x v_x = -\partial_y v_y$.

to the result obtained under the assumption of incompressibility. The second term can be rephrased as $\omega \mathbf{1} \cdot \boldsymbol{\nabla} \eta^{\mathrm{odd}}$, where $\mathbf{1}$ denotes the unit matrix, such that the force density resulting from non-constant odd viscosity bears an additional term pointing to the gradient of $\eta^{\mathrm{odd}} \propto n$ and thus to the density peaks. The last term vanishes for the considered flow as is can be inferred from figure 5.6. Therein, the white marked arrows indicate the flow $\boldsymbol{v}$ at $y = 0$ and the respective x position x_0. Since the flow is purely azimuthal, it is $\boldsymbol{v}(x_0, 0) = v_y \hat{\boldsymbol{e}}_y$ and $v_x = 0$. Accordingly, $\partial_y v_y|_{x=x_0,y=0} = 0$ and $\partial_x v_y|_{x=x_0,y=0} \neq 0$, such that the only term in the matrix of the third term on the right hand side of equation (5.10) is the (y, y) component (lower right matrix element). On the other hand, $\partial_y \eta^{\mathrm{odd}}|_{x=x_0,y=0} = 0$ such that the matrix product vanishes. From the rotational symmetry of the geometry, it follows that the respective term in equation (5.10) vanishes everywhere. Therefore, the presence of odd viscosity in a circularly confined chiral active fluid with radial density inhomogeneities can be written in tensor notation as

$$\partial_\beta \sigma^{\mathrm{odd}}_{\alpha\beta} = \eta^{\mathrm{odd}} \partial_\alpha \omega + \omega \partial_\alpha \eta^{\mathrm{odd}} , \tag{5.11}$$

such that the density-vorticity correlations qualitatively remain unaffected from the oscillating density inhomogeneities entailed in $n(r)$, *i.e.*, the forces resulting from odd stresses point into the direction of the gradient of the vorticity plus a self-amplifying term pointing into the direction of the density gradient.

5.3. Collective rotation in turbulent system

Figure 5.7 shows rotors' trajectories at different densities. In the dilute as well as in the dense configurations, the formation of a robust edge flow is observed as a result of the asymmetric rotational stress at the boundary. However, in the interior of the container particles are performing seemingly chaotic trajectories reminiscent of active turbulence, as shown in figure 5.7. This is because the spontaneous pair interactions of the rotors that induce translation due to the orbital rotation at angular velocity Ω_{pair} at short interparticle distances are stronger than the azimuthal velocity v_φ of the solid body-like rotation, especially in the container centre. Only at higher densities, the mutual steric interactions partially prevent the formation of vortices and thus the solid body-like rotation is easier observed with the bare eye (confer figure 5.7d). In the limit of close-packing, steric interactions prevent the formation of any vortices in the interior of the container and the ensemble will rotate like a true solid body as a whole, where even the relative distances between the rotors are maintained. Nevertheless, the flow profile is on average linear at all densities, as has been pointed out in section 5.1, because the translation in excess to the solid body-like rotation induced by the pair interactions vanishes on average in the centre of the container due to symmetry and only the solid body-like rotation remains. But the strong variations in the velocity and the only weak directed current in the container centre render a quantitative measurement of the azimuthal velocity profile computationally very expensive, especially for very large systems. Figure 5.8 shows the measured flow profiles in different sizes of the confinement. While in small systems (figure 5.8a) the flow field can be determined very accurately, the computational effort for measuring v_φ increases rapidly for increasing R_{o} (figure 5.8b) and the measured v_φ for larger systems here still bears inaccuracies. Nevertheless, the determination of v_φ at the boundary is accurately possible also in large systems, since the asymmetry of the pair interactions reduces the signal to noise ratio of v_φ, *i.e.*, the rotors are not actively transported into the clockwise

direction along the boundary by rotors at radial position $r > R_o$, since these positions are outside of the container and thus not allowed.

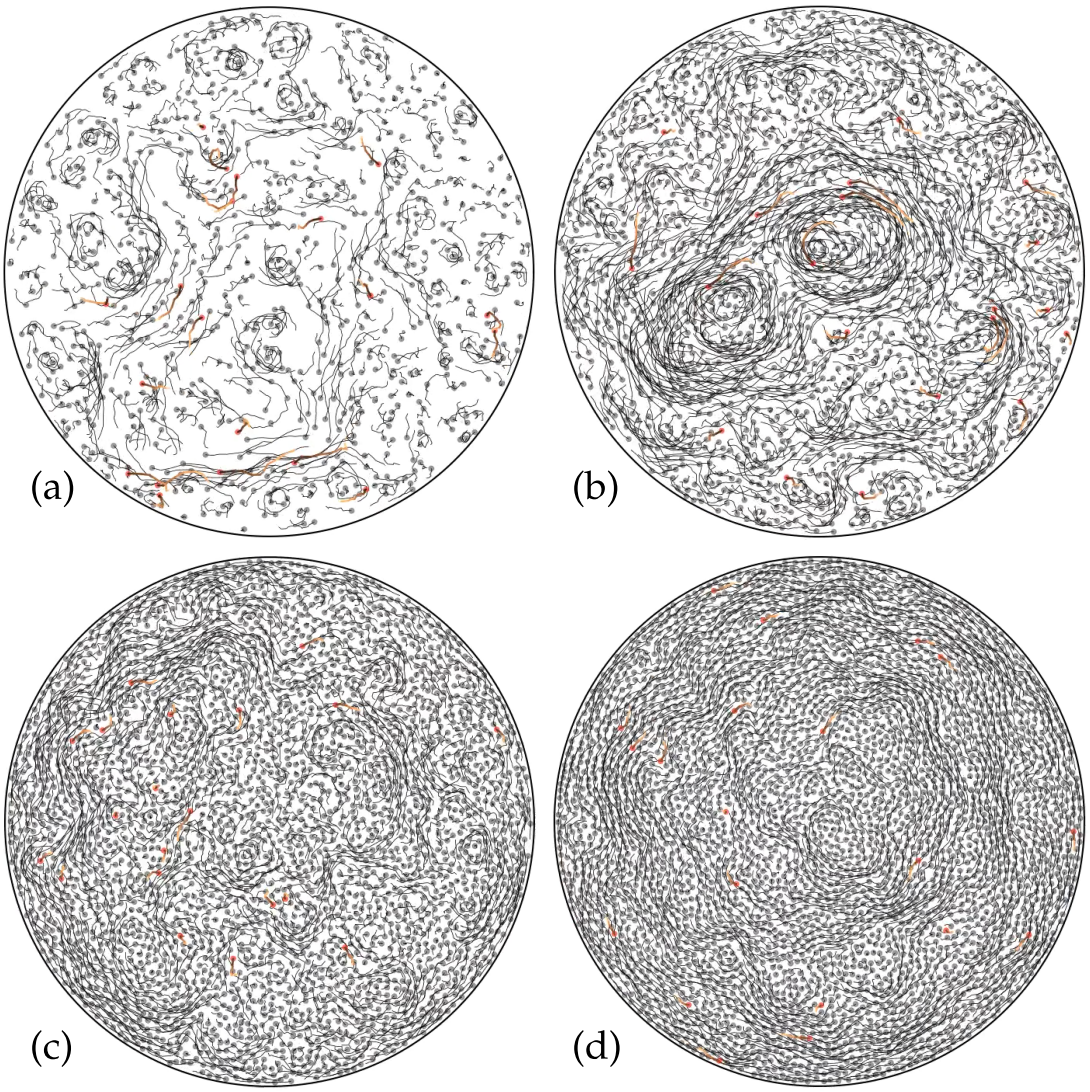

Figure 5.7: Rotors' trajectories at density $\phi = 0.08$ (a), $\phi = 0.18$ (b), $\phi = 0.30$ (c), and $\phi = 0.37$ (d). The length in time of the trajectories is $t\Omega = 6.0$ (a), $t\Omega = 5.0$ (b), $t\Omega = 3.5$ (c), and $t\Omega = 2.5$ (d). The decrease of $t\Omega$ at higher densities is introduced in order to keep the images as comprehensible as possible. In each setup, 20 randomly selected, representative trajectories are highlighted.

Qualitatively, the dynamics of the rotors in a circular container can be regarded as a combination of the solid body-like rotation initiated by the edge flow and the turbulent dynamics induced by the mutual hydrodynamic interactions in the interior of the container, where for simplicity the velocity oscillations at the boundary are neglected for the moment. Consequently, the mean-square displacements shown in figure 5.9 bear a signature of both contributions. At low ϕ, the rotors show anomalous diffusion with an exponent between 1 and 2, *i.e.*, neither showing diffusive nor ballistic transport, as a result of the rotor interactions at low ϕ where the ensemble dynamics is composed of isolated rotors merely showing random walks but nearby rotors are

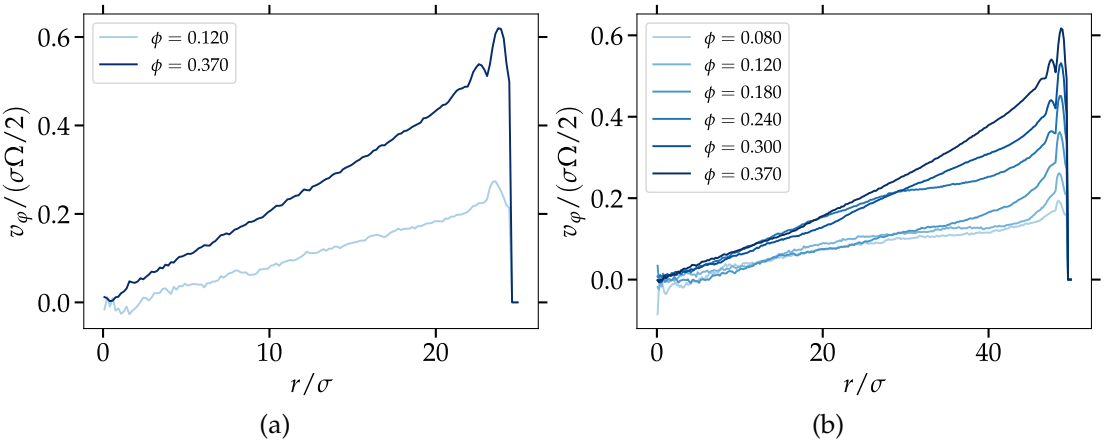

Figure 5.8: Velocity profiles in dependence on the density ϕ and the container size R_o. Confinement radius is (a) $R_o = 25\sigma$, (b) $R_o = 50\sigma$. Densities in (a) are $\phi = 0.12$ (light) and $\phi = 0.37$ (dark), densities in (b) are $\phi = 0.08, 0.12, 0.18, 0.24, 0.30, 0.37$ (from light to dark).

dragged by the mutually generated flows. With increasing ϕ, the amount of isolated rotors decreases leading to a larger exponent of anomalous diffusion. In contrast to the bulk dynamics the rotors actuation in circular confinement is monotonically increasing. This is a consequence of the solid body-like rotation, where sterically *blocked* rotors are still performing the rotation around the confinement centre together with the next neighbours. This can also be observed from the oscillations in the MSD at high ϕ showing that particles are visiting positions at which they have already been, which here means that the particles are performing rotations in the confinement. However, because the mean-square displacement is not a periodic function in the sense of $\langle \Delta r(t) \rangle = \langle \Delta r(t + nT) \rangle$ with $n = 0, 1, 2, ...$, as is expected for particles going on closed circles, even at the highest observed densities the rotors do not conserve their mutual distances and thus do not perform a true solid body rotation but still bear a signature of the underlying turbulent dynamics. Instead, the MSD reaches a plateau dictated by the confinement. The plateau value $\langle \Delta r(t \to \infty) \rangle$ increases with R_o and is reached later in time as the finite area explored by the rotors and thus the time to cover this area increases with R_o.

Following the picture of regarding the ensemble dynamics $\boldsymbol{v}(\boldsymbol{r})$ in circular confinement as a combination of turbulent dynamics $\boldsymbol{v}_{AT}(\boldsymbol{r})$ and a solid body-like rotation $\boldsymbol{v}_{SBR}(\boldsymbol{r})$, *i.e.*, $\boldsymbol{v}(\boldsymbol{r}) = \boldsymbol{v}_{SBR}(\boldsymbol{r}) + \boldsymbol{v}_{AT}(\boldsymbol{r})$, the question arises whether the two contributions can be straightforwardly separated, *e.g.*, by subtracting the solid body rotation from the particle trajectories in order to obtain dynamics reminiscent of turbulence, as in bulk. With regard to this question, the configurational structure of the total velocity field of the rotor ensemble minus a linear steady state profile fulfilling $v_\varphi(0) = 0$ and $v_\varphi(R_o)$ according to measured values, such that the $v_\varphi(r)$ oscillations at the boundary are neglected for simplicity, is presented. Note, however, that a straightforward calculation of the velocity correlation function $\langle \boldsymbol{v}(r + r_0) \cdot \boldsymbol{v}(r_0) \rangle$ or energy spectrum E_q according to equation (1.50) bears influences resulting from the fact that the velocity field is not translational symmetric as a result of the existence of the boundary. However, after subtraction of the solid body rotation, the velocity field is assumed to be on average approximately equivalent in the whole circular domain rendering the implied averages in $\langle \boldsymbol{v}_{AT}(r + r_0) \cdot \boldsymbol{v}_{AT}(r_0) \rangle$ and equation (1.50) well defined quantities. In or-

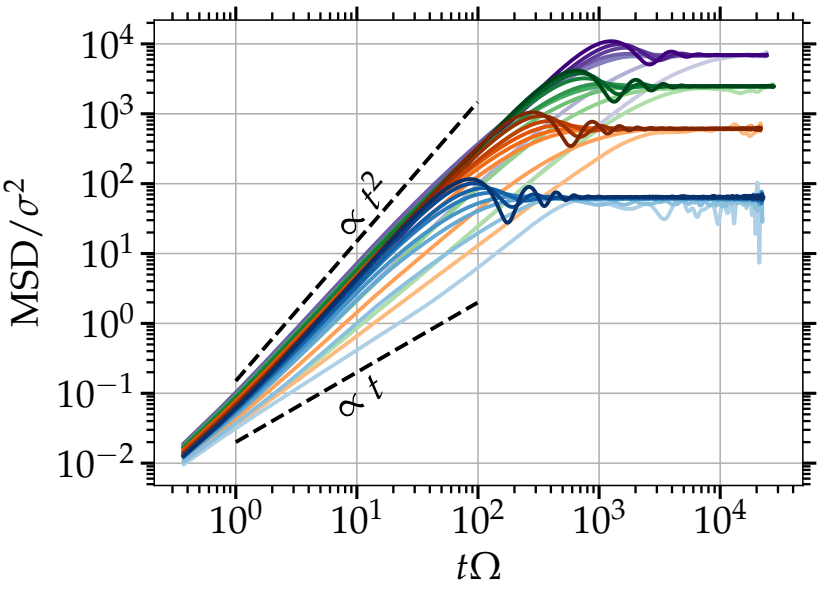

Figure 5.9: Mean-square displacement of rotor ensembles in circular confinement. The confinement radius is $R_o = 8.3\sigma$ (gradient of blues), $R_o = 25.0\sigma$ (gradient of oranges), $R_o = 50.0\sigma$ (gradient of greens), and $R_o = 83.3\sigma$ (gradient of purples), from bottom to top of the terminal values. For fixed R_o, increasing colour darkness represents data with increasing density $\phi = 0.004, 0.020, 0.080, 0.120, 0.180, 0.240, 0.300, 0.370$. The dashed lines $\propto t$ and $\propto t^2$ indicate diffusive and ballistic transport, respectively.

der to efficiently calculate the velocity correlation and the energy spectrum using the Wiener-Khintchin theorem as explained in appendix D, the considered velocity field has to be defined on a square domain. To this end, only the velocity field in a square of edge length $L_{sq} = \sqrt{2}R_o$ inside the confinement is considered, including all possible radii r of $v_\varphi(r)$ along the square diagonal. The results are shown in figure 5.10.

Figure 5.10a shows stronger velocity correlations for higher density as a result of the increase of mutual actuation and cooperative movement with increasing density. Similar to the velocity correlation function in bulk (confer figure 4.3b), the data in figure 5.10a evolves a maximum at $r \approx \sigma$ for the cooperative movement with nearby rotors, decays for increasing distances, and turns negative at even larger distances. The major difference is that in the circular confinement $\langle v_{AT}(r \to 2R_o) \cdot v_{AT}(0) \rangle \to 0$, resulting from the strong directed current at the edge, *i.e.*, at the boundary the rotors do not show turbulent or chaotic dynamics but only the edge flow, such that after subtraction of the solid body rotation the rotors are essentially resting at the boundary.

Energy spectra corresponding to figure 5.10a and for varying R_o at a density which in bulk gives rise to active turbulent dynamics ($\phi = 0.18$) are depicted in figures 5.10b and c, showing a power-law behaviour for sufficiently large confinement sizes. There are two main differences between the E_q here and in bulk. On the one hand, figures 5.10b and c show the formation of a dominant vortex scale, *i.e.*, a maximum in E_q, at the lower end of the q range, which is absent in bulk. This difference is brought into the system by the radial symmetry of the circular confinement. Although the solid body and thus collective rotation is subtracted, the dominant vortex scale emerges by symmetry, *i.e.*, it corresponds to the largest possible vortex taking the

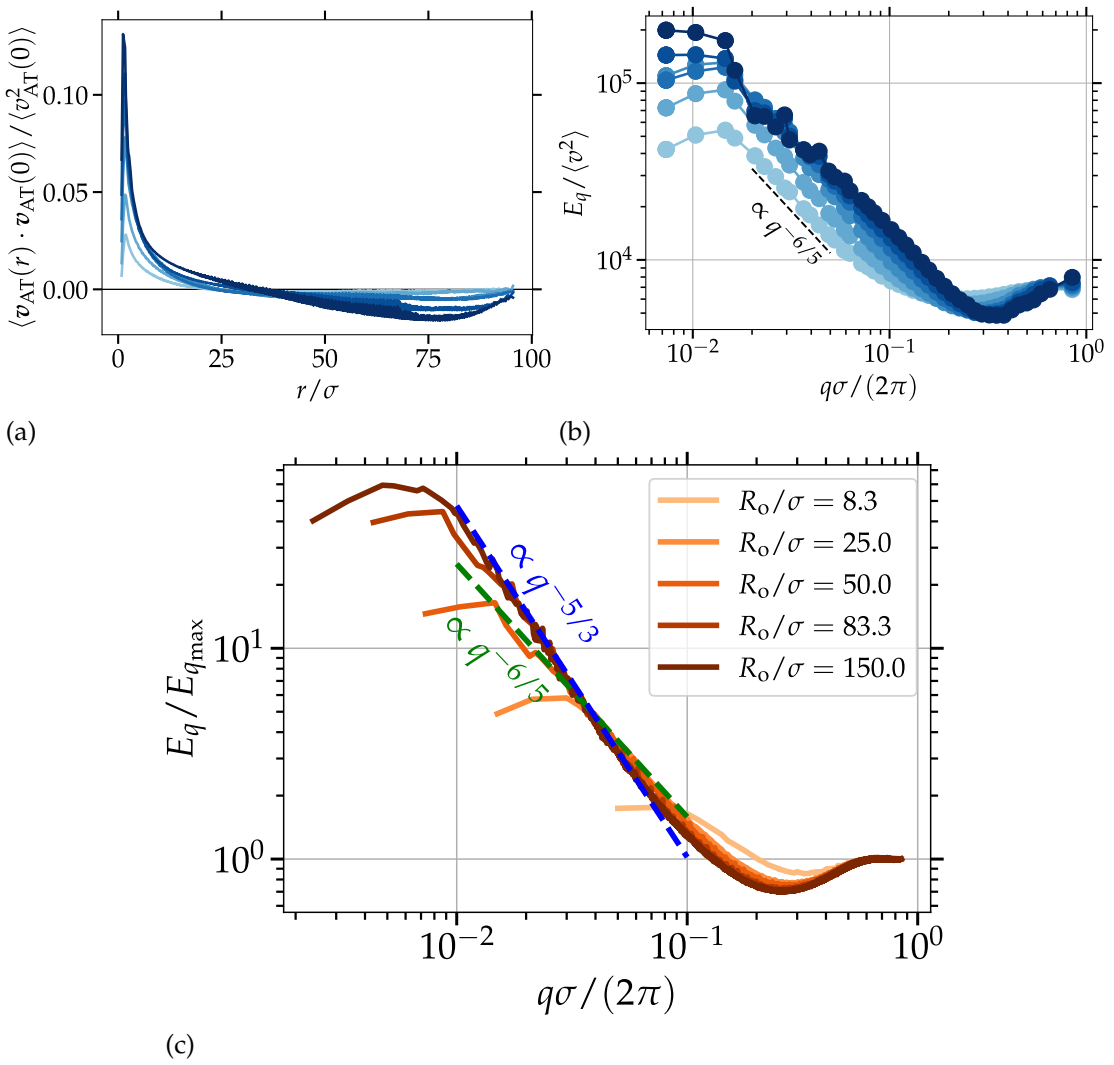

Figure 5.10: (a) Velocity correlation functions obtained from coarse-grained rotor velocity fields in a circular container of size $R_o/\sigma = 50$. (b) Corresponding energy spectra. Colour coding indicates density ϕ analogous to figure 5.4. (c) Energy spectra E_q for varying confinement sizes in a rotor fluid of density $\phi = 0.18$. Blue and green dashed lines indicate power-law scaling for reference.

effectively *resting* rotors directly at the boundary into account then dictates a cutoff for $q \to q_{\min}$. A second difference with respect to the bulk dynamics is the exponent of the power-law decay which is not unique for different values of the confinement radius, whereas in bulk $E_q \propto q^{-5/3}$ is a universal behaviour. Despite the fact that the dynamics still show self-similarity, *i.e.*, a power-law in E_q, the exponent is here altered resulting from change in the energy transfer with respect to the bulk dynamics. Whereas in bulk, the energy is put into the system on the short length scales only resulting from rotor interactions, in the circular confinement energy is injected on the short and long length scales simultaneously. The energy injection on long length, *i.e.*, short q scales comes from the systematic velocity fluctuations initiated by the edge flow which then propagate into the container centre. Consequently, the power-law decay expected from the inverse cascade in bulk cannot be established freely and the resulting decay is different from its bulk analogue, as is exemplarily shown in figure 5.10b for a system of size

$R_o = 50\sigma$ still clearly showing the emergence of a power-law. However, if the energy injection on the small and large q scales are well separated, then the influences of the systematic velocity fluctuations initiated by the edge flow do not reach deep enough into the container and an inverse energy cascade with a scaling behaviour $\propto q^{-5/3}$ on intermediate q scales, emanating from the large q scales, is formed, reminiscent of the bulk dynamics.

5.4. SUMMARY

The breaking of translational and introduction of rotational symmetry in a rotor fluid bearing rotational viscosity η_R and corresponding rotational stresses leads to the formation of an approximately linear stationary velocity profile into the azimuthal direction around the axis of symmetry which is initiated by an edge flow that viscously propagates into the confinement centre. Unbalanced rotational stresses at the boundary, as a result of entropic density oscillations near boundaries [183, 184], yield corresponding oscillations around the linear velocity profile in the vicinity of the boundary. In return, the oscillating velocity profile leads to modulations in the stationary vorticity profile, such that the presence of odd stresses, *i.e.*, odd viscosity, excites additional density oscillations. Balance of osmotic pressure and odd stresses then leads to a non-equilibrium steady-state modulation of the density profile, which bears a signature of the stationary vorticity field. While the oscillating flow profile has already been reported [151], the non-equilibrium steady-state density modulations owing to odd viscosity are first reported here.

Despite the fact that the stationary velocity profile is on average purely azimuthal, the rotors' trajectories seem to be composed of turbulent eddies of different sizes. Assuming that the dynamics in circular confinement can be regarded as a superposition of the stationary profile and turbulent dynamics, shows that the turbulent contributions bear a power-law decay in the energy spectrum, similar to the bulk dynamics. However, a crucial difference to the bulk turbulent dynamics is that in circular confinement, the turbulent contributions are generated not only on the particle scale at high q numbers, but also on the shortest q numbers, *i.e.*, on length scales of the confinement itself, emanating from the edge flow. Accordingly, the unforced power-law $E_q \propto q^{-5/3}$ as observed in the self-similar dynamics in bulk cannot be established due to constraints from both sides of the spectrum.

Chapter 6

Enhanced transport of microrotors in complex geometries

Typically, confining geometries are associated with hindrance of free diffusion and caging resulting from the obstruction due to the confinement [186–189]. In contrast, for chiral active fluids where symmetry breaking leads to the formation of robust edge flows and net collective dynamics, active turbulent transport can be enhanced by the introduction of boundaries and thus locally directed flows. In a two-dimensional periodic square lattice of fixed obstacles of diameter $2R_\mathrm{i}$ and lattice constant L_obs, depending on the rotor density, the size of the obstacles and the lattice constant, the dynamics exhibit the trivial limits of bulk behaviour for simultaneous $2R_\mathrm{i} \to 0$ and $L_\mathrm{obs} \to \infty$, and of caged dynamics for $2R_\mathrm{i} = L_\mathrm{obs}$. Here, it is shown that at intermediate rotor densities, the active transport varies non-monotonous with the obstacle size and is optimised for $2R_\mathrm{i}/L_\mathrm{obs} \simeq 0.1$. Very recently, it has been reported [150] that a circle swimmer, *i.e.*, a particle moving on chiral, circular trajectories [190], as a realisation of chiral active matter, exhibits either enhanced or diminished transport in a obstacle lattice controlled by the obstacle density ($\propto R_\mathrm{i}^2/L_\mathrm{obs}^2$) and noise in the dynamics. However, here we focus on the emergence of collective rotor dynamics around periodic obstacle geometries, where the pattern of the trajectories of the colloids are not imposed but a direct consequence of the mutual hydrodynamic interactions, instead of the dynamics of single circle swimmers [150].

6.1. Edge flow and enhanced layering

The simulation setup is sketched in figure 6.1a. The coupling between the fluid, the obstacles walls, and the rotors is analogous to chapter 5. The geometry is translationally symmetric into the x and y directions with periodicity L_obs, such that integrated over the distance L_obs no net flow is expected [51, 52]. However, an edge current is created at the obstacle boundaries resulting from the locally broken symmetry in rotor density.

The flow around an isolated obstacle is discussed first, corresponding to the limit of $\Lambda \equiv 2R_\mathrm{i}/L_\mathrm{obs} \to 0$ where the obstacles may be approximated as isolated, such that the flow created at the boundary is approximately equal to the flow of a chiral active fluid around a circular exclusion. This setup is qualitatively related to the flow in a circular container and obeys the same equation in polar representation, *i.e.*, equation (5.3) with solution $v_\varphi(r) = ar + b/r$ where the constants a and b need to be fixed using the

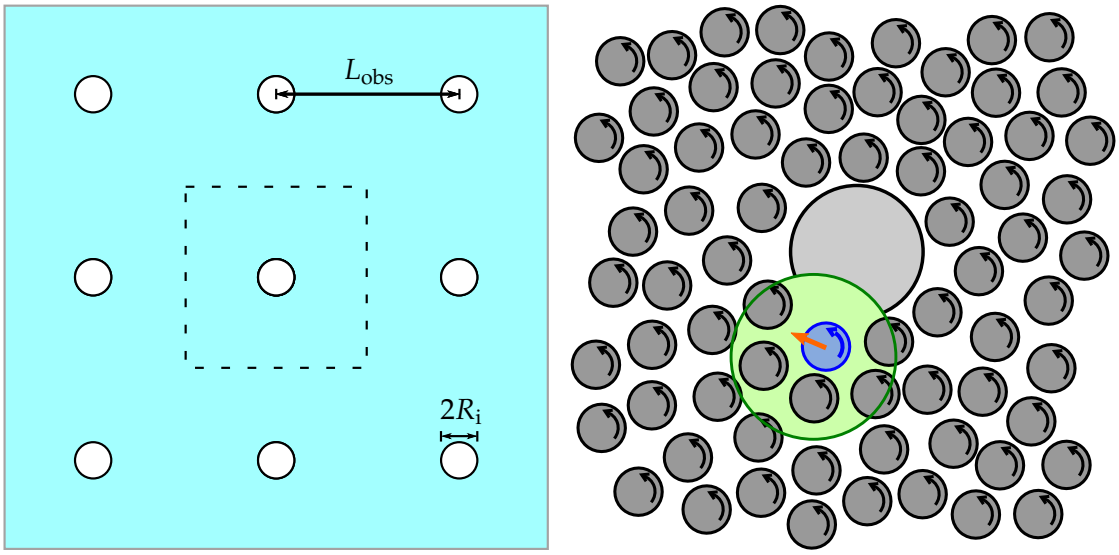

(a) (b)

Figure 6.1: (a) Sketch of the simulation setup in the periodically repeating obstacle geometry. The white circles show the immobile obstacles of diameter $2R_i$. Two neighbouring obstacles are separated by the distance L_{obs}. The two types of simulations of this setup correspond to dynamics in a square domain of size $3L_{obs}$, L_{subs} with 9, 1 obstacles, respectively, each with periodic boundary conditions. The smaller domain is indicated by the dashed line. (b) Illustration of the asymmetric stresses leading to the edge flow.

boundary conditions. Radial exclusion implies $v_\varphi(r \to \infty) = 0$ and a slip boundary is used in order to approximate the condition at the inner boundary, analogous to the discussion in chapter 5. Thus, the outer boundary implies $a = 0$, whereas the inner boundary condition

$$0 = \eta \left\{ \partial_r v_\varphi - \frac{v_\varphi}{r} \right\}_{r=R_i} + \eta_R \left\{ \frac{v_\varphi}{r} + \partial_r v_\varphi - 2\widetilde{\Omega} \right\}_{r=R_i} \tag{6.1}$$

leads to $b = -\eta_R/\eta\, R_i^2 \widetilde{\Omega}$, where $\widetilde{\Omega}$ is again the angular velocity density, and accordingly the induced flow is

$$v_\varphi(r) = -\frac{\eta_R}{\eta} \frac{R_i^2 \widetilde{\Omega}}{r} . \tag{6.2}$$

The collective circulation of the rotor fluid is thus going in the angular direction opposite to the intrinsic rotation which might be surprising at first, but since the dominant contribution to collective rotations in rotor fluids stems from the breaking of symmetry and thus the unidirectional rotational stress experienced by the rotor layers at the obstacle boundary as illustrated in figure 6.1b, the rotation in the opposite direction is induced. Furthermore, v_φ is directly proportional to $\widetilde{\Omega}$, R_i^2, and η_R stemming from the torque experienced by the inner rotor layers which is, for a slip boundary, only opposed by the viscous coupling to the fluid at rest at infinity. However, since in the simulations the MPC solvent is subject to a no-slip boundary at the obstacle surface and at the rotor surfaces, a counteracting torque on the collective rotation arises. Figure 6.2 shows the measured normalised edge flow from simulations in a square simulation

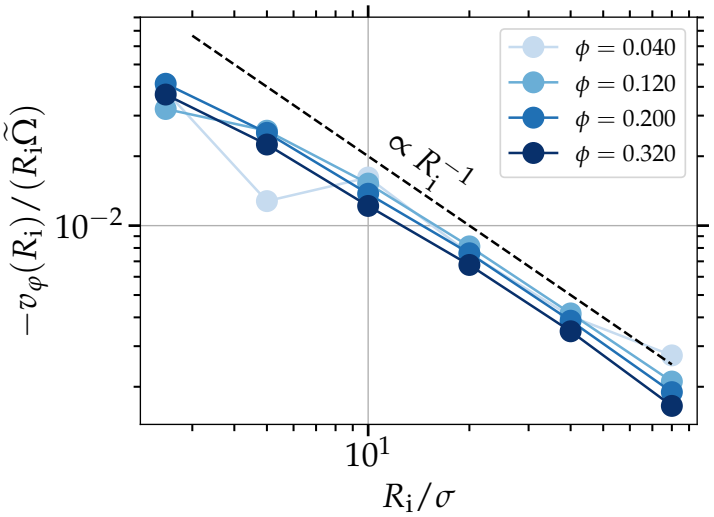

Figure 6.2: Velocity of the edge flow versus R_i at different densities. All simulations have been conducted in a square simulation box with periodic boundary conditions and one obstacle, *i.e.*, $L = L_{obs} = 170\sigma$.

box with periodic boundary conditions and one obstacle, *i.e.*, $L = L_{obs} = 170\sigma$, where v_φ is obtained from an average over the whole range of polar angles. The edge flow from equation (6.2) predicts a linear increase of the induced flow velocity modulus at the obstacle surface with the obstacle size

$$-v_\varphi(R_i)/(R_i\widetilde{\Omega}) = \eta_R/\eta\,. \tag{6.3}$$

Measurements with obstacles of different sizes R_i show that the reduced flow keeps constant for varying R_i and also for various densities. This results from the increasing friction between the rotor fluid and the obstacle surface which linearly grows with the surface of the obstacle $2\pi R_i$, while in equation (6.2) it is neglected. However, if a slip boundary condition between the obstacle surface and the solvent is employed, equation (6.3) holds and this setup can be used in order to determine the elusive rotational viscosity η_R. With increasing density ϕ, $-v_\varphi(R_i)/(R_i\widetilde{\Omega})$ decreases, although the density dependency is divided out by normalisation with the angular velocity density $\widetilde{\Omega}$, because of the density dependence of the effective rotor suspension viscosity $\eta(\phi)$, introduced in chapter 3. Interestingly, for the simulations with $R_i = 80\sigma$, where the periodic boundary conditions imply $\Lambda = 0.94$, and thus only a small channel of width 10σ between two neighbouring obstacles, the resulting $v_\varphi(R_i)$ follows the same trend as for significantly smaller R_i, showing that the edge flow is predominantly determined only by a few rotor layers and the presence of further obstacles has no strong influences on the edge flow.

The presence of the boundary wall of the obstacle induces entropic layering in the rotor fluid which self-enhances resulting from the presence of odd viscosity, analogous to the discussion in section 5.2. Figure 6.3a shows the increase of layering at the obstacle boundary of a rotor fluid (red) with respect to the passive equilibrium colloidal suspension (blue) in the normalised density distributions and figure 6.3c shows the corresponding relative changes. Figures 6.3b and d show how the velocity and vorticity profilesare affected by layering. Comparison of figures 6.3c and d reveals that

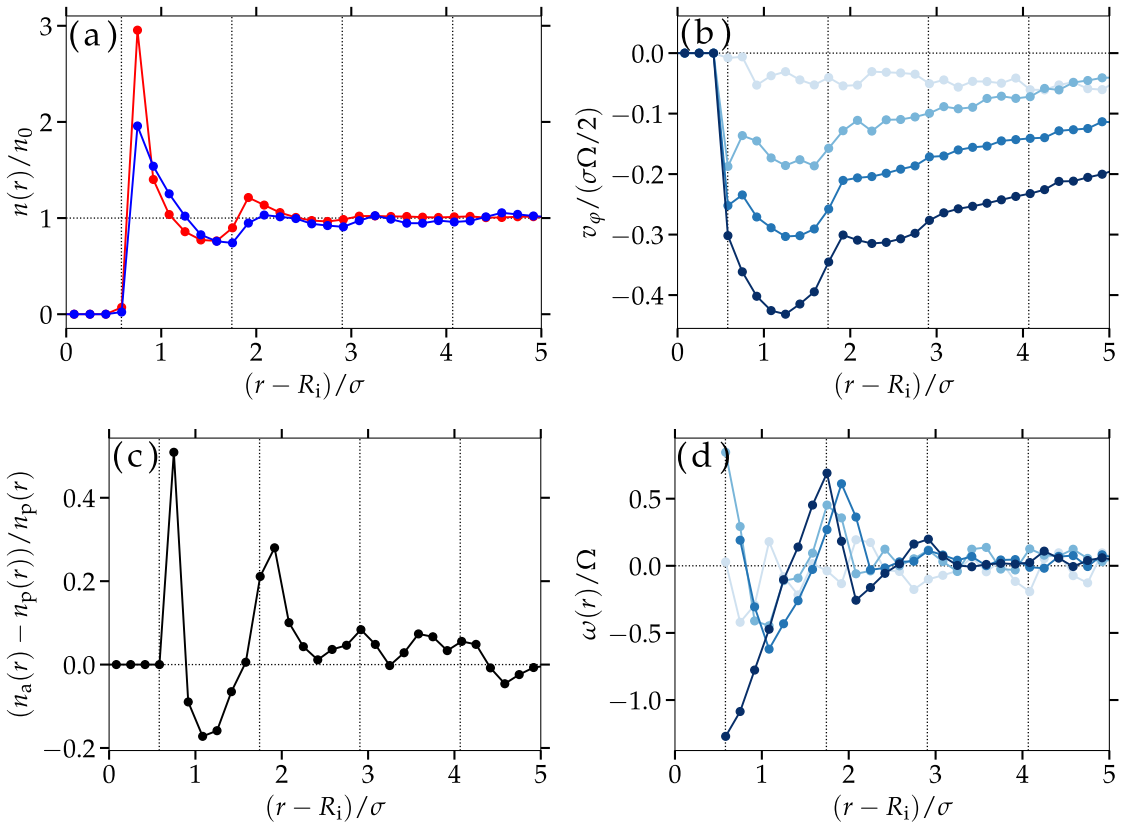

Figure 6.3: Vorticity-density correlations at the obstacle boundary for $\Lambda = 0.06$, $R_i = 5\sigma$, and $L_{obs} = 170\sigma$ obtained from simulations. Dashed vertical lines denote the effective hard core repulsion diameter between the colloid-colloid (σ_*) and colloid-wall interactions ($\sigma_*/2$) (confer appendix A). (a) Radial number density of passive colloids in solution n_p (blue) in comparison to data for rotors n_a (red) at the same density $\phi = 0.32$ normalised with the average value n_0. (b) Velocity profiles in radial dependency from the centre of the obstacle. (c) Changes in the $n(r)$ of the rotor fluid relative to the passive analogue. The difference at $\sigma_*/2$ is set to zero, since the density is here predominantly controlled by the strong repulsion. (d) Normalised vorticity profiles corresponding to (b). Colour coding in (b) and (d) same as in figure 6.2.

the rotor fluid shows rotor accumulation, depletion in regions of positive, negative vorticity, respectively, qualitatively equivalent to the discussion in section 5.2.

6.2. Superposition of active turbulence and systematic flow

The presence of neighbouring obstacles prevents the decay prescribed by equation (6.2) at large distances. Instead, due to symmetry and continuity, the flow needs to be zero on average at the middle point on the connecting line between two obstacles and forms a four tip star-like shape in the area in the middle of four neighbouring obstacles, as is shown in figure 6.4. However, since the rotor dynamics are additionally dictated by the active turbulent behaviour of the rotor fluid and the obtained dynamics may qualitatively be regarded as a superposition of active turbulence and directed flow as indicated in figure 6.5, the measurement of the directed flow becomes increasingly

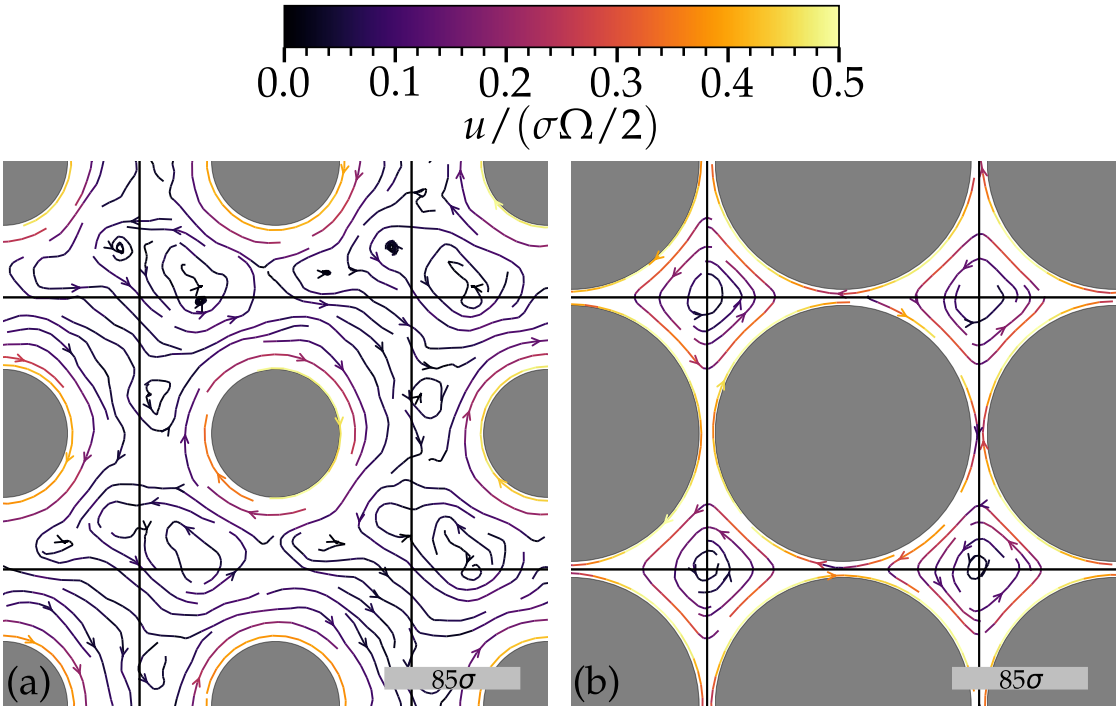

Figure 6.4: Rotor stream lines in a domain of size $L = L_{\text{obs}} = 170\sigma$, *i.e.*, with only one obstacle. The simulation domain is indicated by black lines; each of the domains indicated by the black lines correspond to the same data, *i.e.*, to periodic images. Rotor density is $\phi = 0.32$. (a) $\Lambda = 0.47$. (b) $\Lambda = 0.94$. Obstacles drawn in grey.

difficult far away from the boundaries where it has decayed significantly, such that the flow lines in figure 6.4 show deviations from the symmetric flow induced by the boundaries.

The active turbulent dynamics is influenced by the relative size of the rotor diameter σ, the obstacle radius R_{i}, the separation of obstacles L_{obs} and the system size L. The system size L provides an upper cutoff for the largest possible vortices equivalent to the active turbulence in bulk. On the other hand, increasing Λ means the the relative distance between the obstacles decreases resulting in increasing hindrance of the formation of vortices ranging over the whole system since the obstacle surfaces break vortex formation. The relative ratio of obstacle to rotor size influences the formation of the edge flux according to equation (6.3), because then the rotor fluid cannot be regarded as a continuum. In this thesis, the emphasis is not on this ratio and the rotor continuum limit $2R_{\text{i}}/\sigma \to \infty$ is assumed. The edge flux injects energy into the system on the scale of the size of the obstacles, providing a second energy injection scales for the dynamics in a periodic obstacle lattice, *i.e.*, the rotor and the obstacle scale. The trajectories of rotor dynamics in figure 6.5 show the formation of multi-scale vortices like in bulk and the emergence of jet-like structures at intermediate densities (see figure 6.5c) for $\Lambda = 0.14$ (a)-(d), whereas for $\Lambda = 0.5$ (e)-(h) the vortices and thus the rotor dynamics are predominantly constrained to the area between the obstacles. This behaviour becomes more dominant with increasing Λ, as can be inferred from the time velocity-correlation functions $\langle v(t) \cdot v(0) \rangle$ in figure 6.6, which show an oscillatory behaviour, signature of a rotation of the velocity vector that on average can be associated with the (almost) closed streamlines shown in figure 6.4.

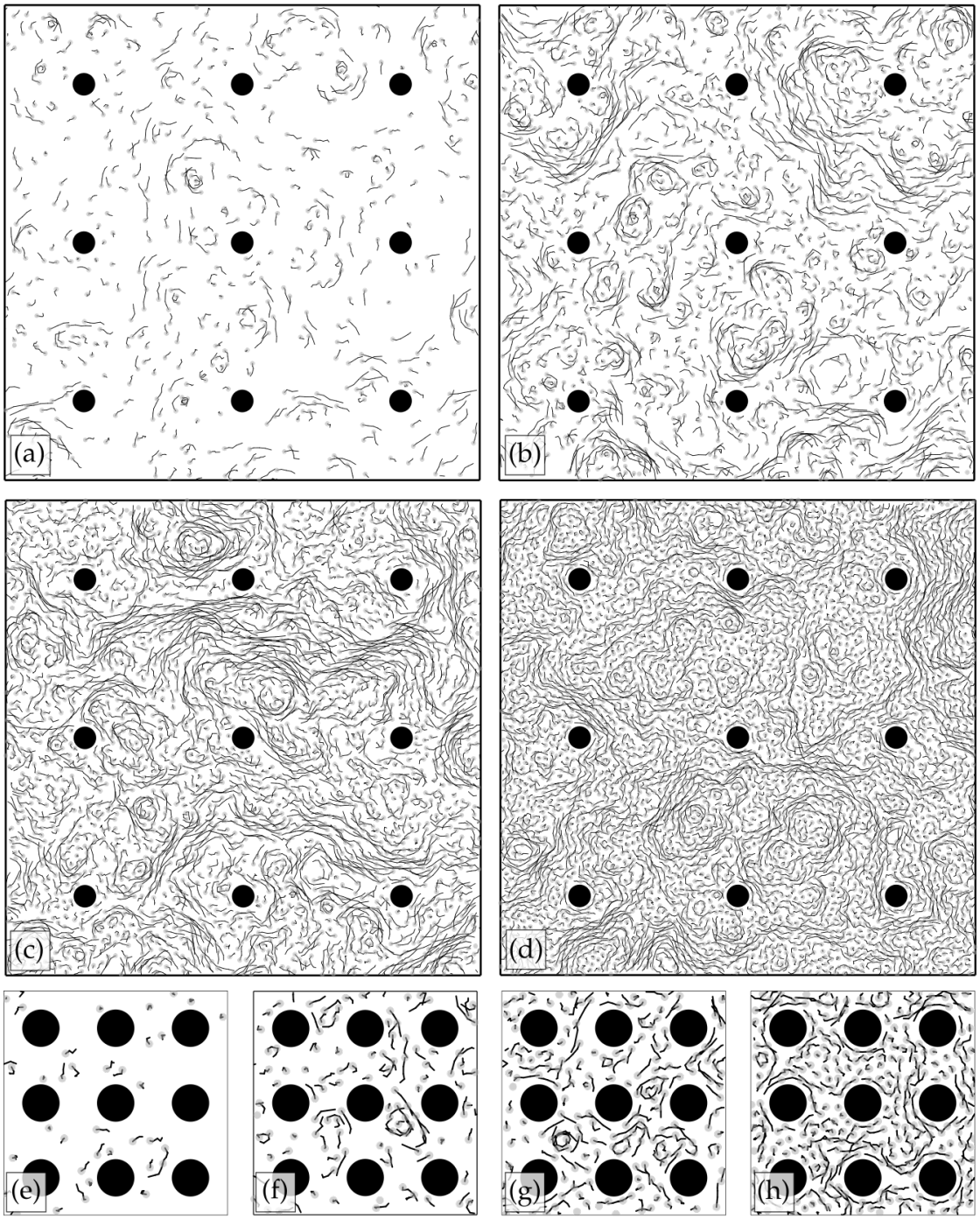

Figure 6.5: Simulation snapshots and superimposed rotor trajectories in systems of size $L = 3L_{\text{obs}} = 105\sigma$ with $\Lambda = 0.14$ (a)-(d), and $L = 3L_{\text{obs}} = 30\sigma$ with $\Lambda = 0.5$ (e)-(h) and periodic boundary conditions. Densities are $\phi = 0.04$ (a) and (e), $\phi = 0.12$ (b) and (f), $\phi = 0.20$ (c) and (g), $\phi = 0.32$ (d) and (h). The trajectories are of length in time $t\Omega/(2\pi) = 3$.

6.3. Edge flow enhances active transport

While for $\Lambda \gtrsim 0.5$ the trajectories of the rotors are effectively constrained or caged by the obstacles, the influence of the generated and directed edge flow on the dynamics

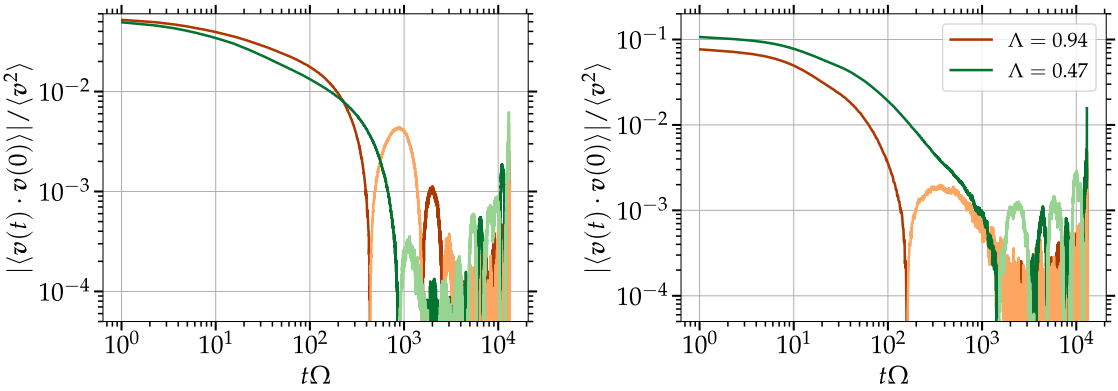

(a) (b)

Figure 6.6: Absolute value of the velocity-correlation function versus normalised time for different values of Λ obtained from time and ensemble averaging in a system of size $L = L_{\text{obs}} = 170\sigma$. Densities are $\phi = 0.32$ (a), corresponding to figure 6.4, and 0.12 (b). Negative values of $\langle \boldsymbol{v}(t) \cdot \boldsymbol{v}(0)\rangle$ are mirrored to the positive domain and drawn in a lighter colour than the corresponding positive values of $\langle \boldsymbol{v}(t) \cdot \boldsymbol{v}(0)\rangle$.

also decreases with decreasing Λ. It is thus of interest to optimise the parameter Λ, acn accordingly the space between obstacles, such that constraints on the trajectories are minimised, while the driving contribution of the edge flow on material transport is maximised.

Figure 6.7a shows the mean-square displacements at different densities in a system with $\Lambda = 0.97$ (confer figure 6.4b) showing caging effects at $t\Omega \approx 10^3$, *i.e.*, the MSD is subdiffusive on the respective timescale. This is because the rotors have already explored the space in between four obstacles and first need to escape through the 10σ wide gap between two obstacles before further space can be explored. The dominant contribution to rotor transport is the edge flow which increases with rotor density as can be seen from equation (6.2). Consequently, the effective diffusion coefficient of the diffusive regime increases with density, as can be inferred from the offset of the extrapolated terminal diffusive regimes in figure 6.7a which increase with density. On the other hand, for $\Lambda = 0.06$ (figure 6.7b) the relatively small size of the obstacles does not induce caging effects. Furthermore, the density dependence of the effective diffusion coefficient of the extrapolated diffusive regime follows a similar dependence as in the bulk dynamics, *i.e.*, it increases with density, reaches a maximum, and decreases by further increase of the density due to the increase of the effective suspension viscosity $\eta(\phi)$.

Figure 6.7c shows the MSD at fixed density for several values of Λ, where the red line with $\Lambda = 0$ corresponds to a system without obstacles for reference, indicating that even at small $\Lambda > 0$, the diffusive rotor transport bears an influence of the presence of the periodically repeating obstacles. The effective collective rotor diffusion coefficient D_{eff}, shown in figure 6.7d emphasises this influence. For $\Lambda \to 0$, D_{eff} approaches the diffusion coefficient D_0 of a corresponding rotor system without obstacles, *i.e.*, a system with $\Lambda = 0$. With increasing Λ, D_{eff} quickly increases and reaches a maximum at $D_{\text{eff}} \simeq 4D_0$ for $\Lambda \simeq 0.1$. It is thus possible to increase the active rotor transport by adding obstacles into the ensemble, where the contribution of energy injection by the induced edge flow dominates over the constrain introduced by the repulsive obstacle surfaces. The edge flux leads to the effective transport of

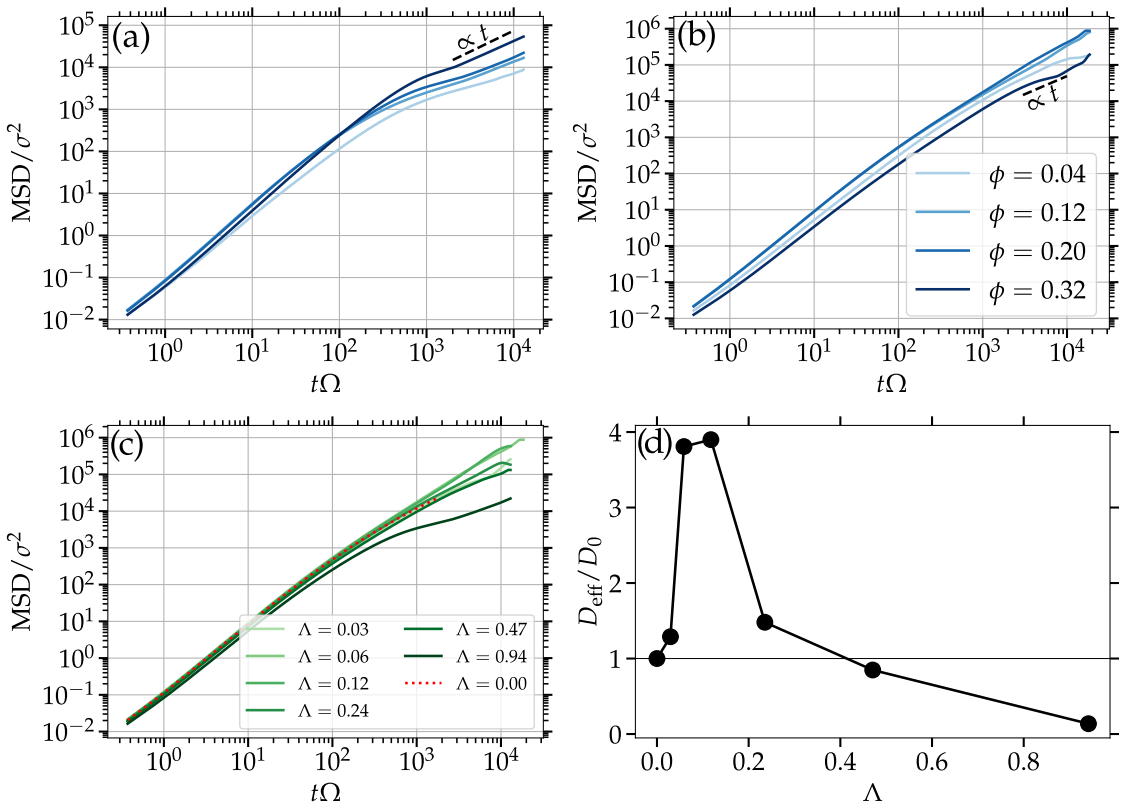

Figure 6.7: Enhanced diffusive transport in a system of size $L = L_{\text{obs}} = 170\sigma$. Mean-square displacements for different values of the density and $\Lambda = 0.97$ (a), $\Lambda = 0.06$ (b), and for fixed density $\phi = 0.20$ and varying Λ (c). Dashed lines in (a) and (b) correspond to diffusive transport. Red data in (c) corresponds to a system without obstacle of the same size. (d) shows effective collective diffusion coefficients obtained from least-square fits to the extrapolated terminal regime in (c).

rotors in the area between the obstacles, shown in figure 6.5c, leading to an increase of diffusive transport by a factor of roughly 4. A further increase of Λ results in a sharp decay of D_{eff}, because the constraining obstacle surfaces become dominant. At roughly $\Lambda \simeq 0.25$, D_{eff} again attains the value D_0 and further increase of Λ results in a relatively soft decay towards vanishing D_{eff} for Λ approaching unity.

6.4. CIRCULAR FLOCKING OF MICROROTORS IN RING-SHAPED CONFINEMENT

A direct consequence of the edge flow in a chiral active fluid with odd viscosity is the enhanced layering at boundaries. Another possible influence of odd viscosity on the dynamics of microrotors in complex geometries has been studied in the scope of the discussions [191] about the results of the experiments presented in [M]. Consider a suspension of microrotors confined between two concentric circular walls, *i.e.*, a ring-shaped or annular confinement. An edge flow into the same angular direction as the rotors intrinsic rotation is induced at the outer wall, and an opposite flow at the inner wall, as shown in figure 6.8a. This behaviour has already been reported in references [51, 52], where in a channel of width $D < 2\sigma$, *i.e.*, two particles cannot pass each other in the channel, this leads to the formation of a net flux along the channel into the direction of flow generated at the outer boundary, because the two generated edge flows are not compensating due to the different curvature at the inner and outer wall. In the current case of $D > 2\sigma$, at intermediate densities different small vortices of sizes up to D emerge. However, with increasing time, the forming vortices merge until all rotors are incorporated into one stable cohesive tank-treading like vortex (see figure 6.8b), which travels in circles through the annulus into the direction of the flow generated at the outer boundary.

Although it was not possible to reproduce the observed circular flocking behaviour with the hydrodynamic simulations in the scope of this thesis, it is believed that the accumulation of rotors in a stable cohesive vortex is caused by the interplay of confinement and density-vorticity correlations due to odd viscosity. Rotors are transported into the centre of the positive vortices that are forming in the ring channel such that the vortices grow upon turning on the rotors intrinsic rotation. The confining walls then additionally stabilise the accumulated vortices, because the walls partially prevent rotors from diffusing out of the vortices, such that the vortex surface through which the rotors can diffuse out is minimised. It is, however, not clear exactly why the thus formed vortex is so stable that eventually all the rotors are incorporated into one single vortex. The net translation along the ring channel then is generated because the edge flows at the inner and outer walls are not compensating, such that the cohesive vortex translates in a tank-treading behaviour through the annulus.

In order to gain deeper understanding of consequences of odd stresses in the described dynamics, hydrodynamic simulations in a parameter range that lays emphasise on the odd stresses in the fluid, *i.e.*, imply a relatively large value of η^{odd}, are suggested to be performed. This can be achieved with multiparticle collision dynamics without the emergence of fluid pumping (appendix C) as explained in the following. The importance of odd stresses in the simulation can be emphasised by decreasing the influence of further contributions, *e.g.*, increasing the Péclet number by decreasing the rotors diffusion. This can be achieved by increasing the fluid density, and accordingly decreasing the rotor diffusion coefficient, which thus emphasises the importance of

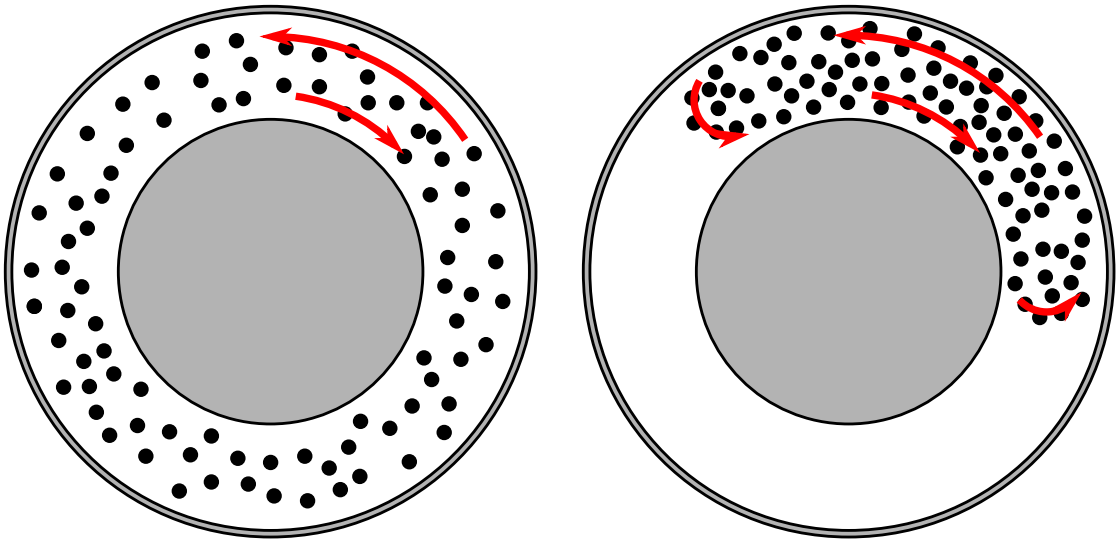

(a) (b)

Figure 6.8: Rotors in annular confinement. (a) Edge flow generation at the inner and outer boundary. (b) Accumulation of rotors and tank-treading dynamics in the confinement.

odd stresses. However, it should be kept in mind that a significant increase of fluid particles renders the simulation computationally very expensive.

Although influences of the substrate friction or from the third dimension, *e.g.*, due to misalignment between the axis of rotation of the microrods and the z-axis, are expected to be negligible, it cannot be ruled out yet, that the observed circular flocking can only be observed in a three-dimensional model.

6.5. Summary

In this chapter, the influence of the introduction of a periodic array of obstacles into the dynamics of rotor ensembles is explained. As a result of local symmetry breaking at the obstacle boundary, an edge flux of magnitude dominated by the viscous coupling of the rotors to the obstacle surface is initiated. For a slip boundary condition between the obstacle surface and the solvent, this edge flux may be employed to measure the rotational viscosity η_r. Symmetry and continuity of the flow then implies a stationary four tip star-like pattern for the average flow which becomes dominant for cases where caging is dominating. The interactions between the obstacle boundary and the rotors together with the stationary flow and thus viscosity pattern imply a self-enhanced boundary layering due to the presence of odd viscosity, similar to the dynamics in circular confinement. This behaviour is expected at any wall in a chiral active fluid. Whether the interplay of odd stresses and complex geometries can lead to the formation of a stable flocking vortex, as observed in the experiments [191], is still a question under investigation.

The collective rotor dynamics can qualitatively be regarded as a superposition of active turbulence and directed motion due to the edge flow. Similar to the active turbulent dynamics in circular confinement, the presence of the obstacles and thus the edge flow implies energy injection on the length scale ΛL_{obs}, *i.e.*, the obstacle size. Furthermore, the formation of active turbulent vortices and thus the rotor dynamics

itself is restricted by the obstacles, an influence which disappears for $\Lambda \to 0$ and becomes predominant for $\Lambda \to 1$. A quantitative analysis of the active turbulent dynamics, *e.g.*, velocity correlation functions or energy spectra, is still lacking, but promises to provide insight into active turbulence on the microscale with energy input on two scales, where the input on the obstacle scale can be varied over a wide range by employing differently sized obstacles. While the influence of the obstacles acts on the one hand constraining, but on the other hand provides an energy injection to the system, the effective diffusivity of the active turbulent rotor transport increases with increasing Λ, reaches a maximum at $\Lambda \simeq 0.1$, and decreases upon further increase of Λ. A similar behaviour was found recently for the dynamics of a chiral Brownian circle swimmer, where the maximum of the diffusivity is reached for $\Lambda \simeq 0.17$ [150]. For the circle swimmer, however, the dominant effect is the size of the diameter of the circular trajectory, which is imposed. In this thesis, the vortical trajectories of the rotors are due to interactions among rotors and with the walls, and are thus a direct consequence of the system, and do not have to be imposed into the model. Since the rotor density explicitly has an influence on the rotors' trajectories, a further analysis of the dependence of the effective diffusion coefficient on Λ for different densities should be performed in the future.

Chapter 7

Binary mixtures of microrotors and passive particles—active turbulent mixing and vortex driven segregation

A potential application of active turbulence is the intentional mixing on the microscale [97], *e.g.*, to effectively spread nutrients or drugs, modelled as inert particles, in a given domain. In mixtures of rotating, counter-rotating, and inert particles, cooperative effects are expected [192, 193], such as the formation of dynamical lanes, vortices, clusters, and gas-like phases [194]. Here, it is shown that translational actuation of rotors and passive particles is only induced by nearby rotors such that the actuated velocity of both species increases with the rotor density, similar to a pure rotor suspension. Nevertheless, the inert particles contribute to the increase of the effective solvent viscosity such that the dynamics of a binary mixture is reminiscent of a pure rotor ensemble depending on both, rotor and total density. The mixture thus shows the emergence of active turbulence at intermediate densities. The rotors mutually exert rotational and odd stresses leading to the formation of vortices where the rotors are dragged into the gradients of vorticity due to the presence of odd viscosity. The passive particles in return are transported into the opposite direction resulting from the increasing pressure in the regions of high rotor density. While in the ensemble dynamics with dynamic vortex formation and dispersion, the emergence odd stresses does not prevent the active turbulent mixing of rotors and passive particles, in systems of sustained vortical flow, vortex driven segregation is observed.

7.1. Counter-rotation of passive particles

Consider a binary mixture of N_a rotationally actuated rotors of diameter σ at angular velocity Ω and packing fraction ϕ_a and N_p passive inert particles of diameter σ_p, angular velocity Ω_p, with ϕ_p, where $\phi_a = N_a\pi(\sigma/2)^2/L^2$ and ϕ_p accordingly. The inert particles are passive in the sense that no velocity or angular velocity is enforced externally, but the particles are not in equilibrium because of the exposure to the nonequilibrium environment. For convenience, the size ration of rotor to passive particle diameter is defined as the aspect ratio $\kappa \equiv \sigma_p/\sigma$ and the ratio of area covered by rotors ϕ_a to the totally covered area $\phi = \phi_a + \phi_p$ as $\psi \equiv \phi_a/\phi$, which will further be referred to

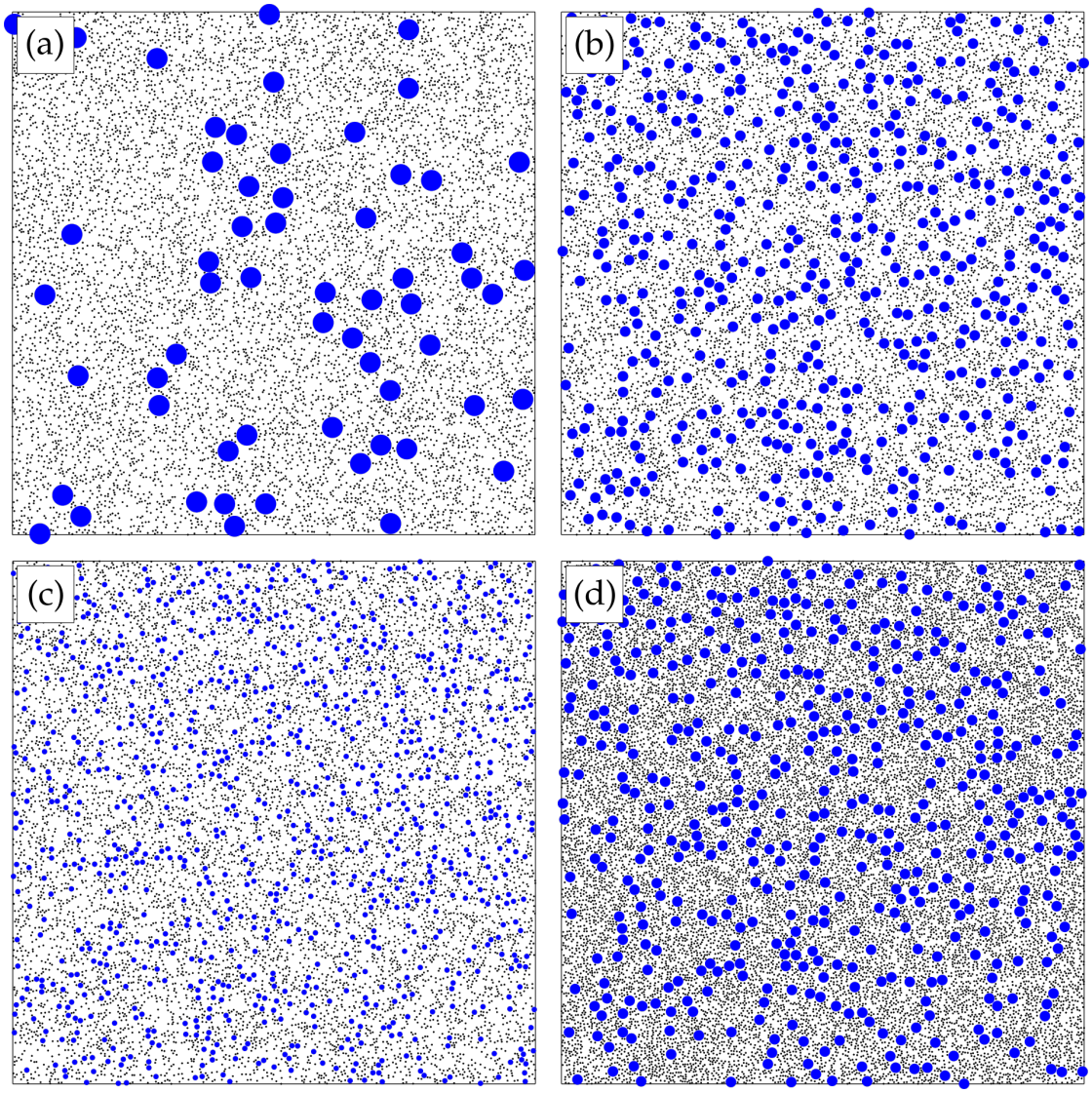

Figure 7.1: Binary mixture simulation snapshots in bulk at $\psi = 0.5$. Rotors in black, passive colloids in blue. (a) $\kappa = 12$ and $\phi = 0.15$; (b) $\kappa = 6$ and $\phi = 0.15$; (c) $\kappa = 3$ and $\phi = 0.15$; (d) $\kappa = 6$ and $\phi = 0.30$.

as the rotor fraction. The translational velocity of a rotor is determined by the flows induced by the angular velocity of its neighbouring rotors instead of its own angular velocity. In this way, studying individual trajectories will not make possible to conclude whether the trajectory belongs to one of the active or passive colloids. However, for fixed κ, the ensemble dynamics exhibits the following trivial limits depending on activity. For $\psi \to 0$ the ensemble only consists out of passive colloids and thus fulfils equilibrium statistical mechanics. On the other hand, for $\psi \to 1$ all involved particles will be rotors, such that the dynamics will be the same as in chapter 3. The nontrivial behaviour for $0 < \psi < 1$ is the subject of this chapter.

Four simulation snapshots of binary mixtures of varying κ are shown in figure 7.1. A single inert particle in a rotor suspension may be regarded as an obstacle that is free to move and free to rotate, implying a rotational edge flow in the opposite direction as the rotor's intrinsic angular velocity, as has been discussed in chapter 6. Resulting from

the viscous coupling of the passive particles to the solvent, the rotors drag the passive particle to rotate with resulting angular velocity Ω_p opposite to that of the rotors Ω. Figure 7.2a shows Ω_p normalised by the input frequency Ω versus the rotor fraction ψ for a system of $\kappa = 1$. The absolute value of Ω_p increases monotonously with ψ and ϕ. For $\psi \lesssim 1$, a passive colloid only encounters rotors, which perform the circulation opposite to the input Ω around the passive particle imposing $\Omega_p < 0$. On the other hand, for $\psi \gtrsim 0$ the passive particles rarely encounter rotors and predominantly experience mutual friction between the passive particles, such that the driving of Ω_p is diminished, thus explaining the monotonous behaviour in ψ. The increase of $|\Omega_p|$ with ϕ results from the associated decreasing average interaction distance between the particles. The inset in figure 7.2a shows that this increase is in accordance with equation (6.2), *i.e.*, the flow around an obstacle (or passive particle) and consequently its angular velocity is proportional to the angular momentum density $\widetilde{\Omega}$, which for fixed ψ is proportional to ϕ. Accordingly, a data collapse is obtained for $\Omega_p/(\Omega\phi)$. The lowest density $\phi = 0.007$ does not obey this data collapse, which can be attributed to the fact that at low density the system is capable of large density inhomogeneities such that $\langle\Omega_p\rangle$ is dominated by next neighbour interactions imposed by the random initial conditions. However, also the data for $\phi = 0.007$ is expected to fall on the same line for a much longer measurement, where the whole phase space is sampled.

Additionally, equation (6.2) shows a dependency of the flow around the obstacle or passive particle on the diameter σ_p, such that the absolute value of Ω_p is expected to increase with increasing σ_p. This dependency is shown in figure 7.2b for fixed ϕ_a, ϕ_p, and σ, showing that $|\Omega_p|$ increases with κ. However, it should be noted that the exact scaling with κ does not coincide with equation (6.2), since the assumption in the calculation of equation (6.2) of a slip wall is not valid for the boundary condition on the surface of the passive particles, but the qualitative behaviour, *i.e.*, $|\Omega_p|$ increases with κ, is the same similar to the discussion in chapter 6. Note that the passive particles display on average a rotary motion. To conclude, it is important to underline that no energy is injected by this rotation, as is the case for the actuated rotation of the rotors. Instead, the passive particles show the emergence of a net rotation due to the coupling to the non-equilibrium solvent which rotates around the passive particles.

7.2. ACTIVE TRANSPORT OF PASSIVE PARTICLES

Employing the linearity of the Stokes equation and the results of Faxén's law (chapter 2), the translational dynamics of the passive and active colloids is only prescribed by the rotor density ϕ_a, because only the rotors induce active flows that advect other particles. The actuated velocity of rotors and passive particles obtained from least-square fits of the mean-square displacements according to equation (1.18), analogous to section 3.1, thus follows $v_a \propto \sqrt{\phi_a}$ at low densities ϕ. However, here the increase of momentum dissipation with increasing rotor density due to the effective fluid viscosity $\eta(\phi)$ is caused by both species, not only by the rotors. Accordingly, the active velocity is expected to follow

$$v_a(\phi_a, \phi) \simeq \Omega\sigma(1 - \phi/\phi_{cp})^{2\phi_{cp}}\sqrt{\phi_a/\pi}\,, \tag{7.1}$$

which is very similar to the behaviour obtained in chapter 3, but here the viscosity increase is controlled by ϕ and the driving advection by ϕ_a. Figure 7.3a shows the measured v_a versus the rotor density ϕ_a for different fixed values of rotor fraction ψ, and $\kappa = 1$ displaying qualitative agreement with the above reasoning. For $\psi = 0.9$ and

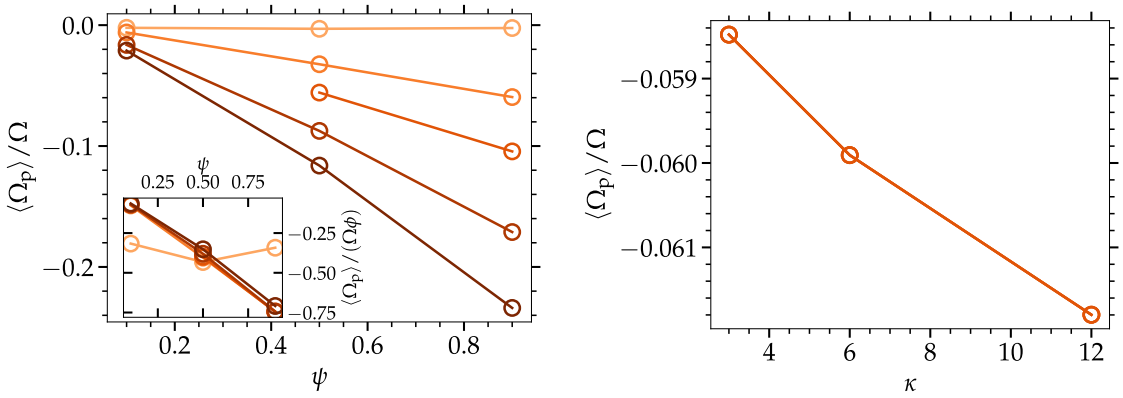

(a) (b)

Figure 7.2: Normalised average angular velocity of the passive particles $\langle\Omega_p\rangle$. (a) $\langle\Omega_p\rangle$ versus rotor fraction ψ for fixed $\kappa = 1$, scale of oranges indicating increasing overall density $\phi = 0.007, 0.08, 0.14, 0.23, 0.32$ (from top to bottom). Inset: Same data additionally normalised by rotor density ϕ. (b) $\langle\Omega_p\rangle$ versus aspect ratio κ for $\psi = 0.5$ and $\phi = 0.15$.

$\psi = 1$, $v_a(\phi_a)$ almost coincide even for large ϕ_a, because the increase of the effective solvent viscosity is here predominantly or only caused by rotors. For $\psi = 0.1$, the actuated velocity $v_a(\phi_a)$ decreases due to the increasing density of passive particles and accompanied increase in the effective viscosity, which is already dominant at $\phi_a \simeq 0.05$. This rotor density for $\psi = 0.1$ corresponds to $\phi \simeq 0.5$ where the increase in $\eta(\phi)$ is expected to dominate, as can be inferred from the line corresponding to $\psi = 1$ at $\phi = \phi_a = 0.5$. Accordingly, the position of the maximum of v_a depends only on the total density ϕ and is shifted to smaller ϕ_a for decreasing ψ.

Extrapolated from the behaviour of v_a of the mixture, self-similar active turbulence is also expected for a binary mixture. However, since in the limit of $\phi_a \to 0$ the mutual rotor actuation decreases and the colloids primarily act like Brownian particles, active turbulence will not emerge for $\psi \to 0$, whereas for $\psi \to 1$ active turbulence as in the rotor fluid will emerge. The energy spectra E_q of binary mixture dynamics are displayed in figure 7.3b for $\phi = 0.23$, $\kappa = 1$, and $\psi = 0.1, 0.5, 0.9$, *i.e.*, $\phi_a = 0.023, 0.115, 0.207$. The mutual steric interactions of rotors at density $\phi = 0.23$ do not prevent the formation of vortices of all sizes, as can be seen in chapter 3. Thus, active turbulence is realised for sufficiently high values of ψ. A self-similar energy spectrum is obtained for $\psi = 0.5$ and $\psi = 0.9$, similar to the pure rotor fluids at the respective densities $\phi = \phi_a$. For $\psi = 0.1$, the mutual actuation of the rotors is not strong enough to obtain self-similar active turbulence, similar to the case of a pure rotor fluid for $\phi \to 0$.

7.3. Segregation due to odd viscosity

The rotors inject angular momentum into the fluid and the system exhibits odd viscosity η^{odd} as discussed in chapter 3. However, interactions between passive particles do not give rise to odd stresses, and even the interactions between passive particles and rotors do not give rise to odd viscosity as the interactions between only rotors do. The rotor-generated mutual flows lead to multi-vortex formation, such that the odd viscosity stemming from the rotor interactions leads to the associated effective

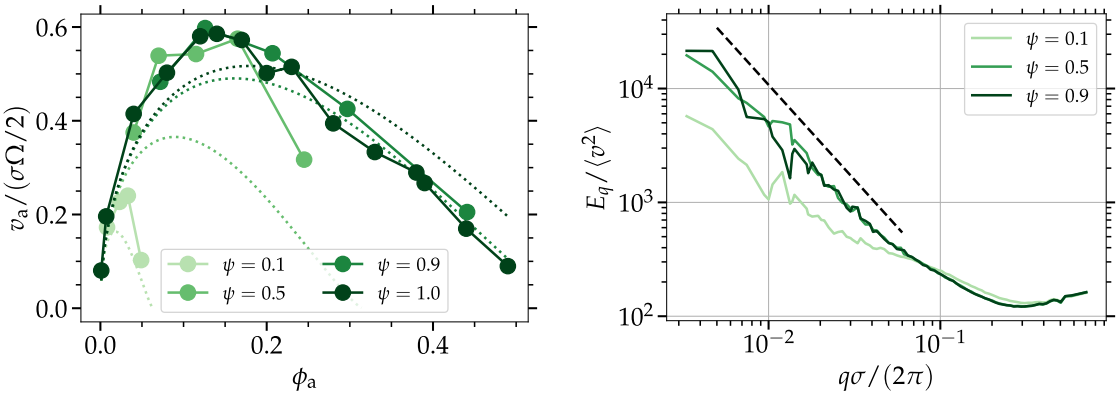

(a) (b)

Figure 7.3: Dynamics of a binary mixture with $\kappa = 1$ for different rotor fractions. (a) Actuated velocity v_a obtained from least-square fits of the mean-square displacements according to equation (1.18) (symbols), and the corresponding $v_a(\phi_a, \phi)$ with dashed lines as calculated from equation (7.1), all multiplied with the fit factor of 3.3 introduced in figure 3.3. (b) Energy spectra at $\phi = 0.23$. The dashed line corresponds to a $q^{-5/3}$ power-law. Positions and velocities of rotors and passive particles are considered in both subplots.

pressure $p^{\text{eff}} = p - \eta^{\text{odd}}\omega$ experienced by the rotors. Consequently, a binary mixture shows the presence of density-vorticity correlations formed by the rotors, *i.e.*, vortices of rotors form in which the rotors experience stresses pointing into the centre of circulation, *i.e.*, $\partial_\alpha\omega$. The odd stresses are then balanced by the finite compressibility and the counteracting pressure increase associated with compression leading to a (temporary) stationary density distribution. The strength of the odd stresses is directly proportional to the odd viscosity provided by the rotors $\eta^{\text{odd}} \propto \phi_a$. On the other hand, the passive particles predominantly feel the pressure increase associated with the increasing rotor density, but not the odd stresses directly. Therefore, passive particles are transported out of the regions of high rotor density and consequently transported opposite to the gradient of vorticity, *i.e.*, $-\partial_\alpha\omega$, to the minima of vorticity.

Figure 7.4 shows simulation snapshots and corresponding vorticity fields where the passive particles' positions are highlighted as bullets. It is observable that passive particles accumulate in the areas of negative vorticity in figure 7.4a-d, for $\kappa > 1$. The same effect, although less pronounced, is also present for $\kappa = 1$, as can be inferred from figure 7.4e-f. In order to understand this effect in more detail, the average local passive particle relative density change $\Delta\phi_p/\phi_p \equiv (\phi_p^{\text{loc}} - \phi_p)/\phi_p$ is plotted against the local vorticity in figure 7.5, where ϕ_p^{loc} is the packing fraction of passive particles in square bins of edge length 12σ, where the same grid has been used in order to obtain the vorticity fields. For all parameter values κ, ψ, and ϕ, the accumulation of passive particles in the regions of negative vorticity is observed, *i.e.*, $\langle\Delta\phi_p\rangle_{\omega<0} > 0$. Figure 7.5a shows that the relative density changes of passive particles increases with increasing rotor fraction ψ. This results from the increase in odd viscosity with increasing rotor density, *i.e.*, $\eta^{\text{odd}} \propto \phi_a$, which is equivalent to $\eta^{\text{odd}} \propto \psi$ for constant ϕ, while the compressibility of the suspension at overall density ϕ for varying ψ remains fixed here. Moreover, the normalisation of the density variations in the inset in figure 7.5a indicates that a data collapse can be obtained by dividing out ψ implying that the extent of the relative density changes is proportional to η^{odd}. Nevertheless, for small rotor

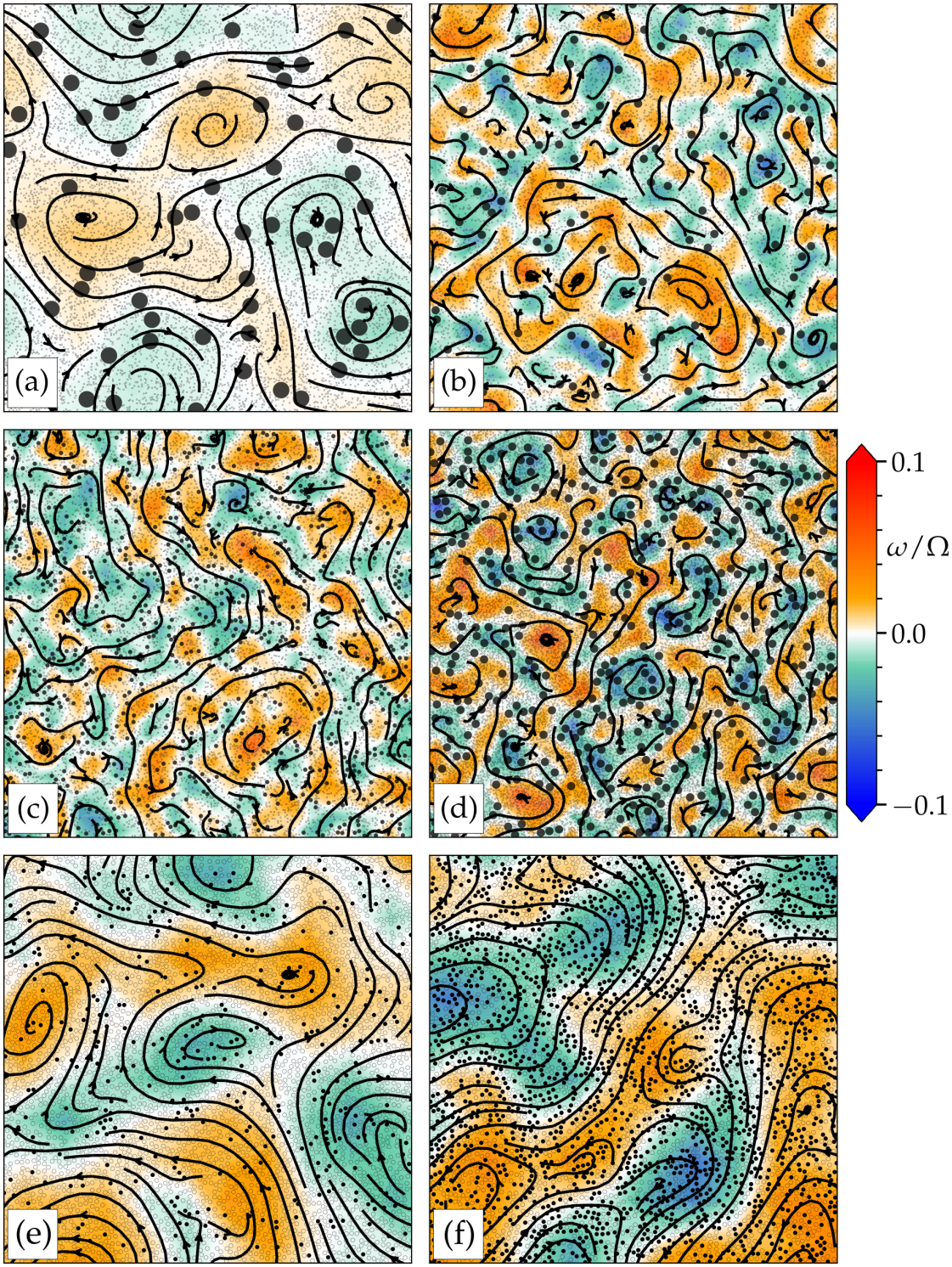

Figure 7.4: Vorticity fields of binary mixtures with superimposed streamlines. Rotors are indicated as small black circles, passive particles are drawn as black bullets. (a) - (d) shows whole simulation domain of size $L^2 = (300\sigma)^2$, whereas (e) - (f) shows a portion of size $L^2 = (100\sigma)^2$. (a) $\kappa = 12$, $\phi = 0.15$, and $\psi = 0.5$; (b) $\kappa = 6$, $\phi = 0.11$, and $\psi = 0.66$; (c) $\kappa = 3$, $\phi = 0.15$, and $\psi = 0.5$; (d) $\kappa = 6$, $\phi = 0.30$, and $\psi = 0.5$; (e) $\kappa = 1$, $\phi = 0.33$, and $\psi = 0.9$; (f) $\kappa = 1$, $\phi = 0.33$, and $\psi = 0.5$.

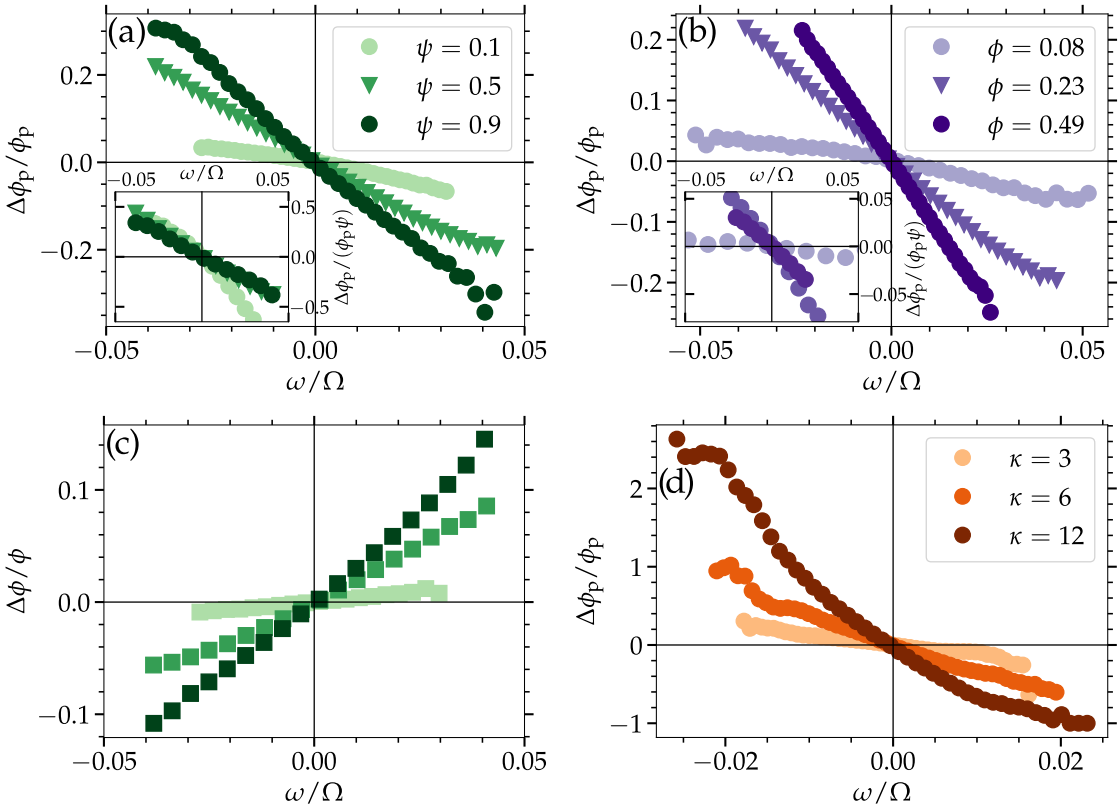

Figure 7.5: Normalised local density variations versus vorticity. (a), (b) and (d) local passive particle density variations. (c) local density variations of the mixture. Parameters are (a) $\kappa = 1$, $\phi = 0.23$, (b) $\kappa = 1$, $\psi = 0.5$, (c) $\kappa = 1$, $\phi = 0.23$, (d) $\phi = 0.15$, $\psi = 0.5$, inset of (b) $\kappa = 1$, $\psi = 0.1$. Inset of (a) shows data from (a) additionally normalised with the rotor fraction ψ. Triangular symbols in (a) and (b) show same data.

fractions ψ, the data shows deviations from the proportionality, *i.e.*, the deviations from the data collapse for $\psi = 0.1$ for $\Delta\phi < 0$ in the inset in figure 7.5a, because the areas of positive vorticity are predominantly populated by rotors at $\psi \to 0$, such that the minimum $\Delta\phi_p/\phi_p \to -1$ is reached quickly. But similar to equation (3.6), the proportionality of the negative slope of $\Delta\phi_p/\phi_p$ to η^{odd} is only expected to hold for small density variations, *i.e.*, in the regime of linear response. For fixed ψ and increasing ϕ, the extent of the relative density change increases (figure 7.5b), although also the compressibility of the passive particles decreases with increasing ϕ. However, the relative density increase associated with $\Delta\phi_p$ is not necessarily a result of compression, but is also realised by segregation. This means that the passive particles of average density ϕ_p can pack roughly as densely as ϕ, when the rotors are absent in the respective area. A decrease of the slope of $-\Delta\phi_p/\phi_p$ is nevertheless associated for $\psi \to 0$, *i.e.*, in the limit of a system consisting only of one species, *i.e.*, passive particles, such that no segregation can be realised, as can be inferred from the inset in figure 7.5b, where the dependence of the relative density changes shows to be non-monotonous in ϕ, resulting from the interplay of increasing rotor density and compressibility.

The overall density changes of both, rotors and passive particles, $\Delta\phi/\phi$ in figure 7.5c shows that the total density ϕ is increased in the areas of positive vorticity implying that the relative density changes of rotors and passive particles are not compensating. That is, the effective pressure $p^{\text{eff}} = p - \eta^{\text{odd}}\omega$ experienced by the rotors

is not equal to the resulting pressure experienced by the passive particles. Consequently, the odd viscosity value cannot be directly inferred from the slopes in figures 7.5a and b. In order to explicitly refer the strength of the relative density changes of the passive particles, the full density changes of both, passive particles and rotors, *i.e.*, $\Delta\phi/\phi = \Delta\phi_a/\phi + \Delta\phi_p/\phi = (A+B)\omega = C\omega$, and the relations of the constants A, B, and C to the odd viscosity of the pure rotor fluid at density ϕ_a have to be worked out in the future. Nevertheless, the dynamics of passive particles in a chiral active fluid can be used in order to show the presence and relative importance of odd viscosity compared to related systems.

For increasing aspect ratio κ the same behaviour $\langle\Delta\phi_p\rangle\big|_{\omega<0} > 0$ is observed as shown in figure 7.5d. However, a reliable measurement of the vorticity and density fields becomes increasingly difficult for increasing κ. This is because the square bins used for coarse-graining the colloid density and vorticity fields on the one hand should be significantly bigger than the passive particles such that the density inhomogeneities are decently obtained, but on the other hand should be considerably smaller than the system size L, because the coarse-grained velocity for a binning size $l_0 \to L$ results in the centre of mass velocity of the whole system, which is zero. [1] In order to quantitatively compare measurements of the relative density changes for a wide range of κ-values, the simulation domain has to be increased significantly, in order to allow for a binning length l_0 with $\sigma_p \ll l_0 \ll L$, valid for all aspect ratios κ simultaneously. Due to depletion interactions [195], there is an entropic attraction between the passive particles, acting on relative distances $r < \sigma + \sigma_p$, which might give additional stability of the density changes, but most likely this is not a significant contribution to the formation of the relative density changes due to the short-ranged character of the attraction.

The transport of rotors and passive particles towards positive and negative vorticity, respectively, is controlled by the momentum diffusivity resulting from odd viscosity ν^{odd}. This process is opposed by the colloids' diffusion controlled by the diffusion coefficient D. Additionally, the dynamic formation and dispersion of vortices in the ensemble makes that the colloids are dynamically moving into different vortices, such that full segregation is prevented. However, in a system of high density ϕ and a correspondingly reduced diffusion coefficient [173], the relative density changes due to the odd stresses intensify while the system evolves leading to growing vortices, until eventually the system is covered by one big and stable positive vortex rotating into the direction of the input frequency of the rotors, and a counter-rotating vortex resulting from continuity and the periodic boundary conditions. The stability of this vortex then implies that rotors are constantly experiencing the stress forces pointing into the centre of the vortex, and the passive particles are consequently transported out of the vortex, *i.e.*, into the direction of the counter-rotating area, leading to segregation of rotors and passive particles. Figure 7.6 shows the evolution of vorticity and passive particle density fields for a binary mixture of $\phi = 0.49$ and $\psi = 0.5$. The areas of positive vorticity clearly tend to be depleted from passive particles, indicating segregation.

[1] For the symbols in figure 7.5d, square bins of length 37.5σ were chosen, because using the same bin size as for the remaining plots in figure 7.5 would predominantly capture the flow of the rotors around the large and slow passive particles, especially for $\kappa = 12$, such that the flow similar to the flow around an obstacle as in chapter 6 yields negative vorticity around the passive particles. Accordingly, a peak, or plateau behaviour would emerge in $\Delta\phi_p/\phi_p$ at negative vorticity. However, the important contribution to the relative density changes is given by the vortices emerging from the rotor dynamics, which is captured by the larger bins, which on the other hand lead to smaller values of the vorticity.

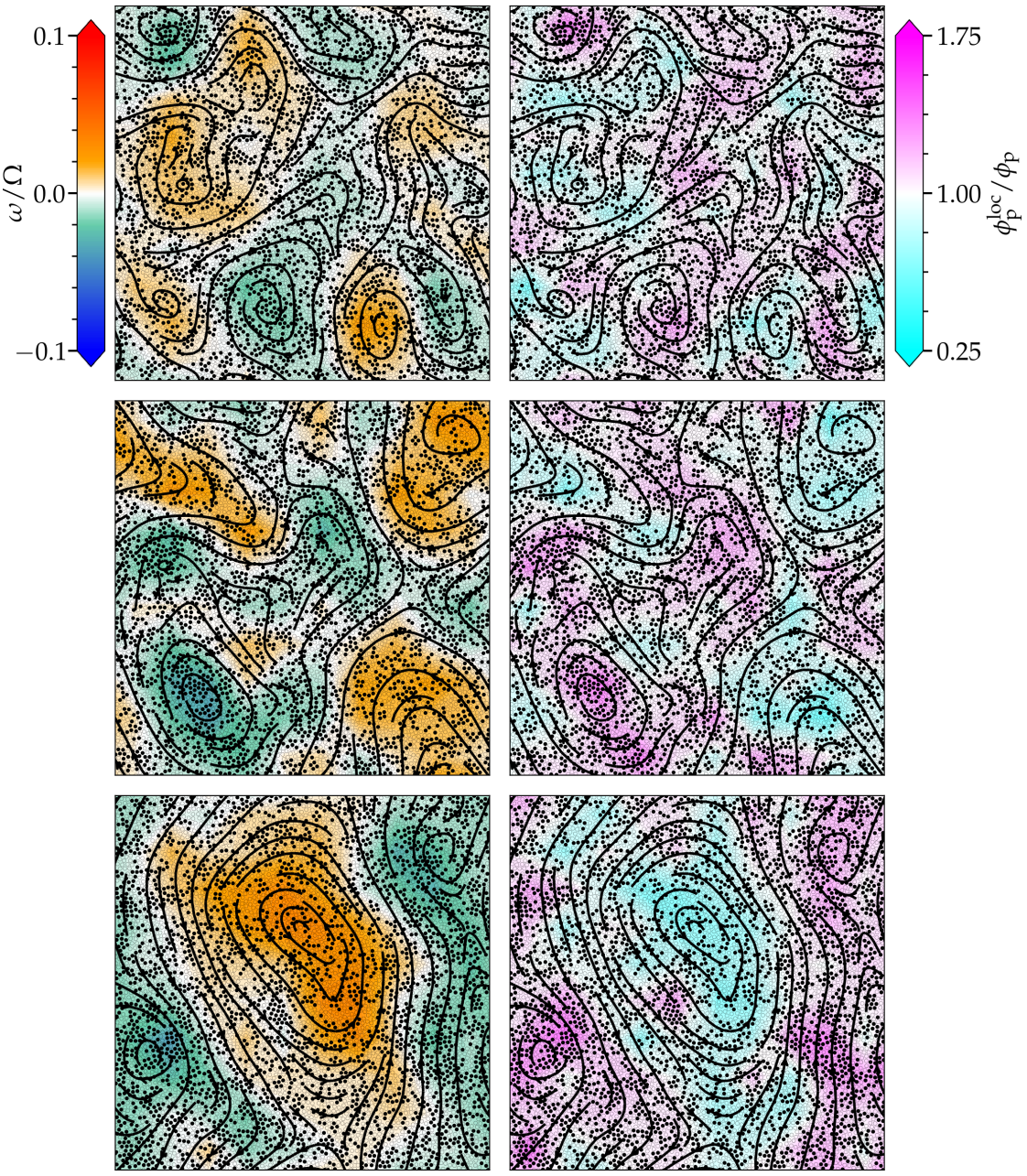

Figure 7.6: Evolution of mixture vorticity fields (left) and corresponding passive particle density fields (right) and superimposed streamlines. Times after initialisation are $t\Omega = 3.7 \times 10^2$ (top row), $t\Omega = 3.7 \times 10^3$ (middle row), $t\Omega = 1.9 \times 10^4$ (bottom row).

7.4. SUMMARY

Rotors inject vorticity into the solvent and suspended active and passive colloids are advected with the induced flows. The passive particles do not inject vorticity into the solvent, although showing a net rotational motion into the direction opposite to the rotors' imposed rotation, as the result of a circular flow around the passive particles imposed by the rotors. Since both, rotors and passive particles are advected by the flows induced by the rotors, the translational dynamics of a binary mixture is controlled by the density of rotating particles, such that the dynamics of all col-

loids can in a mean-field manner effectively be described within the active Brownian particle model depending on the rotor density, similar to section 3.1. However, the effective suspension viscosity increases with increasing density, but here both species contribute, such that the extend of the momentum dissipation depends on the total density ϕ. The collective dynamics of the mixture shows active turbulence, at intermediate rotor densities, and for low enough total densities such that the formation of multi-scale vortices is not prevented by the mutual steric interactions. The dispersion and transport of passive colloids in a suspension of hydrodynamic microrotors can thus be effectively described by a rotor fluid of a total density equal to the density of rotors in the mixture, as long as the steric interactions introduced by the passive particles do not play an important role.

Odd stresses do on average not arise between passive particles, but between the rotors. The correlations of density and vorticity due to odd viscosity imply the accumulation of rotors in the centre of vortices rotating into the same direction as the rotors' intrinsic angular velocity. Consequently, the passive particles are transported out of the respective regions due to the increased pressure associated with the accumulation of rotors. The strength of these local density changes is proportional to the odd viscosity. But the density changes of passive particles and rotors are not compensating and accordingly, the mixture shows a net increase accumulation of material in the positive vortices. The local density changes of passive particles resulting from odd stresses can thus only be used in order to demonstrate the presence and relative strength of odd viscosity in a rotor system, but an explicit measurement of odd viscosity from only the dynamics of passive particles requires an explicit consideration of the odd stresses and the pressure associated with rotor and passive particle accumulation, which has to be worked out in the future. Stable segregation is prevented by the dynamic formation and dispersion of vortices and the diffusive behaviour of the colloids implied by thermal fluctuations. At high densities of the mixture ϕ, the formation of one system-spanning stable vortex is observed and consequently segregation is obtained for $t \to \infty$, because the rotors constantly experience the odd stresses into the centre of the same vortex. A similar behaviour is expected for a binary mixture in a vortex maintaining setup, where the rotors are on average driven into the direction of the constant position of the vortex centre.

Chapter 8

Swimming behaviour of coupled microrotor pairs—from single to collective dynamics

Two rotors of opposite angular velocities $\Omega_1 = -\Omega_2$ mutually induce flows that advect the two rotors as a pair forward. If the relative distance between the two rotors is constrained, then the rotor pair works as a microswimmer [50, 193]. It is shown here, that such a rotor pair generates a flow field similar to a source doublet, implying a propulsion of the rotor pair which can effectively be described with the active Brownian particle model. The propelling rotor pair is referred to as a birotor and a sketch is given in figure 8.1a. The collective dynamics cannot be explained by Brownian modelling of the birotors, because mutual hydrodynamic interactions play an important role. While two oppositely propelling birotors can get stuck due to steric interactions with the thrust centres out of the centre of mass and thus start to rotate, the aggregation of further particles in order to form a motility induced cluster is absent. It is believed that the fluid transport opposite to the propulsion velocity, which in the case of aggregation points away from the building cluster, prevents further aggregation. Small aggregates are constantly forming and dissolving by thermal fluctuations. An experimental realisation of a birotor implies to constrain the relative distance between two rotating colloids, but this constrain must not impede the rotation of the rotors into opposite directions. This is much more cumbersome than other swimmer models, but the analysis of the dynamics of birotors is still lacking. In this chapter, this gap is addressed with a brief analysis of birotors in terms of individual and collective dynamics.

8.1. Flow fields

In 1922, Jeffery studied the steady Stokes flow caused by two equally sized ($\sigma_1 = \sigma_2$) rotors at centre-to-centre distance l_0 and of opposite angular velocities $\Omega_1 = -\Omega_2$ in a resting and infinitely large 2D fluid and showed that no solution to the Stokes equation can simultaneous fulfil the no-slip boundary condition on the rotors surface and at infinity [162]. This scenario is nowadays known as the Jeffery paradox and is related to the case of a moving disc in a 2D fluid in section 1.3.2 [164] and is resolved similarly. In experimental realisations the existence of the third dimension enforces the outer boundary condition, *i.e.*, that the fluid rests at infinity.

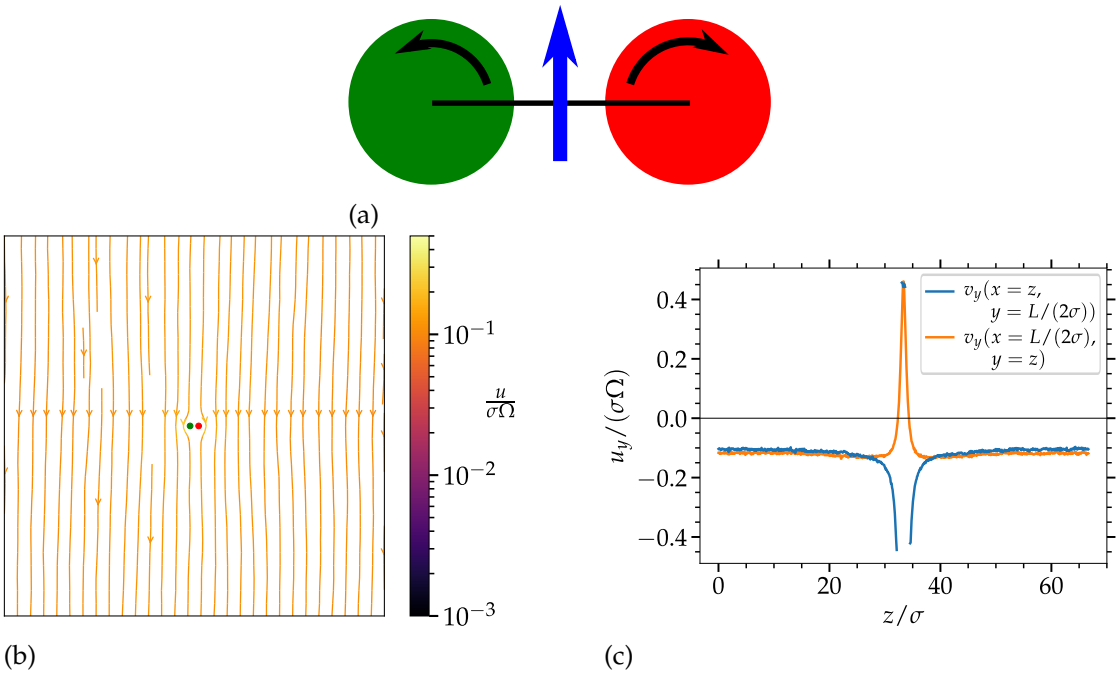

Figure 8.1: (a) Sketch of a birotor. Green, red circles represent positive, negative angular velocity, respectively. Blue arrow indicates direction of propulsion. (b) Flow fields of swimmers in a square simulation domain of dimension $L = 66.6\sigma$ with periodic boundary conditions. Green rotor rotates counter-clockwise, red rotor rotates clockwise. (c) Corresponding average fluid velocities into the y-direction long the horizontal (blue), vertical (orange) line through the rotors' centres, point in the rotors' middle, respectively.

The Jeffery paradox implies that along the line between the rotors perpendicular to the connecting line the flow exhibits a finite flow velocity at infinity [164]. In a multi-particle collision dynamics solvent in a simulation domain of finite size with periodic boundary conditions, this implies that the constant energy input for the rotors motion leads to a flow far field which, in a stationary state, is homogeneous throughout the simulation domain resulting from the lack of flow decay and the self-interactions with the periodic images. This artefact is shown in figure 8.1b which shows the streamlines of the created flow of a birotor fixed in position. Figure 8.1c shows the flow into the (y-)direction perpendicular to the line of centres on the horizontal and vertical lines through the point in the centre of the swimmer, *i.e.*, between the two rotors. The flow into the y-direction at the swimmers surface and its direct vicinity is dictated by the no-slip boundary, *i.e.*, $u_y = \sigma\Omega/2$ on the rotors' surface. However, farther away from the swimmer, the flow reaches a constant plateau value of $u_y \approx 0.1\sigma\Omega$ in both directions indicated in figure 8.1c. The lack of a decay of the flow along the line between the rotors according to the Jeffery paradox qualitatively leads to a flow as indicated in figures 8.1b and c in the steady-state irrespective of the system size.

In order to study the dynamics of birotor swimmers in two dimensions, the influence of the third dimension on the decay of the induced flow has to be incorporated into the simulation technique. Here this is realised by the introduction of a substrate and corresponding friction according to chapter 4. The momentum dissipation into the substrate then guarantees that the flow created by the birotor decays with increasing distance from the swimmer. For different values of the friction length scale λ,

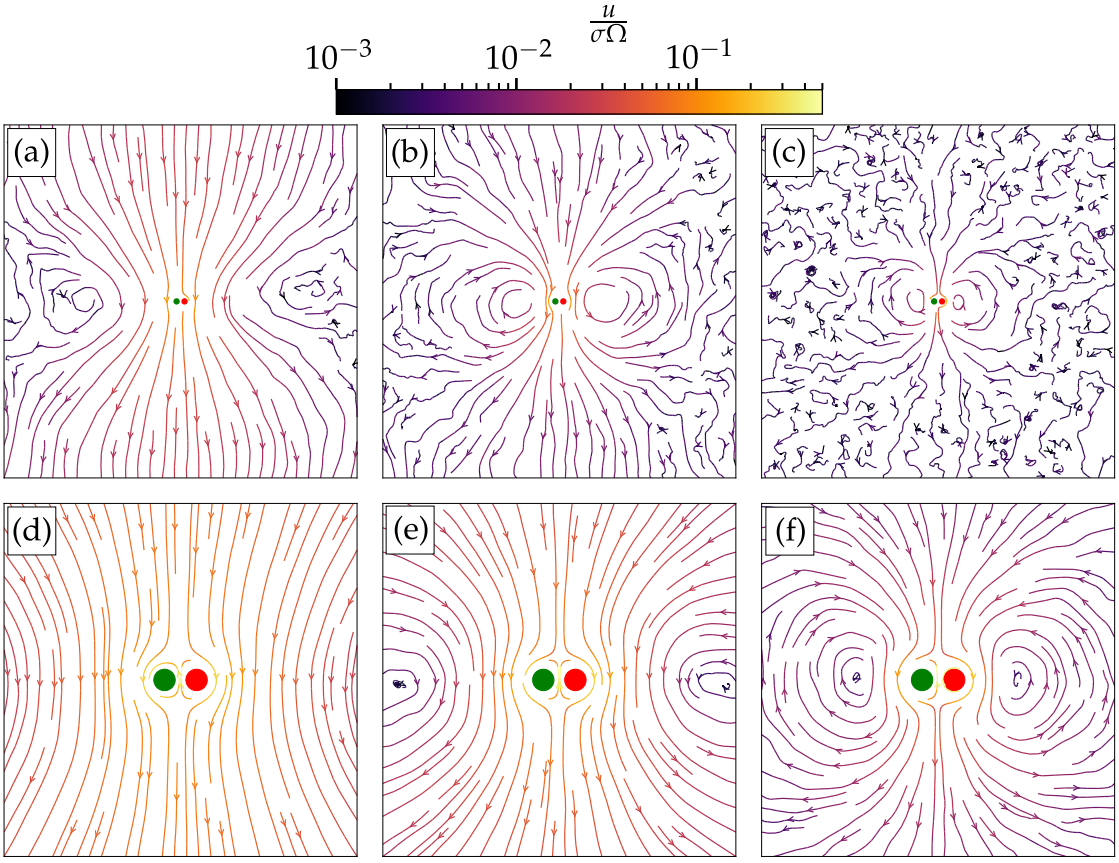

Figure 8.2: Streamlines of the flow created by a swimmers for different values of the substrate friction in a square simulation domain of dimension $L = 66.6\sigma$ with periodic boundary conditions. The first row (a)-(c) displays the whole simulation domain, whereas the second row shows a zoomed in version showing a portion of dimension 16.6σ if the whole domain. Values of substrate friction length scale is $\lambda/\sigma = 19.3$ (a) and (d), $\lambda/\sigma = 9.3$ (b) and (e), and $\lambda/\sigma = 2.9$ (c) and (f).

the resulting flow fields are shown in figure 8.2. With decreasing λ the induced flow on the line connecting the two rotors' centres decays faster, in accordance with the findings in chapter 4, until at some distance from the rotor centre λ_d the flow is on average zero. However, since the fluid is still being pumped over the same line of length $2\lambda_d$, flow continuity leads to the formation of two circular flow patterns with centres at the points where the flow is zero. Consequently, the flow pattern at sufficiently low values of the substrate friction length scale λ is reminiscent of the magnetic field lines of a magnetic dipole. For $\lambda/\sigma = 2.9$ ($\rho_{subs}a^2/m = 5 \times 10^{-3}$, figure 8.2f) the flow has decayed by two orders of magnitude at a distance of approximately 10σ. This value is used for the study of moving birotors in the remainder of this chapter for the paradox-free study of birotor swimmers.

Figure 8.2f shows that the fluid at the left and right boundaries of the green and red rotor, respectively, is pumped downwards resulting from the flow generated at the rotors' outer surfaces. In the vicinity of the birotor, *i.e.*, the region where the flow is similar with and without substrate friction, the flow field looks like a two-dimensional slice of the flow created by a 3D source doublet, also known as a sliplet, which is used in the multipole expansion to obtain the flow created by a sphere moving with velocity

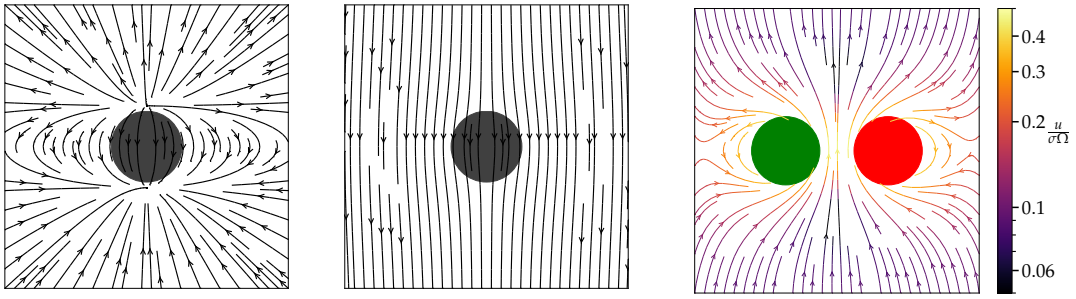

(a) (b) (c)

Figure 8.3: (a) and (b) Two-dimensional slice of the 3D sliplet streamlines corresponding to equation (8.1) in a resting (a) and co-moving (b) frame. Black circle represents a spherical force-free object moving upwards. (c) Streamlines of the birotor flow corresponding to figure 8.2d in a resting frame, *i.e.*, after subtracting the birotor propulsion velocity.

v, where the sliplet (in a fixed lab-frame)

$$u_\alpha(\boldsymbol{r}) = \frac{\sigma^3}{16r^3}\left(3\frac{r_\alpha r_\beta}{r^2} - \delta_{\alpha\beta}\right) v_\beta\,, \tag{8.1}$$

(see figure 8.3a) enforces a no-slip boundary condition on the moving particle surface [196]. It is used as a correction to the Stokeslet flow of a point force, *i.e.*, obtained from the Oseen tensor. A source doublet indeed is assembled from a source and a sink, thus showing reminiscence of a dipole, as can be seen in figure 8.3a. Similar to the Stokeslet, the sliplet flow is generated from point contributions and the finite size of the colloid appearing in equation (8.1) is used to ensure the required boundary condition, such that the flow is only well defined for $r > \sigma/2$. For the flow in a co-moving frame, *i.e.*, a frame in which the particle is fixed in position as in the case of figure 8.2, the particle's velocity v has to be subtracted from equation (8.1) as shown in figure 8.3b, which in terms of the birotor corresponds to figure 8.2. If now the swimmer velocity is subtracted from the flow fields in figure 8.2, a picture of the streamlines corresponding to figure 8.3a is obtained. Figure 8.3c shows the birotor streamlines where the birotor propulsion velocity, extracted from the considerations in section 3.1, $v_\mathrm{p} = u_\varphi(l_0) = \sigma^2\Omega/(4l_0)$ has been subtracted. Comparison of the streamlines of a sliplet (8.3a) and a birotor (8.3c) in resting frames show to be similar. A particle moving through a solvent and creating a sliplet flow field by inducing a surface solvent flow is therefore a minimal model for a force-free swimmer that creates a symmetric flow at the particle surface, *e.g.*, a phoretic swimmer. The flow created by ciliated microswimmers, such as *Paramecium*, which use cilia to generate a flow on the swimmer surface in order to propel [11], also shows a qualitatively similar flow field reminiscent of sliplet [197, 198] and thus birotor induced flow. Additional contributions to the flow field created by the microswimmer, such as the swimmer shape or asymmetries, especially in the case of *Paramecium* which is non-spherical, give rise to a flow field which is not perfectly symmetric, although the far field created by *Paramecium* essentially is a that of a sliplet [199].

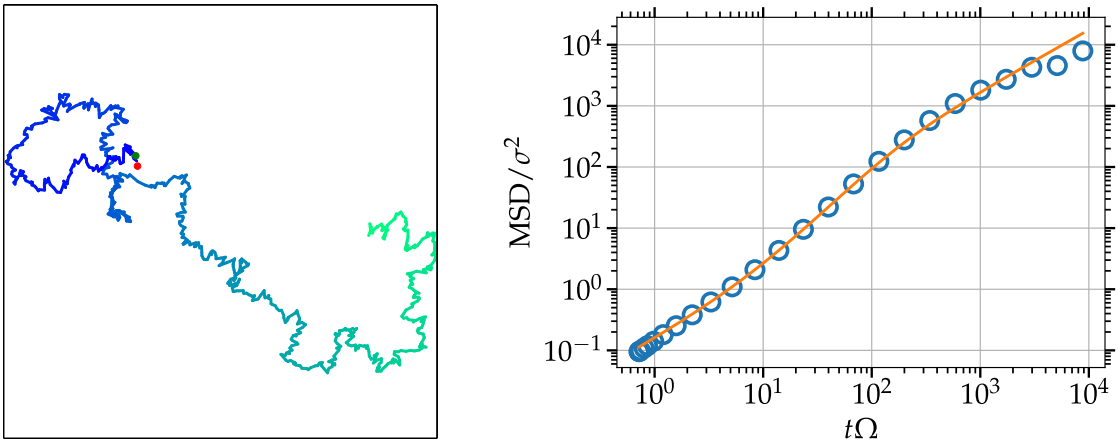

(a) (b)

Figure 8.4: (a) Trajectory of single birotor centre of mass. The colour gradient indicates the time on the trajectory, where darker colour corresponds to later times. Total trajectory length is $t\Omega/(2\pi) = 255$. (b) Mean-square displacements of single birotor dynamics. Symbols denote data averaged over time (see appendix D) and over four independent simulations of length $t\Omega/(2\pi) = 1400$. The line corresponds to a least-square fit to the symbols where the last two symbols have been disregarded. $\lambda/\sigma = 2.9$ has been used in (a) and (b).

8.2. SINGLE SWIMMER DYNAMICS

In order to construct the birotor, a coupling needs to be applied such that the rotors are not separating by thermal noise. In simulations this can be easily achieved by applying a harmonic potential $\mathcal{U}(r) = k(r - l_0)^2/2$ to the relative distance between the rotors r, such that the centre-to-centre distance l_0 is on average maintained, where for the spring stiffness and the centre-to-centre distance $k\sigma^2/k_BT = 1800$ and $l_0/\sigma = 1.25$ where employed in the simulations, ensuring an almost constant separation.

When the birotor is not fixed, the created flows give rise to a propulsion of the swimmer resulting from momentum conservation. The estimated propulsion velocity $v_p = \sigma^2\Omega/(4l_0)$ is only valid in the limit of $\lambda \to \infty$, since the substrate friction diminishes the created flows. Accordingly, with decreasing λ, v_p decreases. Figure 8.4a shows a representative trajectory of a birotor. The dynamics are reminiscent of that of an active Brownian particle what can be quantified in the mean-square displacement shown in figure 8.4b where the dynamics is diffusive on short timescales, ballistic on intermediate timescales, and enhanced diffusive on long timescales (section 1.2.2). The diffusion coefficient for the birotor's diffusive behaviour on short timescales is assumed to be described by the diffusion coefficient of a slightly larger circular object with respect to a single rotor in a two-dimensional flow. The diffusion coefficient of a single rotor in chapter 2 can therefore be used, since the friction on a moving circle in a two-dimensional fluid is for $\mathcal{R}e \to 0$ independent on the circle's diameter. From a least-square fit according to equation (1.18), the propulsion velocity can be inferred as $v_p = 0.56\sigma^2\Omega/(4l_0)$, *i.e.*, the influence of the substrate friction with $\lambda/\sigma = 2.9$ on the created flows reduces the propulsion velocity to 56% of the estimated velocity. The rotational diffusion of the birotor's orientation is analogously obtained as $\tau_r\Omega/(2\pi) = 20.79$, *i.e.*, the swimmers orientation is on average reoriented after approximately 20 rotor revolutions of the intrinsic rotation. Consequently, the birotor's

rotational Péclet number is $\mathcal{P}e_{\mathrm{rot}} \simeq 15$, which says that the birotor travels roughly a length of 15σ before the velocity direction is reoriented.

8.3. Collective dynamics

Although the dynamics of isolated birotors can be described by the active Brownian particle model, the situation is different for an ensemble of birotors in solution which cannot be described as a collection of sterically interacting active Brownian particles. This is because solvent mediated interactions, which are typically neglected when regarding an ensemble of solely sterically interacting active Brownian particles, are known to prevent effects like motility induced phase separation in collective active Brownian dynamics [200]. On the other hand, hydrodynamic interactions may also lead to the emergence of peculiar cluster formation [201], such that *a priori* estimates about the collective behaviour of a certain type of hydrodynamically interacting swimmer ensemble can become arbitrarily complicated, as the hydrodynamic flow fields do.

For the collective birotor dynamics, both hydrodynamic and, due to the approximately elongated shape of a birotor, steric alignment interactions are important. Figure 8.5 shows simulation snapshots of configurations with superimposed trajectories at different birotor density ϕ. For $\phi \to 0$, the dynamics effectively resemble the single birotor, because the rotors can be regarded as isolated. With increasing density, interactions between the birotors become important. In figure 8.5a and b two types of frequent pair interactions are marked. The solid grey circles mark pairs of birotors with opposing propulsion velocity directions, where the steric alignment interactions between the birotors lead to a configuration where the four respective rotor positions lay on the corners of a parallelogram. Resulting from the antiparallel alignment of the propulsion velocities of the two birotors and the fact that the thrust centres do not lay on the same line as the centre of mass of the two birotors, the configuration rotates. On the other hand, the dashed circles mark configurations in which the propulsion velocities of two birotors are parallel, such that they effectively form a channel where the flow between two rotors in a birotor (figure 8.3c) is continued in the second birotor. The rear birotor then follows the front one in a laning-like configuration. However, both sketched configurations are eventually destroyed by thermal fluctuations.

At higher densities, the predominant interactions include many birotors leading to cluster formation with the propulsion velocity of the birotors pointing into the centre of the cluster, as indicated in figure 8.5 in the dash-dotted circles. However, for the considered densities, the clusters are not stable, probably due to the flow induced by the outer rotors in the cluster, which are approximately fixed in space and thus create a flow similar to figure 8.2f pointing into the direction opposite to the propulsion direction, *i.e.*, away from the cluster. Consequently, if a birotor approaches an aggregate, it will be effectively pumped away. In order to get a deeper understanding of the dynamic cluster assembling and disassembling, further investigation is necessary.

The ensemble and time averaged mean-square displacement of the collective birotor dynamics are shown in figure 8.6. At low density the isolated birotors dominate the collective dynamics, and accordingly the mean-square displacement for $\phi \to 0$ approaches the red line corresponding to an isolated single birotor. With increasing density, mutual particle interactions become important and influence the mean-square displacement. On the one hand, the interactions of neighbouring birotors induce that flows deflect the direction of the propulsion velocity, or the birotors collide leading to the rotating parallelogram structure. Accordingly, τ_{r} decreases with increasing den-

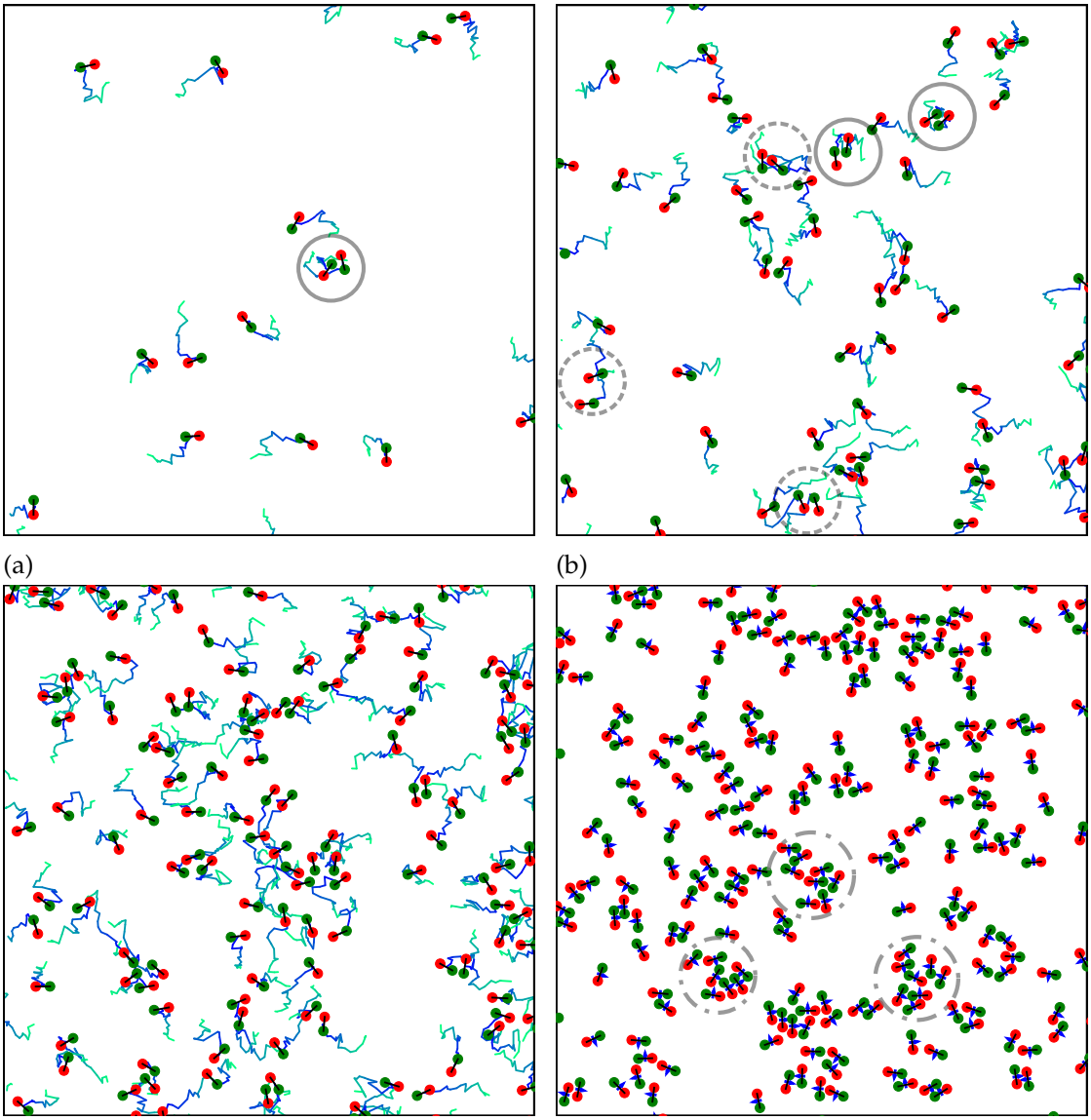

Figure 8.5: (a)-(c) Simulation snapshots of birotor configurations with superimposed trajectories of length $t\Omega/(2\pi) = 6.4$. Zoom-in to 1/9 of the simulation domain. Colour coding of trajectory qualitatively as in figure 8.4a. (d) Snapshots with propulsion indicated by blue arrow. Birotor densities: $\phi = 0.007$ (a), $\phi = 0.028$ (b), $\phi = 0.057$ (c), and $\phi = 0.113$ (d). Grey circles exemplarily emphasise birotor pairs of anti/-parallel orientation in (a) and (b) and small aggregates with average propulsion direction into into cluster centre in (d).

sity, such that the enhanced diffusive regime is reached earlier. Due to the increasing frequency of collisions with increasing ϕ, it is natural to assume that the collective propulsion velocity decreases, as it is the case for active Brownian particles [171]. Consequently, the enhanced diffusion coefficient of the ensemble, *i.e.*, the slope of the terminal diffusive regime, decreases because of the reduced speed and reduction of the ballistic regime due to the more frequent reorientations (section 1.2.2).

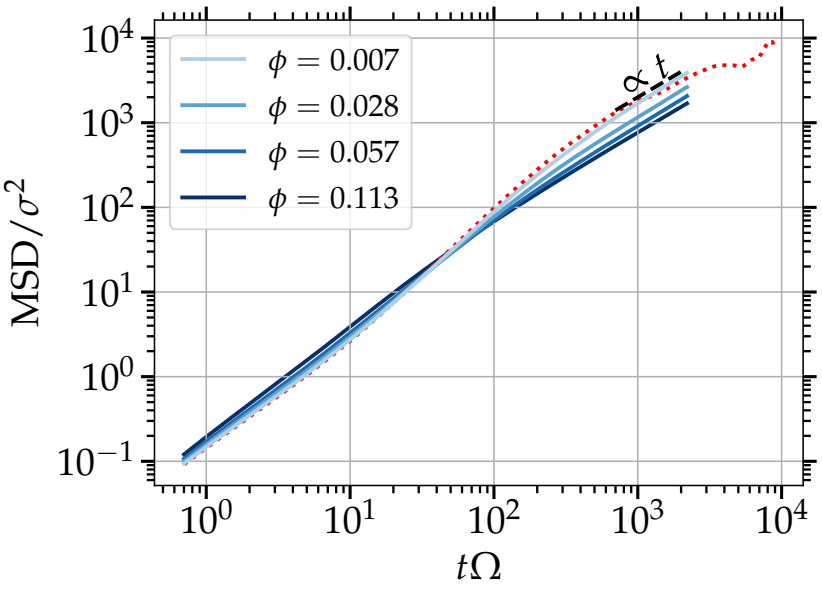

Figure 8.6: Mean-square displacements of collective birotor dynamics. Scale of blues indicates birotor density. Black dashed line indicates (enhanced) diffusive behaviour. Dotted red line is the data for single birotor from figure 8.4b for reference.

8.4. Summary

Although two coupled rotors of opposite angular velocities in a two-dimensional low-$\mathcal{R}e$-flow induce an unphysical flow known as the Jeffery paradox, the dynamics of coupled rotor pairs can be studied in two-dimensional hydrodynamic simulations, if the effect of a frictious substrate is incorporated. The flows induced on the rotating surfaces of the rotors then mutually advect the rotor pair forward. The propelling coupled rotor pair is termed a birotor. The induced flows are reminiscent of a sliplet flow and the rotor pair dynamics can be effectively modelled with the active Brownian particle model. This analogy, however, breaks down when more than one birotor are considered due to the mutual hydrodynamic interactions. For $\phi \to 0$, the birotors can be regarded as effectively isolated and the dynamics resemble the single birotor dynamics, while at low but finite densities, hydrodynamic and steric alignment interactions lead to the formation of laning, in the case of parallel propulsion velocities, and mutually blocked rotating, in the case of antiparallel propulsion velocities, structures of birotors. At higher densities, larger aggregates form where the propulsion velocities of the corresponding birotor point into the centre of the aggregate. These clusters, however, do not grow significantly, presumably due to the hydrodynamic flows induced by the birotors, which induce a flow into the direction opposite to the propulsion velocity, *i.e.*, away from the aggregate, preventing the aggregation of further birotors. This speculation, however, still needs verification, *e.g.*, by a systematic study of the trajectories of birotors in the flows induced by an aggregate. Resulting from thermal fluctuations, the formed structures are not stable and break up eventually. The increasing importance of interactions leads to diminished dynamics, *i.e.*, the rotational diffusion increases and the propulsion velocity decreases. Besides the verification of the reason for the limited size of the aggregates, a study of the size dis-

tribution of aggregates and the dwelling time of a birotor in an aggregate could give further insight into the dynamics of birotors.

Due to their cumbersome architecture, *i.e.*, jointed rotors which are still free to rotate into opposite directions, the birotor model could be regarded as a toy model. However, when the actuation is induced by rotating electric and magnetic fields on rotors where one carries a magnetic dipole and the other one an electric dipole, not only the speed of the birotor could be tuned by the rotation frequency, but also the direction of propulsion could be tuned by rotating one of the fields faster than the other. In order to investigate such a manoeuvrability, further studies of birotors with varying angular velocities are necessary. This could result into micromachines with trajectories that could be interactively controlled, promising interesting potential applications like medicine [26–29]. In this case, it could be that machine learning algorithms might help into the self-regularisation of such systems, in order to bring one of such birotors directly to a target [202–204].

Chapter 9

Concluding summary and outlook

This dissertation investigates a chiral active fluid consisting of hydrodynamically interacting microrotors which is studied mainly by means of particle based hydrodynamic simulations. The results in this thesis are partially compared to experiments of a suspension of rod-like silica colloids with an adhered ferromagnetic bead, such that the colloids carry an magnetic moment perpendicular to the rod axis. When exposed to an externally applied rotating magnetic field, with field lines perpendicular and axis of rotation parallel to the substrate normal, the colloidal rods orient perpendicular to the substrate in a state of synchronous rotation with the rotating field. In this non-equilibrium steady-state of vertical orientation, the rotating rods are termed rotors. The design of the simulations resembles the dynamics of the experimental rotors, where the hydrodynamic influences emanating from the finite length of the rods, and of the substrate are in general neglected. Accordingly, synchronously rotating discs in a two-dimensional explicit multiparticle collision dynamics solvent are simulated, where the discs interact solely via hydrodynamic and steric interactions. In order to prevent the emergence of unphysical torques on rotating objects in a multiparticle collision dynamics solvent resulting from the lack of angular momentum conservation in the generic collision protocol, an angular momentum conserving variant of the collision operator is employed. For the sake of studying the collective rotor dynamics in large ensembles, the simulation is implemented in a massively parallel fashion running on graphical processing units.

The no-slip boundary condition on the surface of each rotor implies a rotational flow that decays with distance from the rotor. The dynamics of isolated rotors at low Reynolds numbers can be effectively described by equilibrium Brownian motion. If two rotors approach, they will on average be transported along the mutually induced rotational flows, implying an orbital translation around the centre of mass of the two rotors, with orbital angular velocity decaying with increasing distance between the rotors. In simulations and experiments, the decay is governed by the same power-law, showing that the experimental flows indeed can be approximated as effectively two-dimensional.

In large ensembles of rotors, the mutually induced orbital dynamics leads to the formation of chaotic rotor trajectories which in a mean-field manner can be mapped on the active Brownian particle model, where the actuated velocity and the rotational diffusion of the velocity orientation explicitly depend on the rotor density. With increasing density, the average relative distance between the rotors decreases, implying an increasing velocity on orbits of decreasing size, such that the actuated velocity increases and the rotational diffusion of the velocity direction decreases with increasing

density. At intermediate densities the actuated velocity reaches a maximum and decreases upon further increase of the density due to the effective solvent viscosity which also increases with density.

The collective dynamics of rotor ensembles shows the emergence of multi-scale vortices of angular velocities of the same and opposite sign compared to the angular velocity of the rotors. On a coarse-grained level, a rotor ensemble can be regarded as a chiral active fluid continuum which can be described with the Stokes equation, if two additional force densities due to odd and rotational stresses, proportional to odd and rotational viscosity, are added. Vortical flows in chiral active fluids with odd viscosity imply the emergence of odd stresses pointing into the centre of circulation along the gradient of vorticity [67], such that rotors with a positive angular velocity accumulate in the vortices of the same orientation of rotation, and are effectively depleted from the vortices of opposite rotational orientation. This behaviour can then be exploited in order to explicitly measure the odd viscosity in the fluid, which dictates the strength of the density inhomogeneities associated with vorticity. The odd kinematic viscosity, *i.e.*, the rotor diffusivity due to odd stresses, measured in simulations and experiments is in satisfactory agreement, and decreases with increasing rotor density due to the decrease of the rotor fluid compressibility. If additionally inert particles are suspended into the solvent, the odd stresses still act predominantly between the rotors leading to the accumulation of rotors in regions of positive vorticity. Consequently, the passive inert particles feel the pressure increase associated with the increasing rotor density in the regions of positive vorticity. Accordingly, the passive particles are transported out of these areas into the areas of negative vorticity, due to the emerging pressure gradient, leading to a segregation of rotors and passive particles under conditions of sustain vortex flow. While chiral active fluids with odd viscosity have been realised already in the literature [41, 74, 151], the study presented here, to the best of my knowledge, shows the first measurement of odd viscosity from the density vorticity correlations resulting from odd stresses, in particle based hydrodynamic simulations. Furthermore, in this thesis, the migration of passive particles associated with the rotor density inhomogeneities in the vortex centres has shown to be a telltale sign of the presence of odd viscosity in a given chiral active fluid. Thus, only tracking the dynamics of labelled inert particles provides an easy and powerful measurement technique, with possible applications in a wide range of systems, especially interesting for measurements in living active systems. A full description considering the effective pressures due to density inhomogeneities of both, passive particles and rotors, and odd stresses has to be taken into account in order to infer the odd viscosity from the dynamics of the passive particles alone. Furthermore, a cohesive state of circular rotor flocking in a ring-shaped confinement has been reported in experiments, which is possibly explained by the density inhomogeneities associated with odd viscosity. However, so far there is no evidence for this statement and further studies should be excited to unravel the origin of the circular flocking.

In the rotor ensemble, energy is injected on the rotor scale and then transported to larger scales leading to the formation of multi-scale vortices ranging over the whole system—a process known as active turbulence of rotating matter. The rotor dynamics shows the emergence of an inverse energy cascade with a self-similar behaviour in the energy spectrum which follows a power-law. Interestingly, the exponent of the active turbulent energy spectrum agrees with the exponent of classical turbulence, *i.e.*, $E_q \propto q^{-5/3}$ which extends along all possible length scales from the particle to the system size, although the dynamics happens at low Reynolds numbers where iner-

tial contributions, which play a crucial role in classical two-dimensional turbulence at high Reynolds numbers, can be neglected. However, in experiments, the friction between the rotor fluid and the substrate impedes the formation of very large vortices, such that a dominant vortex scale in the energy spectrum appears acting as a cutoff to the power-law. This means that energy is dissipated at this scale. In this thesis, the development of an efficient way to simulate the influence of the substrate friction on the rotor dynamics, by the introduction of virtual substrate particles, which partially absorb momentum from the multiparticle collision dynamics solvent, allowed to explicitly prove that the dominant vortex scale stems from the friction at the substrate. Further effects, such as a non-synchronous rotation, that might be of relevance for related experimental realisations, is studied in simulations of rotors that are subject to a constant torque such that out of sync behaviour is allowed. These dynamics show to be qualitatively equivalent to the synchronous rotors' dynamics. Previous work on chiral active fluids have shown either active turbulence or odd viscosity. The numerical and experimental model presented in this thesis shows the simultaneous emergence of both, resulting from the propagation of active and odd stresses over long distances through the solvent, such that the rotor fluid still bears a finite osmotic compressibility. A similar behaviour is expected for related chiral active systems that transmit stresses via hydrodynamics.

The dynamics of rotors in confinement shows the formation of an edge flow along the confining walls, resulting from the breaking of symmetry, *i.e.*, the rotors at the wall only experience active stresses from the rotor side but not from the wall side, implying the formation of a stationary flow. In a circular container, the edge flow propagates into the centre by shear stresses implying a linear flow profile in the steady-state, which coexists with a chaotic active turbulent pattern, such that the collective dynamics can be regarded as a superposition of the stationary flow and active turbulent dynamics. Furthermore, energy is not only injected on the particle scale here, but also on the container scale, resulting from the forced energy transfer due to the edge flow. Accordingly, the energy spectra of the turbulent dynamics alone, *i.e.*, where the linear stationary profile has been subtracted, only shows the same power-law behaviour for systems where the particle scale and the confinement scale are sufficiently separated such that the inverse energy cascade can evolve without influences from the energy injection on the long scales. For sizes of the confinement, where the two scales are not separated enough, the energy spectrum shows the emergence of a power-law, but with an exponent $E_q \propto q^{-\mu}$, where $\mu < 5/3$. With decreasing confinement radius, the energy injection scale approaches the container size, such that eventually no power-law can evolve any more. Resulting from the entropy driven oscillation of density near walls, oscillatory rotational stresses lead to the formation of an oscillating velocity and accordingly also vorticity profile of the chiral active fluid at a wall. Since the rotors are driven along the gradients of vorticity, the edge flow leads to self-enhanced stationary density modulations in the vicinity of boundaries resulting from odd viscosity. The fact that effects of odd viscosity can thus be attested in steady-states simplifies analysis, especially experimental.

While the flow induced at boundaries leads to a local increase of transport, bounding walls are in general known to diminish transport processes. In the case of a particle based chiral active fluid, it is found here that rotor transport in a regular square grid of circular obstacles is maximized for $\Lambda \simeq 0.1$, where Λ is the ratio of obstacle diameter to separation between obstacles. What still remains an open question is whether rotor transport varies along different directions in the lattice, or whether such an effect can

be realised for related lattices. In order to probe the applicability of chiral active fluids as a driving to spread or distribute agents like nutrients or drugs, the behaviour of rotors and possible mixtures of rotors and inert particles, *i.e.*, cargo, in complex environments still has to be studied in more detail. Of special interest for the dynamics in biological systems is the rotor dynamics in irregularly shaped environments, similar to the study of dynamics in a polydisperse obstacle lattice in reference [150], where the authors focus on the dynamics of a single circle swimmer and find out that obstacle polydispersity can enhance transport, because it prevents swimmers from moving on uniform circular orbits. However, the emergence of collective phenomena is completely ruled out in that study, while in this thesis it is the essential contribution to convert rotational into translational dynamics.

The fact that rotational energy can be converted into translational energy in symmetry breaking conditions can be exploited in order to construct a microswimmer out of rotor materials. Explicitly, two counter-rotating colloids with a fixed relative distance induce flows that on average propel the coupled rotor pair, which is referred to as a birotor. The induced flows are reminiscent of the flows created by a sliplet, similar to the flows induced by ciliated symmetric microswimmers, that use cilia in order to generate a fluid velocity on the swimmer surface [11]. While isolated birotors show dynamics which can be effectively described within the active Brownian particle model, the collective dynamics does not show the formation of large clusters as is observed for active Brownian dynamics, as a result of the hydrodynamic flow fields created by the birotors, which pumps the fluid back in order to propel forwards. Accordingly, a small cluster nucleus consisting of birotors with velocities pointing into the centre of the nucleus pushes birotors at the cluster boundary away, such that aggregates do not grow significantly. A thorough investigation of the cluster size distributions and flow fields created by aggregates are still necessary to verify the assumption. The realisation of such a swimmer would allow for a very versatile swimmer model that is capable of being manoeuvred by controlling the rotational frequencies of the two rotors separately. By increasing or decreasing the angular velocity of one rotor, the rotor pair can be steered into a target location, similar to a crawler type vehicle. It is thus of practical relevance to excite further studies on this type of swimmer, in order to probe the applicability of birotors under conditions of practical applications.

In most of the experimental realisations of (spherical) rotating microparticles, it is not natural to assume two-dimensional hydrodynamics, even if the microparticles are effectively constrained to a two-dimensional plane [47, 193, 205]. For a chiral active fluid constructed out of spherical microrotors which are only free to move in a two-dimensional plane, but interact via three-dimensional hydrodynamics, similar results as presented here are expected. For the spheres, the rotation injects energy into the solvent and creates a rotational flow that decays like r^{-2}, thus transports the hydrodynamic interactions over long distances and accordingly will cause the other spheres to translate [50, 170]. Consequently, the same type of the emergence of edge flows, chaotic active turbulent behaviour and correlations between density and vorticity due to odd viscosity are expected. However, since it is not clear yet why the exponent in the energy spectrum of a 2D rotor fluid, *i.e.*, $E_q \propto q^{-5/3}$, reminiscent of classical turbulence emerges, the study of similar dynamics in a three-dimensional solvent might give new insights into the origin of the exponent, which on the one hand might be a result of the two-dimensional flows, but on the other hand may have its origin in the rotational stresses in the chiral active fluid causing the vortical motion, which are still governed by a long-ranged power-law decay of the induced flows in three dimensions.

It is thus not *a priori* evident, which of the here studied effects are also present in chiral active fluids consisting out of self-actively rotating units, or under which circumstances these systems behave as the here studied system, because there is a fundamental difference between rotationally actuated, *i.e.*, particles brought into rotational motion by the application of an external torque, *e.g.*, by the externally imposed rotating electro-magnetic fields on particles carrying an electric of magnetic dipole, and (self-)actively rotating particles, which rotate due to internal energy consumption, *e.g.*, by beating flagella similar to a *Volvox* colony [31]. The reason for this difference is the conservation of angular momentum, where the external actuation allows for the injection of angular momentum. For self-active rotation, the thrust centre of the applied torque has to lay outside the centre of mass and a different flow field is excited [50]. But since actively caused rotations are the main cause for rotations in biological systems, the differences and similarities between systems consisting out of actively and actuated rotating objects are of relevance in order to relate artificial to biological systems.

Appendix A

Numerical model

The numerical model employed for the results presented in the scope of this thesis is explained in this chapter. Furthermore, standard tests to verify the applicability of the model are shown.

A.1. Implementation details

The employed concepts underlying the studied numerical model are presented in section 1.6. In this section, the utilisation of these concepts are explained.

To study the dynamics of actively rotating colloids in two dimensions, an angular momentum conserving variant of multiparticle collision dynamics is employed [51, 134, 138, 206].

Before sorting the fluid particles into collision cells, in order to perform the multiparticle collision, a random grid shift is applied in order to restore Galilean invariance [135].

After each collision, the new post-collision velocities are thermostated on the cell-level using a canonical thermostat providing fluid particle velocities following the Maxwell-Boltzmann distribution [140, 141]. On the one hand, the thermostat remedies the violation of energy conservation consequent to the angular momentum conserving collision protocol. But on the other hand, also energy accumulation due to externally imposed activity is prevented.

Unless otherwise stated, the MPC parameters were chosen as follows. The mass of the fluid particles m, thermal energy $k_\mathrm{B}T$, and linear dimension of the collision cells a were taken to be unity, *i.e.*, $m = 1$, $k_\mathrm{B}T = 1$, and $a = 1$. Thus, these three parameters provide a scale, *i.e.*, the successive parameters and quantities can be expressed in simulation units, *i.e.*, in terms of m, $k_\mathrm{B}T$, and a. The collision time, *i.e.*, the time between collisions, the average particle density, and the rotation angle are $h = 0.02\tau_0$, $\rho = 10m/a^2$, and $\alpha = \pi/2$, respectively. Here, $\tau_0 = a\sqrt{m/(k_\mathrm{B}T)}$. These parameters result in a viscosity of $\eta = 17.9\sqrt{mk_\mathrm{B}T}/a$.

The colloids are modelled as impenetrable no-slip boundaries. In order to optimise the no-slip condition, virtual particles are randomly scattered in the interiors of the colloids, which potentially could be covered by a collision cell that is only partially filled with fluid particles. The (local) density of the virtual particles is chosen such that on average all collision cells contain the same number of particles participating in the collision protocol [144]. The velocities of the virtual particles consist of contributions from the centre of mass and rotational dynamics of the colloids, *i.e.*, the velocity of the boundary, and are complemented by an additional contribution drawn

from a Maxwell-Boltzmann distribution at the ambient temperature. The momentum exchange between colloids and fluid is then performed as described in section 1.6.4, *i.e.*, via the collision protocol and equation (1.63).

The colloids phase space variables are updated following the velocity-Verlet integration scheme [130, 145]. The interaction potential between colloids at interparticle distance r_{ij} is

$$\mathcal{U}(r_{ij}) = \begin{cases} \infty\,, & \text{for } r_{ij} \leq \sigma \\ 4\varepsilon\left[\left(\frac{a}{r_{ij}-\sigma}\right)^{12} - \left(\frac{a}{r_{ij}-\sigma}\right)^{6}\right] + \varepsilon\,, & \text{for } \sigma < r_{ij} \leq \sigma + 2^{1/6}a\ , \\ 0\,, & \text{else} \end{cases} \tag{A.1}$$

i.e., a shifted purely repulsive interaction potential, giving rise to a very steeply increasing force when $r_{ij} \to \sigma$. In case of the study of colloids near a solid wall, the interaction potential between the colloids and the wall with a distance r_i from the wall is

$$\mathcal{U}(r_i) = \begin{cases} \infty\,, & \text{for } r_i \leq \sigma/2 \\ 4\varepsilon\left[\left(\frac{a}{r_i-\sigma/2}\right)^{12} - \left(\frac{a}{r_i-\sigma/2}\right)^{6}\right] + \varepsilon\,, & \text{for } \sigma/2 < r_i \leq \sigma/2 + 2^{1/6}a\ . \\ 0\,, & \text{else} \end{cases} \tag{A.2}$$

Equations (A.1) and (A.2) are tuned such that at least one collision box occupied with fluid is between two colloids, or between colloids and a wall in order to guarantee proper hydrodynamic coupling. Thus, the colloid-colloid (colloid-wall) interaction diameter σ_* differs from the colloid-fluid interaction diameter σ. The second virial B coefficient can be used in order to estimate σ_* [207]. For a hard sphere pair interaction ($\mathcal{U}(r) = \infty$ if $r < \sigma$, $\mathcal{U}(r) = 0$ otherwise), B gives the excluded volume per colloid, *i.e.*,

$$B = -\frac{1}{2}\int \mathrm{d}\boldsymbol{r}\left\{e^{-\beta\mathcal{U}(r)} - 1\right\}\,. \tag{A.3}$$

When applying the same analogy to the colloids described by equations (A.1) and (A.2), the effective hard-disc interaction diameter $\sigma_* = 1.162\sigma$ can be defined. This does, however, not alter the interaction diameter for the interactions between solvent and colloid, which is typically used as a unit of lengths.

A.2. SANITY CHECKS

A.2.1 Poiseuille flow

In order to explicitly measure the viscosity of the simulated fluid, we employ Poiseuille flow. That is, a constant force density is acting on the fluid into the x-direction, while the fluid is constrained to a channel of width L. The employed boundary conditions are $\boldsymbol{u}(x, y = 0) = 0$ and $\boldsymbol{u}(x, y = L) = 0$. As a result, the solution according to equation (1.29) is a parabolic profile

$$u_x(y) = \frac{\rho g}{2\eta} y(y - L)\,, \tag{A.4a}$$

$$u_y = 0\,. \tag{A.4b}$$

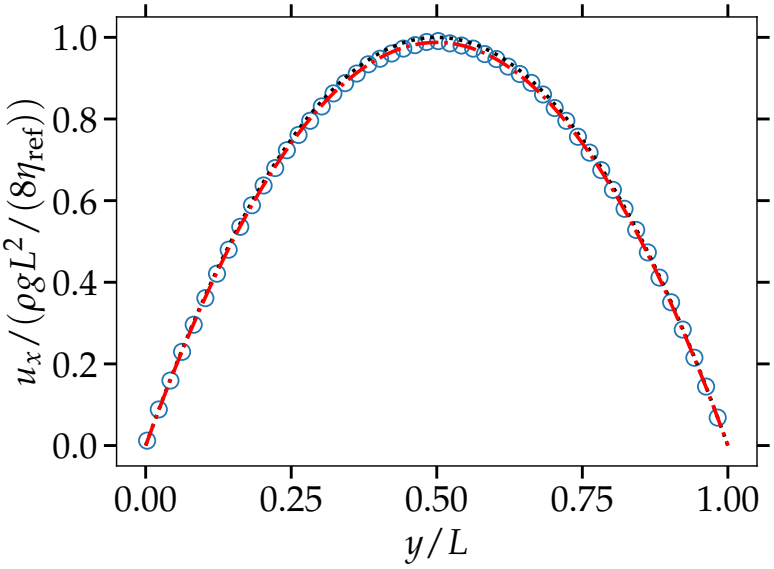

Figure A.1: Velocity profile obtained from Poiseuille flow measurements. The flow is accelerated into the x-direction. Blue symbols represent the measured fluid velocity, the black dashed line is the expected fluid flow following the analytical prediction of η_{ref} in reference [139], the red dashed line is a fit of the fluid flow to equation (A.4a). In simulation units, the employed parameters are $L/a = 200$, $g/(k_{\mathrm{B}}T/(a\,m)) = 0.0005$.

The solution (A.4) can be used to measure the viscosity of the fluid, since all quantities in equation (A.4a) but η are simulation parameters. Thus, η can be calculated from the response of the fluid to the external force density g.

The measured fluid profile is shown in figure A.1. Applying a least-square fit to the flow profile yields $\eta = 1.01\eta_{\mathrm{ref}}$, where η_{ref} is the analytical prediction according to equation (1.64a) from reference [139]. Thus very reasonable agreement with the predicted η is obtained.

A.2.2 Check of angular momentum conservation

When studying circular Couette flow in multiparticle collision dynamics between two concentric cylinders of radii $R_{\mathrm{i}} < R_{\mathrm{o}}$, where the outer cylinder rotates at angular velocity Ω and a no-slip boundary condition is implied, and the inner cylinder is coupled to the fluid via an slip boundary condition, the antisymmetric part of the stress tensor plays an important role [208]. Thus, circular Couette flow can be used to see whether the considered fluid conserves angular momentum, *i.e.*, if the antisymmetric part of the stress tensor is zero.

For the above explained setup, the general solution of the equation of motion and the stress tensor can be written as [116, 208]

$$\begin{aligned} u_\varphi(r) =& Ar + \frac{B}{r}\,, \\ \sigma_{\varphi r} =& \hat{\eta}\left(\frac{1}{r}\partial_\varphi u_r - \frac{u_\varphi}{r}\right) + \eta\partial_r u_\varphi\,, \end{aligned}$$

where in an angular momentum conserving fluid $\hat{\eta} = \eta$, whereas in a MPC fluid

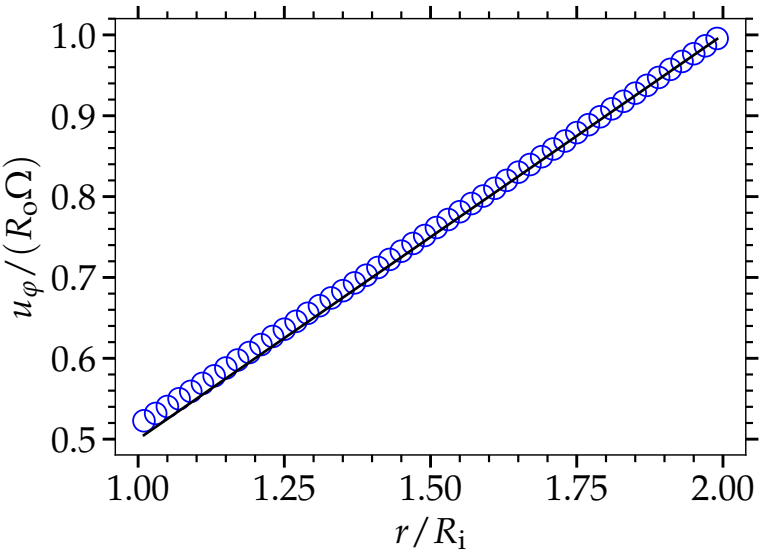

Figure A.2: Azimuthal velocity profile obtained from circular, concentric Couette measurements. The outer cylinder of radius R_o is a rotating no-slip boundary with angular velocity Ω, the inner cylinder of radius R_i is a slip boundary. The blue symbols indicate the measured fluid flow. The black line is the expected fluid flow in equation (A.5). In simulation units, the employed parameters are $R_o/a = 100$, $R_i/a = 50$, and $\Omega\tau_0 = 0.0005$.

without angular momentum conservation, $\hat{\eta} = \eta_{\text{kin}}$. The slip boundary, *i.e.*, $\sigma_{\varphi r}\big|_{r=R_i} = 0$, and the no-slip boundary condition, *i.e.*, $u_\varphi(R_o) = \Omega R_o$ then yield for a and b

$$\begin{aligned} A &= \frac{\Omega X}{1+X}, \\ B &= \frac{\Omega R_o^2}{1+X}, \\ X &= \frac{R_o^2}{R_i^2}\frac{\eta+\hat{\eta}}{\eta-\hat{\eta}}. \end{aligned}$$

Thus, for $\hat{\eta} = \eta$, $B = 0$ and $A = \Omega$, yielding the linear profile

$$u_\varphi(r) = \Omega r \tag{A.5}$$

only for the angular momentum conserving fluid.

The results are shown in figure A.2. The obtained fluid flow agrees very well with the theoretical prediction for an angular momentum conserving fluid, and with reference [208].

A.2.3 Colloidal suspensions

In an equilibrium binary suspension of colloids of different diameter σ_i, with respective masses M_i and moments of inertia I_i, for $i = 1, 2$, the linear velocities $v_\alpha^{(i)}$ in directions $\alpha = x, y$ and the angular velocities $\Omega^{(i)}$ will be distributed according to a

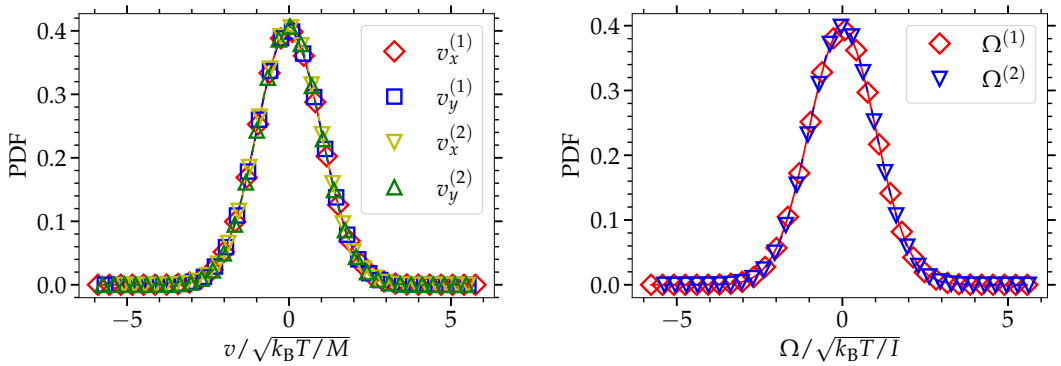

(a) Velocity distribution.

(b) Angular velocity distribution.

Figure A.3: Reduced normalised (angular) velocity distributions. Symbols correspond to histogram simulation data and lines to fits according to equations (A.6). Diamonds and squares correspond to M_1, upwards and downwards triangles correspond to M_2. The employed simulation parameters are $\sigma_1 = 6a$, $\sigma_2 = 20a$, $M_1 = 282.7m$, $M_2 = 314.2 \times 10^1 m$, $I_1 = 127.2 \times 10^1 m\,a^2$, and $I_2 = 157.1 \times 10^3 m\,a^2$.

Maxwell-Boltzmann distribution

$$p(v_\alpha^{(i)}) = \frac{1}{\sqrt{2\pi k_B T/M_i}} \exp\left[-\frac{M_i\left(v_\alpha^{(i)} - \left\langle v_\alpha^{(i)}\right\rangle\right)^2}{2k_B T}\right], \text{ with } \alpha = x, y, \tag{A.6a}$$

$$p(\Omega^{(i)}) = \frac{1}{\sqrt{2\pi k_B T/I_i}} \exp\left[-\frac{I_i\left(\Omega^{(i)} - \left\langle \Omega^{(i)}\right\rangle\right)^2}{2k_B T}\right]. \tag{A.6b}$$

In equilibrium, detailed balance implies $\left\langle v_\alpha^{(i)}\right\rangle = 0$ and $\left\langle \Omega^{(i)}\right\rangle = 0$. Furthermore, the distributions can be transformed to the standard Gaussian of unit variance $p(x) = (2\pi)^{-1/2}\exp\left[x^2/2\right]$, by regarding the distributions of (angular) velocity divided by the root of the expected variance, *i.e.*, $\sqrt{\langle v^2\rangle} = \sqrt{k_B T/M_i}$ or $\sqrt{\langle \Omega^2\rangle} = \sqrt{k_B T/I_i}$, yielding reduced quantities. In that way, all distributions should collapse on one master curve, *i.e.*, on the standard Gaussian of unit variance.

In order to verify the applicability of the employed solvent-solute coupling, the equilibrium probability distributions of the (angular) velocities of a binary mixture are calculated. The resulting reduced (angular) velocity distributions are shown in figure A.3. An data collapse is observed, as is expected for a physically meaningful system. The effective temperatures that can be extracted from the fluctuations of the (angular) velocities, *i.e.*, $k_B T_v^{(i)} \equiv M_i\left\langle\left(v_\alpha^{(i)}\right)^2\right\rangle$ and $k_B T_\Omega^{(i)} \equiv I_i\left\langle\left(\Omega^{(i)}\right)^2\right\rangle$, yield $T_v^{(1)} = 0.99k_B T$, $T_v^{(2)} = 0.96k_B T$, $T_\Omega^{(1)} = 1.02k_B T$, and $T_\Omega^{(2)} = 1.00k_B T$, and thus, correct thermal agitation in a two-dimensional system of hydrodynamically interacting colloids up to minor deviations of at most 4% is obtained.

Appendix B

Experimental setup

The following verbatim quote is taken from [M].
"Silica rods with a magnetic head (Fe_3O_4) are used. The ferromagnetic material is grown on the Janus rods to impose a permanent magnetic dipole moment perpendicular to the rod long axis [209]. Directional growth of silica from nanoparticle encapsulated microemulsions droplets [210, 211] is employed, followed by seeded growth of silica layers, which is a modification of the synthesis protocol of bare silica rods [212], the Stober process. A scanning electron microscopy (SEM) image of these match-stick-like magnetic silica Janus rods is shown in Fig. 2.1a, where the inset shows a transmission electron microscopy (TEM) image highlighting the doping of magnetic nanoparticles at the head. This resulted in slightly tapered colloidal rods of $3.5 \pm 0.3\mu m$ in length, and a head and a tail of diameters of $0.77 \pm 0.08\mu m$ and $0.61 \pm 0.05\mu m$ respectively, measured from SEM images of approximately 70 particles. The ζ-potential of these particles are ~ -65 mV. Each rod possesses a permanent magnetic dipole moment in the end approximately perpendicular to its long axis. These particles were then suspended in deionized water (Millipore, 18.2 MΩ) and loaded into a custom sample chamber built by gluing a teflon cylinder (internal dimension: 1 cm; outer dimension: 2 cm; height: 1 cm) onto a piece of coverslip. The chamber was cleaned with isopropyl alcohol and DI water thoroughly before dried with nitrogen gas. The sample was allowed to rest on a microscope stage for 10 min until all the particles sediment to the bottom. A rotating magnetic field of 150 Gauss at constant angular velocity was applied by a pair of Helmholtz coils. All experiments were conducted at room temperature on an inverted light microscope (Olympus IX73) equipped with a $60\times$ oil-immersion lens (NA of 1.42) and the images were captured by a Ximea color camera (MQ042Cg-CM). The centroids of rotors were determined by a standard Matlab routine [213]."

Appendix C

The effect of pumping in the compressible MPC solvent

In order to further investigate the effect of finite $\mathcal{P}u$, additional results of simulations with larger Ω are shown in the following. Figure C.1 depicts the average fluid density and the forces $F_\perp$ and $F_\parallel$ in a measurement at $\mathcal{P}u = 73$. Clearly, the density inhomogeneities in figure C.1a are more pronounced by a factor of roughly 4 and the area between the colloids is slightly depleted from fluid particles. As a result, the arising pressure will push the rotors together, leading to a roughly 4 times larger attractive force, as can be verified in figure C.1b. The perpendicular force (figure C.1c) is slightly reduced on short inter-rotor distances upon increasing $\mathcal{P}u$. In order to obtain $\mathcal{P}u \ll 1$ for fixed $\mathcal{P}e$ and small $\mathcal{R}e$, it is mandatory to reduce the rotational frequency, *i.e.*, the pumping mechanism, and at the same time to increase the fluid density in order to keep $\mathcal{P}e$ sufficiently large [147]. This, however, increases the computational effort considerably. On the one hand, because of the larger number of fluid particles that are taking part in the angular momentum conserving collision rule. But on the other hand also, because of the decrease of the relevant timescale Ω^{-1}, *i.e.*, a full circulation of a rotor and the associated hydrodynamic effects need more simulation steps for being realised. However, the goal of computer simulations is not to adjust a few system parameters accurately, but rather to capture the relevant effects, as is accomplished with the system parameters from figure 2.8.

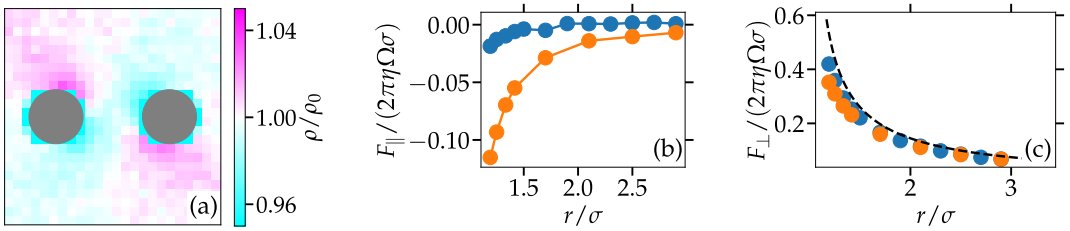

Figure C.1: Influences of fluid density inhomogeneities on the force measurements. (a) shows density inhomogeneities of MPC solvent at $\mathcal{P}u = 73$, corresponding to $\Omega = 0.025/\tau_0$, collision time $h = 0.005\tau_0$, viscosity $\eta = 71.7\sqrt{mk_\mathrm{B}T}/a$ in simulation units. Blue symbols in (b) and (c) represent data from figure 2.8, for reference. Normalisation in (b) and (c) according to a simplified form for the drag force of a circle moving at a speed of $u = \sigma\Omega/2$ through a two-dimensional solvent, equation (1.32).

Appendix D

Calculation of correlation functions

In order to efficiently calculate correlation functions $\langle f(x+y)f(y)\rangle_y$, the Wiener-Khinchin theorem is employed in order to calculate the convolution $\int \mathrm{d}y\, f(x+y)f(y)$ as a multiplication in Fourier space $\hat{f} * \hat{f}^*$ and a back transformation of this result. The computational effort to obtain $\langle f(x+y)f(y)\rangle_y$ is thus reduced to the calculation of the Fourier transform of $f(x)$ and the inverse transform of $\hat{f} * \hat{f}^*$ [214]. If the common Fast Fourier Transform technique is used in order to calculate the the (inverse) transforms, the computational effort of calculating the correlation of a trajectory of M points is reduced from $\propto M^2$ (real space calculation) to $\propto N \log_2 N$ (Wiener-Khinchin theorem).

Since in the simulations time is a discrete variable incrementing in equal units of h, the above scheme can be straightforwardly applied to time correlation functions. A for certain generalisations of time correlation functions such as the mean-square displacement, a recursion method is proposed in reference [214], in order to take advantage of the Wiener-Khinchin theorem. However, in order to calculate space correlation functions, the values of the respective variable first have to be binned on a grid such that the Fast Fourier Transform algorithm can be applied.

Exemplarily, a common calculation is shown in the following. Assuming the velocity field $\boldsymbol{v}(\boldsymbol{r})$ in continuous 2D space $\boldsymbol{r}$ and the velocity correlation function $\langle \boldsymbol{v}(\boldsymbol{r}) \cdot \boldsymbol{v}(0)\rangle$ is desired. Then, first discretise $\boldsymbol{v}(\boldsymbol{r})$ in squares of dimension l_0. Then, calculate the 2D Fourier transform $\hat{\boldsymbol{v}}_{\boldsymbol{q}}$, in order to obtain the power spectral density of $\boldsymbol{v}$, *i.e.*, $\hat{\boldsymbol{v}}_{\boldsymbol{q}} \cdot \hat{\boldsymbol{v}}^*_{\boldsymbol{q}}$. The corresponding energy spectrum E_q is now obtained by averaging the power spectral density over equal q shells in 2D q-space. The velocity correlation function is obtained after calculating the inverse Fourier transform of the power spectral density, *i.e.*,

$$\langle \boldsymbol{v}(\boldsymbol{r}) \cdot \boldsymbol{v}(\boldsymbol{0})\rangle = \frac{1}{(2\pi)^2} \int \mathrm{d}\boldsymbol{q}\, \hat{\boldsymbol{v}}_{\boldsymbol{q}} \cdot \hat{\boldsymbol{v}}^*_{\boldsymbol{q}} e^{i\boldsymbol{q}\cdot\boldsymbol{r}}\,. \tag{D.1}$$

Appendix E

Calculation of coarse-grained values

"Experiments and simulations provide configurations at different times where the rotors positions are well defined. Additionally, in simulations we obtain the instantaneous rotor velocities. In order to obtain the necessary density, velocity, and vorticity fields required in our study a coarse-grained procedure is applied. Density $\rho(r)$ is obtained by averaging the rotors positions in a grid with a bin size that might vary, but typically $(10\sigma)^2$. The bin size should be at least a few colloid diameters in order to identify coarse grain effects, but not much larger, since the structure of small vortices would already be averaged out." [M] In the simulations, the bin size cannot be chosen infinitely large, because a the centre of mass velocity in the periodic simulation domain overall is zero. Accordingly, the bins should also be significantly smaller than the simulation domain. "Coarse-grained velocities are obtained with two configurations at close times, $\boldsymbol{v}(\boldsymbol{r},t) = (\boldsymbol{r}(t+\Delta t) - \boldsymbol{r}(t))/\Delta t$, with the time interval has been chosen such that $\Omega\Delta t \leq 2$, where in simulations higher resolution is possible, which is necessary at high densities due to frequent inter-rotor collisions. The velocity, and thus vorticity fields are then obtained by averaging the rotor velocities in each bin. For the calculation of the energy spectra, we employ a bin size of σ^2 in order to obtain highest resolution in q-space." [M]

Bibliography

[1] Brown, R. Microscopical observations. *Philos. Mag* **4**, 161–173 (1828).

[2] Einstein, A. Über die von der molekularkinetischen theorie der wärme geforderte bewegung von in ruhenden flüssigkeiten suspendierten teilchen. *Ann. Phys.* **322**, 549–560 (1905).

[3] Frey, E. & Kroy, K. Brownian motion: a paradigm of soft matter and biological physics. *Ann. Phys.* **14**, 20–50 (2005).

[4] Dhont, J. K. *An introduction to dynamics of colloids* (Elsevier, 1996).

[5] Doi, M. & Edwards, S. F. *The theory of polymer dynamics*, vol. 73 (Oxford university press, 1988).

[6] Lipowsky, R. The conformation of membranes. *Nature* **349**, 475–481 (1991).

[7] Dieterich, P., Klages, R., Preuss, R. & Schwab, A. Anomalous dynamics of cell migration. *Proc. Natl. Acad. Sci.* **105**, 459–463 (2008).

[8] Bullerjahn, J. T., Sturm, S. & Kroy, K. Theory of rapid force spectroscopy. *Nat. Commun.* **5**, 4463 (2014).

[9] Bunde, A., Caro, J., Kärger, J. & Vogl, G. *Diffusive Spreading in Nature, Technology and Society* (Springer, 2017).

[10] Gompper, G. *et al.* The 2020 motile active matter roadmap. *J. Phys. Condens. Matter* **32**, 193001 (2020).

[11] Elgeti, J., Winkler, R. G. & Gompper, G. Physics of microswimmers—single particle motion and collective behavior: A review. *Rep. Prog. Phys.* **78**, 056601 (2015).

[12] Kruse, K., Joanny, J.-F., Jülicher, F., Prost, J. & Sekimoto, K. Generic theory of active polar gels: a paradigm for cytoskeletal dynamics. *Eur. Phys. J. E* **16**, 5–16 (2005).

[13] Dombrowski, C., Cisneros, L., Chatkaew, S., Goldstein, R. E. & Kessler, J. O. Self-concentration and large-scale coherence in bacterial dynamics. *Phys. Rev. Lett.* **93**, 098103 (2004).

[14] Wagner, M., Roca-Bonet, S. & Ripoll, M. Collective behavior of thermophoretic dimeric active colloids in three-dimensional bulk. *Eur. Phys. J. E* **44**, 1–11 (2021).

[15] Colberg, P. H. & Kapral, R. Many-body dynamics of chemically propelled nanomotors. *J. Chem. Phys.* **147**, 064910 (2017).

[16] Cavagna, A. & Giardina, I. Bird flocks as condensed matter. *Annu. Rev. Condens. Matter Phys.* **5**, 183–207 (2014).

[17] Vabø, R. & Nøttestad, L. An individual based model of fish school reactions: predicting antipredator behaviour as observed in nature. *Fish. oceanogr.* **6**, 155–171 (1997).

[18] Song, W., Xu, X., Wang, B.-H. & Ni, S. Simulation of evacuation processes using a multi-grid model for pedestrian dynamics. *Physica A* **363**, 492–500 (2006).

[19] Helbing, D. Traffic and related self-driven many-particle systems. *Rev. Mod. Phys.* **73**, 1067 (2001).

[20] Schmidt, C. K., Medina-Sánchez, M., Edmondson, R. J. & Schmidt, O. G. Engineering microrobots for targeted cancer therapies from a medical perspective. *Nat. Commun.* **11**, 5618 (2020).

[21] Grosser, S. *et al.* Cell and nucleus shape as an indicator of tissue fluidity in carcinoma. *Phys. Rev. X* **11**, 011033 (2021).

[22] Ilina, O. *et al.* Cell–cell adhesion and 3d matrix confinement determine jamming transitions in breast cancer invasion. *Nat. Cell Bol.* **22**, 1103–1115 (2020).

[23] Medina-Sánchez, M., Schwarz, L., Meyer, A. K., Hebenstreit, F. & Schmidt, O. G. Cellular cargo delivery: Toward assisted fertilization by sperm-carrying micromotors. *Nano Lett.* **16**, 555–561 (2016).

[24] Nagel, A. M., Greenberg, M., Shendruk, T. N. & de Haan, H. W. Collective dynamics of model pili-based twitcher-mode bacilliforms. *Sci. Rep.* **10**, 1–16 (2020).

[25] Worlitzer, V. M. *et al.* Biophysical aspects underlying the swarm to biofilm transition. *Sci. Adv.* **8**, eabn8152 (2022).

[26] Palagi, S. & Fischer, P. Bioinspired microrobots. *Nat. Rev. Mater.* **3**, 113–124 (2018).

[27] Langer, R. New methods of drug delivery. *Science* **249**, 1527–1533 (1990).

[28] Tran, S., DeGiovanni, P.-J., Piel, B. & Rai, P. Cancer nanomedicine: a review of recent success in drug delivery. *Clin. Transl. Med.* **6**, 1–21 (2017).

[29] Kim, D. K. & Dobson, J. Nanomedicine for targeted drug delivery. *Journal of Materials Chemistry* **19**, 6294–6307 (2009).

[30] Noji, H. & Yoshida, M. The rotary machine in the cell, atp synthase* 210. *J. Biol. Chem.* **276**, 1665–1668 (2001).

[31] Pedley, T. J., Brumley, D. R. & Goldstein, R. E. Squirmers with swirl: a model for volvox swimming. *J. Fluid Mech.* **798**, 165–186 (2016).

[32] Fürthauer, S., Strempel, M., Grill, S. W. & Jülicher, F. Active chiral fluids. *EPJ E* **35**, 1–13 (2012).

[33] Lenz, P., Joanny, J.-F., Jülicher, F. & Prost, J. Membranes with rotating motors. *Phys. Rev. Lett.* **91**, 108104 (2003).

[34] Oppenheimer, N., Stein, D. B., Zion, M. Y. B. & Shelley, M. J. Hyperuniformity and phase enrichment in vortex and rotor assemblies. *Nat. Commun.* **13**, 804 (2022).

[35] Drescher, K. *et al.* Dancing volvox: hydrodynamic bound states of swimming algae. *Phys. Rev. Lett.* **102**, 168101 (2009).

[36] Riedel, I. H., Kruse, K. & Howard, J. A self-organized vortex array of hydrodynamically entrained sperm cells. *Science* **309**, 300–303 (2005).

[37] Yang, Y., Qiu, F. & Gompper, G. Self-organized vortices of circling self-propelled particles and curved active flagella. *Phys. Rev. E* **89**, 012720 (2014).

[38] Darnton, N., Turner, L., Breuer, K. & Berg, H. C. Moving fluid with bacterial carpets. *Biophys. J.* **86**, 1863–1870 (2004).

[39] Uchida, N. & Golestanian, R. Synchronization and collective dynamics in a carpet of microfluidic rotors. *Phys. Rev. Lett.* **104**, 178103 (2010).

[40] Howse, J. R. *et al.* Self-motile colloidal particles: from directed propulsion to random walk. *Phys. Rev. Lett.* **99**, 048102 (2007).

[41] Soni, V. *et al.* The odd free surface flows of a colloidal chiral fluid. *Nat. Phys.* **15**, 1188–1194 (2019).

[42] Kavčič, B., Babič, D., Osterman, N., Podobnik, B. & Poberaj, I. Magnetically actuated microrotors with individual pumping speed and direction control. *Appl. Phys. Lett.* **95**, 023504 (2009).

[43] Grzybowski, B. A., Stone, H. A. & Whitesides, G. M. Dynamic self-assembly of magnetized, millimetre-sized objects rotating at a liquid–air interface. *Nature* **405**, 1033–1036 (2000).

[44] Grzybowski, B. A., Jiang, X., Stone, H. A. & Whitesides, G. M. Dynamic, self-assembled aggregates of magnetized, millimeter-sized objects rotating at the liquid-air interface: Macroscopic, two-dimensional classical artificial atoms and molecules. *Phys. Rev. E* **64**, 011603 (2001).

[45] Han, K. *et al.* Reconfigurable structure and tunable transport in synchronized active spinner materials. *Sci. Adv.* **6**, eaaz8535 (2020).

[46] Climent, E., Yeo, K., Maxey, M. R. & Karniadakis, G. E. Dynamic self-assembly of spinning particles. *J. Fluids Eng.* **129**, 379–387 (2006).

[47] Yan, J., Bae, S. C. & Granick, S. Rotating crystals of magnetic janus colloids. *Soft Matter* **11**, 147–153 (2015).

[48] Cao, Z., Jiang, H. & Hou, Z. Designing circle swimmers: Principles and strategies. *J. Chem. Phys.* **155**, 234901 (2021).

[49] Reigh, S. Y., Winkler, R. G. & Gompper, G. Synchronization and bundling of anchored bacterial flagella. *Soft Matter* **8**, 4363–4372 (2012).

[50] Fily, Y., Baskaran, A. & Marchetti, M. C. Cooperative self-propulsion of active and passive rotors. *Soft Matter* **8**, 3002–3009 (2012).

[51] Götze, I. O. & Gompper, G. Dynamic self-assembly and directed flow of rotating colloids in microchannels. *Phys. Rev. E* **84**, 031404 (2011).

[52] Götze, I. O. & Gompper, G. Flow generation by rotating colloids in planar microchannels. *EPL* **92**, 64003 (2011).

[53] Han, K. *et al.* Emergence of self-organized multivortex states in flocks of active rollers. *Proc. Natl. Acad. Sci.* **117**, 9706–9711 (2020).

[54] Kokot, G. & Snezhko, A. Manipulation of emergent vortices in swarms of magnetic rollers. *Nat. Commun.* **9**, 2344 (2018).

[55] Zhang, B., Sokolov, A. & Snezhko, A. Reconfigurable emergent patterns in active chiral fluids. *Nat. Commun.* **11**, 4401 (2020).

[56] Massana-Cid, H., Levis, D., Hernández, R. J. H., Pagonabarraga, I. & Tierno, P. Arrested phase separation in chiral fluids of colloidal spinners. *Phys. Rev. Res.* **3**, L042021 (2021).

[57] Zion, M. Y. B., Modin, A. & Chaikin, P. M. Hydrodynamic spin-orbit coupling in asynchronous optically driven micro-rotors. *arXiv preprint arXiv:2203.11051* (2022).

[58] Kokot, G. *et al.* Active turbulence in a gas of self-assembled spinners. *Proc. Natl. Acad. Sci.* **114**, 12870–12875 (2017).

[59] Goto, Y. & Tanaka, H. Purely hydrodynamic ordering of rotating disks at a finite reynolds number. *Nat. Commun.* **6**, 5994 (2015).

[60] Marchetti, M. C. *et al.* Hydrodynamics of soft active matter. *Rev. Mod. Phys.* **85**, 1143 (2013).

[61] Toner, J. & Tu, Y. Flocks, herds, and schools: A quantitative theory of flocking. *Phys. Rev. E* **58**, 4828 (1998).

[62] Baskaran, A. & Marchetti, M. C. Statistical mechanics and hydrodynamics of bacterial suspensions. *Proc. Natl. Acad. Sci.* **106**, 15567–15572 (2009).

[63] Doostmohammadi, A., Ignés-Mullol, J., Yeomans, J. M. & Sagués, F. Active nematics. *Nat. commun.* **9**, 3246 (2018).

[64] Reinken, H., Klapp, S. H., Bär, M. & Heidenreich, S. Derivation of a hydrodynamic theory for mesoscale dynamics in microswimmer suspensions. *Phys. Rev. E* **97**, 022613 (2018).

[65] Steffenoni, S., Falasco, G. & Kroy, K. Microscopic derivation of the hydrodynamics of active-brownian-particle suspensions. *Phys. Rev. E* **95**, 052142 (2017).

[66] Kaiser, A., Snezhko, A. & Aranson, I. S. Flocking ferromagnetic colloids. *Sci. Adv.* **3**, e1601469 (2017).

[67] Banerjee, D., Souslov, A., Abanov, A. G. & Vitelli, V. Odd viscosity in chiral active fluids. *Nat. Commun.* **8**, 1573 (2017).

[68] Avron, J. Odd viscosity. *J. Stat. Phys.* **92**, 543–557 (1998).

[69] Khain, T., Scheibner, C., Fruchart, M. & Vitelli, V. Stokes flows in three-dimensional fluids with odd and parity-violating viscosities. *J. Fluid Mech.* **934** (2022).

[70] Hosaka, Y., Komura, S. & Andelman, D. Nonreciprocal response of a two-dimensional fluid with odd viscosity. *Phys. Rev. E* **103**, 042610 (2021).

[71] Han, M. *et al.* Fluctuating hydrodynamics of chiral active fluids. *Nat. Phys.* **17**, 1260–1269 (2021).

[72] Souslov, A., Gromov, A. & Vitelli, V. Anisotropic odd viscosity via a time-modulated drive. *Phys. Rev. E* **101**, 052606 (2020).

[73] Abanov, A. Model oddity. *Nat. Phys.* **15**, 1109–1110 (2019).

[74] Yang, Q. *et al.* Topologically protected transport of cargo in a chiral active fluid aided by odd-viscosity-enhanced depletion interactions. *Phys. Rev. Lett.* **126**, 198001 (2021).

[75] Yang, Q. *et al.* Edge transport and self-assembly of passive objects in a chiral active fluid. *Chin. Phys. Lett.* **38**, 128701 (2021).

[76] Tan, T. H. *et al.* Odd dynamics of living chiral crystals. *Nature* **607**, 287–293 (2022).

[77] Scheibner, C. *et al.* Odd elasticity. *Nat. Phys.* **16**, 475–480 (2020).

[78] Braverman, L., Scheibner, C., VanSaders, B. & Vitelli, V. Topological defects in solids with odd elasticity. *Phys. Rev. Lett.* **127**, 268001 (2021).

[79] Chen, Y., Li, X., Scheibner, C., Vitelli, V. & Huang, G. Realization of active metamaterials with odd micropolar elasticity. *Nat. Commun.* **12**, 5935 (2021).

[80] Hargus, C., Epstein, J. M. & Mandadapu, K. K. Odd diffusivity of chiral random motion. *Phys. Rev. Lett.* **127**, 178001 (2021).

[81] Kalz, E. *et al.* Collisions enhance self-diffusion in odd-diffusive systems. *Phys. Rev. Lett.* **129**, 090601 (2022).

[82] Lapa, M. F. & Hughes, T. L. Swimming at low reynolds number in fluids with odd, or hall, viscosity. *Phys. Rev. E* **89**, 043019 (2014).

[83] Yasuda, K. *et al.* Time-correlation functions for odd langevin systems. *J. Chem. Phys.* **157**, 095101 (2022).

[84] Reichhardt, C. & Reichhardt, C. Active rheology in odd-viscosity systems. *Europhysics Letters* **137**, 66004 (2022).

[85] Lou, X. *et al.* Odd viscosity-induced hall-like transport of an active chiral fluid. *Proc. Natl. Acad. Sci.* **119**, e2201279119 (2022).

[86] Banerjee, D., Souslov, A. & Vitelli, V. Hydrodynamic correlation functions of chiral active fluids. *Phys. Rev. Fluids* **7**, 043301 (2022).

[87] Dunkel, J. *et al.* Fluid dynamics of bacterial turbulence. *Phys. Rev. Lett.* **110**, 228102 (2013).

[88] Reeves, C. J., Aranson, I. S. & Vlahovska, P. M. Emergence of lanes and turbulent-like motion in active spinner fluid. *Commun. Phys.* **4**, 92 (2021).

[89] Creppy, A., Praud, O., Druart, X., Kohnke, P. L. & Plouraboué, F. Turbulence of swarming sperm. *Phys. Rev. E* **92**, 032722 (2015).

[90] Giomi, L. Geometry and topology of turbulence in active nematics. *Phys. Rev. X* **5**, 031003 (2015).

[91] Alert, R., Joanny, J.-F. & Casademunt, J. Universal scaling of active nematic turbulence. *Nat. Phys.* **16**, 682–688 (2020).

[92] Qi, K., Westphal, E., Gompper, G. & Winkler, R. G. Emergence of active turbulence in microswimmer suspensions due to active hydrodynamic stress and volume exclusion. *Commun. Phys.* **5**, 49 (2022).

[93] Bourgoin, M. *et al.* Kolmogorovian active turbulence of a sparse assembly of interacting marangoni surfers. *Phys. Rev. X* **10**, 021065 (2020).

[94] Lin, S.-Z., Zhang, W.-Y., Bi, D., Li, B. & Feng, X.-Q. Energetics of mesoscale cell turbulence in two-dimensional monolayers. *Commun. Phys.* **4**, 21 (2021).

[95] Mukherjee, S., Singh, R. K., James, M. & Ray, S. S. Anomalous diffusion and lévy walks distinguish active from inertial turbulence. *Phys. Rev. Lett.* **127**, 118001 (2021).

[96] Bárdfalvy, D., Nordanger, H., Nardini, C., Morozov, A. & Stenhammar, J. Particle-resolved lattice boltzmann simulations of 3-dimensional active turbulence. *Soft Matter* **15**, 7747–7756 (2019).

[97] Wensink, H. H. *et al.* Meso-scale turbulence in living fluids. *Proc. Natl. Acad. Sci.* **109**, 14308–14313 (2012).

[98] Alert, R., Casademunt, J. & Joanny, J.-F. Active turbulence. *Annu. Rev. Condens. Matter Phys.* **13**, 143–170 (2022).

[99] Bratanov, V., Jenko, F. & Frey, E. New class of turbulence in active fluids. *Proc. Natl. Acad. Sci.* **112**, 15048–15053 (2015).

[100] Martínez-Prat, B. *et al.* Scaling regimes of active turbulence with external dissipation. *Phys. Rev. X* **11**, 031065 (2021).

[101] Heidenreich, S., Dunkel, J., Klapp, S. H. & Bär, M. Hydrodynamic length-scale selection in microswimmer suspensions. *Phys. Rev. E* **94**, 020601 (2016).

[102] Doostmohammadi, A., Shendruk, T. N., Thijssen, K. & Yeomans, J. M. Onset of meso-scale turbulence in active nematics. *Nat. commun.* **8**, 15326 (2017).

[103] Guillamat, P., Ignés-Mullol, J. & Sagués, F. Taming active turbulence with patterned soft interfaces. *Nat. Commun.* **8**, 564 (2017).

[104] Opathalage, A. *et al.* Self-organized dynamics and the transition to turbulence of confined active nematics. *Proc. Natl. Acad. Sci.* **116**, 4788–4797 (2019).

[105] Peliti, L. Statistical mechanics in a nutshell. In *Statistical Mechanics in a Nutshell* (Princeton University Press, 2011).

[106] Zwanzig, R. *Nonequilibrium statistical mechanics* (Oxford University Press, 2001).

[107] Sancho, J., San Miguel, M. & Dürr, D. Adiabatic elimination for systems of brownian particles with nonconstant damping coefficients. *J. Stat. Phys.* **28**, 291–305 (1982).

[108] Bullerjahn, J. T., Sturm, S., Wolff, L. & Kroy, K. Monomer dynamics of a wormlike chain. *EPL* **96**, 48005 (2011).

[109] Panja, D. Generalized langevin equation formulation for anomalous polymer dynamics. *J. Stat. Mech. Theory Exp.* **2010**, L02001 (2010).

[110] Lutz, E. Fractional langevin equation. *Phys. Rev. E* **64**, 051106 (2001).

[111] Coffey, W. & Kalmykov, Y. P. *The Langevin equation: with applications to stochastic problems in physics, chemistry and electrical engineering*, vol. 27 (World Scientific, 2012).

[112] Falasco, G., Gnann, M., Rings, D. & Kroy, K. Effective temperatures of hot brownian motion. *Phys. Rev. E* **90**, 032131 (2014).

[113] Rings, D., Schachoff, R., Selmke, M., Cichos, F. & Kroy, K. Hot brownian motion. *Phys. Rev. Lett.* **105**, 090604 (2010).

[114] Das, S., Gompper, G. & Winkler, R. G. Confined active brownian particles: theoretical description of propulsion-induced accumulation. *New J. Phys.* **20**, 015001 (2018).

[115] Mitterwallner, B. G., Lavacchi, L. & Netz, R. R. Negative friction memory induces persistent motion. *Eur. Phys. J. E* **43**, 1–11 (2020).

[116] Landau, L. & Lifshitz, E. *Fluid mechanics*, vol. 6 of *Course of theoretical physics* (Pergamon press, 1987), 2nd edn.

[117] Purcell, E. M. Life at low reynolds number. *Am. J. Phys.* **45**, 3–11 (1977).

[118] Oseen, C. W. über die stokes'sche formel und über eine verwandte aufgabe in der hydrodynamik. *Arkiv Mat., Astron. och Fysik* **6**, 1–20 (1910).

[119] Lamb, H. Xv. on the uniform motion of a sphere through a viscous fluid. *London, Edinburgh Dublin Philos. Mag. J. Sci.* **21**, 112–121 (1911).

[120] Batchelor, G. K. *An Introduction to Fluid Dynamics*. Cambridge Mathematical Library (Cambridge University Press, 2000).

[121] Pozrikidis, C. *Fluid dynamics: theory, computation, and numerical simulation* (Springer, 2017).

[122] Pozrikidis, C. *Boundary integral and singularity methods for linearized viscous flow* (Cambridge university press, 1992).

[123] Sreenivasan, K. R. Fluid turbulence. *Rev. Mod. Phys.* **71**, S383 (1999).

[124] Kolmogorov, A. N. A refinement of previous hypotheses concerning the local structure of turbulence in a viscous incompressible fluid at high reynolds number. *J. Fluid Mech.* **13**, 82–85 (1962).

[125] Boffetta, G. & Ecke, R. E. Two-dimensional turbulence. *Annu. Rev. Fluid Mech.* **44**, 427–451 (2012).

[126] Onsager, L. Statistical hydrodynamics. *Il Nuovo Cimento (1943-1954)* **6**, 279–287 (1949).

[127] Ouellette, N. T. Turbulence in two dimensions. *Physics Today* **65**, 68 (2012).

[128] Kraichnan, R. H. & Montgomery, D. Two-dimensional turbulence. *Rep. Prog. Phys.* **43**, 547 (1980).

[129] López-Castaño, M. A., Seco, A. M., Seco, A. M., Rodríguez-Rivas, Á. & Reyes, F. V. Chirality transitions in a system of active flat spinners. *Phys. Rev. Res.* **4**, 033230 (2022).

[130] Allen, M. P. & Tildesley, D. J. *Computer simulation of liquids* (Oxford university press, 2017).

[131] Gompper, G., Ihle, T., Kroll, D. & Winkler, R. Multi-particle collision dynamics: A particle-based mesoscale simulation approach to the hydrodynamics of complex fluids. In *Advanced computer simulation approaches for soft matter sciences III*, 1–87 (Springer, 2009).

[132] Mousavi, S. M., Gompper, G. & Winkler, R. G. Active brownian ring polymers. *J. Chem. Phys.* **150**, 064913 (2019).

[133] Kapral, R. Multiparticle collision dynamics: Simulation of complex systems on mesoscales. *Adv. Chem. Phys* **140**, 89 (2008).

[134] Malevanets, A. & Kapral, R. Mesoscopic model for solvent dynamics. *J. Chem. Phys.* **110**, 8605–8613 (1999).

[135] Ihle, T. & Kroll, D. Stochastic rotation dynamics: A galilean-invariant mesoscopic model for fluid flow. *Phys. Rev. E* **63**, 020201 (2001).

[136] Pooley, C. & Yeomans, J. Kinetic theory derivation of the transport coefficients of stochastic rotation dynamics. *J. Phys. Chem. B* **109**, 6505–6513 (2005).

[137] Ihle, T., Tüzel, E. & Kroll, D. M. Equilibrium calculation of transport coefficients for a fluid-particle model. *Phys. Rev. E* **72**, 046707 (2005).

[138] Götze, I. O., Noguchi, H. & Gompper, G. Relevance of angular momentum conservation in mesoscale hydrodynamics simulations. *Phys. Rev. E* **76**, 046705 (2007).

[139] Noguchi, H. & Gompper, G. Transport coefficients of off-lattice mesoscale-hydrodynamics simulation techniques. *Phys. Rev. E* **78**, 016706 (2008).

[140] Huang, C.-C., Chatterji, A., Sutmann, G., Gompper, G. & Winkler, R. G. Cell-level canonical sampling by velocity scaling for multiparticle collision dynamics simulations. *J. Comput. Phys.* **229**, 168–177 (2010).

[141] Theers, M., Westphal, E., Gompper, G. & Winkler, R. G. Modeling a spheroidal microswimmer and cooperative swimming in a narrow slit. *Soft Matter* **12**, 7372–7385 (2016).

[142] Lamura, A., Gompper, G., Ihle, T. & Kroll, D. Multi-particle collision dynamics: Flow around a circular and a square cylinder. *EPL* **56**, 319 (2001).

[143] Padding, J., Wysocki, A., Löwen, H. & Louis, A. Stick boundary conditions and rotational velocity auto-correlation functions for colloidal particles in a coarse-grained representation of the solvent. *J. Phys. Condens. Matter* **17**, S3393 (2005).

[144] Götze, I. O. & Gompper, G. Mesoscale simulations of hydrodynamic squirmer interactions. *Phys. Rev. E* **82**, 041921 (2010).

[145] Swope, W. C., Andersen, H. C., Berens, P. H. & Wilson, K. R. A computer simulation method for the calculation of equilibrium constants for the formation of physical clusters of molecules: Application to small water clusters. *J. Chem. Phys.* **76**, 637–649 (1982).

[146] Ripoll, M., Mussawisade, K., Winkler, R. & Gompper, G. Dynamic regimes of fluids simulated by multiparticle-collision dynamics. *Phys. Rev. E* **72**, 016701 (2005).

[147] Theers, M., Westphal, E., Qi, K., Winkler, R. G. & Gompper, G. Clustering of microswimmers: interplay of shape and hydrodynamics. *Soft Matter* **14**, 8590–8603 (2018).

[148] Belushkin, M., Winkler, R. & Foffi, G. Backtracking of colloids: a multiparticle collision dynamics simulation study. *J. Phys. Chem. B* **115**, 14263–14268 (2011).

[149] Shakeri, A., Lee, K.-W. & Pöschel, T. Limitation of stochastic rotation dynamics to represent hydrodynamic interaction between colloidal particles. *Phys. Fluids* **30**, 013603 (2018).

[150] Van Roon, D. M., Volpe, G., da Gama, M. M. T. & Araújo, N. A. The role of disorder in the motion of chiral active particles in the presence of obstacles. *Soft Matter* **18**, 6899–6906 (2022).

[151] Liu, P. *et al.* Oscillating collective motion of active rotors in confinement. *Proc. Natl. Acad. Sci.* **117**, 11901–11907 (2020).

[152] Woodhouse, F. G. & Goldstein, R. E. Spontaneous circulation of confined active suspensions. *Phys. Rev. Lett.* **109**, 168105 (2012).

[153] Vollmer, J., Vegh, A. G., Lange, C. & Eckhardt, B. Vortex formation by active agents as a model for daphnia swarming. *Phys. Rev. E* **73**, 061924 (2006).

[154] Franosch, T. *et al.* Resonances arising from hydrodynamic memory in brownian motion. *Nature* **478**, 85 (2011).

[155] Falasco, G. & Kroy, K. Nonisothermal fluctuating hydrodynamics and brownian motion. *Phys. Rev. E* **93**, 032150 (2016).

[156] Poblete, S., Wysocki, A., Gompper, G. & Winkler, R. G. Hydrodynamics of discrete-particle models of spherical colloids: A multiparticle collision dynamics simulation study. *Phys. Rev. E* **90**, 033314 (2014).

[157] Alder, B. & Wainwright, T. Decay of the velocity autocorrelation function. *Phys. Rev. A* **1**, 18 (1970).

[158] Choi, B. *et al.* Nature of self-diffusion in two-dimensional fluids. *New J. Phys.* **19**, 123038 (2017).

[159] Kawasaki, K. Long time behavior of the velocity autocorrelation function. *Phys. Lett. A* **32**, 379–380 (1970).

[160] Chandler, D. Introduction to modern statistical mechanics. *Oxford University Press, Oxford, UK* (1987).

[161] Leoni, M. & Liverpool, T. Dynamics and interactions of active rotors. *EPL* **92**, 64004 (2011).

[162] Jeffery, G. B. The rotation of two circular cylinders in a viscous fluid. *Proc. R. Soc. Lond. A* **101**, 169–174 (1922).

[163] Watson, E. The rotation of two circular cylinders in a viscous fluid. *Mathematika* **42**, 105–126 (1995).

[164] Ueda, Y., Sellier, A., Kida, T. & Nakanishi, M. On the low-reynolds-number flow about two rotating circular cylinders. *J. Fluid Mech.* **495**, 255–281 (2003).

[165] Behrens, S. H. & Grier, D. G. Pair interaction of charged colloidal spheres near a charged wall. *Phys. Rev. E* **64**, 050401 (2001).

[166] Einstein, A. Eine neue bestimmung der moleküldimensionen. *Ann. Phys.* **324**, 289–306 (1906).

[167] Krieger, I. M. & Dougherty, T. J. A mechanism for non-newtonian flow in suspensions of rigid spheres. *T. Soc. Rheol.* **3**, 137–152 (1959).

[168] Haines, B. M., Aranson, I. S., Berlyand, L. & Karpeev, D. A. Effective viscosity of dilute bacterial suspensions: a two-dimensional model. *Phys. Biol.* **5**, 046003 (2008).

[169] Winkler, R. G., Wysocki, A. & Gompper, G. Virial pressure in systems of spherical active brownian particles. *Soft Matter* **11**, 6680–6691 (2015).

[170] Llopis, I. & Pagonabarraga, I. Hydrodynamic regimes of active rotators at fluid interfaces. *Eur. Phys. J. E* **26**, 103–113 (2008).

[171] Stenhammar, J., Tiribocchi, A., Allen, R. J., Marenduzzo, D. & Cates, M. E. Continuum theory of phase separation kinetics for active brownian particles. *Phys. Rev. Lett.* **111**, 145702 (2013).

[172] Zhang, B. & Snezhko, A. Hyperuniform active chiral fluids with tunable internal structure. *Phys. Rev. Lett.* **128**, 218002 (2022).

[173] Falck, E., Lahtinen, J., Vattulainen, I. & Ala-Nissila, T. Influence of hydrodynamics on many-particle diffusion in 2d colloidal suspensions. *EPJ E* **13**, 267–275 (2004).

[174] Han, K., Glatz, A. & Snezhko, A. Emergence and dynamics of unconfined self-organised vortices in active magnetic roller liquids. *Soft Matter* **17**, 10536–10544 (2021).

[175] Tsai, J.-C., Ye, F., Rodriguez, J., Gollub, J. P. & Lubensky, T. A chiral granular gas. *Phys. Rev. Lett.* **94**, 214301 (2005).

[176] Löwen, H. Chirality in microswimmer motion: From circle swimmers to active turbulence. *Eur. Phys. J.: Spec. Top.* **225**, 2319–2331 (2016).

[177] Van Teeffelen, S. & Löwen, H. Dynamics of a brownian circle swimmer. *Phys. Rev. E* **78**, 020101 (2008).

[178] Koplik, J., Levine, H. & Zee, A. Viscosity renormalization in the brinkman equation. *Phys. Fluids* **26**, 2864–2870 (1983).

[179] Akhmedova, V. & Akhmedov, E. T. *Selected special functions for fundamental physics* (Springer, 2019).

[180] Zhang, H., Be'Er, A., Smith, R. S., Florin, E.-L. & Swinney, H. L. Swarming dynamics in bacterial colonies. *EPL* **87**, 48011 (2009).

[181] van Zuiden, B. C., Paulose, J., Irvine, W. T., Bartolo, D. & Vitelli, V. Spatiotemporal order and emergent edge currents in active spinner materials. *Proc. Natl. Acad. Sci.* **113**, 12919–12924 (2016).

[182] Bricard, A. *et al.* Emergent vortices in populations of colloidal rollers. *Nat. Commun.* **6**, 7470 (2015).

[183] Snook, I. & Van Megen, W. Solvation forces in simple dense fluids. i. *J. Chem. Phys.* **72**, 2907–2913 (1980).

[184] Trokhymchuk, A., Nezbeda, I., Jirsák, J. & Henderson, D. Hard-sphere radial distribution function again. *J. Chem. Phys.* **123**, 024501 (2005).

[185] Henderson, D., Abraham, F. F. & Barker, J. A. The ornstein-zernike equation for a fluid in contact with a surface. *Mol. Phys.* **31**, 1291–1295 (1976).

[186] Bier, M., van Roij, R., Dijkstra, M. & van der Schoot, P. Self-diffusion of particles in complex fluids: temporary cages and permanent barriers. *Phys. Rev. Lett.* **101**, 215901 (2008).

[187] Zhou, F., Wang, H. & Zhang, Z. Diffusion of anisotropic colloids in periodic arrays of obstacles. *Langmuir* **36**, 11866–11872 (2020).

[188] Ghosh, S. K., Cherstvy, A. G. & Metzler, R. Non-universal tracer diffusion in crowded media of non-inert obstacles. *Phys. Chem. Chem. Phys.* **17**, 1847–1858 (2015).

[189] Polanowski, P. & Sikorski, A. Simulation of diffusion in a crowded environment. *Soft Matter* **10**, 3597–3607 (2014).

[190] Kümmel, F. *et al.* Circular motion of asymmetric self-propelling particles. *Phys. Rev. Lett.* **110**, 198302 (2013).

[191] Gao, Y. Personal consultation (2020).

[192] Scholz, C., Ldov, A., Pöschel, T., Engel, M. & Löwen, H. Surfactants and rotelles in active chiral fluids. *Sci. Adv.* **7**, eabf8998 (2021).

[193] Yeo, K., Lushi, E. & Vlahovska, P. M. Collective dynamics in a binary mixture of hydrodynamically coupled microrotors. *Phys. Rev. Lett.* **114**, 188301 (2015).

[194] Yeo, K., Lushi, E. & Vlahovska, P. M. Dynamics of inert spheres in active suspensions of micro-rotors. *Soft Matter* **12**, 5645–5652 (2016).

[195] Asakura, S. & Oosawa, F. On interaction between two bodies immersed in a solution of macromolecules. *J. Chem. Phys.* **22**, 1255–1256 (1954).

[196] Kroy, K., Chakraborty, D. & Cichos, F. Hot microswimmers. *Eur. Phys. J. Spec. Top.* **225**, 2207–2225 (2016).

[197] Ishikawa, T. & Hota, M. Interaction of two swimming paramecia. *J. Exp. Biol.* **209**, 4452–4463 (2006).

[198] Jana, S., Um, S. H. & Jung, S. Paramecium swimming in capillary tube. *Phys. Fluids* **24**, 041901 (2012).

[199] Zhang, P., Jana, S., Giarra, M., Vlachos, P. & Jung, S. Paramecia swimming in viscous flow. *Eur. Phys. J. Spec. Top.* **224**, 3199–3210 (2015).

[200] Matas-Navarro, R., Golestanian, R., Liverpool, T. B. & Fielding, S. M. Hydrodynamic suppression of phase separation in active suspensions. *Phys. Rev. E* **90**, 032304 (2014).

[201] Roca-Bonet, S., Wagner, M. & Ripoll, M. Clustering of self-thermophilic asymmetric dimers: the relevance of hydrodynamics. *Soft Matter* **18**, 7741–7751 (2022).

[202] Schneider, E. & Stark, H. Optimal steering of a smart active particle. *EPL* **127**, 64003 (2019).

[203] Zöttl, A. & Stark, H. Modeling active colloids: From active brownian particles to hydrodynamic and chemical fields. *Annu. Rev. Condens. Matter Phys.* **14** (2022).

[204] Muiños-Landin, S., Fischer, A., Holubec, V. & Cichos, F. Reinforcement learning with artificial microswimmers. *Sci. Robot.* **6**, eabd9285 (2021).

[205] Menzel, A. M., Saha, A., Hoell, C. & Löwen, H. Dynamical density functional theory for microswimmers. *J. Chem. Phys.* **144**, 024115 (2016).

[206] Noguchi, H., Kikuchi, N. & Gompper, G. Particle-based mesoscale hydrodynamic techniques. *EPL* **78**, 10005 (2007).

[207] Shendruk, T. N., Bertrand, M., Harden, J. L., Slater, G. W. & de Haan, H. W. Coarse-grained molecular dynamics simulations of depletion-induced interactions for soft matter systems. *J. Chem. Phys.* **141**, 244910 (2014).

[208] Yang, M. *et al.* Effect of angular momentum conservation on hydrodynamic simulations of colloids. *Phys. Rev. E* **92**, 013301 (2015).

[209] Gao, Y., Balin, A. K., Dullens, R. P., Yeomans, J. M. & Aarts, D. G. Thermal analog of gimbal lock in a colloidal ferromagnetic janus rod. *Phys. Rev. Lett.* **115**, 248301 (2015).

[210] Gao, Y., Romano, F., Dullens, R. P., Doye, J. K. & Aarts, D. G. Directed self-assembly into low-density colloidal liquid crystal phases. *Phys. Rev. Mater.* **2**, 015601 (2018).

[211] Gao, Y., Dullens, R. P. & Aarts, D. G. Bulk synthesis of silver-head colloidal rodlike micromotors. *Soft Matter* **14**, 7119–7125 (2018).

[212] Kuijk, A., Van Blaaderen, A. & Imhof, A. Synthesis of monodisperse, rodlike silica colloids with tunable aspect ratio. *J. Am. Chem. Soc.* **133**, 2346–2349 (2011).

[213] Gao, Y. & Kilfoi, M. L. Accurate detection and complete tracking of large populations of features in three dimensions. *Opt. Express* **17**, 4685–4704 (2009).

[214] Calandrini, V., Pellegrini, E., Calligari, P., Hinsen, K. & Kneller, G. R. nmoldyn-interfacing spectroscopic experiments, molecular dynamics simulations and models for time correlation functions. *JDN* **12**, 201–232 (2011).

Danksagung—acknowledgement

The completion of this thesis was only possible under circumstances which are not given for everybody.

Zuerst muss ich Katharina danken, die mich bei allen erdenklichen Vorhaben unterstützt und immer an meiner Seite stehen wird. Auch weiterhin werden schöne, schwierige, und unangenehme Situationen auf uns zukommen, und wir werden sie zusammen genießen, durchstehen, und zum Guten wenden.

Auch meine Familie und besonders meine Eltern haben einen riesigen Anteil an dieser Arbeit. Ihr wart dazu in der Lage mich während meines Studiums zu unterstützen und habt das mit Freude gemacht. Ganz zu schweigen von den ganzen moralischen und praktischen Hilfen die ihr mir mit auf den Weg gegeben habt. Ohne diese Unterstützung wäre ich jetzt nicht in dieser Situation.

I want to thank Marisol for mentoring me the last three years and helping me to become a better physicist. From the first day that we met, I was sure that you will not leave me alone with the difficult tasks that I might face. And indeed, your door is always open, whether I have a physics related problem or not, and you keenly tackle the issue, without making me feel stupid. Without you, the work as presented would not have been possible. I really enjoy working with you and I hope we will also stay long-term connected.

Auch Gerhard möchte ich danken. Du warst immer bereit mit mir über meine Arbeit zu diskutieren, und hast mich mit Deinen Anregungen, Hinweisen, und Kommentaren maßgeblich unterstützt.

I am very grateful for the collaboration with Yongxiang and Dirk. Although, the possibility for this collaboration was an important ingredient for me to choose this project for my PhD, I would never have guessed that I will feel so comfortable in our meetings.

Among all PhD students in our institute, very special thanks goes to Marisol's students, Carlos, Rodrigo, and Sergi. The help we received from each other sometimes helped me to save hours of redundant work. I received even much more essential help from Carlos, who did not only help me to survive in the first weeks, but also provided me with an introduction to GPU-computing and with CUDA MPC examples and code snippets of inestimable value for my work.

Of inestimable value for my well being during the PhD were all the times that I shared with Raju, Christian and Flo. I enjoyed all of your company, our discussions, (planned) bike trips, the cooking together, and of course also the FIFA evenings. Especially, Raju, for being a very comfortable person to share the room with at conferences, or on common vacations, apart from that one night, you know, where the door was locked... That was very special time that I will never forget.

I am also very grateful for the readiness of all of the members of the committee for this thesis. Prof. Dr. Joachim Krug, Prof. Dr. Hartmut Löwen, Prof. Dr. Malte Gather, and Dr. Jiarul Midya. I am very happy for all of you being part of the committee and thus was also very happy that all of you straightforwardly agreed to be part of the committee.

Zuletzt möchte ich meinen Freundinnen und Mitstreiterinnen aus der Friedensbewegung danken. Unsere gemeinsame Überzeugung und Engagement erden mich regelmäßig, halten mich am Boden, und geben mir die Zuversicht und Kraft alles gemeinsam zu bewerkstelligen.

... der Zukunft zugewandt

Data availability

All collected data and the underlying codes used as explained in section A.1 are archived on the Juelich Data Access (JUDAC) file system in an account under principle investigation of Dr. habil. Marisol Ripoll and can be made available upon reasonable request. The underlying data of manuscript [M] is available from the corresponding authors upon reasonable request.

Erklärung

Hiermit versichere ich an Eides statt, dass ich die vorliegende Dissertation selbstständig und ohne die Benutzung anderer als der angegebenen Hilfsmittel und Literatur angefertigt habe. Alle Stellen, die wörtlich oder sinngemäß aus veröffentlichten und nicht veröffentlichten Werken dem Wortlaut oder dem Sinn nach entnommen wurden, sind als solche kenntlich gemacht. Ich versichere an Eides statt, dass diese Dissertation noch keiner anderen Fakultät oder Universität zur Prüfung vorgelegen hat; dass sie—abgesehen von unten angegebenen Teilpublikationen und eingebundenen Artikeln und Manuskripten—noch nicht veröffentlicht worden ist sowie, dass ich eine Veröffentlichung der Dissertation vor Abschluss der Promotion nicht ohne Genehmigung des Promotionsausschusses vornehmen werde. Die Bestimmungen dieser Ordnung sind mir bekannt. Darüber hinaus erkläre ich hiermit, dass ich die Ordnung zur Sicherung guter wissenschaftlicher Praxis und zum Umgang mit wissenschaftlichem Fehlverhalten der Universität zu Köln gelesen und sie bei der Durchführung der Dissertation zugrundeliegenden Arbeiten und der schriftlich verfassten Dissertation beachtet habe und verpflichte mich hiermit, die dort genannten Vorgaben bei allen wissenschaftlichen Tätigkeiten zu beachten und umzusetzen. Ich versichere, dass die eingereichte elektronische Fassung der eingereichten Druckfassung vollständig entspricht.

Teilpublikationen

J.M., Y. Gao, C.A. Ramírez-Medina, D.G.A.L. Aarts, G. Gompper, and M. Ripoll, *Simultaneous emergence of active turbulence and odd viscosity in a colloidal chiral active system*, 28 September 2022, PREPRINT (Version 1) available at Research Square [https://doi.org/10.21203/rs.3.rs-2072915/v1]

Jülich, 4.11.2022

Joscha Mecke